River landform dynamics detection and responses to morphology change in the rivers of North Luzon, the Philippines

Qing Li

SUBMITTED IN FULFILMENT OF THE REQUIREMENTS FOR THE DEGREE OF

Doctor of Philosophy

SCHOOL OF GEOGRAPHICAL AND EARTH SCIENCES

COLLEGE OF SCIENCE AND ENGINEERING

UNIVERSITY OF GLASGOW

MARCH 2023

Abstract

River morphology detection has been improved considerably with the application of remote sensing and developments in computer science. However, applications that extract landforms within the active river channel remain limited, and there is a lack of studies from tropical regions. This thesis developed and then applied a workflow employing Sentinel-2 imagery for seasonal and annual river landform classification. Image downscaling approaches were investigated, and the performance of object-based image segmentation was assessed. The area to point regression kriging (ATPRK) approach was chosen to downscale coarser 20 m resolution Sentinel-2 bands to finer 10 m resolution bands. All features were set or processed at 10 m resolution before applying support vector machine (SVM) classification. To improve machine learning classification accuracy, Sentinel-2 acquisitions across one year, which incorporates multiple seasons, should be used. For rivers with different hydrological or geology settings, the thesis considered collecting river specific ground truth data to build a training model to avoid underfitting of models from other hydrological/geological settings. Applying the workflow, three landforms (water, unvegetated bars and vegetated bars) were classified within the active channel of the Bislak, Laoag, Abra and Cagayan Rivers, north Luzon, the Philippines, between 2016 to 2021, respectively. The spatial-temporal river landform datasets enabled the quantitative analysis of the river morphology changes. Water and unvegetated bars showed clear seasonal dynamics in all four rivers, whilst vegetated bars only showed seasonality in the rivers located in the northwest Luzon (the Bislak, Laoag and Abra Rivers). This thesis employed correlated coefficients to investigate the longitudinal correlation between river landforms and active width. It was found that vegetated bar areas always have strong significant correlations ($\geq$0.67) with the active widths in all four rivers, whilst correlation coefficients between vegetated bar areas and active widths in the wet season are higher than that in the dry season. Ensemble empirical mode decomposition (EEMD) was applied to detect landform periodicity; this method indicated that water and vegetated bars commonly showed synchronised fluctuations with precipitation, while unvegetated bars had an anti-phase oscillation with precipitation. In the case of EEMD, deviations from periodic consistency in river pattern may reflect the influence of extreme events and/or human disturbance. Coefficient of variation (COV) was then used to evaluate the stability of the landforms; results suggested that the interplay of faults, elevation, confinement and tributary locations impacted landform stability. Finally, tributary inflow impacts on the mainstem river were investigated for eight

tributaries of the lowland Cagayan River, also on Luzon Island. Longitudinal variations in channel morphology and stability, and temporal changes in landform frequency, using Simpson's diversity index and COV, showed downstream widening associated with tributaries that was controlled by water discharge, with a secondary sediment flux effect. Overall, this thesis provided a novel example of combining remote sensing and GIS science, computing science, statistical science, and river morphology science to study the earth surface processes synthetically and quantitatively within river active channels in the tropical north Luzon, the Philippines. This work demonstrated how the fusion of techniques from these disciplines can be used to detect and analyse river landform changes, with potential applications for river management and restoration.

Acknowledgements

When I sit down to write this section of my thesis, I start feeling my PhD project is coming to an end. It has been the longest time that I focused on one thing since I was born but I never regret that I did a PhD in my best youth time. I recall in the autumn of 2018, I traveled 7,931 km from Beijing to Edinburgh to start my new life of PhD in the UK. Everything was completely new to me, and I learned to live independently. I met wonderful supervisors and colleagues here; I met many good friends here; I met my love here.

I would like to thank Professor Trevor Hoey for his great efforts in supervising me, teaching me, and giving guidance to me. I still remember it was drizzling the first day I met with Trevor at the main gate of the University of Glasgow. Trevor guided me to visit the East Quad and introduced me to our school staff. I was lucky to be placed at an office desk with a beautiful garden view, which inspired me a lot to work with a good mood every day. Trevor also provided many opportunities for me to practice my academic communication skills, and these built my confidence in my academic networking. I would like to thank my supervisor Professor Richard Williams, for he was always there supporting me with my PhD project and caring about my physical and mental health. Moreover, Richard helped me a lot on improving my English expressions and writings. I appreciate it very much that Richard gave me a lot of patience for training my academic speaking and writing skills, which will be a great benefit for my future academic life. Trevor and Richard helped me a lot to win my PhD scholarship & travelling and conference fundings, designed a very professional PhD training plan for me, and co-supervised me over the past years. I would like to thank my supervisor Dr. Brian Barrett, for his professional guidance in achieving remote sensing techniques for the whole project. I am grateful for Brian's precise advice for building my classification workflow, which saved me from trouble. Also, Brian always gave me a lot of kindness and support, which encouraged me to be a more optimistic person. I am so lucky to have three wonderful supervisors for my PhD and it is my great honour to be their student. I would also like to thank Dr. Richard Boothroyd who is a research associate of my research group as well as my good friend. Richard Boothroyd worked in the same office as me, and he gave me advice on writing, provided help to my figure visualization, and shared his research experience with me. I would thank my friends & colleagues Pamela Tolentino and Eilidh Stott, for our beautiful memories of working and traveling together in the Philippines and UK. Besides, I would like to say thanks to my

colleagues Esma and John from the Philippines for looking after me very well during my field trip in the northwest Luzon, the Philippines. Meanwhile, I thank my external SAGES supervisor Dr. Mikael Attal, who provided very nice insights of object-based image analysis and supported me to get SAGES travelling fund to Vienna to present my work at EGU2022 conference.

I would also thank all colleagues who I worked with as a GTA staff in the School of Geographical and Earth Sciences. I thank Craig MacDonell for helping me with attending the GIS training workshop in Lisbon and sharing GIS course teaching skills with me. I wish to thank our Graduate School Manager Heather Lambie and Support Administrator Isabel Lightbody for always giving me professional and patient advice/ guidance in the past years. I am so lucky to meet so many nice people in the University of Glasgow, and their kindness, warmheartedness and professional working attitudes built my unforgettable memories in Glasgow.

I want to say thanks to my dear boyfriend Yalei Yang who was a PhD student in Statistics and has just got his PhD certificate. In research, Yalei guided me to the topic of machine learning and code programming. In daily life, Yalei is my excellent partner who supports me to finish my PhD life. We accompanied each other to survive the hardest three years of covid time, and I will also never forget the happy time we stayed together in the UK and Europe. I want to say big thanks to my mother and my father. They gave me faith and courage all the time. They have always been teaching me to be virtuous and honest since I was very young. Although I have not seen them physically for over three years because of Covid and thesis writing, I got their encouragement through video calls every day. I also thank all of my good friends I met in Glasgow who have given me kindness and support, and spent hilarious time with me.

In the end, I would like to thank the China Scholarship Council and University of Glasgow to fund my PhD jointly. Although what I have done in this thesis is just an extremely tiny step of river science, I wish to dedicate this thesis to improving humans' understanding of rivers. I will always keep moving to make our earth better in the future.

Qing Li

March 2023, Glasgow

Author's declaration

Thesis presented here is the result of my original work, except where materials from other sources (e.g. publicly-available remote sensing data and figures) have been properly cited. I should acknowledge that this thesis has not been submitted for any degree at the University of Glasgow or other institutions.

Chapters 4, 5, and 6 in this thesis are presented as an 'Alternative Format Thesis'. The guidelines for an 'Alternative Format Thesis' derived from the University Code of Practice has been followed accordingly; hence the much of the texts, figures, and tables presented in the Chapter 4, 5 and 6 are identical to the published or submitted versions. Parts of the supplementary materials from those papers (e.g. supplementary figures or tables) have been moved into the body of these chapters to provide easier readability of the thesis. As material in Chapters 4-6 is from co-authored papers, the first-person plural (we) is used in those chapters.

Overall texts, figures and tables from the Chapter 4 are reformatted version of a published paper by Qing Li, Brian Barrett, Richard Williams, Trevor Hoey and Richard Boothroyd, 2022, Enhancing performance of multi-temporal tropical river landform classification through downscaling approaches, *International Journal of Remote Sensing*, 4 Volume 43, 2022 - Issue 17, https://doi.org/10.1080/01431161.2022.2139164. Overall texts, figures and tables in Chapter 5 are reformatted version of a manuscript submitted to *Earth Surface Processes and Landforms*, which has been under review, preprint available at https://doi.org/10.31223/X5D66G. Overall texts, figures and tables from the Chapter 6 are reformatted version of a manuscript submitted to *Geomorphology*, preprint available at http://dx.doi.org/10.2139/ssrn.4392184.

Qing Li

March 2023, Glasgow

Data availability

Data for Chapter 4 can be accessed via doi: 10.5525/gla.researchdata.1355.

Data for Chapter 5 and 6 will be accessed after peer-review from the journals.

Notation

The following symbols are used in this thesis:

A	area
ANN	Artificial Neural Network
ATPRK	area to point regression kriging
AW	active width
BA	unvegetated bar accuracy
C	confluence
COV	coefficient of variation
CS	component substitution
D	bedload grain size
DEM	digital elevation model
DT	difference of temperature
EEMD	ensemble empirical mode decomposition
EMD	empirical mode decomposition
ENSO	El Niño–Southern Oscillation
EO	earth observation
EOF	empirical orthogonal function expansion
Eq.	equation
ESA	European Space Agency
EVI	enhanced vegetation index
F	bedload flux
GEOBIA	Geographic Object Based Image Analysis
GPM IMERG	Global Precipitation Measurement
IMF	Instinct Mode Function
K-S	Kolmogorov-Smirnov
LiDAR	Light Detection and Ranging
LR	logistic regression
LSMS	Large Scale Mean Shift
LULC	land use and land cover
M	mainstream/mainstem
MEVI	modified enhanced vegetation index
MRA	multi-resolution analysis
MSI	multispectral instrument
NDMI	normalised difference moisture index
NDVI	normalised difference vegetation index
NDWI	normalised difference water index
NE	northeast
NN	neural networks
NW	northwest
OA	overall accuracy
OBIA	Object Based Image Analysis
P	precipitation
PACE	Pre-Aerosol Clouds and ocean Ecosystem
PCA	principal components analysis
Prop	proportion

Q	discharge
R	ratio
RF	random forest
S	Slope
SAR	synthetic-aperture radar
SD	standard deviation
SDI	Simpson's diversity index
SLIC	simple linear iterative clustering
SP	stream power
SRTM	Shuttle Radar Topography Mission
SVM	support vector machine
T	tributary
TIR	thermal infrared
UAV	Unmanned Aerial Vehicle
USGS	U.S. Geological Survey.
VA	vegetated bar accuracy
VI	vegetation index
W	width
WA	water accuracy

List of Figures

Figure 1-1. Locations of the studied rivers in North Luzon, the Philippines. Background is IfSAR DEM data (Grafil and Castro 2014). Blue lines denote the studied extents of the Bislak, Laoag, Abra and Cagayan Rivers. 17

Figure 2-1. Methods used for water delineation of the current literatures (source: Bijeesh and Narasimhamurthy 2020). 26

Figure 2-2. Hierarchical organisation of a stream system and its habitat subsystems (source: Frissell et al. 1986).....31

Figure 2-3. A sketch of process-based channel pattern classification on sinuosity, braiding and anabranching degrees (source: Brice 1978; Li, Yan, and Boota 2022). 32

Figure 2-4. Schematic diagram of river channel patterns classification (source: Li, Yan, and Boota 2022).....32

Figure 2-5. Identifying different forms of confinement across a range of river types (source: Fryirs, Wheaton, and Brierley 2016). 33

Figure 3-1. Workflow outlining the methods used in this thesis. 42

Figure 3-2. Samples of Sentinel-2 imagery for a section of the Bislak River captured on six dates at an approximate 2-month interval in 2019.....43

Figure 3-3. Aerial images and their corresponding field ground pictures in 2019. (i)-(ii) are from the upper reach of the Bislak River; (iii)-(iv) are from mid-reach of the Bislak River; (v)-(vi) are from lower reach of the Bislak River. 45

Figure 3-4. (a)-(c) Manually digitised river landform classification on three dates in 2018 in a short reach of the Bislak River. (d) overlay of the water extent from the images in (a)-(c)....46

Figure 3-5. Comparison of (a) a manually digitized classification map with (b) Sen2cor based scene classification map.....47

Figure 3-6. Segmentation examples using Large Scale Mean Shift method. (a) Sentinel-2 Level 2A image for part of the Bislak River, 1.01.2018. (b) ATPRK image of the same area. (c)mean value of Band 6 in the ATPRK image after segmentation. (d) enlarged area (see boxes in a,b,c). 49

Figure 3-7. Comparison of (a) LSMS segmentation map and (b) manually digitised ground truth map. See text for explanation of the blue box in (a). 50

Figure 3-8. Ten sub reaches of the experimental area on the Bislak River with serial numbers. 51

Figure 3-9. Ground truth object mutual corrections workflow. 51

Figure 3-10. The 'Thiessen-channel' segments generation procedure. See text for details. ...54

Figure 3-11. An example of a random data series decomposition using sifting method (source: Kong et al. 2015). For the random series (blue lines) in (a) and (b), the upper and lower red dot lines in (b) denote the envelopes of the random data series. The green line in (b) is the mean curve of the envelopes. (c) presents the results using sifting process to decompose the random series in (a) and (b). 58

Figure 4-1. (a) Study area showing locations of the (b) Bislak, (c) Laoag and (d) Abra Rivers in northwest Luzon, the Philippines.....67

Figure 4-2. Workflow for river landform classification. 70

Figure 4-3. Selected imagery extent for building optimal training model in the Bislak River. Background is the true colour Sentinel-2 image dated 1 January 2018.....72

Figure 4-4. Ten sub-reaches of the experimental area with serial number. Background is the true colour Sentinel-2 Level-2A image dated 1 January 2018. 73

Figure 4-5. Sample of segmentation results for (a) super-resolution, (b) resampling and (c) ATPRK. Segmented Objects are categorised by red boundaries. Background images are the composite of band 5 (central wavelength: 704.1 nm), band 6 (central wavelength: 740.5 nm)

and band 7 (central wavelength: 782.8 nm) of downscaled Sentinel-2 Level-2A images dated 1 January 2018. 75

Figure 4-6. Classification on an upstream reach of Bislak River; (a) is the true colour Sentinel-2 image with training and testing area, (b) is the manually digitised ground truth representing white extent in (a), and (c) is the output classification. Background image is the true colour Sentinel-2 Level-2A image dated 1 January 2018. 77

Figure 4-7. Time series for the testing accuracy of the multi-temporal training model across three years (2017-2019). 79

Figure 4-8. Comparisons of three testing datasets evaluated by overall accuracy (OA), water accuracy (WA), unvegetated bars accuracy (BA) and vegetated bars accuracy (VA). 80

Figure 4-9. Subset classification results of Bislak, Laoag and Abra Rivers across different times of different years. Complete classification coverages can be accessed from the link in the Data Availability section. 82

Figure 5-1. (a) The Philippines; red box is the study area in north-west Luzon shown in (b); (b) The Bislak, Laoag and Abra catchments, with extents of riverscapes that were analysed shown as black lines. (c - e) PlanetScope satellite imagery (dated December 2019) showing representative reaches of each river (image centres: Bislak 18.23 N,120.65 E; Laoag 18.13 N, 120.67 E; Abra 17.63 N, 120.68 E), with extents indicated on (b). (f - i) Oblique photographs of riverscapes along the Bislak River. 89

Figure 5-2. The timing of Sentinel-2 imagery acquisitions used in seasonal change investigations, for the Bislak, Laoag and Abra Rivers. 90

Figure 5-3. Ensemble Empirical Mode Decomposition (EEMD) on GPM IMERG catchment-averaged (every 10 days) precipitation data from the Abra catchment. (a) Upper plot (blue) is the precipitation data for the Abra River catchment. The subsequent five plots (green) are decomposed Instinct Mode Functions (IMFs), and the lowest plot (purple) is the residual of the decomposition. (b) The significance of the IMFs, where T = mean period (years) and E = Energy density. The mean period, the energy density for the added noise and confidence bands

are calculated using the method of Huang (2004). (c) IMF amplitude in quantity peak as a function of signal frequency from fast Fourier Transformation (Cerna and Harvey 2000). This shows the dominant frequencies of each IMF, which correspond to the main periods of the decomposed components. 94

Figure 5-4. Classified river landforms for a segment of the Abra River during a one-year period. Seasonal variation in landforms is evident during the year. 96

Figure 5-5. Longitudinal and temporal variation in landform proportions, and active width (AW), of the Bislak, Laoag and Abra rivers between February 2016 and July 2021. Distance starts from the estuary to the upstream. Classification maps are available from the digital data supplement (available after peer-review).....97

Figure 5-6. River segmentation of the Bislak, Laoag and Abra Rivers. 99

Figure 5-7. Landform frequency maps for the (a) Bislak, (b) Laoag and (c) Abra Rivers. ...100

Figure 5-8. (a) Longitudinal trend in active width (AW) and mean area of three landforms (water, unvegetated bars, vegetated bars) for the Abra River, for wet and dry seasons. (b) Matrix plots represent correlations between mean values of landform areas and AW. Histograms illustrate mean value distributions at equal spaced spatial distance along the river. Kernel distribution estimation is shown using contour plots. Tables above each matrix plot summarise correlation coefficients (r) and associated statistical significance (p) between landform areas and AW in wet season and dry season. 102

Figure 5-9. (a) Longitudinal trend in active width (AW) and mean proportion of three landforms (water, unvegetated bars, vegetated bars) for the Laoag River, for wet and dry seasons. (b) Matrix plots represent correlations between mean values of landform proportions and AW. Histograms illustrate mean value distributions at ~410 m spatial distance along the river. Kernel distribution estimation is shown using contour plots. Tables above each matrix plot summarise correlation coefficients (r) and associated statistical significance (p) between landforms proportion and AW in wet season and dry season. 103

Figure 5-10. Ensemble Empirical Mode Decomposition (EEMD) IMF for precipitation (P; IMF 4) and landform (water, unvegetated bars, vegetated bars; IMF 2) areas. IMF 2 data (blue lines) are presented for sub-reaches (numbers as in Figure 5-6) for the Bislak, Laoag and Abra Rivers. In all cases, the periodicity is c.12-13 months. Red vertical lines are at each annual peak. Periods with light grey shading are not consistent with neighbouring reaches, whereas the light green shading shows periods that are consistent. See the text for explanations. 106

Figure 5-11. Detection of morphology change (in red and blue circle) between 2020 and 2021 in sub reach 2 of Abra River. 107

Figure 5-12. Mapped morphologic seasonal change and yearly change in a sub-reach of Abra River.....109

Figure 5-13. Channel settings, including active width, degree of confinement (confined / partly confined / unconfined), compared to the covariance (COV) spatial landform series for the Bislak, Laoag and Abra Rivers (water, unvegetated bars and vegetated bars shaded in thick lines are represented by smoothed values). Distance starts from the estuary to the upstream. 111

Figure 6-1. Cagayan River study area: (a) Global location of the Philippines. (b) The Cagayan River network on Luzon Island, the Philippines. (c) Study segment of the Cagayan River showing the location of remote sensing landform classification training and test areas, where T1-T8 are major tributaries. Reaches in the wet (d) and dry (e) seasons; (d) and (e) are true colour images from Sentinel-2 acquisitions. 120

Figure 6-2. (a) Averaged annual peak accumulated precipitation (10 days) for 2018-2021 in the Cagayan catchment, based on analysis of Integrated Multi-satellite Retrievals for Global Precipitation Measurement (GPM IMERG) data. (b) Digital Elevation Model of the Cagayan catchment, from 5 m resolution IfSAR data (Grafil and Castro 2014). White lines show the mainstem and tributary network. T refers to tributary. 122

Figure 6-3. Ratios of tributary to mainstem area (A_R), area times precipitation ($A_R \times P_R$), slope (S_R) and stream power (SP_R) for each tributary in a segment of the Cagayan River. Ratios are

shown as proportional symbols, normalised by the largest value among the eight ratios. T1 to T8 are in the direction from north to south. 127

Figure 6-4. Longitudinal variation in elevation, active width and river landform proportion (water, unvegetated and vegetated bars) for a segment of the Cagayan River, the Philippines. Distance to downstream is measured from a point 28 km upstream of the sea. Landform proportions are shown from 19 March 2018 to 14 September 2021. Elevation is shown along a transect that corresponds to the longitudinal valley bottom. Active width and landform proportions are shown along a transect that corresponds to the centreline of the active channel. The valley bottom line is c.10 km longer than the channel centreline. Vertical dashed lines on the figure indicate tributary locations. Relative SP_R values (0 to 1 scale, where 1 is the largest measured SP_R ratio) are noted on the elevation plot. 128

Figure 6-5. (a)-(c) Landform frequency of studied period; (d) landform classification on 12 February 2020; (e) True colour Sentinel-2 image on 12 February 2020. White rectangles represent typical vegetated bars. 130

Figure 6-6. (a) Relationship between predicted (from Eq. 6-7) and observed bankfull river width. (b) Width changes downstream of tributaries as a function of stream power ratio (SPR). 133

Figure 6-7. Longitudinal trends in active width and confinement, with positions of anthropogenic bank structures. (b-d) Longitudinal trends in coefficient of variation (COV) for water area, unvegetated bar area and vegetated bar area. 135

Figure 6-8. River landform diversity measured using Simpson's Diversity Index (*SDI*) at river confluences along a segment of the Cagayan River. *SDI* is in the range 0 (the same landform type present on all images) to 1 (each landform type is present in 33.3% of the available images). Darker shading shows where landform types vary most between images during the four-year study period. Both forced bars (e.g., point bars on (d), (e), (g) and (h)) and free bars (bar complexes on (a), (d), (f) and (g)) show high diversity due to unvegetated sediment deposits being colonized by vegetation during dry seasons. 136

Figure 7-1. (a) Locations of Bislak, Laoag, Abra and Cagayan River catchments in north Luzon. (b) Climate types in North Luzon (source: Tolentino et al. 2016). 139

Figure 7-2. Landform classification maps in the Cagayan River using $Model_{NW}$ and $Model_{NE}$. (a)-(f) were derived from $Model_{NW}$ and (g)-(l) were derived from $Model_{NE}$. 141

Figure 7-3. (a) Longitudinal trends in active width (AW) and mean area of three landforms (water, unvegetated bars, vegetated bars) for the Cagayan River, for wet and dry seasons. (b) Matrix plots representing correlations between mean values of landform areas and AW. Histograms illustrate mean value distributions at ~440 m intervals along the river. Labels summarise correlation coefficients (r) and associated statistical significance (p) between landforms' areas and AW in wet and dry seasons. 145

Figure 7-4. Matrix plots to represent correlations between mean values of landform proportions and AW. Histograms illustrate mean value distributions at ~440 m intervals along the river. Labels summarise correlation coefficients (r) and associated statistical significance (p) between landforms proportion and AW in wet and dry seasons. 146

Figure 7-5. Simpson's diversity indices of the Bislak, Laoag, Abra and Cagayan Rivers. ...152

List of Tables

Table 2-1. Latest remote sensing technology and sensors used for water resources, hydrological fluxes, drought and flood mapping (Wang and Xie 2018). Additional sensors/satellites reviewed in this thesis were denoted by *. 25

Table 3-1. Bislak, Laoag, Abra and Cagayan River preliminary investigations. 41

Table 4-1. Sentinel-2 acquisition dates for each river from 2017 to 2019. 68

Table 4-2. Selected indices for processing classification. 69

Table A1. Numbers of training and testing objects for landforms when applying the three downscaling approaches. 71

Table A2. Numbers of objects used in the single-date model. 72

Table A3. Numbers of objects used in the multi-date model. 73

Table 4-3. Accuracy assessments for resampling, ATPRK and super-resolution approaches. (All values range between 0 – 1, whereby 0 indicates the lowest accuracy and 1 indicates the highest accuracy.) 76

Table 4-4. Accuracies on different dates in 2018 using training model from single date. (All values range between 0 – 1, whereby 0 indicates the lowest accuracy and 1 indicates the highest accuracy.).....78

Table 4-5. Test accuracies of Laoag River in 2018. (All values range between 0 – 1, whereby 0 indicates the lowest accuracy and 1 indicates the highest accuracy.).....81

Table 4-6. Test accuracies of Abra River in 2019. (All values range between 0 – 1, whereby 0 indicates the lowest accuracy and 1 indicates the highest accuracy.).....81

Table 5-1. Assessment of SVM classification performance for the Bislak, Laoag and Abra Rivers for a selection of years. For each metric, a value of 1.0 would indicate perfect agreement. 95

Table 5-2. Correlations between landforms and active width (AW) for the Bislak, Laoag, Abra Rivers for wet and dry seasons. r refers to correlation coefficient, where r $\geqslant$ 0.60, text is bold. p refers to significance. 104

Table 6-1. Sentinel-2 acquisition dates for the Cagayan River from 2018 to 2021. Dates are in the format of DD/MM. 125

Table 6-2. Ratios of tributary to mainstem area (A_R), precipitation (P_R), slope (S_R) and stream power (SP_R) for each tributary in the segment of the Cagayan River. 126

Table 6-3. Slope and bankfull width changes after tributary inputs to the main Cagayan River (S_d: 5 km downstream averaged slope; S_u: 5 km upstream averaged slope; W_d: 100 m downstream width; W_u: 100 m upstream width; $Q_R = A_R \times P_R$). 131

Table 6-4. Sediment evaluations from Google Street View pictures on the nearby bridges. 133

Table 7-1. Comparisons between machine learning models used in three rivers of Northwest Luzon and the Cagayan River. 141

Table 7-2. Earth surface observations and measurements in the Bislak, Laoag, Abra and Cagayan Rivers. 143

Table 7-3. Seasonality in the Bislak, Laoag, Abra and Cagayan Rivers. 148

Table 7-4. Channel settings of the Bislak, Laoag, Abra and Cagayan Rivers. 150

Table 7-5. Examples using indices in river morphology studies which are excluded from this project. 154

Contents

Abstract i
Acknowledgements iii
Author's declaration v
Data availability vi
Notation 1
List of Figures 3
List of Tables 10
Contents 12
Chapter 1 - Introduction 16
1.1. Automated River Landform Detection 16
1.2. River landform dynamics and responses 18
1.3. Research Objectives and Aims 19
1.4. Thesis Structure 20
Chapter 2 - Background 22
2.1. Land Use and Land Cover (LULC) detection 22
2.1.1. Surface Water Detection 24
2.1.2. Vegetation and soils 26
2.2. Geomorphic patterns and classification of rivers 29
2.2.1. River pattern 29
2.2.2. Remote sensing application in river morphology detection 34
2.3. Remote sensing image segmentation and classification 35
2.3.1. Planform-based method 36
2.3.2. Contour-model based method 36
2.3.3. Traditional object-based method 37
2.3.4. Machine learning object-based method 39
Chapter 3 - Methods 41
3.1. Introduction 41
3.2. Materials 42
3.2.1. Remote sensing data selection 42
3.2.2. Aerial images and field observation 43
3.2.3. Unsupervised classification using Sen2Cor tool 45
3.2.4. Image Segmentation 47

3.2.5. Corrections on manually digitised ground truth objects 49
3.3. Spatial-temporal dataset generation 52
3.4. Ensemble Empirical Mode Decomposition 55
3.4.1. Sifting Procedures 55
3.4.2. EEMD 59
3.5. Simpson's index of diversity 59
3.6. Coefficient of variation 61
Chapter 4 - Enhancing performance of multi-temporal tropical river landform classification through downscaling approaches 62
Highlights 63
Abstract 63
4.1. Introduction 64
4.2. Study Area 66
4.3. Datasets and methods 67
4.3.1. Sentinel-2 imagery and ground truth digitisation 67
4.3.2. Image Pre-processing 68
4.3.3. Geographic Object Based Image Analysis (GEOBIA) machine learning 69
4.3.4. Downscaling choice 70
4.3.5. Optimal training model 71
4.3.6. Optimal testing dataset 74
4.4. Results and Discussion 75
4.4.1. Comparison of downscaling approaches 75
4.4.2. Training model investigation 76
4.4.3. Testing dataset selection 79
4.4.4. Model performance in nearby rivers 80
4.5. Conclusions 83
Chapter 5 - Seasonal and annual tropical river pattern change detection using machine learning 84
Abstract 85
5.1. Introduction 85
5.2. Study area 88
5.3. Data and methods 89
5.3.1. Sentinel-2 acquisitions 89
5.3.2. Geographic object-based image analysis 90

5.3.3. Catchment-averaged accumulated rainfall totals 92
5.3.4. Ensemble Empirical Mode Decomposition 92
5.4. Results 95
5.4.1 Machine learning model classification performance 95
5.4.2 River landform classification 96
5.4.3 Active width impacts on area and proportion of landforms 101
5.4.4 Temporal changes in sub-reach landforms 105
5.5. Discussions 107
5.5.1 River pattern classification 107
5.5.2. Spatial river landform sensitivity to channel settings 110
5.6. Conclusions 112
Chapter 6 - Response of a lowland tropical river to tributary inputs, Cagayan River, the Philippines 114
Abstract 115
Highlights 115
6.1. Introduction 116
6.2. Study Area 118
6.3. Data and Methods 120
6.3.1. Tributary rivers and sub-catchments 120
6.3.2. Precipitation 121
6.3.3. Elevation and Slope 122
6.3.4. Stream Power ratio 123
6.3.5. Support Vector Machine (SVM) landform classification 124
6.4. Results 126
6.4.1. Tributary stream power 126
6.4.2. River landform classification 127
6.4.3. Landform Frequency 129
6.5. Analysis and discussion 130
6.5.1 Slope increase and bankfull width expansion 130
6.5.2. Landform diversity at confluences 134
6.6. Conclusions 136
Chapter 7 - Discussion 138
7.1. River landform classification strategy 139
7.2. Seasonality in tropical river patterns of north Luzon 143

7.3. River landform dynamic change analysis 150
7.4. Perspectives of research 152
Chapter 8 - Synthesis and Conclusions 155
8.1. Assessment of Research Objectives 155
8.2 Conclusions 157
References 160
Appendix 195
A.1 195
A.2 196
A.3 197
A.4 198
A.5 199
A.6 200
A.7 201
A.8 202
A.9 202
A.10 203
A.11 203
A.12 204

Chapter 1 - Introduction

1.1. Automated River Landform Detection

Remote sensing technology has been widely employed in studying spatial-temporal geomorphological change in recent years. Free-access earth observation data with revisiting time varying from 10 days (e.g. Sentinel-2) to 16 days (e.g. Landsat 9) and software tools (e.g., Python, R) allow studies over large areas and recent several decades, especially enable explorations in remote regions where ground data are difficult to access. However, use of earth observation data remains very limited in many tropical regions, particularly due to persistent cloud cover, especially in the rainy seasons, that limits the use of visible wavelength imagery. However, recent growth in the accessibility of open data and new tools to fuse/merge images (Henshaw et al. 2019; Wang et al. 2016) have increased the potential to derive sufficient information to reliably detect landform and landcover. Recent image analysis research uses both pixel-based analysis (Khatami et al. 2016) and object-based analysis (Demarchi et al. 2020), often combined with image downscaling and machine learning classification, which together enhance spatial and temporal image interpretations and so extend understanding of geomorphological change with increasing spatial and temporal resolutions (Talukdar et al. 2020).

River morphology has been extensively investigated for several decades, using maps, aerial photography and, increasingly, satellite imagery (Baena-Escudero et al. 2019; Huylenbroeck et al. 2020; Rusnak et al. 2018; Smith et al. 2016). Many studies of river morphology and landform change are within temperate and Arctic regions (Bertrand and Liebault 2019; Demarchi et al. 2017; Vercruysse and Grabowski 2021), whilst river dynamics in the tropics remain less discussed (Dingle et al. 2019; Vijith and Dodge-Wan 2018), especially for remote areas. Many tropical regions experience frequent extreme weather events (e.g., typhoons, floods, extreme rainfalls). Highly variable water level, high turbidity and associated suspended sediment loads, high current velocity and mobile bed materials show important differences from temperate regions (Davies et al. 2008), although the lack of data from the tropics affects our ability to make reliable comparisons (Boulton et al. 2008). Hence, there is a pressing need to map river landform change in the tropical rivers more accurately and over larger areas. Machine learning provides one way to increase landform detection accuracy and to speed up

data collection. In many cases, mapping high spatial resolution in-channel landcover is very common and showing good classification performance (Demarchi et al. 2017). However, case studies of mapping high-resolution spatial-temporal landcover change using machine learning remain infrequent (Fazelpoor et al. 2022; Rodrigues et al. 2018; Zhiyi Fu 2020). Therefore, there is an opportunity to develop an efficient and straightforward operating workflow to enhance open data performance for river landforms classification. This development is the first goal of this thesis. The resulting spatial-temporal river landform datasets are then used to analyse the dynamics of the studied rivers, extending the database of Global River dynamics research into North Luzon, the Philippines. The rivers selected for this research are the Bislak, Laoag and Abra Rivers in northwest Luzon and the Cagayan River in northeast Luzon, the Philippines (Figure 1-1).

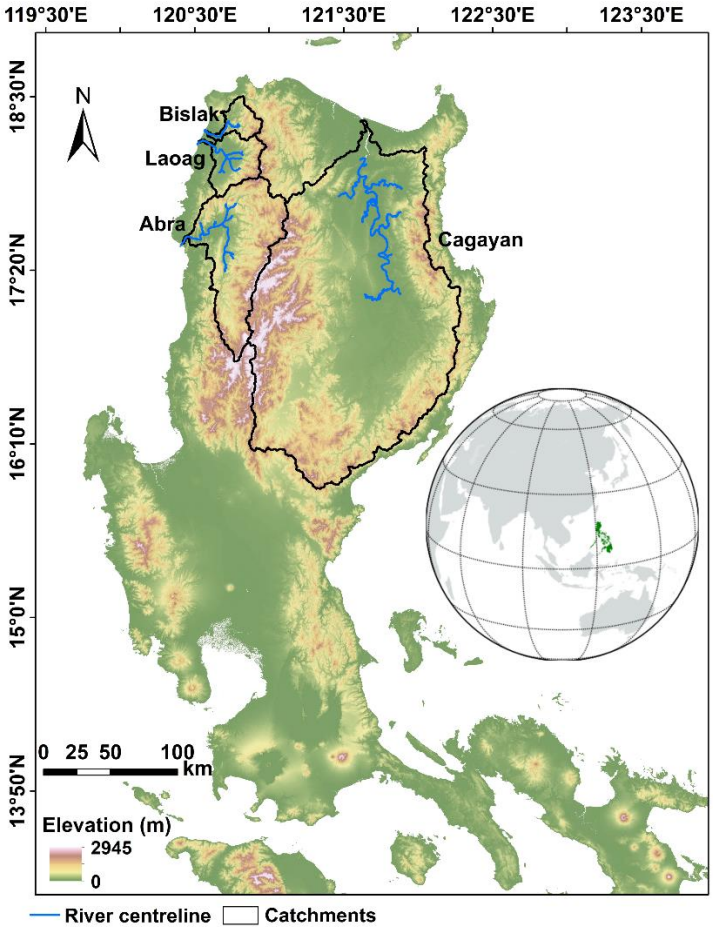

Figure 1-1. Locations of the studied rivers in North Luzon, the Philippines. Background is IfSAR DEM data (Grafil and Castro 2014). Blue lines denote the studied extents of the Bislak, Laoag, Abra and Cagayan Rivers.

1.2. River landform dynamics and responses

Given datasets of spatial-temporal classified river landforms (water, unvegetated bars, vegetated bars), the dynamics of these landforms and their spatial patterns can be investigated by a variety of approaches. To address the research objectives, in addition to visual inspection of sequential maps, this project uses statistical analysis, signal decomposition, landform frequency mapping and Simpson's diversity index mapping to detect patterns of river landform stability and change. Using multi-year continuous spatial-temporal data, investigation of spatial-temporal dynamics is applied to trace river landform developments (e.g., bar migration, vegetation growth and retreat). In the tropics, seasonality is a key factor impacting the landform detection and dynamics, and north Luzon exhibits distinct wet and dry seasons (Tolentino et al. 2022). Rivers show different behaviours in the dry and wet seasons, and external controls of channel setting (e.g., valley confinement, faults, tributaries, etc.) also influence the alluvial landforms. The annual wet and dry seasons cause variations in precipitation, temperature, and extreme event frequency that cause water drainage, sediment transport and vegetation growth to vary significantly between seasons. The seasonal dynamics of water drainage, sediment transport and vegetation processes cause adjustments to river landforms thereafter. For example, consistent high precipitation during the wet season brings high volumes of water and sediment. When input sediment volumes surpass the sediment transport capacity of the river, aggradation occurs, altering the bankfull width of the river (Candel et al. 2021). Persistent lateral or in-channel vegetated bars, which retain vegetation throughout both dry and wet seasons, protect these parts of the river system from being occupied by water channels.

Using extensive data sets of spatial-temporal river landform change from automated recognition, this project investigated the dynamics of river landforms in dry and wet seasons and over several years. The studied river catchments range in spatial scale from 586 km^2 (Bislak) to 27,684 km^2 (Cagayan). The Cagayan River is in a different climate zone to the other three rivers (Tolentino et al. 2016) and has less pronounced seasons compared to the rivers of northwest Luzon. The geological setting of the three northwest rivers produces contrasting patterns of confinement and drainage network structures, which are used to enhance understanding of river dynamics in this region. The larger Cagayan River has an extensive lowland reach and eight large tributaries that supply additional water and sediment to the mainstem of this lowland reach. Hence, the Cagayan River is used as a contrast with the steeper

rivers in the northwest, and also to specifically examine the impacts of tributaries on tropical river morphology and dynamics.

Rapid tracing river landform by generating spatial-temporal dataset gives potentials to enhance knowledge of river dynamics and thus, provide the insights and advice for river management work. The patterns of river landforms can reflect the landcover/land use change in the region caused by altering water flows (e.g. seasonal floods or extreme precipitations, water storage by dams), sediment volumes (e.g. sediment transport, gravel mining), ecosystem behaviours (e.g., vegetation growing and retreating, anthropogenic farming and fishing). Quantitative spatial-temporal analysis of river landform in this research enables to precisely detect landcover/land use change in the river channels, and therefore, encourages analysing reasons and processes making the river patterns. This work improves the efficiency of river dynamics analysis and predictions, which benefits the river restoration and management in the future.

1.3. Research Objectives and Aims

This project initially aims to develop a procedure for efficiently detecting and analysing spatial and temporal tropical river landform dynamics using free-access high resolution Sentinel-2 acquisitions. The project is designed to build a 'bridge' between remote sensing technology and river geomorphology. Hence, having processed the available remote sensing data using new tools, a range of geomorphological analyses were investigated. The project is not only intending to extend remote sensing applications to river landform detection, but also to explore cutting edge river geomorphology research by novel use of open remote sensing data.

To achieve the overall aim, the following objectives were identified:

(1) to design and apply an automated river landform classification workflow using free Sentinel-2 multi-spectral data and validate with manually digitised ground truth data;

(2) to further develop and evaluate the classification workflow in (1) by applying it to four rivers in North Luzon inter- and intra-annually, producing data for spatial-temporal analysis;

(3) to generate river landform (water, unvegetated bars and vegetated bars) spatial-temporal classification maps for the Bislak, Laoag, Abra and Cagayan Rivers, using the classification workflow in (2);

(4) to evaluate whether there is strong seasonality in the morphological dynamics of the North Luzon rivers and, if so, explore how the river landforms interplay with each other and with the active channel width;

(5) to assess how the river landforms respond to external river channel settings (valley confinement, faults, tributaries, etc.); and, how does river morphology respond to tributary inflows;

(6) to discuss how the generated data can be used to identify the impact of disturbance analysis on landforms change.

1.4. Thesis Structure

This thesis' empirical chapters are based on papers that have been published (Chapter 4) or manuscripts submitted for publication and archived on pre-print servers (Chapter 5 and Chapter 6). Further,

(1) Chapter 1 briefly has introduced the motivation for designing this project and has proposed the main aim and objectives.

(2) Chapter 2 reviews the relevant literatures. In this chapter, river geomorphological investigations and land surface detection research are introduced, and remote sensing applications to river morphology is reviewed.

(3) Chapter 3 presents the data and methods used in this research. The field location and observations are introduced firstly, then the project workflow is presented to justify the approach used, and finally some of methods are used to derive and analyse river geomorphology information are presented.

(4) Chapter 4 is from a published paper (doi: 10.1080/01431161.2022.2139164) in International Journal of Remote Sensing (Li et al. 2022). This paper investigated the optimal

workflow and models for river landform classification in the three northwest Luzon rivers. Accordingly, it establishes the principles for the river landform classifications used in the following chapters.

(5) Chapter 5 is from a submitted paper to Earth Surface Process and Landforms (preprint doi: 10.31223/X5D66G). This paper presents spatial-temporal river landform classification for the northwest Luzon rivers, and analyses seasonality, the effects of channel settings and temporal change of landforms over five years.

(6) Chapter 6 is from a submitted paper to Geomorphology (preprint doi: 10.2139/ssrn.4392184). This paper presents spatial-temporal river landform classification for a larger river, the Cagayan River in northeast Luzon, over four years. The paper focuses on the river response to eight large tributaries joining the lowland mainstem of the Cagayan River.

(7) Chapter 7 is a discussion that reviews all the classification for the four rivers, in four sections: River landform classification strategy; Seasonality in tropical river patterns of north Luzon; River landform dynamic change analysis; and, perspectives for future work.

(8) Chapter 8 answers the research objectives and presents the conclusions from the whole thesis.

Chapter 2 - Background

River pattern and landform changes are caused by multiple factors, including internal controls (e.g. processes of hydrology, sedimentology and ecology) and external controls (e.g. climate change, extreme events and human disturbance). River landscapes and its process in corridors are impacting each other under the frame of river systems (Ward et al. 2002). Hupp and Rinaldi (2007) suggested that water is the most proximal control on spatial patterns of perennial riparian vegetation in temperate fluvial systems. In the meantime, the riparian vegetation may also highly impact sediment erosion and deposition rates. Tropical river systems are often characterised by highly seasonal dynamics of water discharge and sediment loads (Milliman and Meade 1983; Syvitski et al. 2014), causing rapid channel migration or processes rates (Dingle et al. 2019). Additionally, human pressures on land use/cover can also alter the fluvial units' spatial patterns and trends (e.g., water conservation, gravel mining, and farming) (Mainali and Chang 2018; Xu et al. 2018). In recent years, many studies focused more on river management at reach scale, however, since the river landforms change at one location may induce the response of landforms at another location along the river, it is also important to establish network understandings at a larger scale (e.g., catchment scale) to maintain the river systematic sustainability (Gurnell et al. 2016). Hereby, integrating spatial-temporal landform patterns and processes from upstream to coast is essential to examining environmental controls and interactive schemes between the controls (e.g. bar stability response to stream power) in the river (Fausch et al. 2002; Gurnell et al. 2016; Ward et al. 2002), which provides insights to river structural complexity and river regulations/managements.

2.1. Land Use and Land Cover (LULC) detection

Land Use and land Cover generally refer to different concepts but are often used interchangeably (Hua 2017). Land Cover tends to describe the physical earth surface instead of human habitats which are defined as Land Use (Hua 2017). Along with the remote sensing technology development in recent decades, land change detection techniques have also been developed and extended (Singh 2010; Lu et al. 2010; Abd El-Kawy et al. 2011). Change detection was defined as the process of identifying differences in the state of an object or phenomenon by observing it at different times (Lu et al. 2010; Singh 1989). In practice of LULC change detection, multi-temporal remote sensing acquisitions provided accurate and timely data for quantitively observing the geographic objects and tracing the dynamics of the

LULC. Remotely sensed data has been applied to a variety of research. Lu et al. (2010) summarised ten aspects of research achieved by remote sensing, which are (1) land use and land cover (LULC) change; (2) forest and vegetation change; (3) forest mortality, defoliation and damage assessment; (4) deforestation, regeneration and selective logging; (5) wet land change; (6) forest fire and fire-affected area detection; (7) landscape change; (8) urban change; (9) environmental change (including drought monitoring, flood monitoring, monitoring coastal marine environments, desertification and landslide detection) ; and (10) other applications such as crop monitoring, shifting cultivation monitoring, road segments and change in glacier mass balance and facies. Beyond these aspects, a review of change detection applications from Théau (2022) also suggested several new topics: (11) habitat fragmentation; (12) herbivory such as insect defoliation and grazing; (13) invasive species; (14) soil moisture conditions; (15) georisk (e.g., earthquakes, volcanoes, subtle deformation, structural integrity); (16) permafrost monitoring (e.g., surface temperature, tree line); (17) water quality (e.g., temperature, productivity); (18) aquaculture (e.g., productivity); (19) oil spill (e.g., detection, oil movement).

There are a variety of methods to detect the LULC change. Singh (2010) illustrated ten techniques used in past decades: univariate image differencing; image regression; image ratioing; vegetation index differencing; principal components analysis (PCA); post - classification comparison; direct multi-date classification; change vector analysis; background subtraction; Kolmogorov-Smirnov test (K-S test). Théau (2022) also referred additional methods: linear transformation such as PCA and tasseled-cap transformation; multi-temporal spectral mixture analysis; and combined approaches of above methods. Singh (2010) concluded that these conventional methods have not been widely compared to each other. A lot of research only selected two or three methods to do comparisons, and conclusions varied from different case studies. The simple techniques such as image differencing, can sometimes perform better than more sophisticated transforms like PCA method. However, sophisticated techniques are good at dealing with bigger and more complicated data. With the development of computer science, in recent years, machine learning method has attracted massive interests in recognising LULC change and achieved very good progresses in practice (Demarchi et al. 2017; Demarchi et al. 2020; Liu et al. 2021; Maxwell et al. 2018).

In past decades, multi-spectral, hyper-spectral and thermal infrared (TIR) remote sensing data have been the most favoured for monitoring LULC change (Gago et al. 2015; Gerhards et al.

2019; Govender, Chetty, and Bulcock 2007; Hook et al. 1992; Melis et al. 2020). Multi-spectral remote sensing system, which usually measure between three to six spectral bands within the visible to middle infrared region of the electromagnetic spectrum (Govender, Chetty, and Bulcock 2007), has been improved to more spectral bands with the remote sensing technology development. For example, Sentinel-2 mission achieved observing 13 bands for one acquisition (https://sentinels.copernicus.eu/web/sentinel/sentinel-technical-guides). Hyper-spectral remote sensing system usually captures many, very narrow, contiguous spectral bands throughout the visible, near-infrared, mid-infrared, and TIR portions of the electromagnetic spectrum (Govender, Chetty, and Bulcock 2007; Nalepa 2021). Although TIR data is included in the hyper-spectral remote sensing system, it has been widely and individually investigated for improving land surface detection quality in recent years. Remote sensors from satellite (e.g., Landsat, Sentinel, MODIS) and Unmanned Aerial Vehicles (UAVs) provide acquisitions containing the wavelengths which are sensitive for recognising different LULC types such as dry bare soil, green vegetation and clear water (Govender, Chetty, and Bulcock 2007). A variety of indices such as Normalised Difference Water Index (NDWI) and Normalised Difference Vegetation Index (NDVI) were developed to differentiate a specific landform with a range of wavelength from others (Lu et al. 2010). Section 2.1.1 and 2.1.2 will further review the research about LULC detections on water, soils and vegetation.

2.1.1. Surface Water Detection

Surface Water is a critical resource that form the basis of all life and needs to be conserved for the future generation (Bijeesh and Narasimhamurthy 2020; Govender, Chetty, and Bulcock 2007). Whilst water can also be a source of inducing natural disasters such as floods and water logging (Gerhards et al. 2019). Therefore, it is essential to monitor and predict water change on the earth surface. Nowadays, remote sensing and Geographic Information System (GIS) technologies remain the most important role in detecting, measuring, and analysing water resources, drought and flood risk management (Wang and Xie 2018). For example, spectral response from remote sensing data can be used to determine whether the water body is pure or turbid, as pure water and turbid water have different spectral signature (Bijeesh and Narasimhamurthy 2020). Beyond of this, the special water issues (e.g., water resource mapping, satellite rainfall measurements, runoff simulation, flood induction mapping, etc.) were analysed and discussed by combining remote sensing, GIS, geostatistics and hydrological models together (Wang and Xie 2018). A work from Wang and Xie (2018) reviewed latest

remote sensing technology and sensors used for water detection (Table 2-1). Aside from the Table 2-1, the very popular Sentinel family from the Copernicus program has attracted a lot of attention since the first launch of Sentinel-1A in 2014 (Desnos et al. 2014). Sentinel satellites provided free-access moderate-high resolution data covering the world. For example, Sentinel-2 multi-spectral imagery have been widely used in global remote regions where are lack of commercial satellite detections (Li et al. 2022). Schmitt (2020) fused Sentinel-1 and Sentinel-2 on a pixel level to achieve the large-scale inland water mapping. Veettil et al. (2021) developed and automatic water extraction model through Sentinel-2 data and Google Earth Engine. Salama et al. (2022) presented a validation procedure for water quality products derived from Sentinel-2 (multi-spectral instrument) and Sentinel-3 (ocean and land colour instrument) in estuarine waters. Tarpanelli et al. (2021) illustrated the potentials of Sentinel-3 for river discharge assessments. Sentinel programme has a shorter history than many other satellite programmes (e.g., Landsat and MODIS), in the future work, Sentinel family has a great potential to integrate issues of water detection and encourage more systematic research on land surface/ground water.

Table 2-1. Latest remote sensing technology and sensors used for water resources, hydrological fluxes, drought and flood mapping (Wang and Xie 2018). Additional sensors/satellites reviewed in this thesis were denoted by *.

Application Fields	**Specific Contents**	**Examples of Sensors or Satellites**
Water resources	Snow	AVHRR, Terra/Aqua MODIS, Landsat, SSM/I, AMSR-E, CryoSat, Sentinel-1/2/3*, Gaofen*, etc.
	Glaciers	Landsat, ASTER, SPOT, ICESat, SRTM, Sentinel-2*, Gaofen*, etc.
	Soil moisture	SSM/I, AMSR-E, SMAP, SMOS, Gaofen*, Sentinel-1/2*, etc.
	Groundwater	GRACE, Sentinel-1*
	Shallow/coastal water depth*	UAV*, RapidEye*, Sentinel-1*, etc.
	Lakes, reservoirs, rivers and wetlands	MODIS, Landsat, SPOT, ICESat, GRACE, SRTM, Sentinel-1/2*, etc.
Hydrological fluxes	Precipitation	NEXRAD, TRMM, GPM, etc.
	Evapotranspiration	MODIS, Landsat, GRACE, MODIS*, MERSI-2*, AIRS*, Gaofen*, etc.

	River. Reservoir or lake discharge	MODIS, ENVISAT, Landsat, SRTM, ICESat, Sentinel-3*, etc.
Drought/ flooding	Drought and flooding	MODIS, Landsat, Grace, UAV, AMSR-E, SMAP, SMOS, ENVISAT, ASAR, Sentinel-1/2, etc.

According to a review from Bijeesh and Narasimhamurthy (2020), there are four primary water delineation approaches, which are respectively single band methods, spectral index based method, machine learning based method, spectral unmixing based method (Figure 2-1).

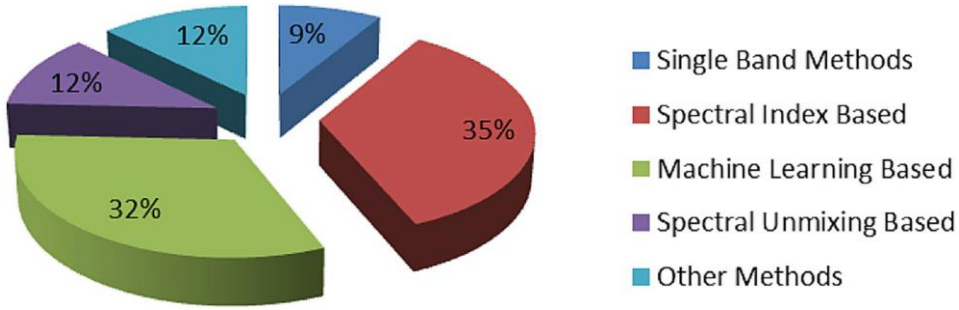

Figure 2-1. Methods used for water delineation of the current literatures (source: Bijeesh and Narasimhamurthy 2020).

Single band methods extract water features by selecting a threshold value on the band, which easily cause mixing of water pixels with those of different cover types in some cases (Du et al. 2012). Spectral Index based methods, such as Normalised Difference Water Index (NDWI), combined multiple bands of different reflectance for improved surface water detection (Rokni et al. 2014). Machine learning classification algorithms, such as random forest (RF), support vector machine (SVM) and neural networks (NN), are usually adopted to delineate surface water (Ma et al. 2017). Spectral unmixing is a process of decomposing a mixed pixel into its constituent spectra, which is also called as end-member extraction (Bijeesh and Narasimhamurthy 2020). There are also some other surface water delineation methods, such as a combination of spectral index and unmixing method (Luo et al. 2016), a combination of spectral index and machine learning method (Li et al. 2022).

2.1.2. Vegetation and soils

Similar to the illustrations in section 2.1.1, the way of capturing vegetation cover mainly relies on multi-spectral imagery or hyper-spectral imagery from sensors as examples in Table 2-1.

Apart from optical sensors referred in Table 2-1, acoustic sensors such as side-scan sonar, echo-sounder (Abukawa et al. 2013; Nelson, Cheruvelil, and Soranno 2006) shows advantages in aquatic settings, as they perform well in turbid or optically deep waters, especially while detecting submerged aquatic vegetation (Rowan and Kalacska 2021). The remote sensing technology offers a practical and economical means to study vegetation over land area as well as underwater areas (submerged aquatic vegetation) for both marine and freshwater ecosystem (Xie, Sha, and Yu 2008).

Before employing remote sensing technology to detect vegetation, it is crucial to identify the research either at vegetation community or species level (Xie, Sha, and Yu 2008). In general, images with low resolutions may be only adopted at vegetation community level, whereas images with higher resolutions are used for fine-detailed vegetation classification (i.e., vegetation species). Medium resolution imagery (e.g., Landsat TM and ETM+) are mostly beneficial for vegetation community level mapping (Xie, Sha, and Yu 2008). Medium to high resolution imagery have been explored for vegetation species detection in recent years. For example, Sentinel-2 (10- 60 m) has been employed to classify seven grassland plant communities with an overall accuracy of 0.78 by using SVM classifier (Rapinel et al. 2019). To train the SVM classifier model, Rapinel et al. (2019) carried out field sampling for plant communities at 2 m resolution to obtain the ground truth data. This is an example that medium to high resolution imagery has the potential to recognise the vegetation at the species level, however, it still mostly relies on assistance with field samplings at high resolution (1- 10 m) (Adagbasa, Adelabu, and Okello 2019; Demarchi, Bizzi, and Piegay 2017; Rapinel et al. 2019).

Xie, Sha, and Yu (2008) reviewed a variety of vegetation classification algorithms, including traditional supervised classification (e.g., SVM and Maximum Likelihood Classification) and unsupervised classification (e.g., Hidden Markov Model), and some improved classifier such as Artificial Neural Network (ANN) and fuzzy logic approaches. In many cases of lacking ground truth references, spectral vegetation index (VI) such as Normalised Difference Vegetation Index (NDVI) and EVI (Enhanced VI) remains to be one of the most important tools for mapping vegetation covers (DeFries, Hansen, and Townshend 1995). In recent years, machine learning approaches, including traditional machine learning and deep learning, have widely been applied to LULC detection. It has been reviewed that supervised machine learning approaches achieved outstanding performance for classifying LULC and remain to be the most popular branch of LULC classification (Talukdar et al. 2020; Ma et al. 2017).

In addition, soils are critical foundations for vegetation (Davidson and Janssens 2006; Liu et al. 2008), and hence, for the vegetated bars in the river channel. Remote sensing played a critical role in detecting soil surface roughness and moisture (Anderson and Croft 2009), which encouraged distinguishing the vegetated soil surfaces from unvegetated bars in the river channel. For example, there also evidences that Thermal Infrared (TIR) has provided access to detect soil surfaces in recent research (Gago et al. 2015; Gerhards et al. 2019; Melis et al. 2020). Proxies such as the day-night difference of temperature (DT) and Apparent Thermal Inertia, which can be obtained through remote sensing, have been successfully employed for detecting soil moisture (Hook et al. 1992; Melis et al. 2020). Moreover, the thermal inertia has the capacity for differentiating soils and rocks (high thermal inertia) from shales and gravels (low thermal inertia) (Melis et al. 2020). Therefore, according to the objectives of the research issues and available data (resources), designing an appropriate study level of vegetation mapping is very essential for selecting adequate sensors. Nevertheless, climate conditions (especially atmospheric conditions) and technical issues for image interpretation are also very important factors for sensors selection (Xie, Sha, and Yu 2008).

The major sources of error found in LULC classification are the shadows of mountains and clouds (Bijeesh and Narasimhamurthy 2020). In river channels, mountains less likely affects LULC detection, but clouds and cloud shadows are unavoidable covering the remote sensing images, especially in the tropical regions where undergo frequent weather change (Kubota et al. 2017). Digital elevation models (DEMs) can be effectively used in combination with multispectral/ hyperspectral data to mitigate the effect of clouds in the image to obtain a higher classification accuracy (Bijeesh and Narasimhamurthy 2020). There are emerging efforts for reducing clouds effects on LULC detection. For example, with the planned launch of the Pre-Aerosol Clouds and ocean Ecosystem (PACE) in 2022, and the data streaming from the Sentinel missions, Earth Observation (EO) technology is devoting for a long-term sustainable data flow, forming the basis for its operational use (Groom et al., 2019). Alternatively, using spatiotemporal data fusion to get a fused cloud-free image has been commonly adopted while doing seasonal LULC change studies (Lu et al. 2019). Therefore, considering clouds/shadows/mountains effects on the LULC detection and choosing an appropriate way to mitigate the cloud effects cannot be ignored.

Choosing appropriate remote sensing products relies on preliminary knowledge of research objectives and data availabilities. In cases of LULC change studies, water, soils, vegetation,

anthropogenic structures, clouds, shadows are all factors which should be considered carefully. With developments of remote sensing techniques, more earth observation data and technique innovations are expected to strengthen LULC detection in the future.

2.2. Geomorphic patterns and classification of rivers

River morphology has been changing frequently due to climate change and human activities in the past decades (Grill et al. 2019; van Vliet et al. 2013), exhibiting a high degree of non-linearity and complexity (Agnihotri, Ohri, and Mishra 2019; Boota et al. 2021). According to a review paper published in 2022, river morphology research has been gradually increasing since 2001, especially from 2015 to 2020 (Li, Yan, and Boota 2022). Scientists from different background studied river morphology from different aspects. For example, geomorphologists and geologists are interested in river patterns (planforms) and what that pattern reveals about river history and behaviours (Fotherby 2009; Schumm 1985). Sedimentologists focus on the distribution of sediment within the bend, bed forms within the channel, and sedimentary structures (Church 2006; Schumm 1985). Scientists of hydraulics pay attention to hydrological process of river formation (Crosato and Mosselman 2009). In practice, many studies synthetically analyse the river morphology change using knowledges from geomorphology, sedimentology, and hydraulics (Bridge and Demicco 2008; Cristiano, ten Veldhuis, and van De Giesen 2017; Ferguson 1987b). This thesis takes accounts of river pattern and pattern change as the foremost topics, whilst sedimentary and hydrology factors are combined to study the river processes and environmental controls on the river morphology. This section aims to review the river pattern studies and Chapter 6 will introduce more about river morphology research from aspects of sediment aggradation and deposition, and stream power.

2.2.1. River pattern

There are three major categories of stream channels according to the nature of materials through which a river flows, which are bedrock rivers, semi-controlled rivers, and alluvial rivers. Bedrock rivers and semi-controlled rivers are relatively stable and less concerned about river pattern change (Schumm 1985). The alluvial rivers, as consequences of having bed and banks composed of sediments which are transported by the stream, is the major type for analysing pattern change (Schumm 1985). The longitudinal pattern of a river is a complex structure, usually responding discontinuously at different spatial scales (Kondolf et al. 2016).

Frissell et al. (1986) presented an example of a hierarchical organisation of a stream system (Figure 2-2), which were: stream system (at 1000 m scale); segment system (at 100 m scale); reach system (at 10 m scale); pool/riffle system (at 1 m scale); microhabitat system (at 0.1 m scale). Kondolf et al. (2016) proposed that the appropriate philosophical underpinnings for channel classification depend on the purpose of the study and is specific in terms of scale and regional context. However, data availability of the studied area cannot be ignored when thinking about scale. There are three main data sources for collecting the data for river morphology research, which are remote sensing data, field sampling data and auxiliary data (e.g., statistical yearbooks, historical photos, street view pictures from social media or google maps, etc.) (Li, Yan, and Boota 2022). Among these data sources, remote sensing data are highly visited for monitoring river morphology, which accounts for 73% of the studied research in a hydromorphology review paper (Belletti et al. 2014). In practice, remote sensing data, field sampling data and field observation pictures, and some street view pictures (e.g. from google maps), are all resources to maximise knowledge of the river systems. To compact information deriving from these data and visualise river patterns efficiently, there are three approaches could be considered while extracting river information: (1) Segmentation, which is one of the properties of the longitudinal signal, plays a key role in classifying channel landforms without being totally arbitrary (Frasson et al. 2017; Kondolf et al. 2016). Frasson et al. (2017) defined three types of segmentation strategies which are on arbitrary length, identification of hydraulic controls and sinuosity. Although this method simplifies river patterns by a specific characteristic of the river, in the meantime, it is lack in presenting sophisticated information within the river channel; (2) Maps generation, carrying out the corresponding measurements and analyses, is an important tool presenting the morphological characteristics of rivers and offering valuable information for the river evolution with their rigorous mathematical foundation (Li, Yan, and Boota 2022; Nass et al. 2011). Maps of a specific theme presented continuous spatial information of specific characteristic(s) quantitatively and intuitively, which have been widely used in river system analysis; (3) Feature parameter extraction (e.g. Figure 2-3), which is a crucial transition from qualitative to quantitative analysis of river morphology, has been developed by numerous parameters such as length, width, sinuosity index, braiding degree, the variability of the rivers over time (Li, Yan, and Boota 2022). To some extent, this method integrates segmentation and maps generation to extract river patterns by planform patterns and controls together.

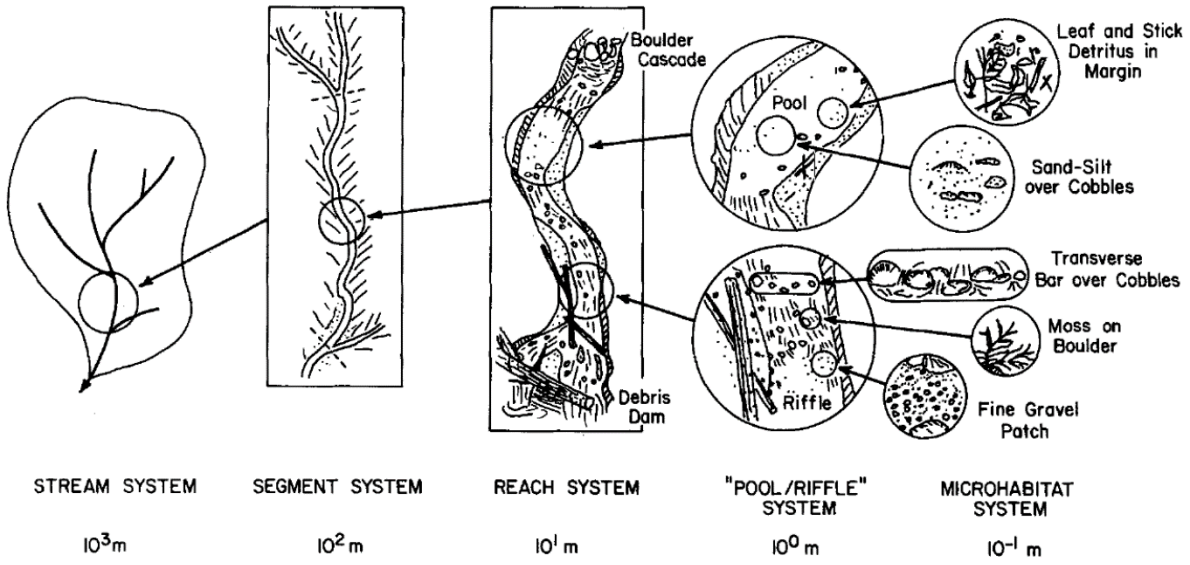

Figure 2-2. Hierarchical organisation of a stream system and its habitat subsystems (source: Frissell et al. 1986).

Leopold and Wolman (1957) quantitively classified channel patterns into straight, meandering and braided channel basing on relationships between slope and bankfull discharge, which was an early case of process-based classification. The process-based classification has been enlarged and revisited with additional patterns such as sinuous, anabranching (Figure 2-3), wandering and anastomosing rivers (Nanson and Croke 1992; Smith and Smith 1980) (Figure 2-4). As the definition develops, six river patterns are commonly used nowadays, which are: straight (single relatively straight channel); meandering (single channel bending); wandering (transitional channel from single channels to fully braided channels); braiding (multiple channel networks with bars or islands); anabranching (multiple relatively stable channel networks with bars or non-flooding islands); anastomosing (multiple channel systems having major secondary channels that separate and re-join the main channel to form a network) rivers (Bridge and Lunt 2006; Carling, Jansen, and Meshkova 2014; Carson 1984; Leopold and Wolman 1957; Nanson and Knighton 1996; Schumm 1985).

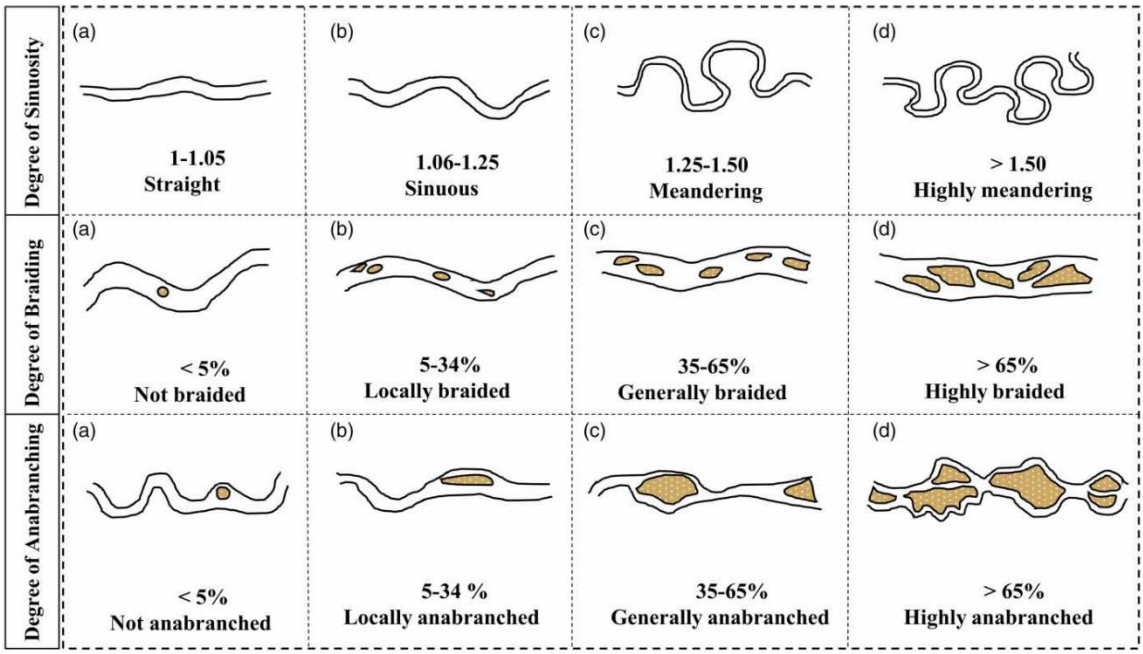

Figure 2-3. A sketch of process-based channel pattern classification on sinuosity, braiding and anabranching degrees (source: Brice 1978; Li, Yan, and Boota 2022).

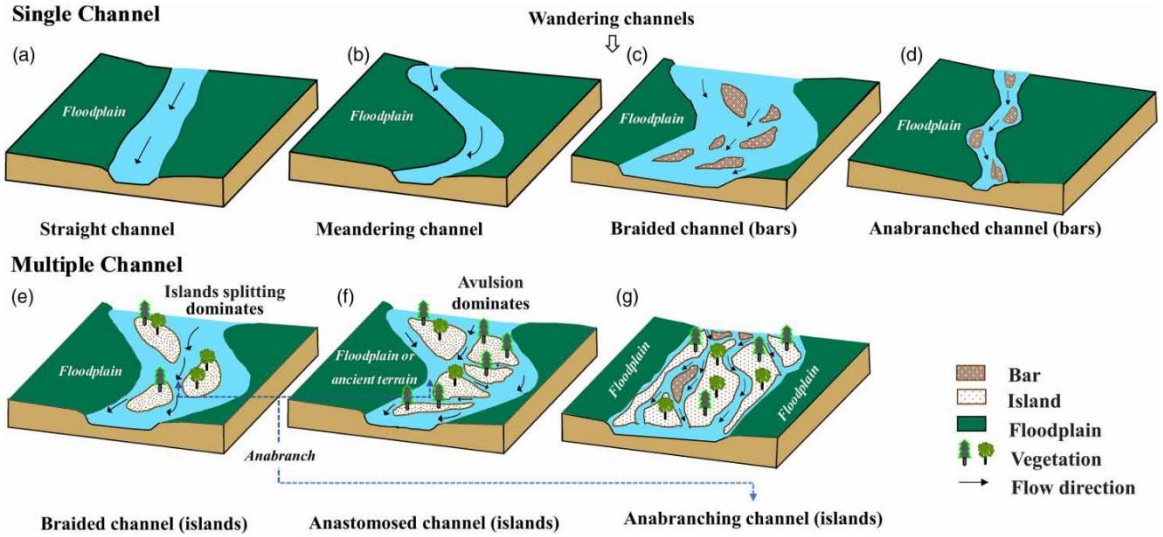

Figure 2-4. Schematic diagram of river channel patterns classification (source: Li, Yan, and Boota 2022).

Apart from the planform styles above, geomorphologists also developed principles to divide the river into different segments. For example, Fryirs, Wheaton, and Brierley (2016) divided

the river into segments according to the confining margin. Figure 2-5 shows how they defined the valley margin, valley bottom margin, channel margin, and hence confining margin. The river can be confined or partly confined on the longitudinal patterns. Along with gradient, discharge and sediment regime, valley confinement is a primary control on river morphology (Fryirs, Wheaton, and Brierley 2016). For example, valley confinement is identified as the determining factor of braided river in the central Platte River (Fotherby 2009). Garcia Lugo et al. (2015) indicated that confinement may result in different degrees of spatial variability of the bed topography. Carbonari, Recking, and Solari (2020) used flume experiments of gravel-bed river physical model to suggest that lateral flow confinement influences bedload transport rate, however, differences in lateral flow confinement resulted in the same average active channel width (i.e., the width over which sediment transport occurs). Therefore, taking account of confinement in river morphology study is enhancing the comprehensive understanding of processes in the river and predict the river behaviours for river managements.

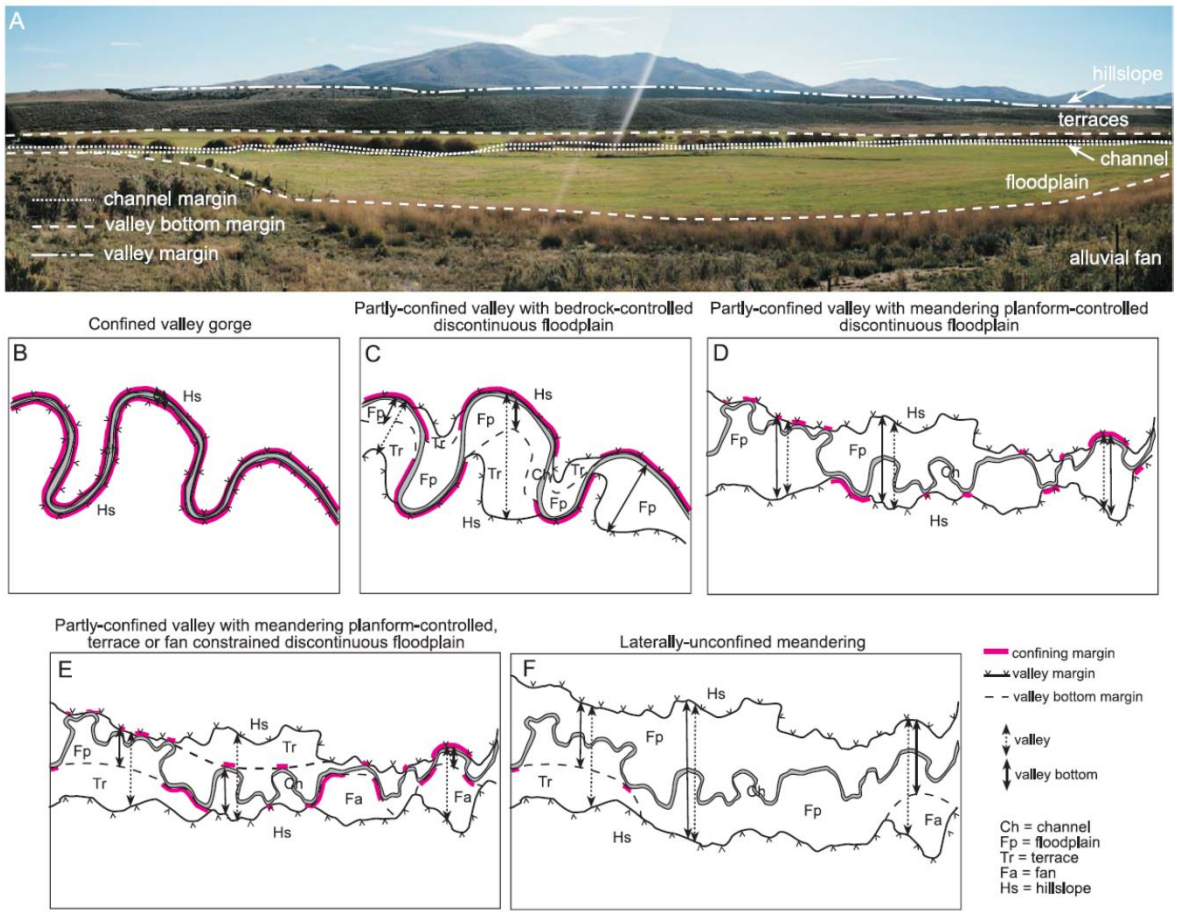

Figure 2-5. Identifying different forms of confinement across a range of river types (source: Fryirs, Wheaton, and Brierley 2016).

Basing on the sedimentary concepts, Schumm (1963) classified rivers by the principles whether their beds are stable, eroding or aggrading, and further defined the river types through the dominance of suspended load, mixed load or bedload sediment transport. Church (2006) summarised channel patterns in the state of sediment supply, sediment calibre and channel gradient. River bars are the main landform in the channel and characterised as large sediment deposits, separating by channels, emerging during low flows (Crosato and Mosselman 2020). Nevertheless, river bars form important fluvial or riparian habitats (Crosato and Mosselman 2020), and fluvial or riparian habitats also alter river bars formation and erosion (Bartley et al. 2008). The river pattern can be defined by the bar mode, where alternate bars are typical of meandering rivers whilst multiple bars characterise braided rivers (Crosato and Mosselman 2020). In straight and weak sinuous river channels, periodic bar development can enhance bank erosion, and hence resulting in longitudinal channel width variation, forcing channel expansion or contraction downstream (Bridge and Demicco 2008). Bars mobility can reflect the hydraulic process and impact the channel pattern change (Singh et al. 2017; Church 2006).

Hierarchical classification has been widely accepted and applied to river morphology pattern research (Kondolf et al. 2016). From climate zone scale to reach-level scale (Kondolf et al. 2016) and then diving into landform (i.e., water, bars, vegetated islands) scale (Jaballah et al. 2015; Omer et al. 2020; Phiri et al. 2020), combining the conventional process-based classification with the landform-based classification using remote sensing data and technologies provides a great potential to explore the river morphology change and dynamics, and probably to investigate the fractal structures of river planforms and river's fractal behaviours (Nur et al. 2016; Shen et al. 2011; Nikora 1991; Pentland 1984).

2.2.2. Remote sensing application in river morphology detection

Obtaining data from interpretation of images often includes the use of categorical information and expert-based opinions which may be biased by operators' experience and can be inconsistent. These issues limit their implementation and may call into question their suitability for monitoring purposes, which demand objective and repeatable assessments. There is a pressing need for an operative, multi-scale framework for the evaluation of the hydro-morphological status of river systems (Gurnell et al. 2016). Using Earth Observation (EO) datasets, geomorphological indices can be routinely quantified across multiple spatial scales, from sub-reach units up to entire basins, with continuous objective and consistent information

(Horacio, Ollero, and Perez-Alberti 2017). Precisely mapped in-channel morphological units, and their change over time, are important tools for understanding river morpho-dynamics. These data also provide useful indicators of changes in potential ecosystem productivity (Belletti, Dufour, and Piegay 2015). There is a rapidly increasing capacity to quantify rates of change using remote sensing data from an ever-increasing range of platforms, hence improved theoretical and empirical methods for analysing and predicting these rates are urgently required. Increased computing power and big data handling protocols are now enabling geographic classification to be used widely for understanding Earth processes, and statistical machine learning is an emerging approach in this field (Maxwell, Warner, and Fang 2018). For example, Lopez- Fuentes et al. (2017) trained and tested three different deep learning algorithms for the task of water segmentation to analyse video streams in real-time in order to automatically detect anomalies such as sudden water extent increases.

For remote sensing image information detection, traditional machine learning approach is mostly to combine a software-derived segmentation with a traditional machine learning process (Ma et al. 2017). Machine learning has a strong ability to deal with big data and its analysis will be more objective. Nowadays, many algorithms have been developed to do machine learning in a lot of research fields (Jordan and Mitchell 2015). However, several main algorithms are commonly and widely used, which are Logistic Regression (LR), Support Vector Machine (SVM), Random Forest (RF) and Neural Network (NN). These algorithms have been applied in variety of classification cases and achieved relatively good results, whilst SVM performed well in the most cases of landscape classification studies (Ma et al. 2017). Deep learning is also a kind of machine learning which gains big popularity these years and it basically achieve by enhanced algorithms of Neural Network (Holden, Saito, and Komura 2016; Ohsaki et al. 2017; Schneider and Guo 2018). For fluvial morphology studies, some researchers have achieved quite good classification results using SVM (Costa, Foody, and Boyd 2018; De Luca et al. 2019; Demarchi, Bizzi, and Piegay 2016). Therefore, in this research, SVM was firstly chosen as the machine learning algorithm.

2.3. Remote sensing image segmentation and classification

Section 2.2 illustrated that remote sensing data have been highly enrolled in the river morphology classification. Segmentation is one of the most important steps of remote sensing image analysis before doing the classification. Segmentation can be regarded as a pre-process

to differentiate studied geographical units from other units, substantially for extracting landcovers with homogenous nature (Frasson et al. 2017; Song et al. 2016; Ye et al. 2018). Applying classification within segmented extent can be more efficient with less noise from other landcover units. A variety of segmentation methods have been developed in recent decades of years. In this chapter, the segmentation methods are categorised into four items, which are planform-based method, contour-model based method, traditional object-based method and machine learning object-based method, respectively. The latter three items are based on remote sensing images, focusing on delineating geomorphological units from each other, while the first item is mainly based on geomorphological features, dividing rivers into segments.

2.3.1. Planform-based method

The planform-based method focuses on the features of landform information obtained from earth observation data, for example, digital elevation models. Attributes such as channel sinuosity and wetted width of rivers can be derived to segment the landscapes. Altenau et al. (2017) demonstrated the calculation of water surface heights and slopes from airborne Ka-band (defined as frequencies in the range 26.5- 40 GHz) measurements from the AirSWOT platform over the Tanana River, Alaska. Frasson et al. (2017) compared three different river segmentation strategies used to group river nodes into reaches: (1) reaches of arbitrary (fixed) lengths, which simply breaks up reaches at regular intervals measured along the rivers' centrelines; (2) hydraulic control reaches, which consists of identifying hydraulic controls by searching for inflection points on the water surface profile; and (3) sinuosity-based reaches, which takes into consideration river planform features, breaking up reaches according to channel sinuosity. Gailleton, et al. (2019) presented a segmentation approach for the reproducible extraction and quantification of knickpoints from river long profiles. The method extracts slope-break knickpoint locations using changes in channel steepness calculated by integrating a method of segmenting channels into reaches of different channel steepness (Mudd et al., 2014) and a denoising technique (Condat, 2013).

2.3.2. Contour-model based method

In recent years, research on active contour models has become increasingly popular (Han and Wu 2017). Contour model is usually achieved by defining land unit/object borders to generate

a parametric curve or contour (Han and Wu 2017). River remote sensing images can be considered to be composed of two parts, which are the river area and the background area. The segmentation of contour models aims to define the river contour and derive the river areas. Although the intensity of river area is low as well as uniform (homogeneous part) and background area is relatively high and complex (inhomogeneous), there are still a variety of interference areas of the remote sensing images, the intensities of which are similar to the river areas. To suppress the effect of these interference areas when segment the river remote sensing image, Song et al. (2016) proposed a novel active contour model based on cross entropy, which combines the cross-entropy information of the image to improve the curve accuracy. However, over-segmentation in some cases can deduce the generality of the models. To solve this problem, Han and Wu (2017) proposed a novel active contour model based on modified symmetric cross entropy, which can not only improve the segmentation accuracy but also enhance the segmentation efficiency. Li and Sheng (2012) proposed an automated scheme for glacial lake dynamics mapping using Landsat image and DEM based on a case study in the Himalayas, which was a kind of contour-based segmentation, and they delineated glacial lakes with multi-level changing segmentation thresholds. In their case, the automated threshold detection was achieved by bimodal histogram of NDWI. Active river channel extraction is one of contour-based segmentation methods. In this thesis, a new active channel extraction approach developed by Boothroyd et al. (2021) was introduced to extract the active river channel from the whole catchment, within which the river landform classification can be processed with less interference from background imagery signals.

2.3.3. Traditional object-based method

With many high-resolution remote sensing products available for free and new technique developments, some researchers also work on improving the segmentation accuracy with high quality images and new techniques. Up to the present, many water bodies products can be obtained from online websites, such as the Shuttle Radar Topography Mission (SRTM) water body data (Slater et al. 2006), which is an international research effort that obtained digital elevation models on a near-global scale from 56°S to 60°N. The resolution of the raw data is one arcsecond (30 m along the equator). Synthetic-aperture radar (SAR) images are also particularly popular in remote sensing image research these years as they can be downloaded from the Sentinel source freely. Ciecholewski (2017) reported a method of river channel segmentation in polarimetric SAR images, which obtained watersheds in combination with

average contrast maximisation. Duan et al. (2017) proposed a way to implement SAR Image segmentation based on convolutional-wavelet neural network and Markov random field. In a word, similar to the work of (Han and Wu 2017) above, the target of the proposed work is to enhance the accuracy of river channel segmentation.

To understand the earth surface in more detail, the concept of object-based image segmentation was proposed and has been welcomed by many researchers. Object-based image segmentation is a so-called classification-based segmentation aiming to create a series of objects (Benz et al., 2004). Meanwhile, Ye et al. (2018) gave a review of accuracy assessment for object-based image analysis based on per-pixel to per-polygon approaches. Comparing to the pixel-based image analysis, which has been tested by research based on 209 articles, the object-based image segmentation performs much better on geographical issues concerning land cover/ use classification (Ye et al. 2018).

With the current urgent demand for automated segmentation methods, a variety of researchers are working for establishing frameworks for segmentation as well as classification to detect the dynamics of the earth surface. For object-based segmentation, the automated frameworks are productive combining remote sensing images and DEM data, as automated frameworks combine four spectral bands data of images and slope data to enrich the information for improving the segmentation accuracy. For example, (Dragut and Eisank 2012) tested an automated object-based classification of topography from SRTM data; Zhang and Xie (2013) processed HyMap Data to map vegetation in the Kissimmee River watershed; Demarchi et al (2016) segmented a river in Italy with very high-resolution images and Light Detection and Ranging (LiDAR) data. These works are all produced image objects with multi-resolution segmentation algorithm (Benz et al., 2004), which can be achieved directly in a software calling eCognition Developer. The multi-resolution segmentation algorithm is generally applied to segment river patterns into geomorphological objects, then with the machine learning method, the geomorphological objects were classified as geomorphological units. However, the eCognition Developer is a commercial software which is not free accessed. In this thesis, an alternative free-open software OrfeoTool box has been employed to generate the geomorphological objects basing on the layers from one remote sensing acquisition. It replaces the eCognition Developer but not changes the framework of the object-based image analysis. This kind of framework can achieve classification in an automated way, but it would be in the context of a hierarchical workflow.

2.3.4. Machine learning object-based method

To enhance the universality of segmentation, some researchers derived ideas from machine learning. Machine learning uses computational algorithms to learn (analyse) large sets of data inputs and outputs, and train the machine to automatically recognise patterns or make decisions (Helm et al. 2020). Machine learning has been becoming an efficient tool in detecting a variety of image information. Machine learning has been adapted to management and prediction of risk events. For example, Lopez-Fuentes et al. (2017) proposed to use a water segmentation technique to analyse video streams in real-time in order to automatically detect anomalies such as sudden water extent increases. They trained and tested three different deep learning algorithms for the task of water segmentation and compare their performances. For remote sensing image information detection, machine learning approach is mostly combined software-derived segmentation (see previous paragraph) with a traditional machine learning classifier such as support vector machine and random forest.

Garcia et al. (2017) developed a machine learning approach for agricultural parcel delineation through agglomerative segmentation. This approach can be regarded as a machine learning object-based method and it follows the rule that each object is characterized not only by its spectral, shape or texture features, but also by its neighbour objects, its sub- and super-objects, of which the larger segments are referred to as super-objects of the smaller segments and the smaller segments are referred to as sub-objects of the larger segments (Johnson and Xie 2013).

The machine learning object-based segmentation can be achieved by a theory of super pixel. A super pixel is a small, local, and coherent cluster which contains a statistically homogeneous image region according to certain criteria such as colour, texture, among others (Ren and Malik 2003). Super pixels techniques enhance image segmentation in a cluster way, which do not focus on segmenting meaningful objects (Schick and Stiefelhagen 2011). The techniques performed well on reducing the influence of noise and intra-class spectral variability and preserving most edges of images. It can also improve the computational speed of the segmentation of meaningful objects (Achanta et al. 2012). Super pixel processing originated from the segmentation method called simple linear iterative clustering (SLIC) (Achanta et al. 2012), which can only work in the RGB colour space. The SLIC version used in work of Garcia et al. (2017) corresponds to the work implemented by (Gonzalo-Martin et al. 2016), which extends the methods to work with multispectral images. The super-pixel technique is currently

tested in crop field classification research but have not been widely used in river patterns segmentation. Although the super-pixel technique has a high potential to well classify the river landforms, this thesis still focusses on doing the machine learning classification using the traditional object-based image analysis workflow to maintain the river patterns being classified in a more common way. However, the super-pixel method can be an example for river patterns classification in the future work.

The methods illustrated above segment the river morphology at different scales, which inspires a hierarchical segmentation workflow for classifying river landforms at a finer scale for this research. Contour-based method can segment river channel from background context on the remote sensing images, and planform-based method divided the channel into reaches according to planform patterns. Then traditional object-based segmentation or machine learning object-based segmentation can segment geographical objects within the river channels/reaches, which will be prepared for further object-based classification.

Land surface detection/delineation and remote sensing image segmentation/classification were reviewed in this chapter, which provide technological background for river landform classification of this thesis. This chapter presented literatures using a variety of geomorphic pattern to analyse and interpret river processes and river morphology.

Chapter 3 - Methods

3.1. Introduction

Chapter 1 introduced the locations of the four studied rivers in the north Luzon, the Philippines. This chapter is introducing the four rivers quantitatively by preliminary investigations. The Bislak, Laoag and Abra Rivers lie in the same climate zone (marked by type I), but the Cagayan is in a different climate zone (marked by type III) according to research by Wichmann (1904). Table 3-1 listed measured data of studied main channel length and maximum elevation within this distance of length. It indicated that, with cases of four studied rivers, the smaller the river catchment, the steeper the averaged river slope. The averaged gradient of studied lowland Cagayan River is very flat, with finer riverbed sediment grainsize. Chapter 5 introduces the Bislak, Laoag and Abra River and investigate these three rivers synthetically. Chapter 6 illustrates the Cagayan River dynamics and tributary impacts on the mainstem river.

Table 3-1. Bislak, Laoag, Abra and Cagayan River preliminary investigations.

River Name	Catchment Area (km^2)	Main channel length (km)	Maximum elevation (m)	Averaged Gradient (m/m)	Climate zone	Start distance to the river mouth (km)	Riverbed type
Bislak	586	55.882	272.742	0.0049	I	0	gravel
Laoag	1261	50.073	145.860	0.0029	I	0	gravel
Abra	4893	93.350	141.163	0.0015	I	0	gravel
Cagayan	27684	181.563	24.9	0.0001	III	28	sand/silt

This thesis aims to assess river morphology change using free-to-access remote sensing data and tools. A workflow was designed (see Figure 3-1) for river landform change analysis in the active channels of the tropical Bislak, Laoag, Abra and Cagayan Rivers. This chapter outlines the processes carried out in this workflow and complement the methods that are detailed in Chapters 4-6. Chapters 4-6 each include descriptions of methods used to process images, generate morphological data and to analyse the results. In this chapter, some background to these methods is provided to justify the particular methods used in later chapters and to provide some technical details. In Chapter 7, four studied rivers were compared and discussed systematically from aspects of landform stability, diversity, seasonality, and geology controls. This chapter illustrates the methods and preliminary investigations.

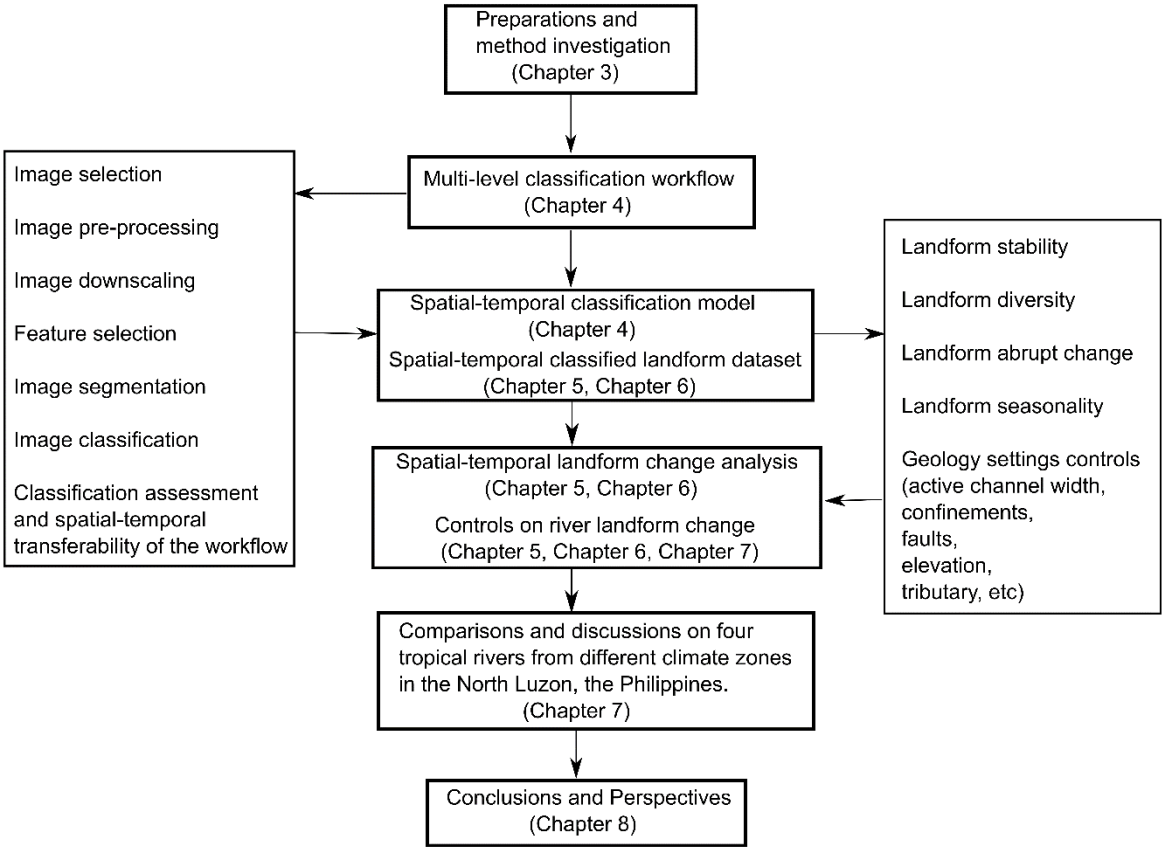

Figure 3-1. Workflow outlining the methods used in this thesis.

3.2. Materials

3.2.1. Remote sensing data selection

The studied rivers are within the tropics where climate is warm with distinct wet and dry seasons, and rates of landform change can be rapid. In the Sentinel-2 acquisitions, the remote sensing imagery could be reflecting different spectral ranges (Figure 3-2 a,b and d-f) and sometimes images were partly or fully obscured by heavy clouds (Figure 3-2 c) . Although there are existing methods for removing the clouds by splicing the remote sensing imagery with patches from neighbouring dates, the imagery from the neighbouring date provides a different spectral range which could make the spectral reflectance of the patched imagery inconsistent. As for the pre-processing object-based image segmentation depends on spatial relationships on pixel reflectance between neighbouring pixels, while clouds removing method would disturb the spatial relationships between neighbouring pixels. To avoid the potential for machine learning classification models within one imagery scene becoming unstable, all the imagery that is classified in this thesis is from a single original acquisition, without any use of

mosaic imagery. In practice of selecting remote sensing acquisitions, the cloud covering situations varied from different years. In the studies of the following chapters, two-month interval was set to collect Sentinel-2 acquisitions. However, due to cloud coverings, slightly longer/ shorter temporal interval could be decided by using the closest date, which is with clear river channel observation, to originally designed interval date. In the Bislak, Laoag and Abra Rivers, two-month/ three-month interval is mostly common for capturing images. However, in the Cagayan River, no clear imagery was observed in December to January and only one clear imagery was observed in February across four studied years, which sometimes made temporal interval being extended to four months. In addition to cloud cover problems, river landforms (Figure 3-2) show obviously different spectral reflectance from water, unvegetated bars and vegetation across the whole year. Therefore, in this thesis, multi-seasonal imagery with low proportions of clouds is used for image analysis and river morphology mapping.

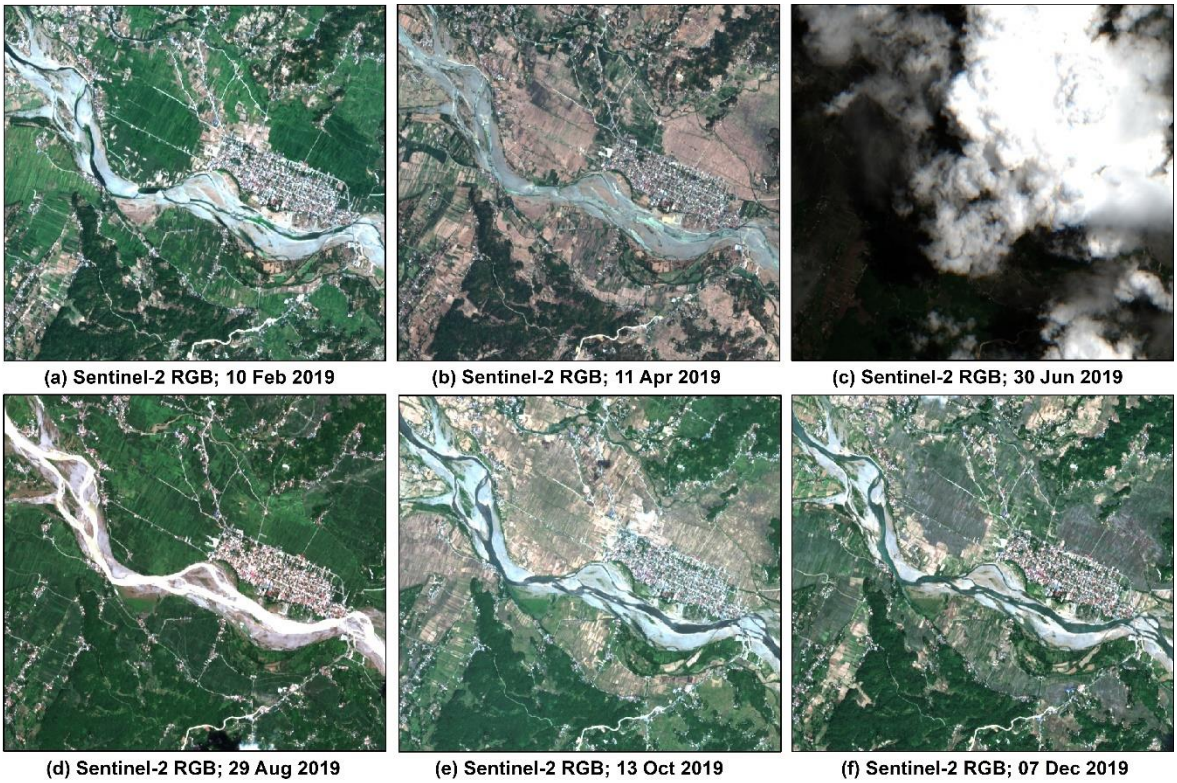

Figure 3-2. Samples of Sentinel-2 imagery for a section of the Bislak River captured on six dates at an approximate 2-month interval in 2019.

3.2.2. Aerial images and field observation

To have an intuitive sense of local landform types within the active channel, higher resolution aerial images were acquired, and field observation took place in 2019 at one of the sites used

in the thesis, the Bislak River. Aerial images were acquired as part of an airborne survey of the Bislak River on 21 March 2019. A D8900 aerial camera was used to collect RGB imagery with a spatial resolution of 0.2 m. The aerial images came from a parallel project led by the PhD supervisory team, and were used to aid plans for field observations used in this thesis. Due to this ongoing project, more data are available for the Bislak than for the other three sites used in the thesis. Consequently, method development and testing were conducted primarily on the Bislak River. Field observation by the author took place in November 2019. From these field observations (Figure 3-3), the upper reach of the Bislak River was found to have sediments dominated by boulders and the water in the dry season is usually very clear and shallow, whilst the vegetation is quite sparse within the active channel. In the mid reach of the river, the sediments are much finer than that in the upper reach, an include silts, sands and gravels. Within this part of the river course, in-channel vegetation was observed to be widespread and locally dense. The lower reach has a mixture of gravel and sand sediments according to field observations, and is extensively mined for aggregates. Aerial visual observations show that the morphologies of the mid-reach (Figure 3-3iii) and of the lower reach (Figure 3-3vi) are very similar to each other, however, the sediment sizes in the mid-reach (Figure 3-3c) and in the lower reach (Figure 3-3f) show considerable variation. In this thesis, the focus is not on identifying sub-types of water, sediment, and vegetation. Instead, the focus is on three main types of landforms within the river channel, which are: water, unvegetated bars and vegetated bars.

Figure 3-3. Aerial images and their corresponding field ground pictures in 2019. (i)-(ii) are from the upper reach of the Bislak River; (iii)-(iv) are from mid-reach of the Bislak River; (v)-(vi) are from lower reach of the Bislak River.

3.2.3. Unsupervised classification using Sen2Cor tool

To investigate how river landforms change in north Luzon, and to plan field research at an early stage, manually digitised maps created from Sentinel-2 Level 1C imagery were used. Figure 3-4a-c shows manually digitised landforms within a short reach of the Bislak River on three dates in 2018. The landforms were classified into the three types noted previously, which are vegetated islands (vegetated bars), bars (unvegetated bars) and river channels (water). Figure 3-4d presents that the locations of river channels changed significantly over the three dates in 2018. The water area increased due to seasonal rainfall from March to July and decreased from July to November within one year, which might indicate seasonal characteristics of landform change that follow the seasonal climate.

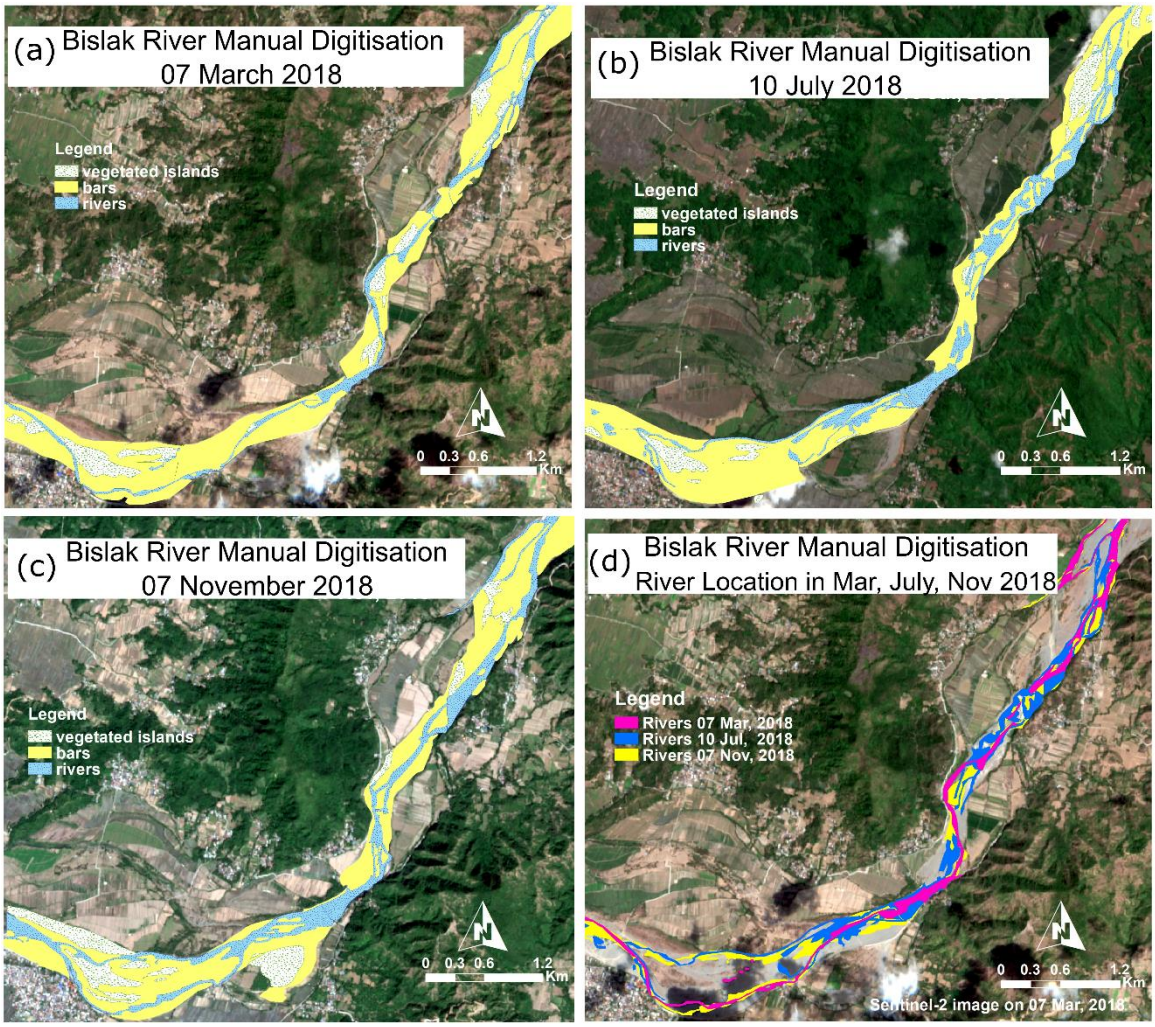

Figure 3-4. (a)-(c) Manually digitised river landform classification on three dates in 2018 in a short reach of the Bislak River. (d) overlay of the water extent from the images in (a)-(c).

For Sentinel data analysis, Level 2A products with atmospheric correction are expected to perform better than Level 1C products (Drusch et al. 2012). Level 2A products can be derived from Level 1C products using the Sen2cor plugin tool in the SNAP software (https://step.esa.int/main/download/snap-download/previous-versions/).Sen2cor also provides an automated detection method for land cover. Through Sen2cor, a classification map was generated using the Level 2A product for 7 March 2018 (Figure 3-5b). The manually digitised map for 7 March 2018 is presented to allow a comparison with the Sen2cor based scene classification map. There are three types of landforms in the manually digitised map, whilst Sen2cor classified objects into five types of landcover and one unclassified type. In this case, a large proportion of objects alongside the river channel were attributed to unclassified units. Additionally, some manually digitised bars were attributed to unclassified units and some manually digitised river channels were classified as dark feature shadows in the Sen2cor based

classification map. Figure 3-5 suggests that the classification model from the Sen2cor plugin does not fit the landcovers within the studied river. For example, some water bodies were classified as 'Dark feature shadow' and unvegetated bars are not classified to one type of landcover. Meanwhile, some vegetated bars were not recognised in the Figure 3-5b. Therefore, a classification model fitting to the ground truths of the studied river was needed. In this thesis, a classification model was designed by a machine learning method, which has been widely used and agreed to be an efficient tool for processing remote sensing image classifications (Demarchi et al. 2016; Ma et al. 2017).

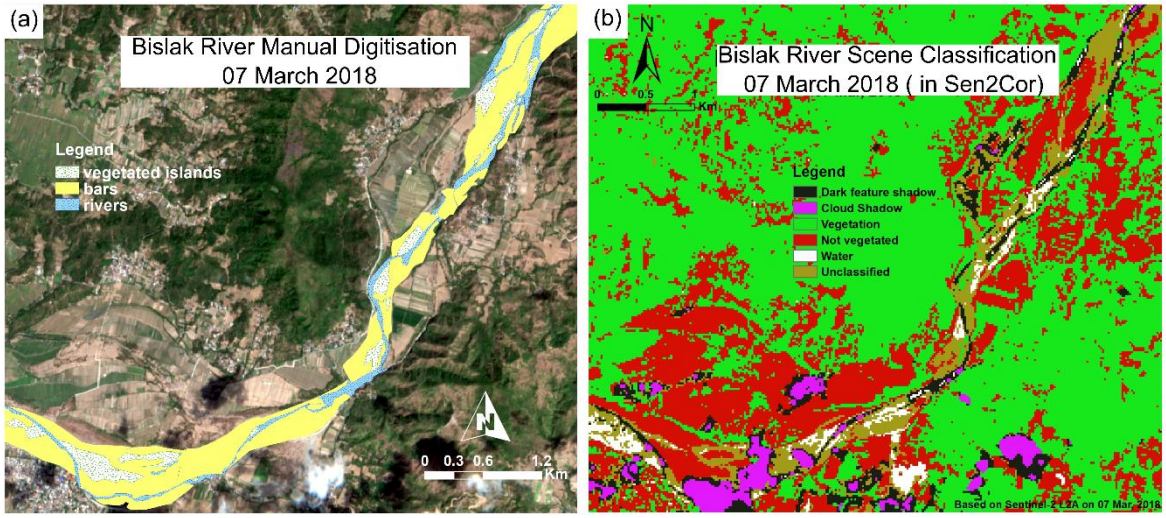

Figure 3-5. Comparison of (a) a manually digitized classification map with (b) Sen2cor based scene classification map.

3.2.4. Image Segmentation

The machine learning procedure usually consists of four phases: data preparation; image fusion/downscaling; image segmentation; and, image classification. As described in section 3.2.1, Sentinel 2 Level 1C data should be firstly processed into Level 2A using the Sen2cor tool. Then, four bands at 10 m resolution and six bands at 20 m resolution were prepared for image fusion/downscaling. Image downscaling is to downscale coarser resolution images into finer resolution images which can be achieved by a variety of approaches. These approaches are illustrated and compared in more details in Chapter 4. To analyse all bands at the same spatial scale, the six bands at 20 m resolution were fused into 10 m resolution by image downscaling methods. The procedure for selecting a good downscaling method is introduced and discussed in Chapter 4. Chapter 4 also compares and investigates an optimal model for

image classification. In the current chapter, only image segmentation will be introduced (Figure 3-6).

In this experiment, 15 features have been incorporated in the machine learning model. For example, band 6 of one Sentinel-2 acquisition can be chosen as one 'feature', and an NDVI map derived from the same Sentinel-2 acquisition can also be denoted as one 'feature'. In the case of this thesis, the features are requested to be consistent with each other at spatial scale as well as from same date. The 15 features include four 10 m resolution bands and six 10 m resolution bands downscaled from 20 m resolution bands of Sentinel-2 acquisition, and five 10 m resolution maps of environmental indices which are listed in Table 4-2 in Chapter 4. The 15 features were composited firstly in the ArcMap 10.8, and then processed by Large Scale Mean Shift (LSMS) segmentation to obtain the geographical objects (one object is a patch of pixels with homogeneous nature). LSMS algorithm is an iterative way to find patches of related pixels neighbouring to an initial pixel and then envelop them into an object (Comaniciu and Meer 2002; Ming et al. 2011). Thereby, the segmentation map contains an attribute with 15 features values, in which each segmented object has 15 features, whilst each feature was denoted by the mean value of all pixels in one object. Combining the channel segmentation map with the manually digitised map, every segmented geographical object was allocated to a ground truth type, which were: water, unvegetated bars, vegetated bars, and others.

The LSMS generates a vector data file containing the regions extracted using the MeanShift algorithm, which can be adopted from Orfeo Toolbox software version 6.6.1 (https://www.orfeo-toolbox.org/). There are three key parameters that need to be set accurately to generate a high-quality image segmentation, which are: spatial radius, range radius and minimum segment size. Spatial radius refers to the radius of the spatial neighbourhood for averaging, in which higher values will result in more smoothing and also longer processing times. Range radius corresponds to the threshold on spectral signature Euclidean distance to consider neighbourhood pixel for averaging, in which higher values will be less edge-preserving and lower values will lead to less noise smoothing. Minimum segment size is set for merging segments that have the closest spectral signature. In practice, the three parameters need to be tested and adjusted multiple times until a good segmentation result (objects fitting to the land units properly) is achieved. Here, Figure 3-6d presents an example of good segmentation results using spatial radius (set by 7), range radius (set by 13) and minimum

segment size (set by 42), which were experimented for multiple times until geographical objects were bounded relative properly.

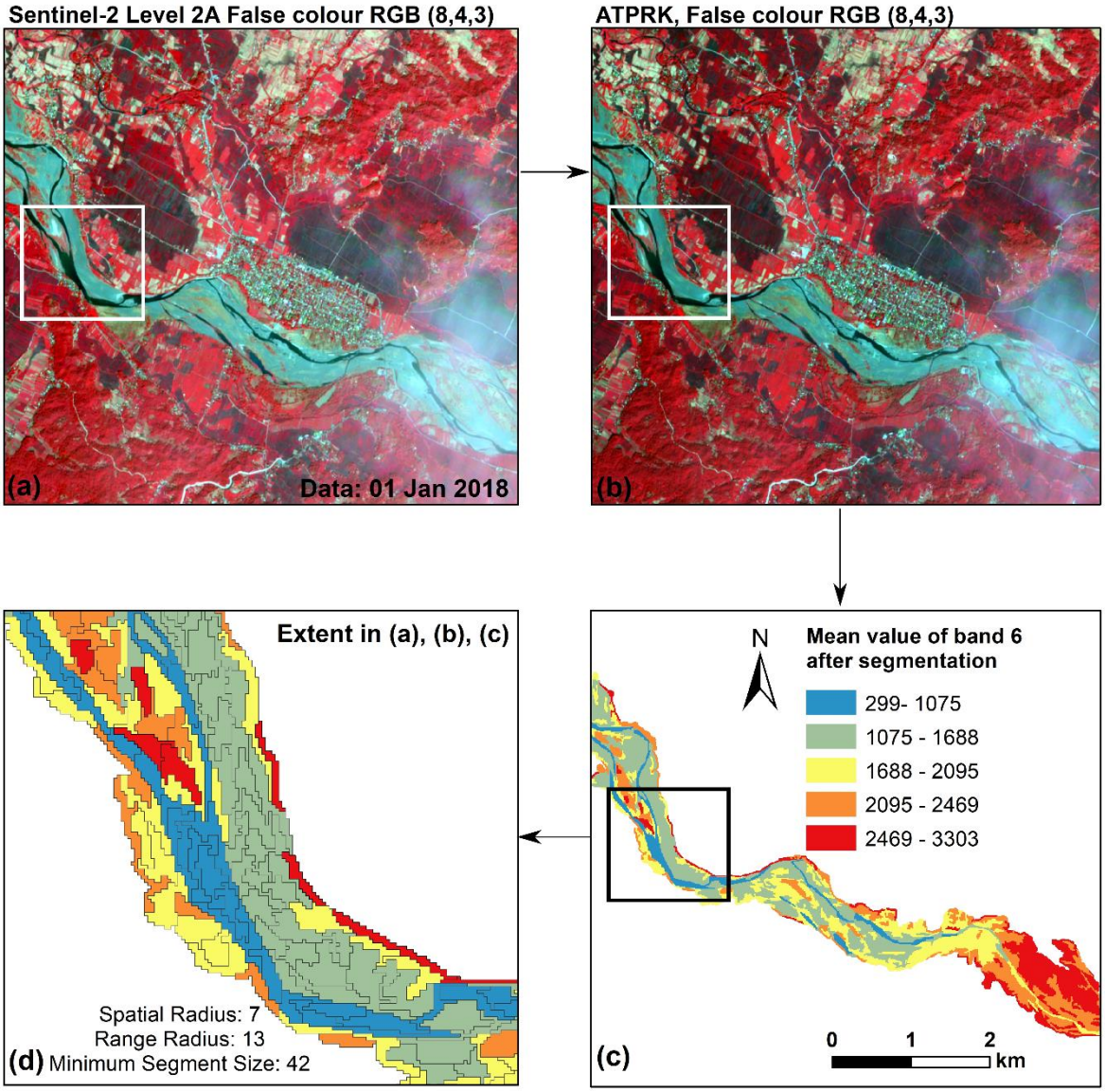

Figure 3-6. Segmentation examples using Large Scale Mean Shift method. (a) Sentinel-2 Level 2A image for part of the Bislak River, 1.01.2018. (b) ATPRK image of the same area. (c)mean value of Band 6 in the ATPRK image after segmentation. (d) enlarged area (see boxes in a,b,c).

3.2.5. Corrections on manually digitised ground truth objects

The manually digitised ground truths are usually interpreted visually, which is unrealistic to apply at a pixel scale. For example, in Figure 3-7, the object (within the blue boundary in Figure 3-7a) was classified as a unique object differing from surrounded objects (denoted by grey boundaries). This research defined landform by giving type of majority pixels to the object.

From the true colour image, although the object bounded in blue has a small proportion of vegetation, it was defined as unvegetated landform, but it is manually classified as vegetated landform in Figure 3-7b. It is very easy to generate a heterogeneous bar while doing manual digitisation, especially doing the classification at a large spatial scale. Although a typical landform can be allocated to the objects one by one after doing LSMS segmentation, the relatively rough digitising work can help saving a lot of time when there are massive objects. In a 19 km reach, the number of segmented objects can vary from c.1200 to 1500 so that manual classification of the segmented objects would be a big cost.

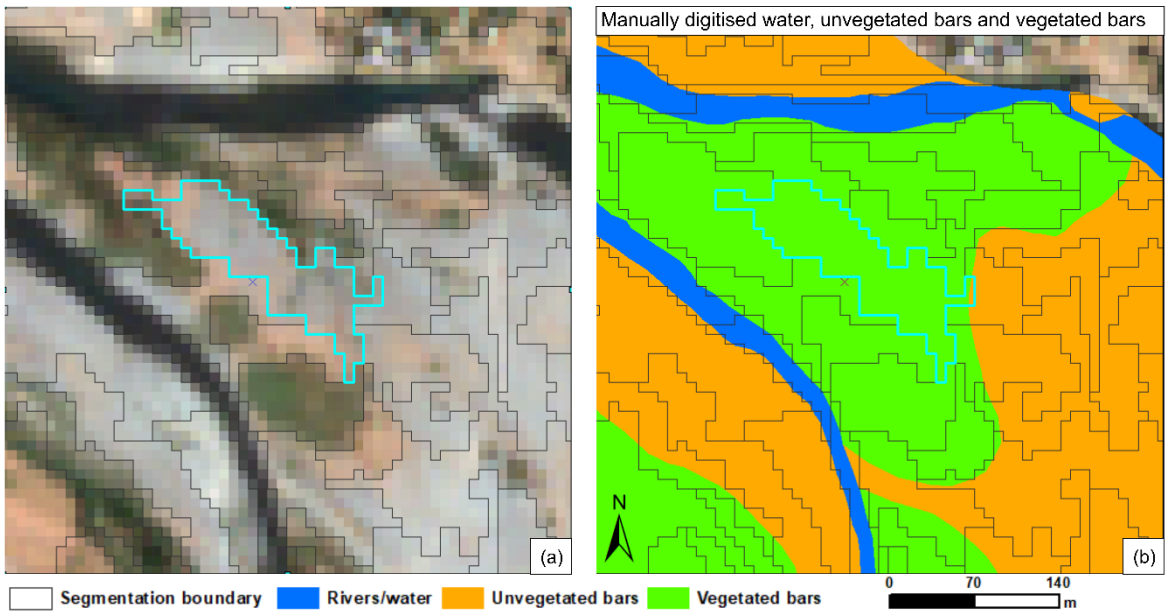

Figure 3-7. Comparison of (a) LSMS segmentation map and (b) manually digitised ground truth map. See text for explanation of the blue box in (a).

In the early stage of investigation on improving ground truth accuracy, a ‘mutual correction’ workflow was proposed. In this workflow, firstly, a 19 km reach of Bislak River was selected as the experimental area, and ten blocks were defined according to the equal distance along the river centreline and given a serial number (Figure 3-8). Then, ten blocks of sub reaches were divided into a training dataset and a testing dataset.

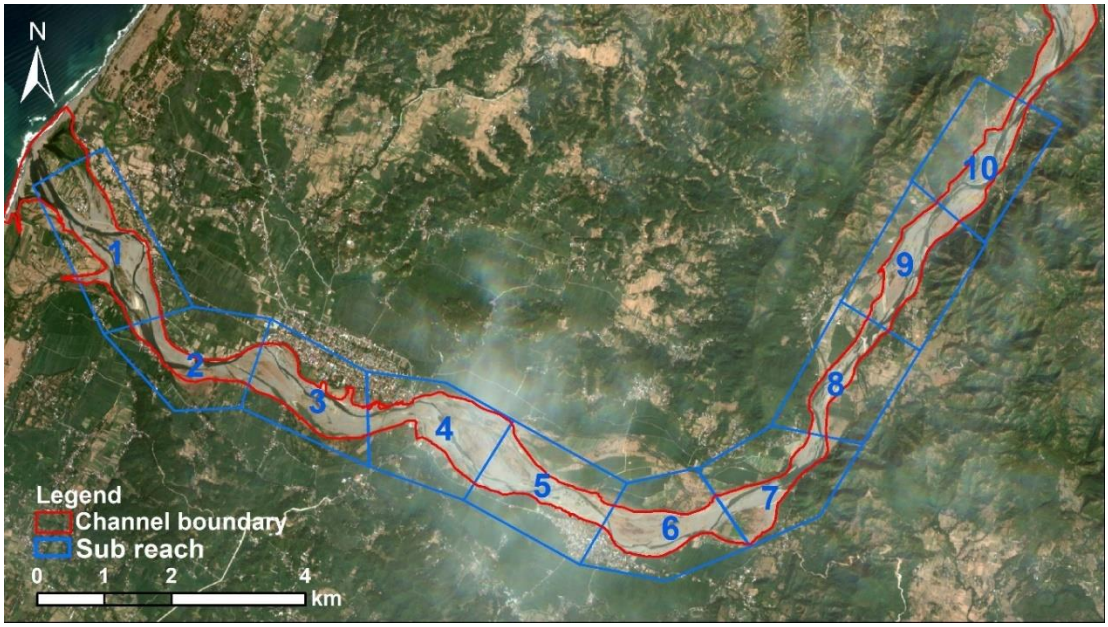

Figure 3-8. Ten sub reaches of the experimental area on the Bislak River with serial numbers.

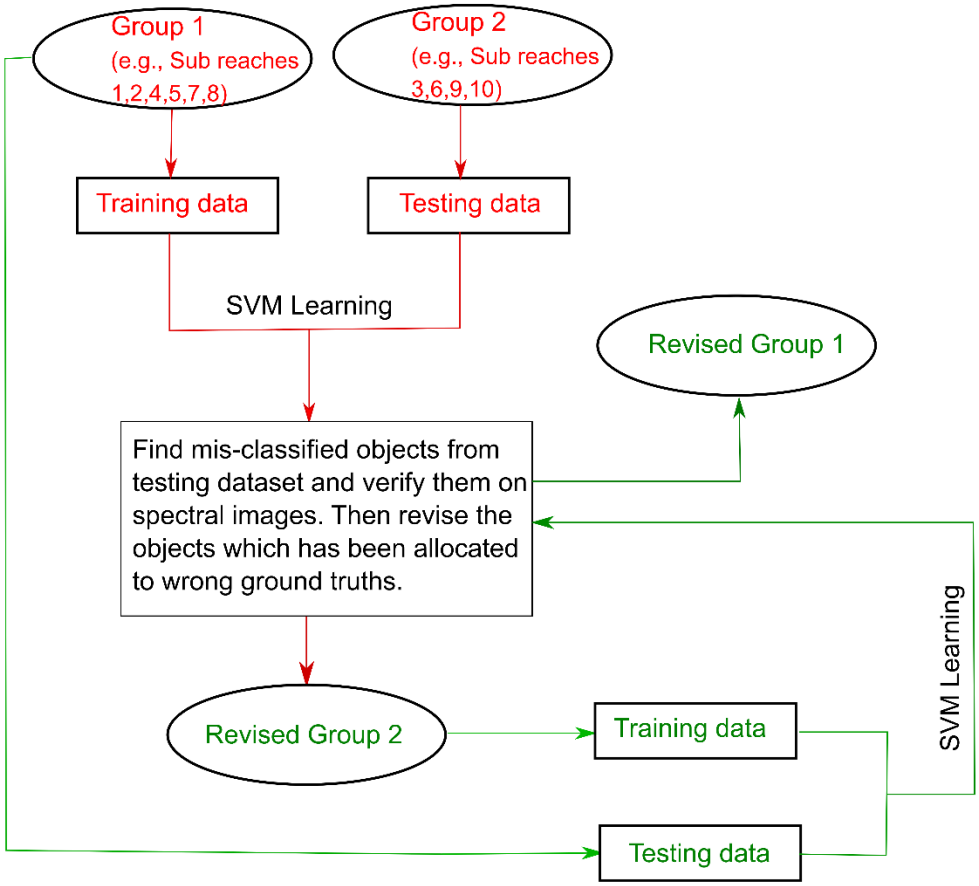

Figure 3-9. Ground truth object mutual corrections workflow.

Figure 3-9 gives an example of one mutual correction between Group 1 and Group 2. In this case, Group 1 was formed by sub reaches 1,2,3,5,7,8 which contains 798 objects in total, whilst Group 2 was combined by sub reaches 3,6,9,10 which contains 506 objects in total. Firstly, Group 1 was set as training dataset and Group 2 was the testing dataset. Then the SVM classification was processed on Group 1 and Group 2 giving an accuracy score of 0.85. Secondly, misclassified objects from Group 2 were manually verified on the spectral images. Thirdly, revised Group 2 was set as the training data and Group 1 was defined as the testing data. Then another round of SVM classification was engaged. The new classification accuracy is 0.88. Lastly, again, misclassified objects of Group 1 were manually verified on the spectral images. Thus, one procedure was completed, and ground truths of Group 1 and Group 2 were both corrected.

To understand how well the mutual correction workflow worked, new combinations for two groups were selected. In this case, sub reaches 2,3,5,6,8,10 containing 692 objects were gathered as Group 1 and sub reaches 1,4,7,9 containing 612 objects were gathered as Group 2. Then Group 1 was trained, giving a validation accuracy of 0.9. After training in SVM, the model was tested on Group 2 and a test accuracy of 0.92 was obtained. The classification performance has been improved to some extent through correcting the ground truths. However, when the misclassified objects were referred back to the spectral image, there are still some objects classified incorrectly against the ground truths. This potentially requires another round of verifications using the same workflow. The experiment in this section suggested that the mutual correction workflow did improve classification against the manual digitised ground truth, but it may take several rounds on the workflow to get a well classified ground truth map. Therefore, in the practice of the following chapters of this thesis, allocating a typical landform to the segmented objects one by one remains to be the first option for manual digitising work. However, in the future study, when there are very high numbers of objects, the mutual correction workflow may be able to take advantage of new technology and tools to accomplish faster and better manual landform digitisation.

3.3. Spatial-temporal dataset generation

This thesis utilises spatial-temporal analysis to study the river landform change. Therefore, generating the spatial-temporal dataset along the rivers required the greatest effort through making river landform classification maps for each date throughout the studied time period.

Thiessen Polygons generation was achieved in ArcGIS Desktop 10.8. Tools used in ArcToolbox are denoted in *italics* below:

Step 1. Use *Collapse Dual Lines to Centreline* tool to generate the centreline of the active channel (Figure 3-10a);

Step 2. *Split* the centreline in *Step 1* into predetermined equal distance segments (Figure 3-10a);

Step 3. Convert *Feature Vertices to Points* on the line segments in *Step 2* and get output end points (Figure 3-10a);

Step 4. *Create Thiessen Polygons* on the output end points in *Step 3* (Figure 3-10b);

Step 5. *Clip* the Thiessen polygons (Figure 3-10b) using the active channel shapefile (Figure 3-10c) to get the 'Thiessen-channel. shp' layer;

Step 6. Apply *Zonal Statistics as Table* to the river landform classification map (raster at 10× 10 m) and 'Thiessen-channel. shp'. By this way, the sum area of a specific landform within its 'Thiessen-channel' segment can be calculated, which means the landform areas/proportions can be measured at an equal distance along the river.

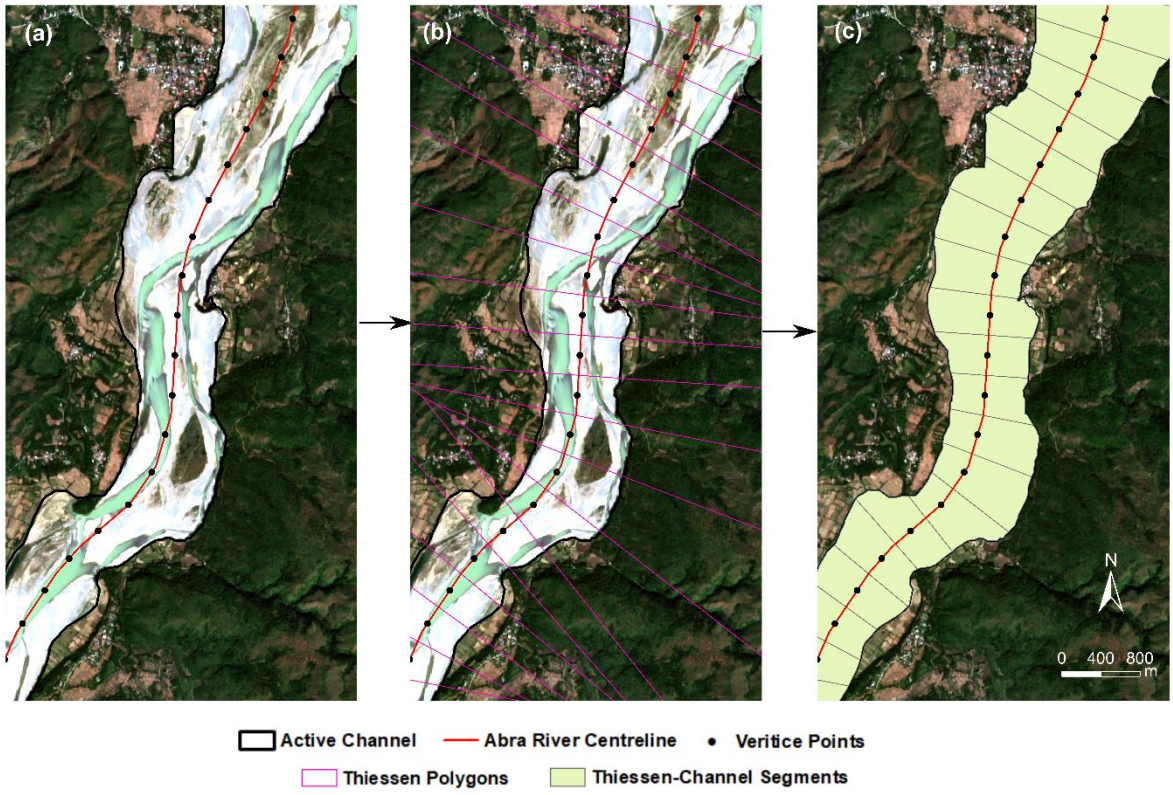

Figure 3-10. The 'Thiessen-channel' segments generation procedure. See text for details.

Considering the span of Sentinel-2 remote sensing data is very short for recognising the permanent vegetated islands, the active channel width includes distance across vegetated islands within the active channel. For the Bislak River, the selected active centreline was divided into 100 segments with approximate 410 m for each segment. For the studies in the other three rivers in the following chapters, the centreline would be divided into segments with equal distance at approximate 410 m, too. Through the procedure displayed in Figure 3-10, the active channel width at equal along-channel distances can also be calculated by converting the Thiessen polygons to line features. By measuring lengths of these lines, active widths along the river channel can be captured. This method is used in Chapter 5 and Chapter 6 to generate the spatial-temporal landform area/proportion and active channel width datasets, which enable the use of spatial-temporal statistics and analyses of the landform changes in the Bislak, Laoag, Abra and Cagayan Rivers.

Alternatively, mapping the frequency of particular landforms is another way to present spatial-temporal data. In this thesis, frequency maps were generated from rasterised river landform classification maps. The calculation was applied to 10× 10 m pixels using all the maps

generated for the studied period. |For example, in mapping water frequency, the procedure counts the number of pixels denoted by water, and divides number of times that water is recorded at each pixel by the total number of maps available at the same pixel location. Therefore, a water frequency map is generated which can also present how it is likely that water appears at a specific location based the full historical data set.

In analysing the spatial-temporal data, the two approaches above are both important and performed well for different purposes. Therefore, choosing appropriate analysis tools is a key step before extracting the spatial-temporal information.

3.4. Ensemble Empirical Mode Decomposition

3.4.1. Sifting Procedures

This project involves generation and analysis of time series of river landforms for four rivers. To detect the temporal changes in these data sets, Ensemble Empirical Mode Decomposition (EEMD) was used to decompose the temporal signals in the data. EEMD is appropriate as the data are likely to be non-stationary and the time series that are available are relatively short. This section illustrates the procedure for using Empirical Mode Decomposition (EMD), which is the first step of EEMD to sift the data into components, which are referred to as Intrinsic Mode Functions (IMFs). EMD is a signal decomposition method to directly extract the energy associated with various intrinsic time scales, which are the most important parameters of the system. To illustrate the method, consider a random time series $x(t)$, as shown in Figure 3-11 (Kong et al. 2015), for which the EMD method can be explained by the following steps:

Step 1. As shown in the Figure 3-11b, for the time series $x(t)$, the upper and lower envelopes are used to connect all the local maxima and local minima through fitting cubic splines. The mean value of the upper and lower envelopes is defined as $m_1(t)$ (Figure 3-11b).

Step 2. $m_1(t)$ in *Step* 1 is subtracted from $x(t)$ and an IMF $h_1(t)$ is obtained as:

$$h_1(t) = x(t) - m_1(t) \qquad (3-1)$$

Step 3. Regard $h_1(t)$ as a new data series, and repeat *Step* 1 and *Step* 2 for *k* times as:

$$h_2(t) = h_1(t) - m_2(t)$$

$$h_3(t) = h_2(t) - m_3(t)$$

$$\vdots$$

$$h_k(t) = h_{k-1}(t) - m_k(t) \qquad (3-2)$$

until it reaches to a stop criterion determined by Huang et al. (1998), which can be accomplished through limiting the size of the standard deviation (*SD*) computed from two consecutive sifting results as:

$$SD_K = \frac{\sum_{t=0}^{T} |h_{k-1}(t) - h_k(t)|^2}{\sum_{t=0}^{T} h_{k-1}^2(t)} \qquad (3-3)$$

When SD_K is smaller than a predetermined value, the sifting process is stopped (Kong et al. 2015). Huang et al. (1998) suggested that SD_K between 0.2 to 0.3 is a very rigorous limitation for the difference between successive siftings. In this case, the highest frequency component of the data series is denoted as the first IMF (Kong et al. 2015):

$$C_1(t) = h_k(t) \qquad (3-4)$$

$C_1(t)$ is expected to contain the finest scale or the shortest period component of the signal. Through the same way other lower frequency components are obtained as:

$$C_2(t) = h_{k-1}(t)$$

$$C_3(t) = h_{k-2}(t)$$

$$\vdots$$

$$C_n(t) = h_1(t) \qquad (3-5)$$

Step 4. To obtain the residual of the decomposition, every IMF should be extracted from $x(t)$ step by step:

$$r_1(t) = x(t) - C_1(t)$$

$$r_2(t) = r_1(t) - C_2(t)$$

$$\vdots$$

$$r_n(t) = r_{n-1}(t) - C_n(t) \qquad (3-6)$$

When the sifting process stops according to the decision equation (3-3), the residual $r_i(t)$ should become a monotonic function from which no more IMF can be extracted, or the residual becomes so small that it is much less than the predetermined value of substantial consequences (Huang et al. 1998). Therefore, according to the calculations above, the data can be presented in summary form as:

$$x(t) = \sum_{i=1}^{n} C_i(t) + r_n(t) \qquad (3-7)$$

Additionally, Huang (2004) explains how to calculate the mean period for IMFs, which is:

$$T_n = \frac{N}{N_p} \qquad (3-8)$$

Where *T* is the mean period of IMF, N represents the total data series number and N_p gives the total number of local maxima (number of peaks).

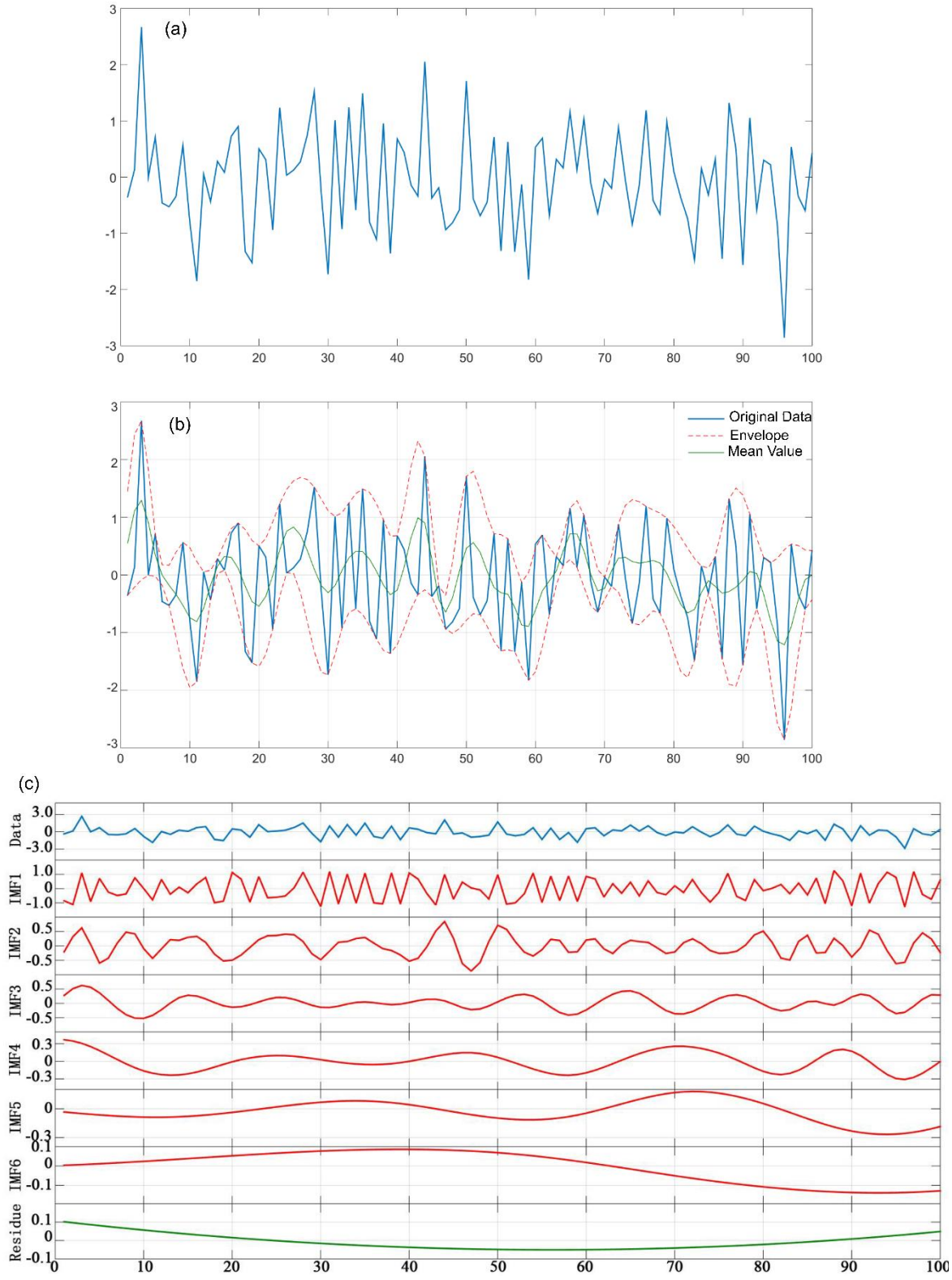

Figure 3-11. An example of a random data series decomposition using sifting method (source: Kong et al. 2015). For the random series (blue lines) in (a) and (b), the upper and lower red dot lines in (b) denote the envelopes of the random data series. The green line in (b) is the mean curve of the envelopes. (c) presents the results using sifting process to decompose the random series in (a) and (b).

3.4.2. EEMD

In 3.4.1, the sifting process of EMD has been introduced. The method of Ensemble Empirical Mode Decomposition (EEMD) is derived from EMD and is used to solve problems of mode mixing in EMD by adding white noise to the signal (Huang 2004). The EEMD method is an effective signal detection tool for non-stationary data. For example, it has been widely used in detecting signal change and extracting signal information from the physical world to analyse natural disasters and human activity disturbance (Gaci 2016; Lei et al. 2009; Zhu and Malekjafarian 2019). A case study of using EEMD to decompose precipitation time series and IMF interpretation is shown in Chapter 5. The description of the EEMD algorithm is shown (Kong et al. 2015) as:

Step 1. A random white noise series $w_m(t)$ is added to the data series $x(t)$:

$$x_m(t) = x(t) + w_m(t) \qquad (3-9)$$

Step 2. $x_m(t)$ then is decomposed using EMD:

$$x_m(t) = \sum_{i=1}^{n} C_{i,m}(t) + r_{i,m}(t) \qquad (3-10)$$

Step 3. Repeat Step 1 and Step 2 for M times using different white noise series.

Step 4. Then the means of the corresponding IMFs can be calculated as:

$$C_i(t) = \frac{1}{M} \sum_{m=1}^{M} C_{i,m}(t) \qquad (3-11)$$

3.5. Simpson's index of diversity

Simpson's diversity index (Simpson 1949) has been widely used for quantifying the diversity of plant and animal species (Keylock 2005), and is also considered to be a good tool for evaluating landscape diversity (Nagendra 2002). There are two concepts incorporated within Simpson's diversity index, which are richness and evenness. In landscape classification cases, richness is measured as the number of landscape types per sample, and evenness is measured

as the abundance of the different landscape types making up the richness of the sample. In this thesis, river landform types are characterised at 10×10 m pixel resolution by transforming shapefile maps to raster maps in ArcMap 10.8. For example, there are 30 records at a specific pixel location from 30 dates, within which water shows 10 times, unvegetated bars appears 10 times and vegetated bar records 10 times. Therefore, the richness of this case is 3 types (water, unvegetated bars and vegetated bars), whilst the evenness is very high because the three landforms captured the same opportunity (each has 10 times) in records, which indicates a very high diversity at this pixel location over the record period. Simpson's index of diversity considers both richness and evenness. Simpson's index is firstly calculated by the equation as:

$$D = \frac{\sum n(n-1)}{N(N-1)} \qquad (3-12)$$

where D represents the Simpson's diversity index, n is the number of a specific type of landform over the record period and N is the total number of all landforms. Using the Cagayan River as an example, there are 20 records in total at a specific pixel location (N= 20), and it records water 7 times, unvegetated bars 7 times, vegetated bars 6 times and other type (e.g., clouds, shadows, etc.) 0 times, for which the calculation is:

$$D = \frac{7 \times 6 + 7 \times 6 + 6 \times 5 + 0}{20 \times 19} \qquad (3-11)$$

Therefore, in this case, the Simpson's index D= 0.3. To makes index follow the rule of the greater the value, the greater the sample diversity, the Simpson's index of diversity (SDI) is defined by the equation as:

$$SDI = 1 - D \qquad (3-12)$$

Thus, the SDI of the Cagayan River case above is 0.7 as calculated. *SDI* lies between 0-1 (Keylock 2005; Nagendra 2002; Simpson 1949). In this study, the greater values of SDI indicate more diverse landform types and lower values show more stable conditions. Chapter 6 and Chapter 7 presents mapping of Simpson's index of diversity for the river landforms in the Bislak, Laoag, Abra and Cagayan Rivers.

This chapter introduced preliminary work of designing an appropriate method structure for this thesis. In addition, some basic steps for extracting spatial-temporal dataset, which were not included in Chapters 4, 5, 6, were presented. These preliminary and basic steps guided the research in the following chapters.

3.6. Coefficient of variation

This thesis analyses river landform temporal stability by the means of calculating coefficient of variation (COV) (Bedeian and Mossholder 2000) using temporal data at spatial distance. The equation of COV (C_v) is presented as:

$$C_v = \frac{\sigma}{\mu} \qquad (3-13)$$

Where σ represents the standard deviation of the temporal data while μ represents the mean value of the temporal data. The higher value of COV indicates higher instability, vice versa. In the Chapter 5 and 6, along the longitudinal distance in each studied river, temporal area of each landform is calculated by COV to study the landform stability at a specific distance. This calculation does not provide richness and evenness information which are considered by Simpson's diversity index. However, COV fast plots temporal data stability at distance, which enable us to intuitively visualize spatial stability change using a 2-D plot in a more efficient way, especially when comparing with other rivers together.

Chapter 4 - Enhancing performance of multi-temporal tropical river landform classification through downscaling approaches

The following chapter is a reformatted version of a manuscript published on the International Journal of Remote Sensing by Qing Li, Brian Barrett, Richard Williams, Trevor Hoey and Richard Boothroyd, which is available at https://doi.org/10.1080/01431161.2022.2139164.

Highlights

- Choice of downscaling approach influences the performance of river landform classification from satellite imagery and should be considered in river and flood management.
- An efficient and straightforward operating workflow was developed for automated river landform classification with high accuracy that supports an improved understanding of the use of machine learning approaches in river landforms recognition.
- Freely available and easy-to-access remote sensing datasets can help extend the operating workflow to difficult-to-access or remote regions and allow for complete regional and/or national coverage.

Abstract

Multi-temporal remote sensing imagery has the potential to classify river landforms to reconstruct the evolutionary trajectory of river morphologies. Whilst open-access archives of high spatial resolution imagery are increasingly available from sensors such as Sentinel-2, there remains a fundamental challenge of maximising the utility of information in each band whilst maintaining a sufficiently fine resolution to identify landforms. Although image fusion and downscaling methods on Sentinel-2 images have been investigated for many years, there is a need to assess their performance for multi-temporal object-based river landform classification. This investigation first compared three downscaling methods: area to point regression kriging (ATPRK), super-resolution based on Sen2Res and nearest neighbour resampling. We assessed performance of the three downscaling methods by accuracy, precision, recall and F1-score. ATPRK was the optimal downscaling approach, achieving an overall accuracy of 0.861. We successively engaged a set of experiments to determine an optimal training model, exploring single and multi-date scenarios. We find that not only does remote sensing imagery with better quality improve river landform classification performance, but multi-date datasets for establishing machine learning models should be considered for contributing higher classification accuracy. This paper presents a workflow for automated river landform recognition that could be applied to other tropical rivers with similar hydro-geomorphological characteristics.

4.1. Introduction

Multi-temporal classification of river landforms is essential to understanding how river planform changes through time (Boothroyd et al. 2021) and reconstructing the evolutionary trajectory of river morphologies (Spada et al. 2018). Such changes manifest intra-annually, for example, as a result of seasonal changes in vegetation cover (Gurnell 2014; Serlet et al. 2018) or over longer timescales, as a result of variations in water and sediment supply or autogenic adjustments (Hohensinner et al. 2021; Mandarino, Maerker, and Firpo 2019; Vargas-Luna et al. 2019). Two technological developments offer the potential to realise multi-temporal river landform classification at catchment spatial scales, across multiple years. First, open-access archives of high spatial resolution imagery are increasingly available from satellite sensors such as Sentinel-2, which offer considerable potential for improving land cover investigations at the regional level (Phiri et al. 2020). Second, a variety of machine learning approaches have been developed and applied to achieve fast, objective and accurate land-cover mapping (Maxwell, Warner, and Fang 2018). Various landscape classifications have been demonstrated using Sentinel-2 over the past five years (Korhonen et al. 2017; Phiri et al. 2020; Sonobe et al. 2018; Yang et al. 2017). However, the potential of Sentinel-2 to classify river landforms using a hierarchical object-based workflow has been less explored (Carbonneau et al. 2020; Demarchi, Bizzi, and Piegay 2016).

When using data acquired by multi-resolution sensors such as Sentinel-2, a fundamental challenge for fluvial applications is to maximise the utility of information in each band whilst maintaining a sufficiently fine resolution to identify landforms. Lanaras et al. (2018) reviewed methods of enhancing the spatial resolution of remotely sensed multi-resolution images and differentiated these methods into three types: (i) pan-sharpening per band (e.g., area to point regression kriging, ATPRK); (ii) inverting an explicit imaging model (e.g., super-resolution method); and (iii) supervised machine learning based approaches.

The ATPRK algorithm was originally developed for downscaling MODIS imagery (Wang et al. 2015) and was subsequently applied to Sentinel-2 imagery (Wang et al. 2016). In Sentinel-2 image fusion cases, ATPRK was shown to outperform pan-sharpening per band approaches such as component substitution (CS) and multi-resolution analysis (MRA) (Wang et al. 2016). Sentinel-2 has four bands at fine resolution instead of one panchromatic band that covers a wider range of the spectrum. Before applying the ATPRK algorithm to Sentinel-2 data, a single

‘panchromatic band’ from four fine bands of the Sentinel-2 acquisition is required. In this case, ‘hyper-sharpening’ was considered to extract a single band by two schemes, which are the ‘selected band scheme’ (choose one band from four fine bands) and the ‘synthesised band scheme’ (synthesise one band using four fine bands), respectively (Selva et al. 2015). Wang et al. (2016) shows that the ‘synthesised band scheme’ contributes more accurate downscaling results when combined with the ATPRK approach. For the case of establishing the synthesised ‘panchromatic’ band, Wang et al. (2016) calculated weights of each fine band using a regression model between the fine band and visiting coarse band. A linear combination of four fine bands was used to generate the synthesised band. Thereby, ATPRK not only utilises all four fine bands to achieve image fusion, but it also preserves the original spectral properties of the coarse band data from Sentinel-2 imagery.

Brodu (2017) developed a geometry-based super-resolution approach, which aimed to compensate for the absence of a real panchromatic band. First, information shared by natural objects between neighbouring pixels is detected. Then, common aspects of the shared geometric information across all bands are extracted. In addition to common information, independent geometric information is separated from high-resolution bands and then applied to unmix the low-resolution pixels, but their overall reflectance should be preserved. The super-resolution approach is available through the Sen2Res plugin in the widely used European Space Agency (ESA) SNAP software (del Rio-Mena et al. 2020; Freitas et al. 2019; Kuan et al. 2020; Laso et al. 2020).

The ATPRK and super-resolution approaches incorporate relations between coarse and fine bands. In contrast, supervised machine learning approaches (e.g. deep neural networks) rely on example data. Although the machine learning approach is more adapted to complex and general relations, the need for large training datasets and high computing resources are obstacles to implementation (Lanaras et al. 2018), especially when applied at large spatial-temporal scales. In addition to the downscaling approaches above, the nearest neighbour resampling approach has been favoured to detect land cover from Sentinel-2 due to its simple computation and fast processing when downscaling coarse bands to fine bands (Daryaei et al. 2020; Kuan et al. 2020; Zheng et al. 2017). The nearest neighbour resampling approach assigns the value of the nearest coordinate location of the input pixel to the corresponding output pixel, and thus is a simple and efficient approach. However, nearest neighbour resampling is not suitable for applications that consider the textural properties of images because it can lead to pixel level geometric

discontinuities (Roy and Dikshit 1994). The development of these different approaches presents a need to assess the best approach to image downscaling before undertaking image segmentation and classification.

This paper aims to compare the three resolution enhancing approaches above, and to identify the most accurate method for Sentinel-2 based tropical river landform classification. Specifically, the paper seeks to address the following questions: (Q1) Which image downscaling approach (ATPRK, super-resolution and nearest neighbour resampling) is optimal for classifying tropical river landforms? (Q2) For a single river, is multi-temporal training data required to classify landforms for multiple periods in a year? (Q3) Is the training model for one year transferable to other years? (Q4) Is the training model transferable to nearby rivers with similar hydrogeomorphic properties?

4.2. Study Area

The study area in northwest Luzon, the Philippines, experiences frequent tropical storms and cyclones, which bring heavy precipitation causing landslides and flooding in the region (Faustino-Eslava et al. 2013). The area is dominated by a sub-tropical East Asian monsoon climate (Liu et al. 2009). In the northwest Philippines, the wet season begins with increased rainfall around May to June and continues until rainfall decreases around October to November (Kubota et al. 2017).

Our investigation focused upon three watercourses in Luzon: the Bislak, Laoag and Abra Rivers (Figure 4-1). These gravel-bed rivers are all characterised by planforms that include water, unvegetated bars and vegetated bars/islands. Relating to the spatial resolution of the satellite imagery available for analysis, image processing focused on sufficiently wide sections of the rivers that their morphology could be adequately resolved (Gilvear and Bryant 2016). The 39 km long section of the Bislak River has a mean width (MW) of 375 m; it is the shortest of the three rivers and has relatively small tributary inputs compared to the other two rivers. The 47 km long section of the Laoag River has a MW of 580 m and has three approximately equally sized tributaries, whose MW varies from 237 m to 424 m. The Abra River (MW:2441 m, 82 km section length) has three main tributaries; one large tributary has a MW of 1804 m in upper lowland and has extensive agricultural development within the active channel.

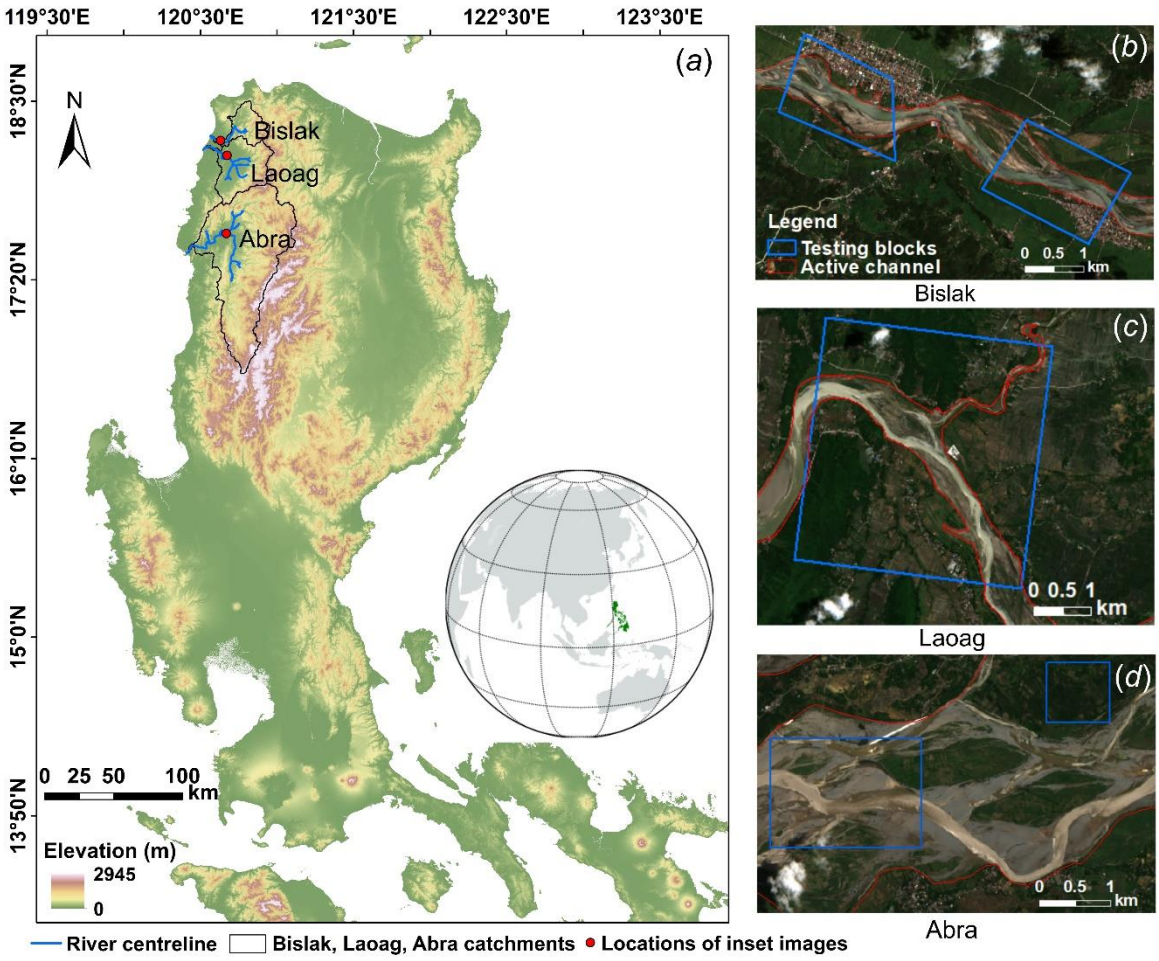

Figure 4-1. (a) Study area showing locations of the (b) Bislak, (c) Laoag and (d) Abra Rivers in northwest Luzon, the Philippines.

4.3. Datasets and methods

4.3.1. Sentinel-2 imagery and ground truth digitisation

Sentinel-2 provides imagery with 13 multispectral bands varying from 10 m to 60 m resolution and data availability since 23 June 2015. In this study, Sentinel-2 imagery acquired between January 2017 and December 2019 were analysed. Data were accessed through the USGS Earth Explorer Portal (https://earthexplorer.usgs.gov/; Table 4-1). A cloud-free Sentinel-2 image (with very small proportion of haze clouds) acquired on 1 January 2018, under growing vegetation and low water flow conditions, was initially used to develop a manually digitised ground truth map of landforms in the Bislak River (water: 1.93 km^2, unvegetated bars: 6.28 km^2, vegetated bars: 6.15 km^2). The ground truth map was used to assess the results from the three approaches to downscaling. To train and validate a multi-temporal model, Sentinel-2

acquisitions of the Bislak River for six dates in 2018 were selected for digitisation. To test the transferability of the multi-temporal Bislak training model to other years, Sentinel-2 acquisitions on six dates in both 2017 and 2019 were used. To test the transferability of the training model to other nearby rivers, Sentinel-2 acquisitions of the Laoag River on six dates in 2018 and of the Abra River on six dates in 2019 were used.

Table 4-1. Sentinel-2 acquisition dates for each river from 2017 to 2019.

River	2017 (DD/MM)	2018 (DD/MM)	2019 (DD/MM)
Bislak	16/01, 16/04, 15/06, 03/09, 28/10, 07/12	01/01, 07/03, 01/05, 10/07, 20/07, 18/09, 07/11	10/02/, 11/04, 30/06, 29/08, 13/10,07/12
Laoag	-	01/01, 07/03, 01/05, 10/07, 18/09, 07/11	-
Abra	-	-	11/01, 27/03, 16/05, 25/07, 13/09, 22/11

4.3.2. Image Pre-processing

The L1C image datasets were atmospherically corrected using Sen2Cor within the ESA SNAP software. Bands with 10 m and 20 m resolution were used to build the machine learning model. In this case, bands at 20 m resolution were processed to 10 m resolution using three downscaling approaches: super-resolution (Brodu 2017), ATPRK (Wang et al. 2016) and nearest neighbour resampling. The super-resolution approach used in this study was directly achieved by the Sen2Res tool in SNAP (version 7.0). The nearest neighbour resampling was also performed in SNAP while the ATPRK approach was run in MATLAB R2019a.

In addition to the Sentinel-2 bands, five environmental indices (Table 4-2) were generated and incorporated into the machine learning model, resulting in a total of 15 features (10 multi-spectral bands and 5 environmental indices) for the river landforms classification. The 5 environmental indices have been widely used in a variety of studies for extracting vegetation and water extent from remote sensing images (Rokni et al. 2014). EVI2 was originally designed to be used for sensors without a blue band to produce an EVI-like vegetation index and may reveal different vegetation dynamics (Jiang et al. 2008). Therefore, in this research, we try to incorporate both EVI and EVI2 into our dataset to run the machine learning.

Table 4-2. Selected indices for processing classification.

Features	Description	Resolution(m)	Formula	Reference
NDVI	Normalised Difference Vegetation Index	10	(band 8- band 4)/ (band 8+ band 4)	Carlson and Ripley (1997)
NDMI	Normalised Difference Moisture Index (Change in water content of leaves)	10	(band 8-band 11)/ (band 8+band 11)	Bangira et al. (2019)
NDWI	Normalised Difference Water Index (Water content in water bodies)	10	(band 3-band 8)/(band 3+band 8)	Gao (1996)
EVI	Enhanced vegetation index	10	2.5× (band 8A-band 4)/ (band 8A+6×band 4-7.5×band 2+10[a])	Huete et al. (2002)
EVI 2	Enhanced vegetation index	10	2.5× (band 08-band 4)/ (band 8+2.4×band 4+10[a])	Jiang et al. (2008)

4.3.3. Geographic Object Based Image Analysis (GEOBIA) machine learning

GEOBIA was employed for image segmentation and classification. The Large-Scale Mean Shift (LSMS) algorithm in Orfeo Toolbox (version 6.6.1) was used for the segmentation of objects within the river channel. Three landforms within the river were defined by manually digitising water, unvegetated bars and vegetated bars. The objects were trained together with the manually digitised ground truth map and input into the Support Vector Machine (SVM) model and subsequently evaluated, following the workflow described in Figure 4-2. For the SVM model, regularisation parameter of 1.0 and scale radial basis function kernel were used and implemented using scikit-learn in Python 3.7.

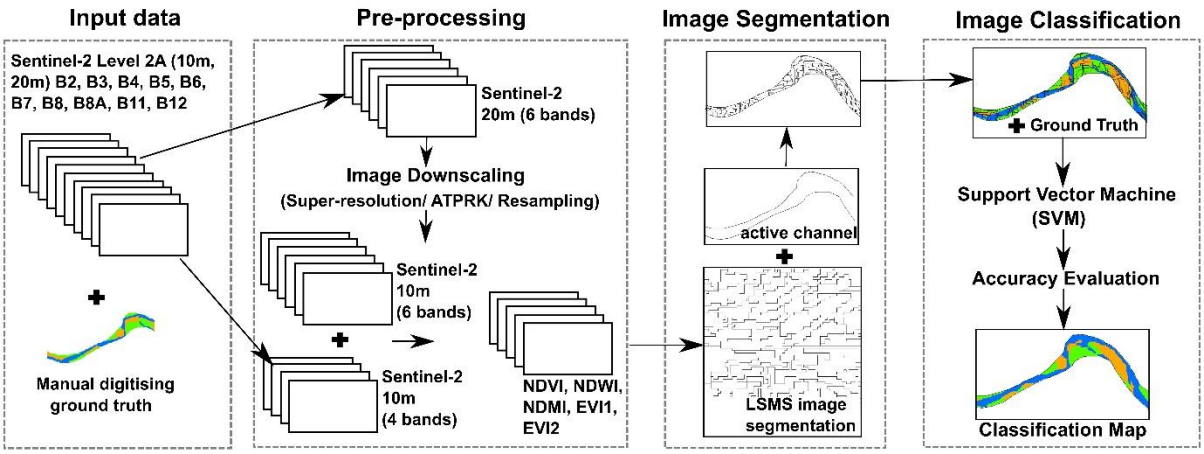

Figure 4-2. Workflow for river landform classification.

4.3.4. Downscaling choice

Sentinel-2 images for the Bislak River on 1 January 2018 were used to compare the three downscaling approaches. In this case, the Bislak River was firstly divided into 10 blocks, using a 7:3 split for training and testing blocks. The numbers of training and testing objects are given in Table A1. Image processing efficiency and classification performance were assessed for all of the three approaches (Figure 4-2). The classification accuracy of each dataset was evaluated using the overall accuracy, precision, recall and f-1 score. The binary classification can be measured by building a confusion matrix which records correctly and incorrectly recognised examples (Sokolova, Japkowicz, and Szpakowicz 2006). Goutte and Gaussier (2005) considered each object with a binary label which accounts for correctness of the object, where true positive (TP) represents positive class being classified as positive; false positive (FP) represents negative class being classified as positive; false negative (FN) represents positive class being classified as negative; true negative (TN) represents negative class being classified as negative. Through this definition, accuracy, precision and recall are measured by:

$$Accuracy = \frac{TP + TN}{TP + FP + FN + TN} \qquad (4-1)$$

$$Precision = \frac{TP}{TP + FP} \qquad (4-2)$$

$$Recall = \frac{TP}{TP + FN} \qquad (4-3)$$

The F1 score can be interpreted as a harmonic mean of the precision and recall, where an F1 score reaches its best value at 1 and worst score at 0 (Sokolova, Japkowicz, and Szpakowicz 2006; Goutte and Gaussier 2005). F1 score can be calculated by:

$$F1 = \frac{2 \times (Precision \times Recall)}{Precision + Recall} \qquad (4-4)$$

Beyond overall accuracy of the classification, per-class accuracies (water accuracy (WA), unvegetated bar accuracy (BA) and vegetated bar accuracy (VA)) were also considered.

Table A1. Numbers of training and testing objects for landforms when applying the three downscaling approaches.

Downscaling approach	Dataset	Number of objects			
		Total	Water	Unvegetated bars	Vegetated bars
Resampling	Training	747	71	456	220
	Testing	330	69	173	88
ATPRK	Training	751	76	455	220
	Testing	317	70	160	87
Super-resolution	Training	10219	1432	4550	4237
	Testing	5262	794	2170	2298

4.3.5. Optimal training model

To investigate an optimal machine learning model, both the training and testing data selections were considered. This study started landform classification using a single-date model (for both training and testing datasets) and a six-date model (for both training and testing datasets). In this case, the training model (Figure 4-3) generated on 1 January 2018 was initially set (Table A2), and then tested on the whole reach (red extent of Figure 3) for the remaining five dates in 2018. In this experiment, the ‘unknown units’ (e.g., urban structures, cloud and shadows, were named as ‘others’ and incorporated in the training model. To gain a better understanding of the classification performance of unknown units, the testing site from 10 July 2018, which is partly covered by clouds, was extended by 20 m outside the active channel boundary to incorporate urban pixels. In this way, a mixed group of ‘others’ was prepared for testing.

Figure 4-3. Selected imagery extent for building optimal training model in the Bislak River. Background is the true colour Sentinel-2 image dated 1 January 2018.

Table A2. Numbers of objects used in the single-date model.

Date	Number of objects					
2018	Dataset	Total	Water	Unvegetated bars	Vegetated bars	Others
1 Jan	Training	1304	203	694	376	31
1 Jan	Testing	380	92	188	100	0
7 Mar	Testing	1131	175	662	291	3
1 May	Testing	1043	156	615	267	5
10 July	Testing	1463	225	482	448	308
18 Sept	Testing	1065	431	555	71	8
7 Nov	Testing	1026	258	556	204	8

Consequently, a modified approach was conducted on a new group of training and testing datasets. Firstly, a 19 km reach of the Bislak River (Figure 4-3) was selected as the experimental area within which ten sub-reaches were established, given serial numbers and allocated to either training or testing datasets (Figure 4-4).

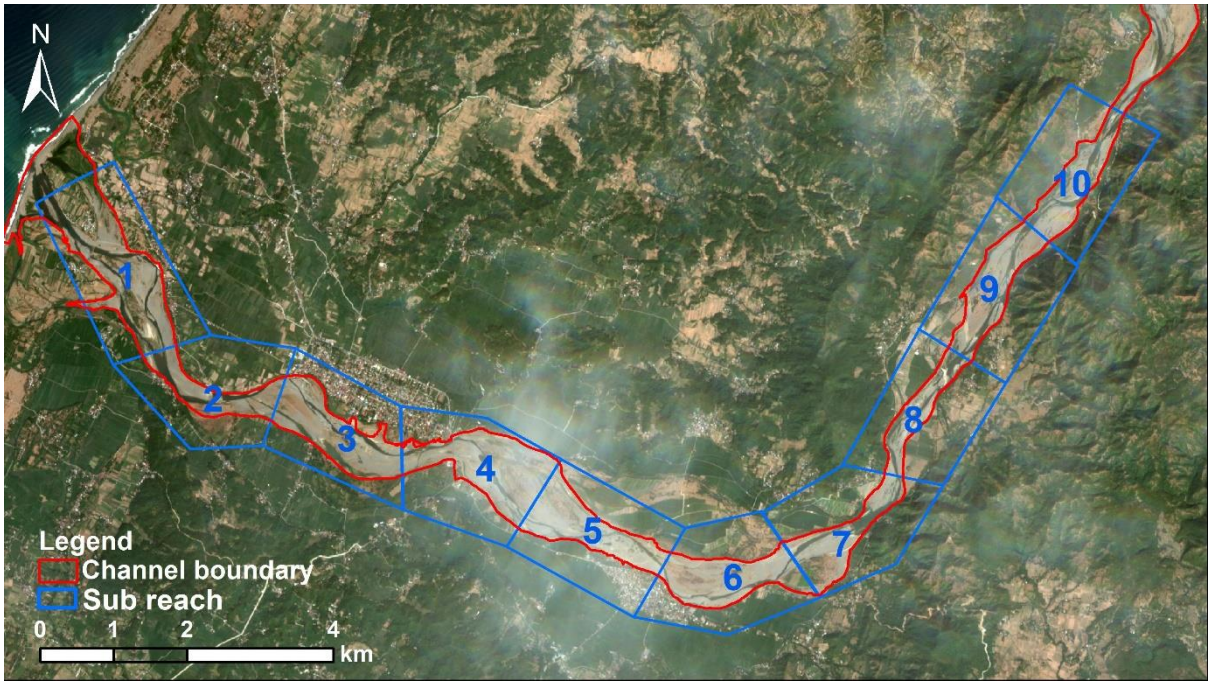

Figure 4-4. Ten sub-reaches of the experimental area with serial number. Background is the true colour Sentinel-2 Level-2A image dated 1 January 2018.

The training dataset (Table A3) was combined by objects from blocks 1,2,4,6,7 and 10 for six dates in 2018 (1 January, 7 March, 1 May, 20 July, 18 September, 7 November). In this case, we added the class 'others', which incorporate unknown objects (occupying 1.1% of whole data). With the SVM algorithm, the training model was established and validated on the objects from blocks 3,5,8 and 9 (Figure 4-4; partly shown in Figure 4-1b) of the same dates. Furthermore, imagery observations indicate that three landform types (water, unvegetated bar and vegetated bar) are always present and change locations within blocks 3 and 5 in different seasons. To assess the general performance of the machine learning model for different years, the training model was tested on the objects from blocks 3 and 5 of Bislak River in 2017 and 2019 (Table A3). We avoided blocks that were obscured by clouds.

Table A3. Numbers of objects used in the multi-date model.

Sub-reaches on dates	Number of objects					
	Dataset	Total	Water	Unvegetated bars	Vegetated bars	Other
6 dates in 2018	Training	3933	871	2112	908	42
16/01/2017	Testing	216	42	136	38	0
16/04/2017	Testing	225	32	146	47	0
16/06/2017	Testing	130	24	86	20	0
03/09/2017	Testing	210	59	74	77	0

28/10/2017	Testing	227	48	116	63	0
07/12/2017	Testing	205	34	113	58	0
01/01/2018	Testing	480	79	266	135	0
07/03/2018	Testing	404	63	258	83	0
01/05/2018	Testing	408	50	241	117	0
20/07/2018	Testing	418	104	192	122	0
18/09/2018	Testing	411	177	161	73	0
07/11/2018	Testing	407	106	215	84	2
10/02/2019	Testing	231	35	165	31	0
11/04/2019	Testing	221	29	146	46	0
30/06/2019	Testing	91	17	42	32	0
29/08/2019	Testing	224	90	92	42	0
13/10/2019	Testing	194	64	100	30	0
07/12/2019	Testing	204	53	104	47	0

4.3.6. Optimal testing dataset

To investigate the performance of different testing datasets, three combinations of segmented objects were explored: (i) river objects from one single date; (ii) river objects from six dates in a year, including heavy cloud cover dates (over 30% heavy clouds covering the studied river); and (iii) river objects from four less cloudy (under 30%) dates in a year. Thus, in this section, the training dataset consisted of 7458 objects from the 10 Bislak sub-reaches of every two months (6 months in total) in 2018, including ‘water’, ‘unvegetated bar’, ‘vegetated bar’ and ‘others’. To identify an optimal testing dataset, three forms of data tests were designed and applied to the machine learning model. Firstly, the training model was tested on channel objects from single dates in 2017 and testing accuracies were calculated. Secondly, the training model was tested on all channel objects of six dates in 2017, including days with heavy cloud cover (≥30%) acquisitions. Lastly, the training model was tested on all channel objects from four dates in 2017, representing the less cloudy (≤30%) acquisitions. Blocks 3 and 5 in Figure 4 (Table A3) were extracted for the accuracy assessment. The classification performance was compared between the three testing scenarios and an optimal testing dataset was selected for further landforms classification analysis. The machine learning model was then applied to the Laoag and Abra Rivers to investigate the transferability of the model. The testing sub-reaches of these rivers are shown in Figure 4-1c and 4-1d.

4.4. Results and Discussion

4.4.1. Comparison of downscaling approaches

Figure 4-5 shows a sample of the segmentation results. The 20 m resolution bands of Sentinel-2 were downscaled to 10 m resolution using the Sen2Res based super-resolution approach, ATPRK, and nearest neighbour resampling. The LSMS segmentation algorithm was subsequently employed to segment the composite bands processed by each approach into objects. As described in section 3.2.5, with multiple experiments for selecting parameters, the range radius and minimum segment size for the super-resolution approach shows a large difference compared to both resampling and ATPRK methods. Specifically, the super-resolution approach requests only 1 minimum segment size for delineating the channel landforms well, while the resampling and ATPRK methods use 42 minimum segment sizes to differentiate the objects within the channel. The minimum segment size refers to the criterion that is set for merging adjacent small segments with the closest spectral signature after segmentation. Thus, different choices of parameters lead to different sizes of segmented objects. Moreover, the different segmentation procedures result in datasets of varying sizes at same spatial extent, with super-resolution capturing 154841 objects after segmentation, resampling retrieving 1077 objects, and ATPRK retrieving 1068 objects.

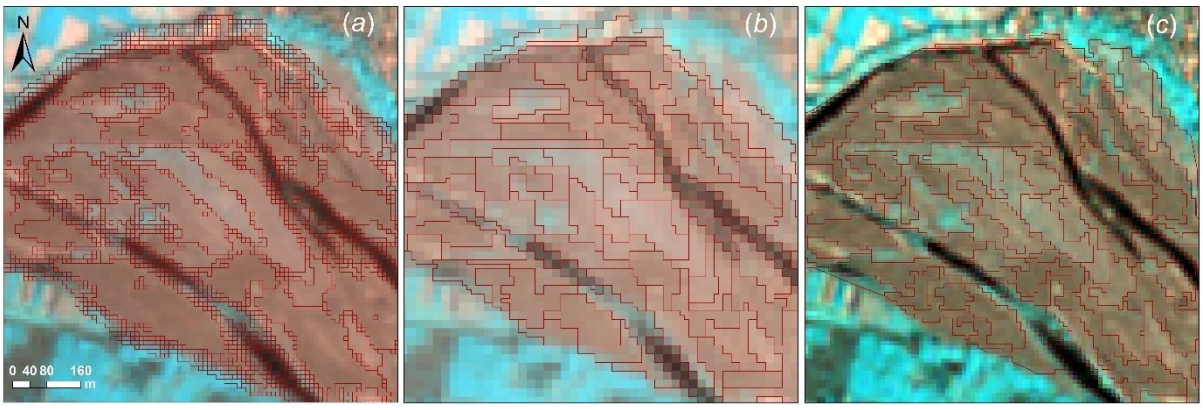

Figure 4-5. Sample of segmentation results for (a) super-resolution, (b) resampling and (c) ATPRK. Segmented Objects are categorised by red boundaries. Background images are the composite of band 5 (central wavelength: 704.1 nm), band 6 (central wavelength: 740.5 nm) and band 7 (central wavelength: 782.8 nm) of downscaled Sentinel-2 Level-2A images dated 1 January 2018.

The subsequent classification performances for the three approaches designed in section 4.3.4 are displayed in Table 4-3. The ATPRK classification performed best among the three methods. However, in this case, the methods were compared at different object scales (minimum segment sizes are varying between three approaches, see Figure 4-5). To fit generic ground truths to the segmented objects well, the minimum segment size of image objects with ATPRK and resampling approaches was chosen as much larger than that with super-resolution approach. This means that segments from ATPRK and resampling images preserved more spatial geometric information since it is easier to find similar adjacent segments to represent spatial features. This might be explained by prior geometric interruptions of the super-resolution method, which was introduced in section 4-1. Classification of water areas based on resampling implied that the misclassified water bodies always occur in narrow channels, whilst ATPRK performed well in these narrow channels. This result is expected, given that the difference between the expected spatial detail interpretation from ATPRK and the resampling methods, explained in section 4-1. This initial experiment provided a first overall comparison of the three downscaling approaches for classification of the Bislak River's landforms. The results indicate that the image downscaling approaches can be essential to process object-based classification using Sentinel-2 imagery. The results show that the ATPRK method can outperform the other approaches in rivers of the type found in this region. While resampling performs slightly better than ATPRK for the unvegetated bar and vegetated bar classification accuracies, when it comes to spatial details, the water accuracy is only approximately half that of ATPRK. Thus, the ATPRK approach was used to address research questions 2 to 4.

Table 4-3. Accuracy assessments for resampling, ATPRK and super-resolution approaches. (All values range between 0 – 1, whereby 0 indicates the lowest accuracy and 1 indicates the highest accuracy.)

	Accuracy	Precision	Recall	F1-score	WA	BA	VA
Resampling	0.785	0.832	0.785	0.771	0.435	0.971	0.693
ATPRK	0.861	0.871	0.861	0.859	0.871	0.950	0.690
Super-resolution	0.681	0.707	0.681	0.676	0.484	0.842	0.596

4.4.2. Training model investigation

To determine the robustness of the training model based on 1 January 2018 data, the objects of the whole reach were used as a training dataset (Figure 4-6a red extent) and the model tested

on a different reach (Figure 4-6a white extent), located farther upstream in the catchment with fewer unknown objects (e.g., clouds and urban units). The cross-validation accuracy of the model was 0.91 and the test accuracy for this upstream reach was 0.929. Cross-validation uses different portions of the training data to train the model over k-folds or iterations and the validation assesses the model performance (validation accuracy). The final (optimised) model is then applied to the test set to provide an unbiased estimate of the final model (testing accuracy). The cross-validation accuracy and test accuracy were both very high which indicates the model fitted well to the upstream reach data. The accuracy of water classification was 0.891, that of unvegetated bars was 0.941 and vegetated bars was 0.940. The lower accuracy of water might be caused by narrower channels in the upstream, making water objects more difficult to recognise in some places and leading to misclassification. Generally, the whole test accuracy is close to the validation accuracy, and the classifier performed well for classifying the landforms in the upstream reach on 1 January 2018.

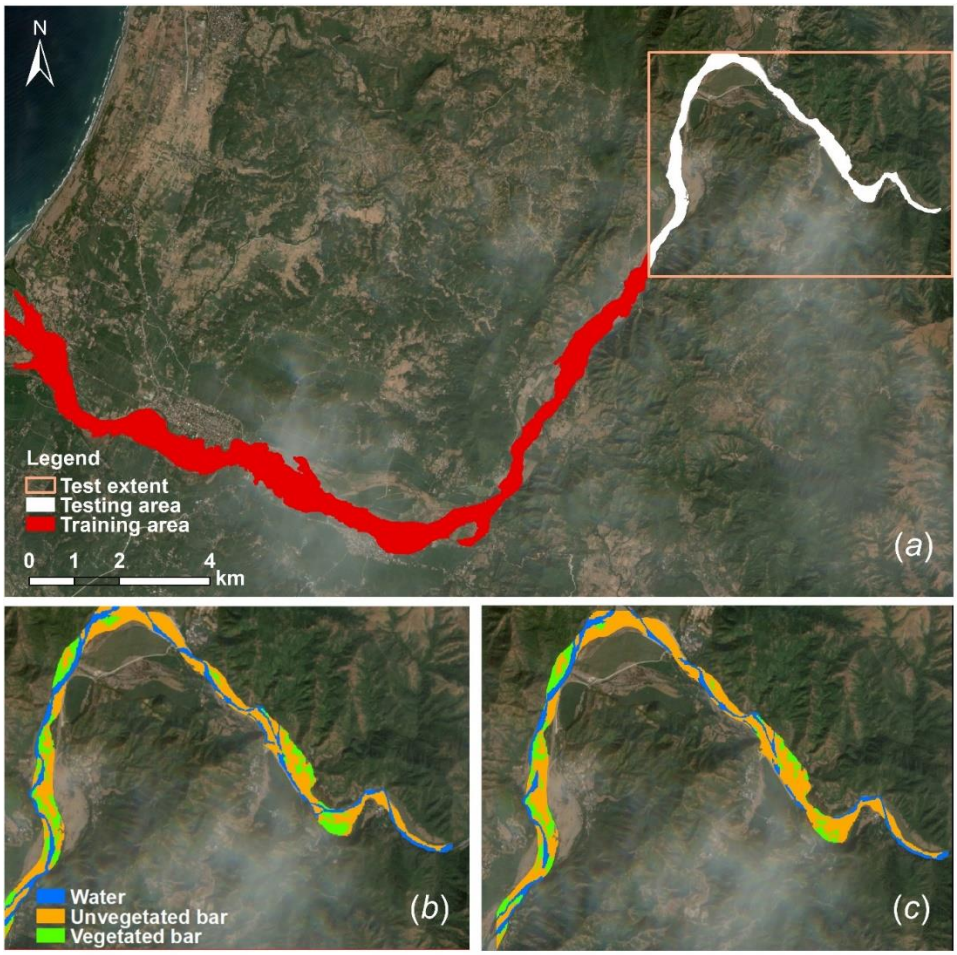

Figure 4-6. Classification on an upstream reach of Bislak River; (a) is the true colour Sentinel-2 image with training and testing area, (b) is the manually digitised ground truth representing

white extent in (a), and (c) is the output classification. Background image is the true colour Sentinel-2 Level-2A image dated 1 January 2018.

To investigate the training model (red extent in Figure 4-6a) performance across a broader temporal scale, five acquisitions over the Bislak River between 7 March 2018 and 7 November 2018 were selected for testing. Table 4-4 displays the accuracies across all dates. It can be seen from Table 4-4 that the 1 January 2018 training model does not perform well for all dates in 2018. The training model developed in the dry season fitted March and November images very well, both of which are in the dry season. The testing result was good (overall accuracy is 0.85) on 1 May 2018, which is a transition period between the dry and wet seasons. The 18 September had the poorest performance, which is at the end of the wet season. At this time in the year, it is likely that vegetation growth and suspended sediment load contribute to changes in the spectral properties of vegetated bars and water (Welber, Bertoldi, and Tubino 2012). In addition to water, unvegetated bars and vegetated bars, we incorporated a very small proportion (2%) of unknown units, which were named 'others', into the training model in this experiment. We tested performance using objects from 10 July 2018, including 308 objects defined as 'others'. Most objects in this category are urban structures aligned with the active channel of the river, and some are clouds or cloud shadows. The results showed that only 7 objects were misclassified (accuracy is 0.98), which implies the 'unknown units' are not the cause of low accuracies on 10 July 2018. Rather, these low accuracies are probably caused by the lack of a seasonal consideration in the training model. Thus, establishing an optimal training model for the research area should incorporate acquisitions across different periods during both the dry and wet seasons.

Table 4-4. Accuracies on different dates in 2018 using training model from single date. (All values range between 0 – 1, whereby 0 indicates the lowest accuracy and 1 indicates the highest accuracy.)

Date in 2018	OA	WA	BA	VA
07 March	0.90	0.96	0.91	0.87
01 May	0.85	0.41	0.94	0.93
10 July	0.61	0.40	0.86	0.48
18 September	0.57	0.23	0.48	1
07 November	0.92	0.94	0.89	0.99

Consequently, the new modified training model established on sub-reaches across different seasons in 2018 was designed and tested on objects of different dates from 2017 to 2019 (Table A3). Figure 4-7 combines the testing accuracies based on dates across the three years. The overall accuracy for the model is mostly between 0.80 and 0.90. The best classified

unit is unvegetated bar (most accuracies ≥ 0.90) and the poorest classified unit is vegetated bar (accuracies vary between 0.54 and 0.91). Vegetation types/ species/reflectance could probably cause the poor vegetation classification, which could be examined by higher resolution imagery or field evidence. Water can generally be well classified (accuracies mostly above 0.80) except for a few dates. These observations demonstrated that using data from multiple dates in constructing the training model can lead to performance that is superior to a single-date training model.

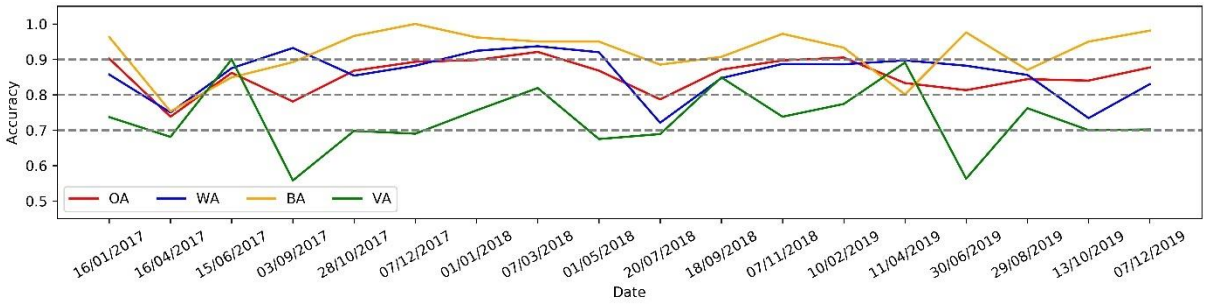

Figure 4-7. Time series for the testing accuracy of the multi-temporal training model across three years (2017-2019).

4.4.3. Testing dataset selection

We investigated testing datasets for establishing an optimum machine learning model for river landform classification in the region. From the results presented in section 4.4.2, a multi-date training model is more favourable for local channel landform classification. Thus, we used a multi-date training model (section 4.3.5) to run testing to define an optimal testing dataset. The method has been described in section 4.3.6 and the test experiment accuracies are displayed in Figure 4-8. In general, the training model on 10 blocks in Figure 4-4 and tested on objects of four cloud free dates (Train_10_test_4) contributes the best performance for the river landforms classification. This model performed best for water and vegetated bars except in April 2017, when a single date testing dataset provided higher accuracies. However, for unvegetated bar units, the single date testing dataset obtained much lower accuracies compared to the multi-date testing dataset (including both heavy clouds and less clouds datasets) in April and September 2017. However, in the case of unvegetated bar units, the heavy cloud-based testing dataset performs slightly better than the dataset with less cloud. The testing results for unvegetated bars may be explained by the low water volume and high sediment exposure in the dry season. Additionally, most mis-classified vegetation objects were classified as

unvegetated bars (see Table 4-4), which is likely related to there being sparse vegetation in these objects. From results in this section, we suggest that considering the format of the testing dataset could help when deriving different objective classification results. To pursue an overall high accuracy classification when unvegetated bars are the dominant river landform, we recommend using a multi-date based, low cloud cover dataset to define the classification. Moreover, to study landform change in a season which is very short or that shows difference from the whole year, such as April in this case, a testing dataset from a single date might be more effective.

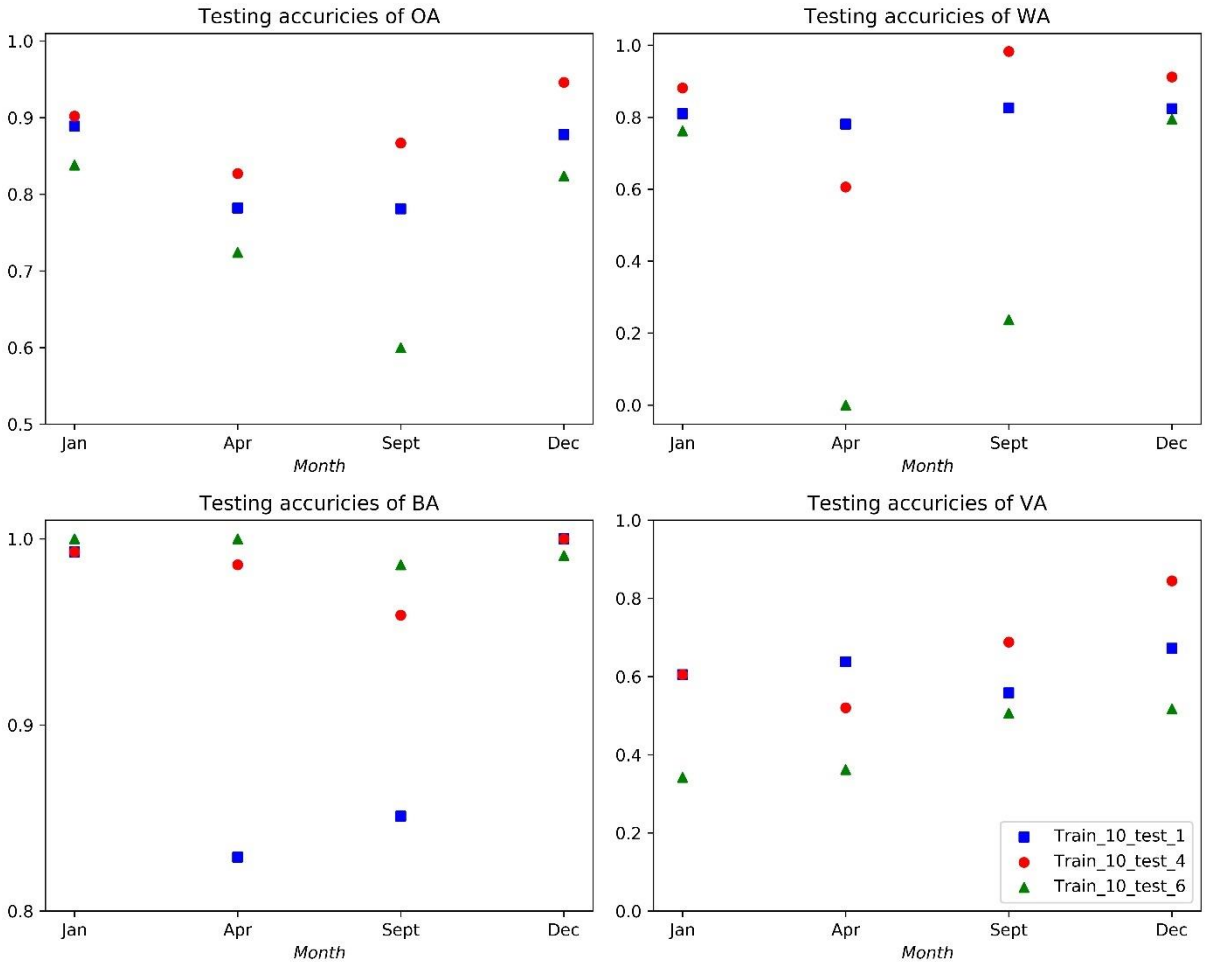

Figure 4-8. Comparisons of three testing datasets evaluated by overall accuracy (OA), water accuracy (WA), unvegetated bars accuracy (BA) and vegetated bars accuracy (VA).

4.4.4. Model performance in nearby rivers

To explore the transferability of the developed machine learning model, further testing was performed in two nearby rivers: the Laoag and Abra Rivers. For the Laoag River, object

samples from six cloud free acquisitions in 2018 (Figure 4-1c) were collected for model testing. The total number of testing samples in the Laoag River is 2037 (training: testing ≈ 10:3). For the Abra River, object samples from six cloud free acquisitions in 2019 (Figure 4-1d) has 2424 testing samples in total (training: testing ≈ 10:4). Tables 4-5 and 4-6 show the test accuracies for the Laoag River in 2018 and Abra River in 2019, respectively. Here, we used a multi-date based testing dataset to run the classification.

Table 4-5. Test accuracies of Laoag River in 2018. (All values range between 0 – 1, whereby 0 indicates the lowest accuracy and 1 indicates the highest accuracy.)

Date	OA	WA	BA	VA
01/01/2018	0.893	0.933	0.897	0.806
07/03/2018	0.840	0.895	0.812	1.000
01/05/2018	0.862	0.778	0.905	0.750
10/07/2018	0.834	0.946	0.862	0.510
18/09/2018	0.883	0.951	0.834	0.679
07/11/2018	0.878	0.976	0.835	0.833
2018 (whole year)	0.866	0.937	0.860	0.735

Table 4-6. Test accuracies of Abra River in 2019. (All values range between 0 – 1, whereby 0 indicates the lowest accuracy and 1 indicates the highest accuracy.)

Date	OA	WA	BA	VA
11/01/2019	0.852	0.879	0.955	0.573
27/03/2019	0.892	0.875	0.955	0.770
16/05/2019	0.878	0.831	0.978	0.674
25/07/2019	0.859	0.861	0.965	0.765
13/09/2019	0.892	0.979	0.915	0.815
22/11/2019	0.864	0.946	0.978	0.662
2019 (whole year)	0.872	0.901	0.959	0.721

These results indicate that, for the whole year, the overall accuracies, water accuracies and unvegetated bar accuracies within nearby rivers are equal or above 0.86, while vegetated bar accuracies are equal or below 0.735. Specially, the vegetation accuracies of 10 July 2018 on Laoag River, and 11 January 2019 on Abra River are lower than 0.600. This lower accuracy is related to the low proportion of vegetated objects within the testing sub-reaches, which enhance the misclassification. Finer resolution remote sensing data might help to improve the vegetation accuracy for low or sparsely vegetated areas (Huylenbroeck et al. 2020). Most mis-classified vegetation objects were classified as unvegetated bars, and notably, the unvegetated bar classification performance is good (>0.812) across all dates of both rivers. The machine

learning model can be regarded as reasonably robust across the different rivers and is subsequently applied to further Sentinel-2 images to generate a dataset of river patterns within the region (Figure 4-9).

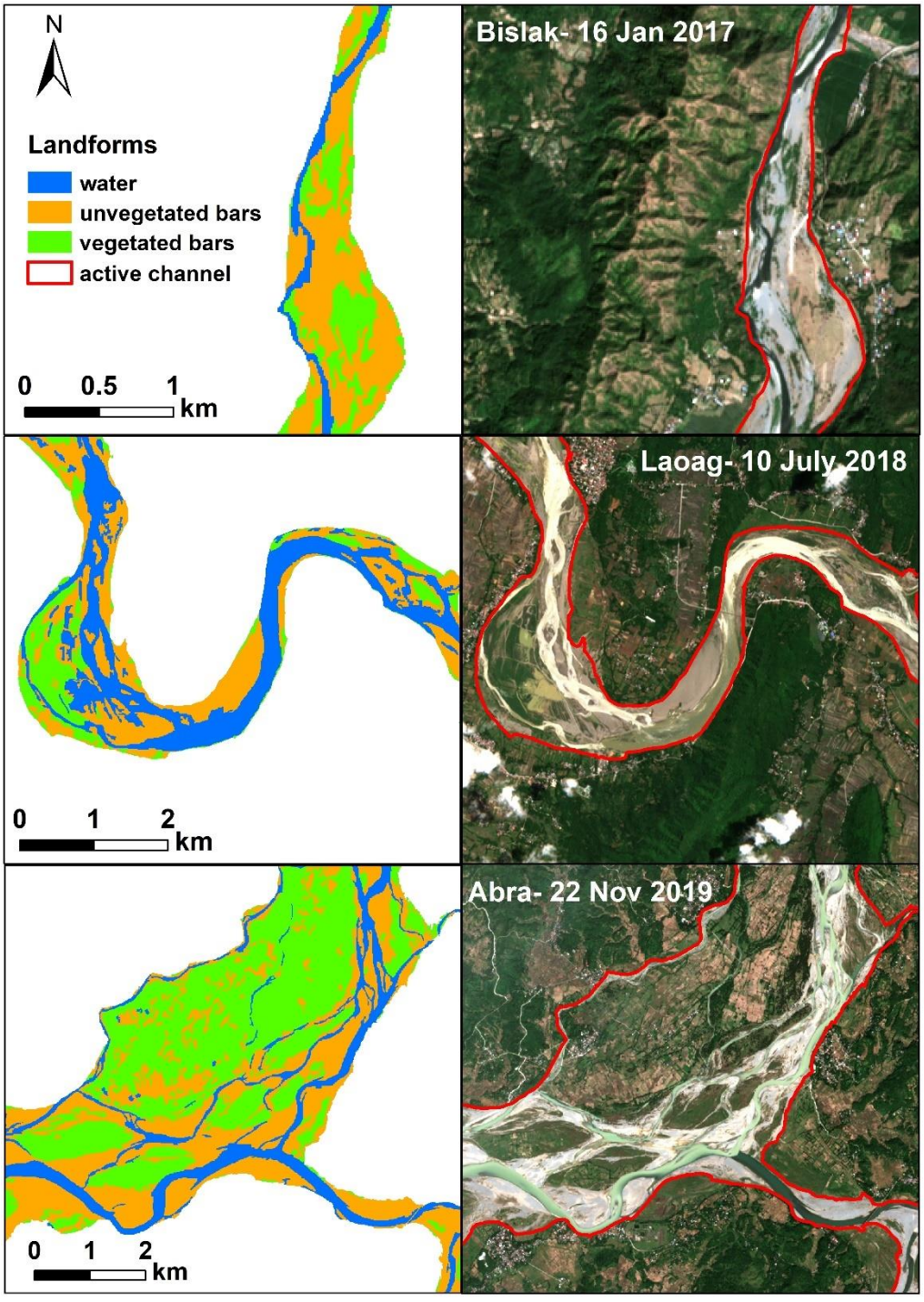

Figure 4-9. Subset classification results of Bislak, Laoag and Abra Rivers across different times of different years. Complete classification coverages can be accessed from the link in the Data Availability section.

4.5. Conclusions

This investigation shows the ATPRK approach to downscaling outperforms the alternatives of nearest neighbour resampling and super-resolution for river landforms classification. A new image processing workflow for the purpose of river landform classification was developed and tested across tropical rivers in the Philippines. We also demonstrated that using a multi-temporal dataset across seasons to build a training model is superior to single-date and single-season models. We recommend using testing data at similar temporal ranges to train data and achieve higher classification accuracy. Whilst the scale between ground truth mapping and image segmented objects could impact classification accuracy, our set of experiments (during image pre-processing, downscaling, segmentation, classification) demonstrate optimal data/image processing and river landforms classification modes to improve the classification performance. The results show that the proposed workflow can be used for river landforms classification across three neighbouring catchments, and it is possible that the training model could successfully be applied to other tropical rivers in the Philippines and beyond with similar hydro-geomorphological characteristics.

Chapter 5 - Seasonal and annual tropical river pattern change detection using machine learning

The following chapter is a reformatted version of a manuscript in review for the Earth Surface Processes and Landforms, by Qing LI, Richard D. WILLIAMS, Trevor B. HOEY, Brian BARRETT, Richard J. BOOTHROYD, available at https://doi.org/10.31223/X5D66G.

Abstract

Rivers in the tropics are more likely to exhibit seasonal changes in pattern than those in temperate regions because of strongly seasonal rainfall. However, such changes in seasonal tropical river patterns have not been widely investigated. Machine learning methods are used in this study with Sentinel-2 multispectral remote sensing images to classify active channel landforms (water; unvegetated bars; vegetated bars) of the Bislak, Laoag and Abra Rivers, north-west Luzon, the Philippines. River patterns are classified five or six times per year from 2016 to 2020. Spatial and temporal trends were investigated, in the context of the rivers' active width, valley confinement, tectonic setting and precipitation. Results show a variety of relationships between each landform unit and active width, but a strong correlation was shown between active width and vegetation area in dry and wet seasons. Rivers were divided into sub-reaches based on observed patterns of water frequency and confinement; Ensemble Empirical Mode Decomposition (EEMD) was then used to decompose the landform time series and precipitation record. EEMD indicates that water and vegetated bars commonly show synchronised fluctuations with precipitation, while unvegetated bars have an anti-phase oscillation with precipitation. It also suggests that deviations from periodic consistency in river pattern may reflect the influence of extreme events and/or human disturbance. At the river system scale, faults perpendicular to the channel centreline were associated with an increase in vegetated bar stability. Overall, the interplay of faults, elevation, confinement and tributary locations impact landform stability. This investigation demonstrates that in tropical regions river pattern should be considered as a dynamic entity as characterising pattern from a single time period may misrepresent a river's character. EEMD is also demonstrated to be an appropriate statistical technique in geomorphology to decompose datasets that are generated from contemporary applications of machine learning to remotely sensed imagery.

5.1. Introduction

River channel pattern is a function of a variety of factors including longitudinal gradient, stream power, transport capacity, and bank strength (Buffington and Montgomery 2022; Church 2006; Kondolf et al. 2016). Previous studies on river pattern classification (Demarchi, Bizzi, and Piegay 2017; Ham and Church 2012; Horacio, Ollero and Perez-Alberti 2017) have been typically approached from a temporally static perspective, focusing on categorising planform at low flow. Whilst this approach is adequate for many meandering rivers in

temperate regions, in other climate settings, the aerial proportions of water, exposed sediment and vegetation, which comprise the planform of a river, may substantially vary through a year (Ashworth and Lewin 2014). Braided rivers have more rapid and complex processes of channel formation (Ashmore 2013). Hicks et al. (2020) illustrated the chanllenges and pressures of braiding rivers in the New Zealand, which are going through extreme natural events and anthropogenic stresses such as braidplain conversion to farmland and invasive vegetation. This is particularly pertinent for multi-channel rivers in tropical and sub-tropical climates, where rivers are strongly influenced by rapid vegetation growth rates, and significant seasonal variation in flows due to storms and typhoons (Syvitski et al. 2014). In addition, channel pattern may vary in response to variations in sediment supply from, for example, landslides (Abanco et al. 2021) and volcanic events (Gran and Montgomery 2005) or autogenic adjustments (Paola 2017). In the last decade, archives of satellite imagery of a sufficiently high spatial resolution to map channel pattern have become available at a temporal frequency that enables inter- and intra-annual mapping (Boothroyd et al. 2021). This creates opportunities to investigate the spatial and temporal patterns of tropical rivers, which are characterised by a variety of channel forms (Latrubesse et al., 2005). To this end, here, we focus on assessing the multi-temporal dynamics of channel pattern for a set of three rivers in the Philippines. In doing so, we expand the representation of these relatively under-investigated tropical river systems (Dingle et al. 2019) in our global scale understanding of river pattern dynamics.

A variety of multi-temporal investigations have demonstrated how the fundamental fluvial landforms that define river pattern can be mapped from historical airborne and satellite imagery archives, typically by digitising and then quantifying the extent of water, unvegetated bars and vegetated bars (Corenblit et al. 2020; Dingle et al. 2019; Hajdukiewicz and Wyzga 2019; Hooke 2022; Mandarino, Maerker, and Firpo 2019; Reid and Brierley 2015; Saleem et al. 2020). For example, Serlet et al. (2018) manually digitised water, unvegetated bars and vegetated bars in a channelised regulated river, from a set of aerial images that covered 80 years, to investigate the co-evolution of alternate bars and vegetation along a 33 km long reach of the temperate, anthropogenically impacted Isère River, France. Whilst manual digitisation of maps and aerial imagery has been widely used to investigate the temporal and spatial dynamics of fluvial systems, including river pattern change, this approach is time consuming and potentially less objective than automated approaches. Machine learning (Jordan and Mitchell 2015) has been widely applied to automate landcover classification using remotely sensed satellite data, using both conventional (e.g., pixel- and object-based machine learning

strategies) and deep learning (e.g., convolutional neural network) approaches (Phiri et al. 2020; Prakash, Manconi, and Loew 2020). With respect to conventional approaches, a variety of algorithms are commonly used, including Logistic Regression (LR), Support Vector Machines (SVM), Random Forests (RF) and Artificial Neural Networks (ANN) (Holden, Saito, and Komura 2016; Ohsaki et al. 2017; Schneider and Guo 2018). In fluvial geomorphology, SVM has been demonstrated to perform well to classify fluvial landforms (De Luca et al., 2019; Demarchi, Bizzi, and Piegay 2016) but there are still few large scale or multi-temporal examples to achieve a widely operative, objective framework for consistent river system characterisation (Gurnell et al. 2016).

To reap the benefits of analysing multi-temporal channel pattern data, an integration of spatial and temporal analysis is needed. However, existing practices mostly lack temporal statistical analysis of spatial series. Saleem et al.'s (2020) quantification of planimetric channel changes along a 112 km reach of the tropical River Padma, Bangladesh, for ten timesteps during a 100-year period is a typical example; whilst changes in landform patterns are quantified, they are not analysed statistically. Whilst overlaying maps of different time periods is an intuitive and straightforward approach to present spatial-temporal changes, this approach is not suitable for big spatial-temporal data analysis. Rather, a statistical temporal analysis is needed to enable quantitative analysis of river system dynamics. One method with potential to achieve this is Ensemble Empirical Mode Decomposition (EEMD), which has been developed to undertake time series analysis in a variety of scientific fields (Huang et al. 1998; Ridder 2011; Wang and Zhang 2020), without requiring that the data are stationary. This method decomposes time series into several constituent components, each of which has a corresponding timescale, and a trend. Xu et al. (2019) employed EEMD to decompose vegetation indices from remote sensing imagery and temperature series, then investigated relationships between vegetation change and climate change. This demonstrates how EEMD can be applied to investigate earth observation data, which inspired the use of EEMD to decomposing landform time series in our investigation.

In this paper, we apply a machine learning workflow (Li et al. 2022) to classify multi-temporal fluvial landforms rapidly and objectively from the mountain front to the coast for the tropical Bislak, Laoag and Abra Rivers in north-west Luzon, the Philippines. The resulting dataset is then used to investigate four research questions: (1) What are the impacts of channel setting (i.e., active width, catchment size, confinement, tributaries, elevation) on landform (water,

unvegetated bars, vegetated bars) patterns? (2) How do landform areas and proportions vary spatially along each river? (3) What are the seasonal patterns in these landform distributions, how consistent are they across the three rivers, and what drives these patterns? (4) What multi-year temporal trends are there in landform area across the sub-reaches of each river, and how do these relate to precipitation patterns?

5.2. Study area

Our investigation focuses upon three gravel-bed rivers in north-west Luzon, the Philippines: the Bislak, Laoag and Abra Rivers (Figure 5-1). For each river, the riverscape that was analysed included the river network in each catchment from the coast to a point upstream where channels were greater than 95% confined on both valley sides. This yielded study lengths of 39, 47 and 82 km, respectively for the Bislak, Laoag and Abra Rivers. Compared to the other two rivers, the Bislak does not have a significant tributary input within the study area (Tolentino et al. 2022). The Laoag has three similar sized tributaries and the Abra has three tributaries with different catchment areas.

The island of Luzon is dominated by sub-tropical East Asian monsoon climate (Liu et al. 2009). Tropical cyclones (Cinco et al. 2016) are frequent and cause landslides, flooding and channel change in the region (Abanco et al. 2021; Abon, David, and Pellejera 2011; Kim 2019). Notably, more than 50% of tropical cyclone induced rainfall in the Philippines occurs in north-west Luzon (Bagtasa 2017). In this region, catchments are characterised by strong seasonality of rainfall, with a wet season from May to October and a dry season from November to April. Mean annual rainfall in the Bislak catchment is 2019 mm, with a maximum monthly mean of 546 mm in August (Tolentino et al. 2022). In the region where Bislak catchment in, averaged monthly rainfall increased from 1969 to 2018 (Tolentino et al. 2022). Climate change impacts in west and east Luzon are different; from analysis of 32 years of monthly rainfall distributions, rainfalls measured at all western stations of the Philippines (including stations in the west Luzon) increased (or decreased) synchronously, whereas rainfall fluctuations at eastern stations of the country propagated southward and can be influenced by the winter monsoon, which has long-term variability in the Philippines (Kubota et al. 2017). Additionally, an analysis of records from 1901 to 2013 indicated rainfall in north-west Philippines increased around May to June and decreased around October to November (Kubota et al. 2017).

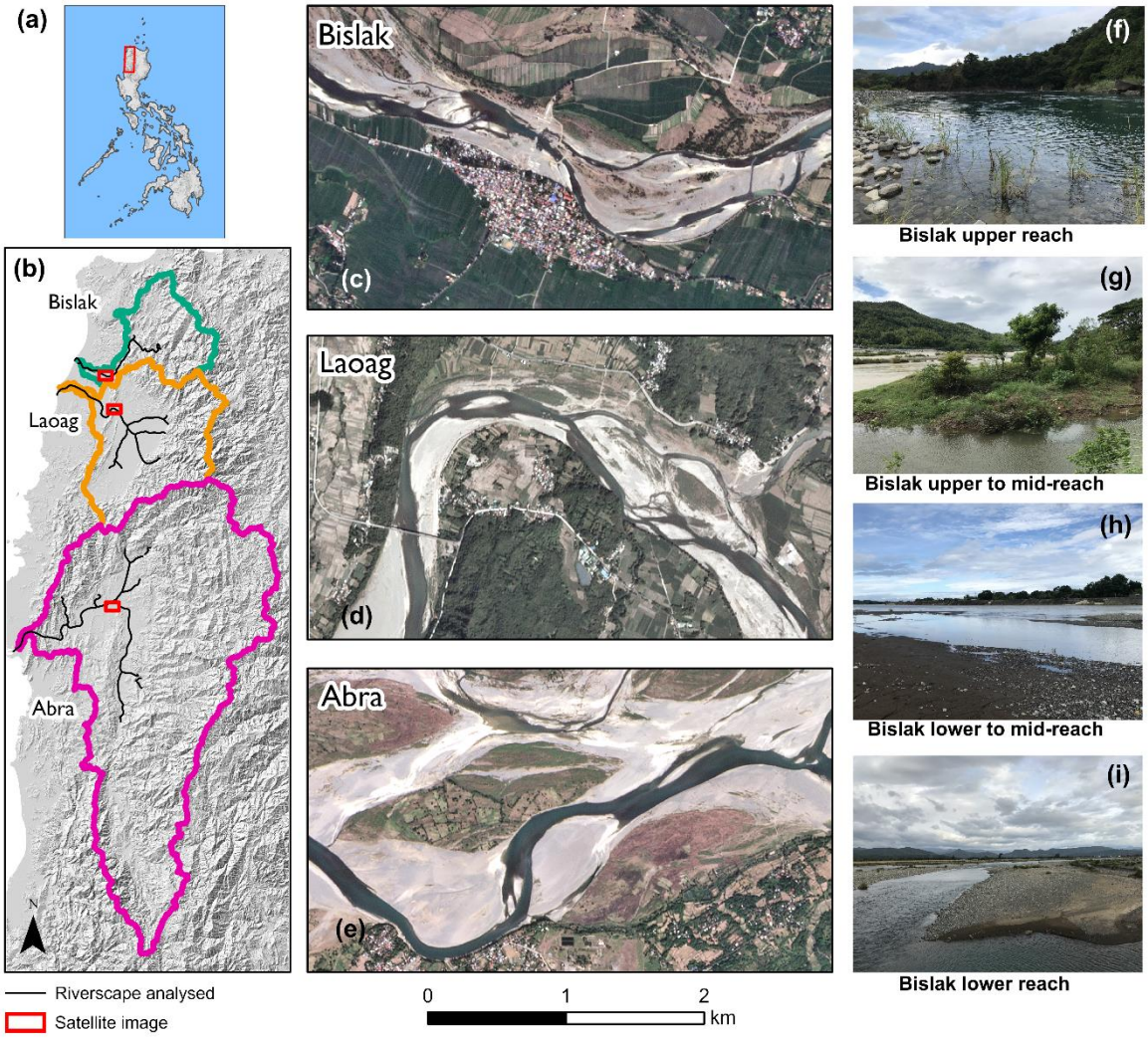

Figure 5-1. (a) The Philippines; red box is the study area in north-west Luzon shown in (b); (b) The Bislak, Laoag and Abra catchments, with extents of riverscapes that were analysed shown as black lines. (c - e) PlanetScope satellite imagery (dated December 2019) showing representative reaches of each river (image centres: Bislak 18.23 N,120.65 E; Laoag 18.13 N, 120.67 E; Abra 17.63 N, 120.68 E), with extents indicated on (b). (f - i) Oblique photographs of riverscapes along the Bislak River.

5.3. Data and methods

5.3.1. Sentinel-2 acquisitions

The Sentinel-2 mission comprises a constellation of two identical satellites launched on 23 June 2015 and 7 March 2017. The multispectral instruments (MSI) onboard the pair of satellites enable monitoring of the Earth's land cover typically using 10 m resolution imagery across four spectral bands and/or 20 m imagery across six spectral bands (Korhonen et al. 2017; Phiri et al. 2020). Sentinel-2's capability of revisiting all continental land surfaces between 56°S and

82.8°N every five days has encouraged many investigations on land cover dynamics of the Earth's surface (Phiri et al. 2020; Sonobe et al. 2018; X. C. et al. 2017), including river change (Rabanaque et al. 2022; Spada et al. 2018). However, in tropical areas the presence of clouds can substantially reduce the frequency of Sentinel-2 imagery that is suitable for land cover mapping; for the three rivers in this study, imagery acquisitions with good visibility were sometimes spaced two to three months apart. Nevertheless, to investigate the seasonal changes in river patterns, we were able to obtain five or six Sentinel-2 Level-1C (Top-Of-Atmosphere reflectance) acquisitions from the USGS Earth Explorer portal (http://earthexplorer.usgs.gov) for every year between 2016 and 2020 (Figure 5-2). These acquisitions had less than 5% cloud cover across the channel area and were typically well temporally distributed throughout each year.

Figure 5-2. The timing of Sentinel-2 imagery acquisitions used in seasonal change investigations, for the Bislak, Laoag and Abra Rivers.

5.3.2. Geographic object-based image analysis

Ten bands at resolutions of 10 m and 20 m from Sentinel-2 MSI acquisitions and five environmental indices calculated from the Sentinel-2 data were selected to prepare learning features for image classification. Atmospheric correction was then applied to Sentinel-2 Level-1C products (Top-Of-Atmosphere reflectance) to generate Level-2A products (Bottom-of-Atmospheric reflectance) using the sen2cor processor developed by the European Space Agency (Main-Knorn et al. 2017). Using the Level-2A imagery, the ATPRK image fusion

algorithm (Wang et al. 2016) was applied to downscale 20 m imagery to 10 m resolution (Li et al. 2022). Subsequently, the five water and vegetation environmental indices were calculated from 10 m bands (including original 10 m bands and downscaled 20 m bands). The five environmental indices were: normalised difference vegetation index (NDVI; Carlson and Ripley 1997); normalised difference moisture index (NDMI; Wilson and Sader 2022); normalised difference water index (NDWI; Gao 1996); modified enhanced vegetation index 1 (MEVI1; Huete et al. 2002); modified enhanced vegetation index 2 (MEVI2; Jiang et al 2008). As NDMI, MEVI1 and MEVI2 were originally developed for Landsat and MODIS satellite imagery, for Sentinel-2 Level-2A downscaled imagery, indices tended to have values outside of a -1 to 1 range. To maintain bounded conditions (-1 to 1), we added a constant 10a to the denominator of each of these indices (A. R. Huete 1988; Ji et al. 2011). For this case, we tested the constants by giving integers to a. We found a = 4 maintained the range from -1 to 1 for NDMI and MEVI2, while a = 5 maintained the range from -1 to 1 for MEVI1 (Li et al. 2022). Consequently, a set of fifteen 10 m resolution layers were produced for each acquisition. These layers included the Sentinel-2 processed spectral bands, and the water and vegetation environmental indices. The set of layers were segmented into geographical objects (i.e., patches of pixels) using the Large Scale Mean Shift (LSMS) algorithm (Comaniciu and Meer 2002; Ming et al. 2011), employing open-access Orfeo Toolbox 6.6.1 software.

To bound the segmented geographical objects within the river channel, we generated an active channel extent for each river. We first detected the annual averaged area containing water and unvegetated bars homogeneously within the active channel (Boothroyd et al. 2021). We automatically closed gaps in the annual active channel area caused by vegetated islands using standard image processing techniques. For vegetated bars connected to the active channel, we manually edited the active channel area to include the vegetated bars. In the active channel, the segmented objects were manually allocated into three landform units (water, unvegetated bars and vegetated bars) and no data units (objects obscured by clouds or scattered urban units) to generate the ground truth dataset. Subsequently, these object samples were ready for SVM machine learning. For the machine learning model, the training dataset was built with imagery data of the Bislak River from six dates in 2018; as reported in Li et al. (2022), including imagery from all seasons resulting in a higher model performance than only using data from a single season. The classification model was tested and assessed using overall accuracy (OA), water accuracy (WA), unvegetated bar accuracy (BA) and vegetated bar accuracy (VA).

Accuracy was assessed using images of the: Bislak River in 2017 and 2019; Laoag River in 2018; and Abra River in 2019.

5.3.3. Catchment-averaged accumulated rainfall totals

There is a paucity of ground-based rainfall measurements in north-west Luzon, especially in catchment headwaters. To quantify and compare catchment-averaged accumulated rainfall totals for the periods between Sentinel-2 image acquisitions, we therefore used satellite-derived precipitation data from the Integrated Multi-satellite Retrievals for Global Precipitation Measurement (GPM IMERG) mission. The satellite-derived precipitation estimates have a spatial resolution of 0.1° and a temporal resolution of 30 minutes (Huffman et al. 2019). Across the Philippines, satellite-derived estimates from GPM IMERG show good agreement with ground-based rainfall measurements from synoptic stations and automatic rain gauges but a paucity of ground-based rainfall measurements are reported in the Northern Cordillera mountains (Veloria et al. 2021). We ingested shapefiles for the Abra, Bislak and Laoag catchments into Google Earth Engine and clipped the global GPM IMERG product to each catchment's extent. Due to variation in catchment size and shape, the number of GPM IMERG cell centres varied per catchment (Abra = 66; Bislak = 12; Laoag = 21). We calculated catchment-averaged accumulated rainfall totals (mm) per 10 days for the period between 1 January 2016 and 10 July 2021.

5.3.4. Ensemble Empirical Mode Decomposition

Time series decomposition was applied to analyse temporal trends in the remote sensing results. Numerous signal decomposition methods have been applied to geomorphic data, many of which require data that are stationary (mean and variance constant over time). Our time series are short and are expected to contain seasonal cycles and potentially longer-term trends, all of which preclude a stationarity assumption. Processing methods for non-stationary data such as spectrograms, wavelets, and the empirical orthogonal function expansion (EOF), each have shortcomings when applied to data from physical measurements (Huang et al. 1998). An alternative approach, Empirical Mode Decomposition (EMD) has therefore been proposed to process non-stationary and non-linear series into components at different frequencies (Huang et al. 1998). Using this method, the decomposed component (signal) is referred as the Instinct Mode Function (IMF). Here, we use a derivative of EMD, Ensemble Empirical Mode

Decomposition (EEMD), which solves the mode mixing problem encountered in EMD by adding white noise to the signal (Mohguen and Bekka 2015; Torres et al. 2011). Specifically, EEMD provides a way to decompose our river landform time series which were sampled at unequal time steps due to the availability of cloud-free satellite images.

EEMD was implemented using the PyEMD library in Python v3.6 (Laszuk, 2017). Since EEMD has not been widely used in geomorphology, we illustrate the technique for the Abra River precipitation time series (Figure 5-3). The same method was applied to precipitation data for the Bislak and Laoag Rivers and to the three river landform data sets. In this analysis, noise width was set to 0.2 and 100 trials were performed (Huang 2004; Ridder 2011). The precipitation series was decomposed into five IMFs and one residual series (Figure 5-3a), where each IMF corresponds to an instantaneous frequency, which is usually interpreted to have physical meaning at a characteristic time scale. The residual can be interpreted as the local mean trend of the original data (Huang et al. 1998). Figure 5-3a shows that the mean precipitation for the Abra River catchment has a decreasing trend over the past 5.5 years.

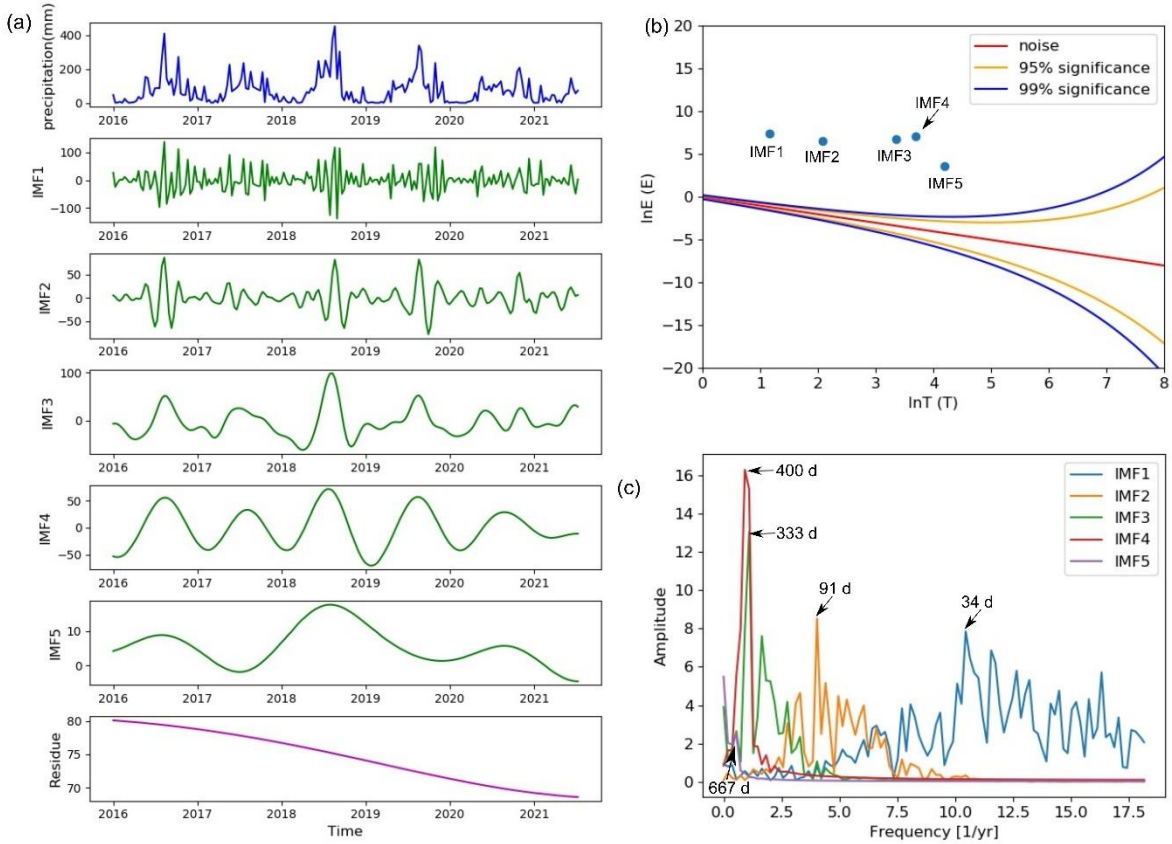

Figure 5-3. Ensemble Empirical Mode Decomposition (EEMD) on GPM IMERG catchment-averaged (every 10 days) precipitation data from the Abra catchment. (a) Upper plot (blue) is the precipitation data for the Abra River catchment. The subsequent five plots (green) are decomposed Instinct Mode Functions (IMFs), and the lowest plot (purple) is the residual of the decomposition. (b) The significance of the IMFs, where T = mean period (years) and E = Energy density. The mean period, the energy density for the added noise and confidence bands are calculated using the method of Huang (2004). (c) IMF amplitude in quantity peak as a function of signal frequency from fast Fourier Transformation (Cerna and Harvey 2000). This shows the dominant frequencies of each IMF, which correspond to the main periods of the decomposed components.

Previous work (Kong et al. 2015) has shown that the highest frequency signal (IMF1) can contain signal noise. To test the significance of all the IMFs, we used Huang's (2004) method for the IMFs and for white noise (Figure 5-3b). All five IMFs (Figure 5-3b; blue dots) from the Abra precipitation data are significant (>99% level). To investigate the possible physical meaning of these significant IMFs, the frequency against amplitude plot (Figure 5-3c) shows the main frequencies (periods) within each IMF. Each IMF contains instantaneous frequencies, so each IMF may be associated with more than one timescale if there are multiple peaks in the frequency series. For example, IMF4 has only one peak at a frequency of 1.09 year (400 days), whereas, the other IMF plots show multiple peaks, that may indicate multiple environmental

driving factors within the decomposed component. EEMD results from the precipitation data for both, Bislak and Laoag Rivers also produce single peaks for IMF4 (see supplementary Figure A1 and Figure A2), with an annual period (≈1.09 year), hence IMF can be used to analyse annual precipitation fluctuations. Similarly, IMF2 has a period of 91 days (Figure 5-3c) and is interpreted as a seasonal fluctuation, the magnitude of which varies considerably between years (Figure 5-3a). Using the same decomposition method for landform area time series, we compare IMF4 for precipitation with similar frequency (period) for the landform data to identify temporal responses in river landform units to annual precipitation variability.

5.4. Results

5.4.1 Machine learning model classification performance

The SVM classification training model was built from six dates of Bislak River imagery, distributed across all seasons in 2018. Table 5-1 summarises the model's performance for selected years for the three rivers. Overall Accuracy (OA) exceeds 0.86 for all rivers, indicating that the machine learning model has an appropriate efficiency to classify fluvial landforms for rivers in north-west Luzon. Although the recognition efficiency of vegetated bars is lower than that of water and unvegetated bars, Vegetation Accuracy (VA) still exceeds 0.70 for all test cases. To illustrate the classification, Figure 5-4 presents the classification results across different seasons in 2019, for the Abra River. The spatial distribution of landforms suggests there could be a seasonal cycle of river pattern change; vegetation extent and water cover increased between March and September and decreased between September and January of the next year.

Table 5-1. Assessment of SVM classification performance for the Bislak, Laoag and Abra Rivers for a selection of years. For each metric, a value of 1.0 would indicate perfect agreement.

River (Year)	Overall Accuracy (OA)	Water Accuracy (WA)	Unvegetated Bar Accuracy (BA)	Vegetated Bar Accuracy (VA)
Bislak (2017)	0.904	0.883	0.981	0.752
Bislak (2019)	0.897	0.868	0.948	0.789
Laoag (2018)	0.866	0.937	0.860	0.735
Abra (2019)	0.872	0.901	0.959	0.721

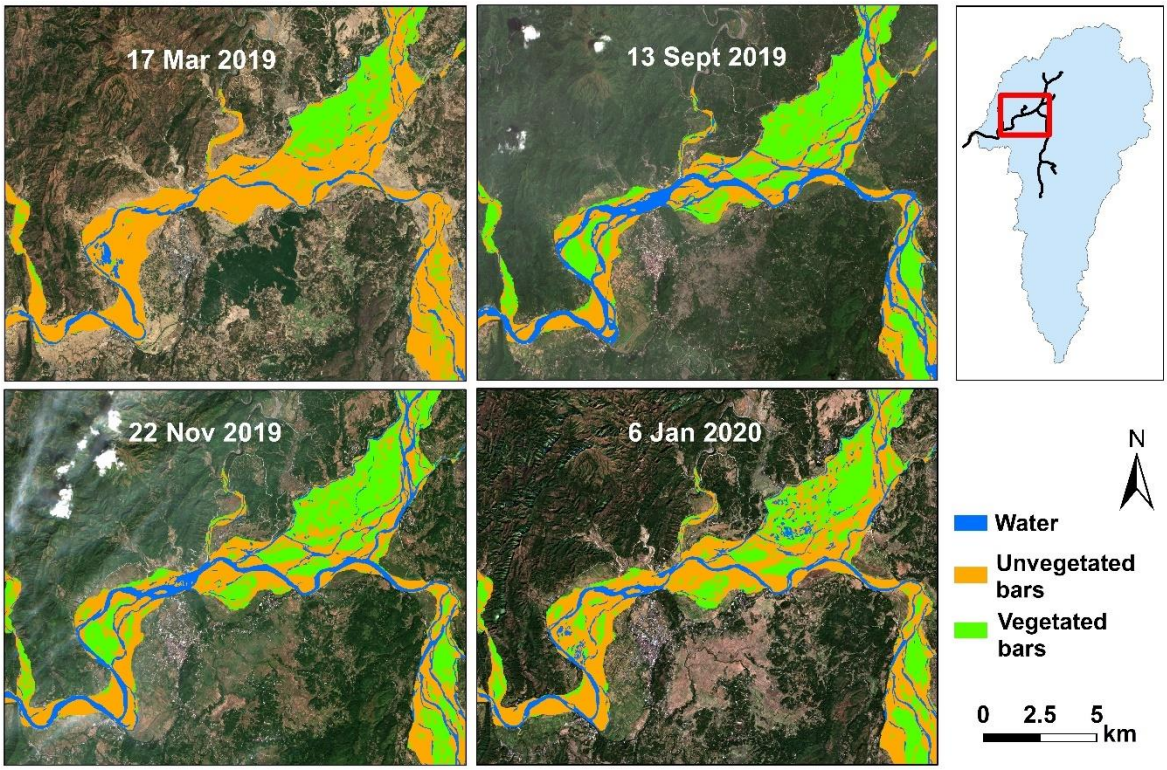

Figure 5-4. Classified river landforms for a segment of the Abra River during a one-year period. Seasonal variation in landforms is evident during the year.

5.4.2 River landform classification

Following the acceptable performance of the SVM machine learning model, the model was then applied to classify river landforms for the 5.5 year long imagery dataset, for the three rivers. Figure 5-5 shows how the proportions of water, unvegetated bars and vegetated bars change longitudinally and temporally. A proportional cover approach is used to show the data because it removes the influence of active width (AW) on observed change. From a spatial perspective, the results show a variety of landform changes from downstream to upstream. In general, for all three rivers, there were higher proportions of vegetated bars for reaches that have greater active widths (AWs). For the Laoag and Abra Rivers, reaches located closer to the sea had greater proportions of water extent relative to mid- and upper reaches. This may be due to the contribution of tributary inflows to these rivers. However, in other ways the Laoag and Abra rivers are different. The lower reach of the Laoag River had a relatively high proportion of vegetation whilst the proportion of bars is relatively low compared to the mid- and upper- reaches. For the mid reach (9 - 32 km from the sea) of the Abra River, the vegetated

bars occupied a lower proportion of the reach relative to mid-reaches of the Laoag River. For this reach, the proportion of vegetated and unvegetated bars were relatively similar.

Temporal patterns in landform proportions (Figure 5-5) were synchronised across the three rivers, showing yearly variation throughout the study area for each river. In general, the proportion of vegetation started to increase after late May and then decreased before early February in the subsequent year. These annual dynamics can also be seen in the mapped landform changes for the Abra River in 2019-2020 (Figure 5-4). For many reaches, Figure 5-5 indicates that there were corresponding temporal changes in water proportion. However, for some reaches, there was a slight increase in vegetated bar proportion and a decrease unvegetated bar proportion, whilst the water proportion remained stable. This phenomenon probably indicates seasonal vegetated island development.

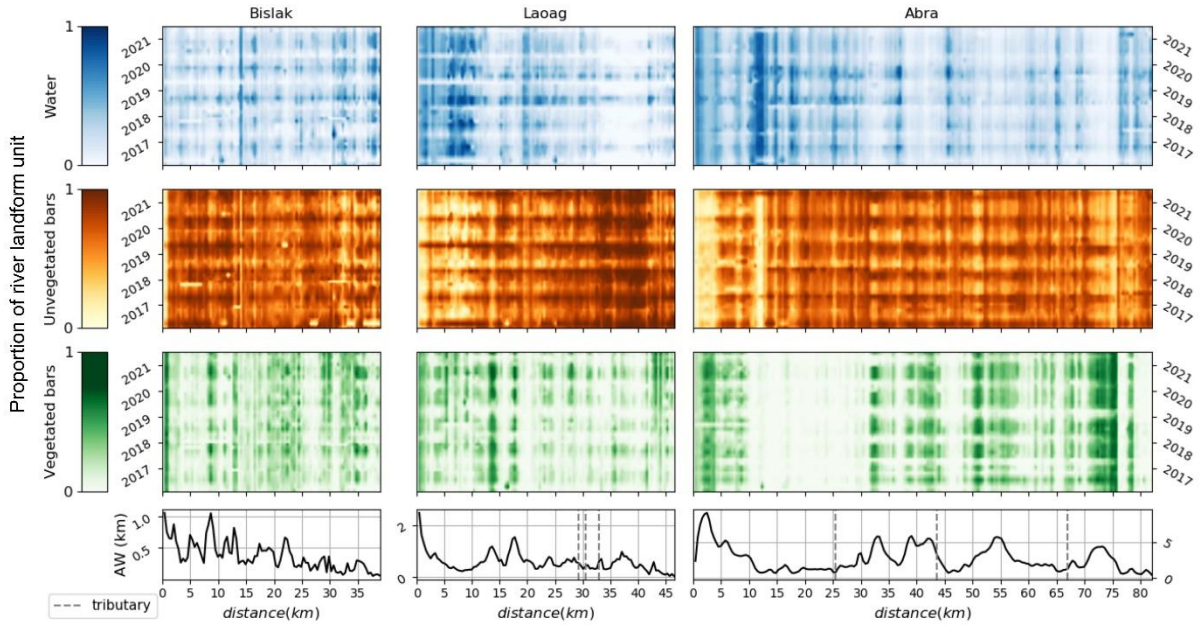

Figure 5-5. Longitudinal and temporal variation in landform proportions, and active width (AW), of the Bislak, Laoag and Abra rivers between February 2016 and July 2021. Distance starts from the estuary to the upstream. Classification maps are available from the digital data supplement (available after peer-review).

To analyse and compare temporal changes in landform pattern from a spatial perspective, the three rivers were segmented into sub-reaches based on water frequency and river confinement. Figure 5-6 and Figure 5-7 shows five-year water frequency maps for the Bislak, Laoag and Abra Rivers, together with contextual information on topography, fault lines (PHIVOLCS 2015) and confinement. Confinement was assessed by overlaying the active channel extent

with the mapped valley floors. Valley floors were manually mapped in GIS using a nationwide DEM (Grafil and Castro, 2014). We defined the valley margins morphologically, by identifying breaks in slope from relatively flat, low elevation areas to relatively steep hillslopes. Segment divisions were set when: (i) the water frequency map showed a change in river pattern from multi-thread to single thread, or vice-versa; (ii) there was a change from unconfined to confined valley, when over 90% of the proportion of the river was confined on both banks; and (iii) there were confluences. The Bislak, Laoag and Abra Rivers were segmented into 9, 10, and 16 sub-reaches respectively.

Figure 5-6 shows that faults in the study region, and thus geological structure and position of high ground, are generally oriented north to south, Thus, rivers would typically flow along this approximate axis. An example from the Bislak River (Figure 5-6a) provides a view of river cutting through the high ground to reach sea (base) level to the immediate west. As rivers can incise at about the same rate as mountain uplift (often about 1mm/year) (Maxwell et al., 2018), incised meanders in the Bislak River provide evidence for river downcutting during uplift. Sub-reach 7 and 8 of the Bislak River might be a graben with faults on both sides where the hills are uplifting and the basin in the middle is subsiding.

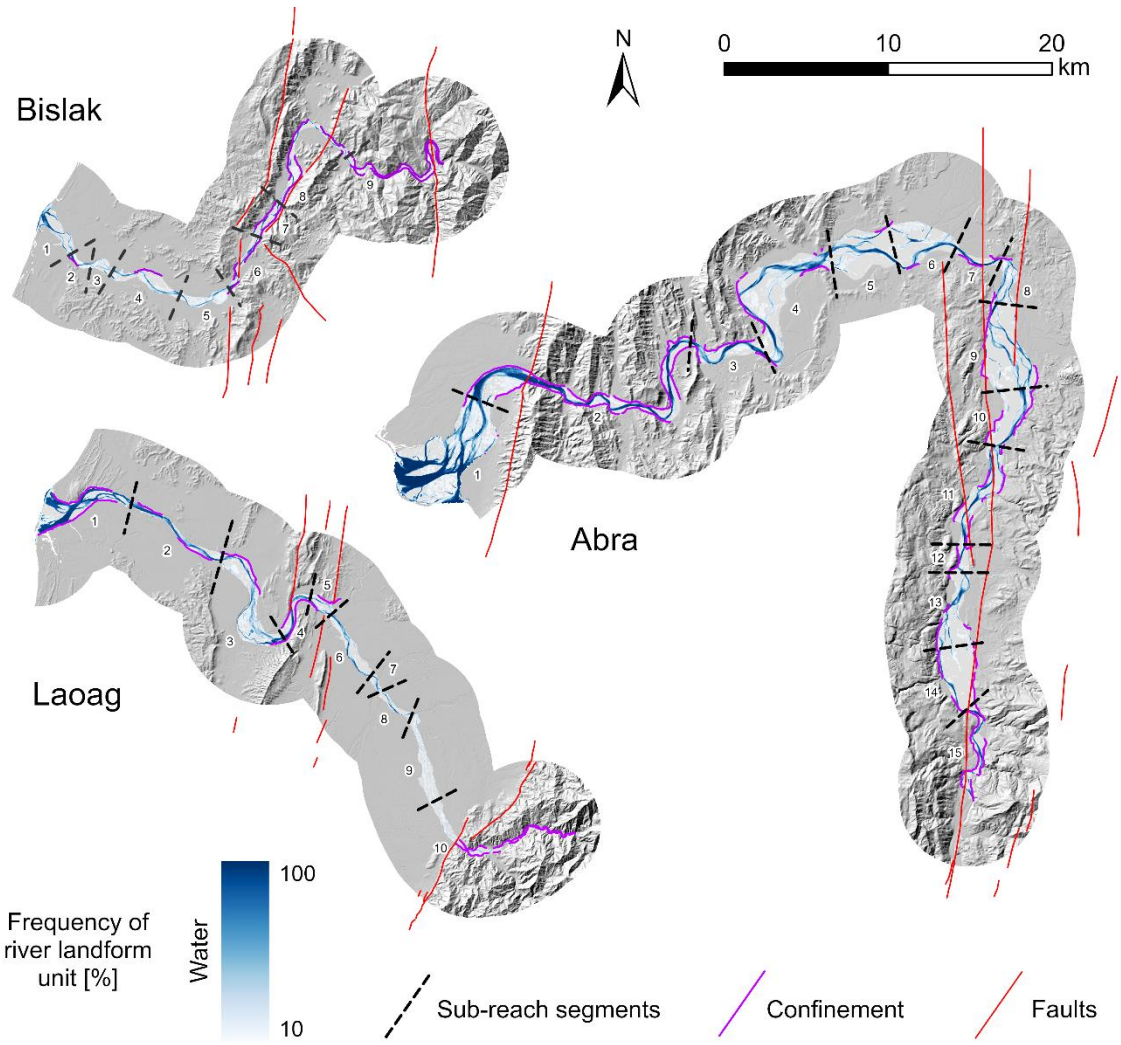

Figure 5-6. River segmentation of the Bislak, Laoag and Abra Rivers.

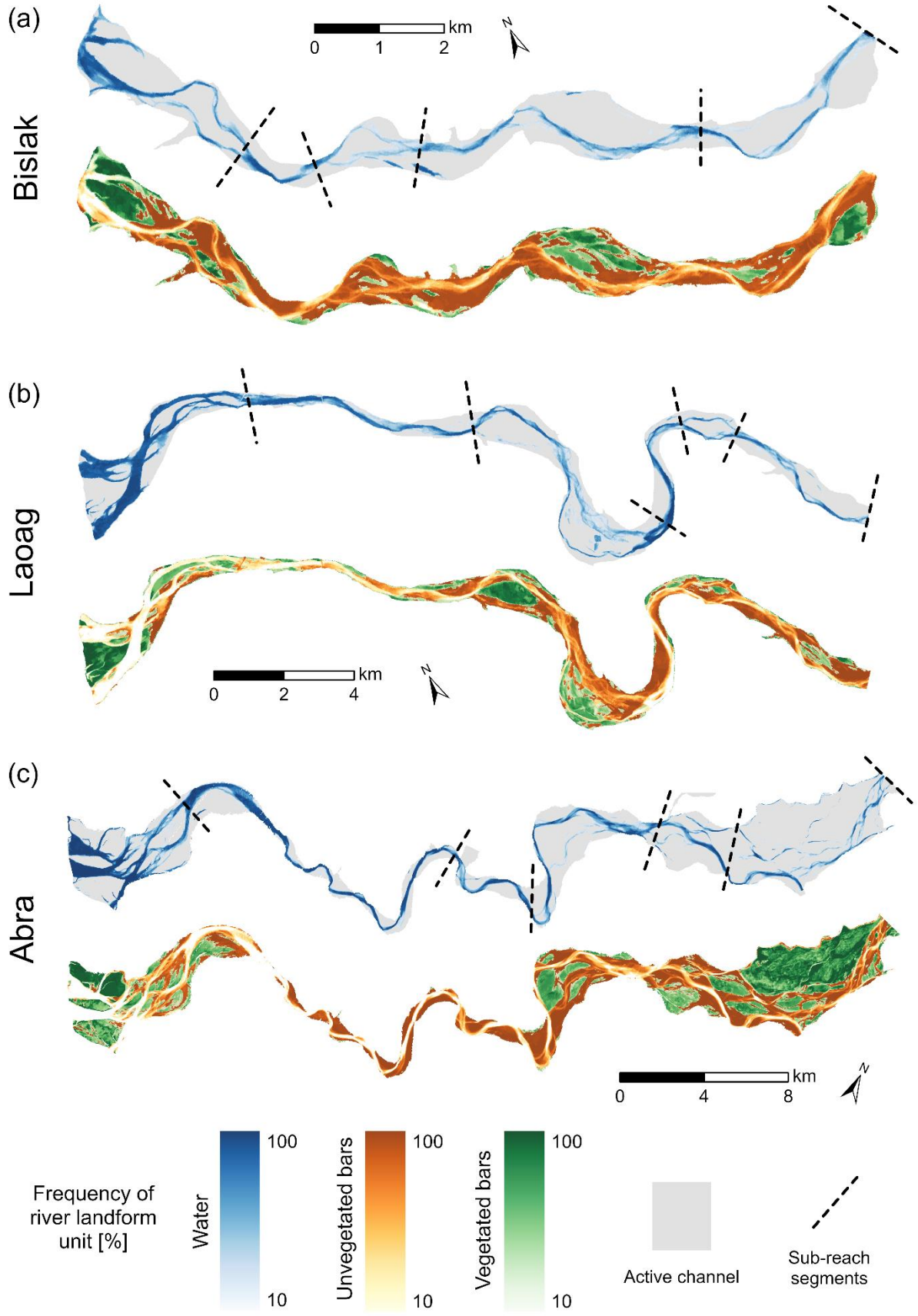

Figure 5-7. Landform frequency maps for the (a) Bislak, (b) Laoag and (c) Abra Rivers.

5.4.3 Active width impacts on area and proportion of landforms

To examine the potential relationships between active width (AW) and the three landforms, mean values of area and proportion in the dry and wet season were investigated for the three rivers, using data from each river segment (Table 5-2). Results for the areal analysis of the Abra River are shown in Figure 5-8 whilst results from the proportional analysis for the Laoag River are shown in Figure 5-9. Supplementary figures (A3 to A6) show the results for the other area and proportion combinations for the three rivers. Correlation coefficients were calculated between AW and mean landform area/proportion, for dry and wet seasons. Figures A7 to A12 present the correlation coefficients for the five-year duration time series, from February 2016 to November 2020. Overall, the data in Figures 5-8 to 5-9, and A3-A12, enable both spatial and temporal trends in the relationship between AW and landforms to be investigated; these are considered in turn in the next two sub-sections.

With respect to landform area (Table 5-2, Figure 5-8b, A3 and A4), there are positive correlations between the three landforms and AW across all three rivers ($Area_{water} < Area_{veg} < Area_{bars}$ in the Bislak River, generally $Area_{water} < Area_{bars} < Area_{veg}$ in the Laoag and the Abra Rivers). Water area is moderately impacted by AW in this region. This contrasts to vegetation and bars, which are strongly controlled by AW. The results also indicate that the strength of the correlation between AW and vegetation area perhaps relates to river catchment spatial scale, since the coefficient values of AW-$Area_{veg}$ in the three rivers increases with catchment size. In addition to relationships between landforms and AW, $Area_{veg}$ and $Area_{water}$ also have a significant moderate correlation (0.71 in Bislak River; 0.64 in Laoag River; 0.61 in Abra River) in dry season.

For proportional analysis (Table 5-2, Figure 5-9b and A5, A6), only $Prop_{veg}$ in Abra River has a moderately high and significant correlation with AW (>0.60 in both dry and wet seasons). The correlation between $Prop_{veg}$ and AW in the Laoag and Bislak Rivers were both significant weak positive (<0.6), with the coefficient in Bislak River lower than that in Laoag River. For this case, the spatial scale of the river probably also has an impact on the correlations between vegetation proportion and active width in the region; this is an example of the river scale impacts on vegetation area and active width that were discussed above. For the Bislak and Laoag River, no high or moderate correlation coefficients (≥0.6 or ≤-0.6) between $Prop_{landform}$ (any landform proportion) and AW were observed. However, during the dry season, across all

three rivers, $Prop_{water}$ and $Prop_{bars}$ all had a strong significant negative correlation (≤-0.7). Moreover, in the wet season of Laoag River, $Prop_{water}$ and $Prop_{bars}$ had a strong significant negative correlation (-0.79), which is different from the other two rivers. Additionally, $Prop_{veg}$ and $Prop_{bars}$ had negative correlations (<-0.6) in the Bislak River for both seasons; in the Laoag River, a negative correlation (-0.64) only occurred in the dry season. By contrast, for the Abra River, there was only a weak negative correlation (-0.47) between $Prop_{veg}$ and $Prop_{bars}$.

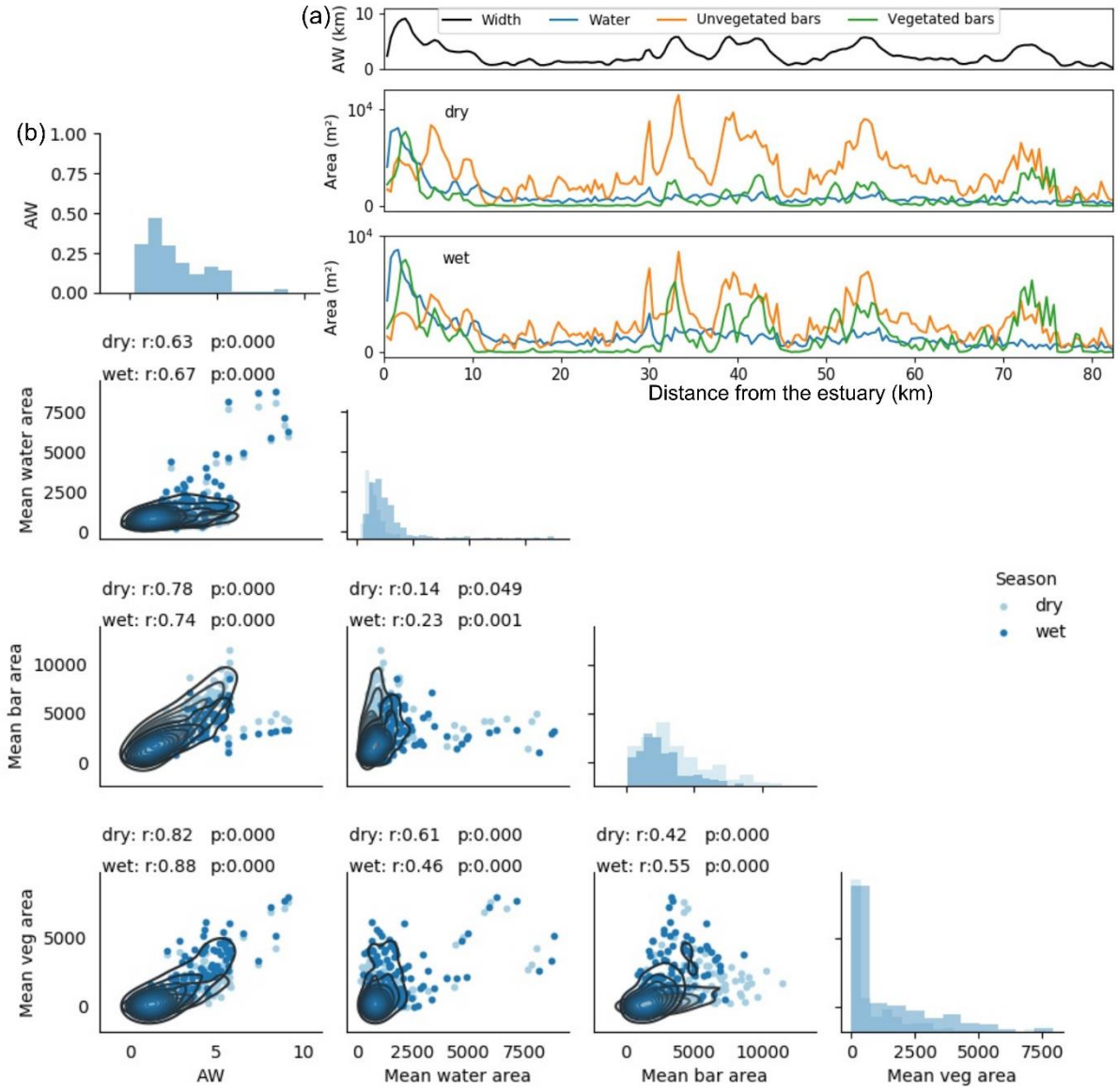

Figure 5-8. (a) Longitudinal trend in active width (AW) and mean area of three landforms (water, unvegetated bars, vegetated bars) for the Abra River, for wet and dry seasons. (b) Matrix plots represent correlations between mean values of landform areas and AW. Histograms illustrate mean value distributions at equal spaced spatial distance along the river. Kernel distribution estimation is shown using contour plots. Tables above each matrix plot

summarise correlation coefficients (r) and associated statistical significance (p) between landform areas and AW in wet season and dry season.

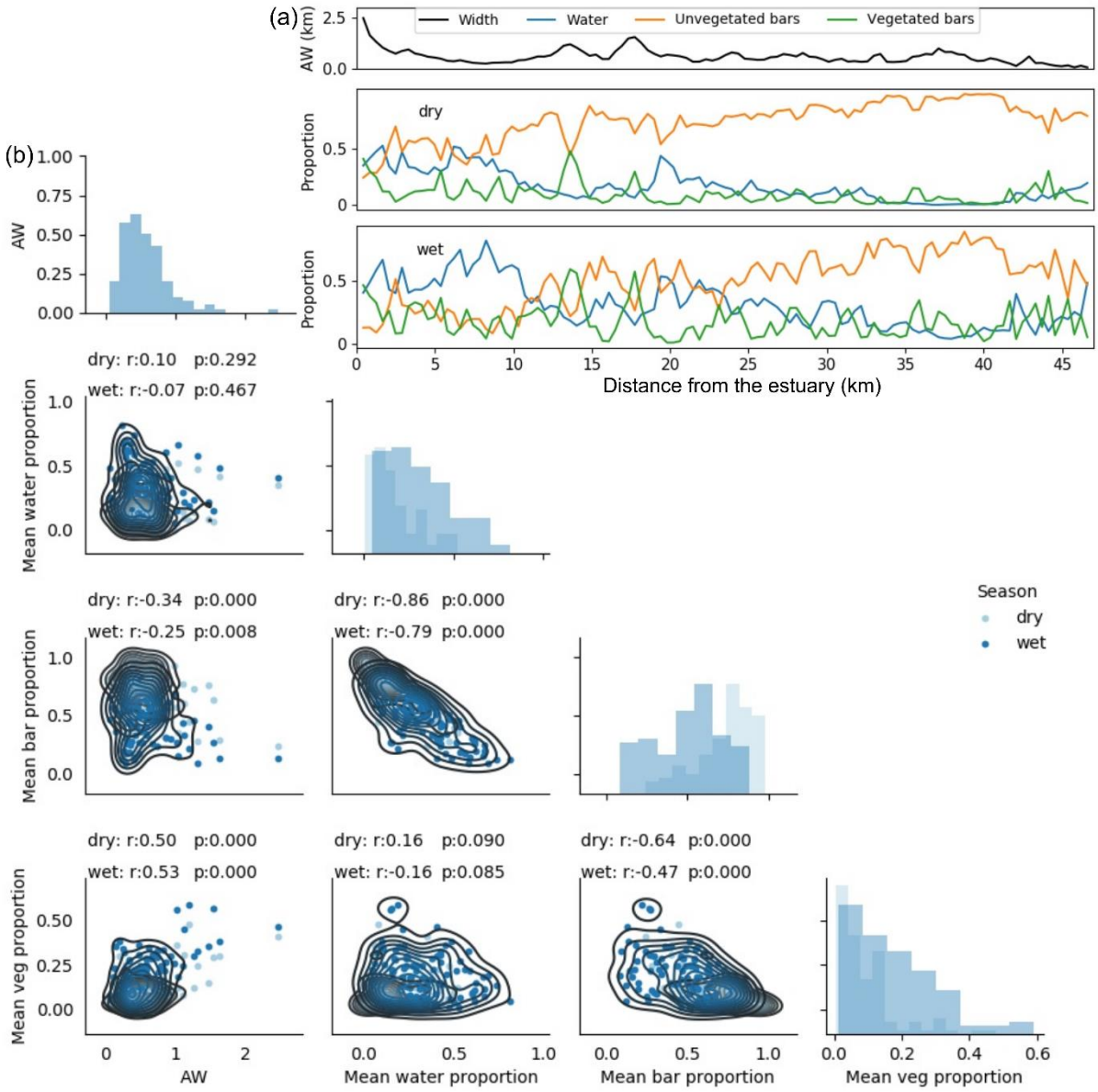

Figure 5-9. (a) Longitudinal trend in active width (AW) and mean proportion of three landforms (water, unvegetated bars, vegetated bars) for the Laoag River, for wet and dry seasons. (b) Matrix plots represent correlations between mean values of landform proportions and AW. Histograms illustrate mean value distributions at ~410 m spatial distance along the river. Kernel distribution estimation is shown using contour plots. Tables above each matrix plot summarise correlation coefficients (r) and associated statistical significance (p) between landforms proportion and AW in wet season and dry season.

Table 5-2. Correlations between landforms and active width (AW) for the Bislak, Laoag, Abra Rivers for wet and dry seasons. r refers to correlation coefficient, where r≥ 0.60, text is bold. p refers to significance.

Approach	River	Season	Water-AW		Bar-AW		Veg-AW	
			r	p	r	p	r	p
Area	Bislak	Dry	0.46	<0.001	**0.86**	<0.001	**0.67**	<0.001
		Wet	**0.60**	<0.001	**0.78**	<0.001	**0.76**	<0.001
	Laoag	Dry	**0.64**	<0.001	**0.73**	<0.001	**0.81**	<0.001
		Wet	**0.69**	<0.001	0.50	<0.001	**0.86**	<0.001
	Abra	Dry	**0.63**	<0.001	**0.78**	<0.001	**0.82**	<0.001
		Wet	**0.67**	<0.001	**0.74**	<0.001	**0.88**	<0.001
Proportion	Bislak	Dry	-0.45	<0.001	0.18	0.087	0.31	0.002
		Wet	-0.41	<0.001	-0.09	0.404	0.42	<0.001
	Laoag	Dry	0.10	0.292	-0.34	<0.001	0.50	<0.001
		Wet	-0.07	0.467	-0.25	0.008	0.53	<0.001
	Abra	Dry	-0.24	0.001	-0.17	0.014	**0.61**	<0.001
		Wet	-0.35	<0.001	-0.32	<0.001	**0.65**	<0.001

The above analysis indicates that the relationship between AW and each of the three landforms varies between wet and dry seasons. To further investigate this relationship, from a temporal perspective, we selected the combinations that had above moderate correlation (>0.6). Then we calculated the correlation coefficients for specific dates, instead of using mean values for the wet and dry seasons, with the objective of minimising the temporal range of significant high correlations. The results are shown for the three rivers in Figures A7-A12, for area and proportion respectively. The correlation between $Area_{veg}$ and AW was commonly high for the three rivers. Specifically, vegetation area shows higher correlation to the AW in the wet season compared to that in the dry season. However, for each river, the first dry date was always associated with a high correlation between $Area_{veg}$ and AW, indicating there is a lag in AW impacts on vegetation area. The strongest correlations between AW and $Area_{veg}$ occurred from early July to early December every year. The AW correlations to $Area_{bar}$ were also similar for the three rivers. However, for the Bislak and Laoag Rivers, $Area_{bar}$ was overall more synchronised with AW in the dry season. Beyond relationships with *Area*, the proportional analysis showed that the increase in $Prop_{water}$ corresponded to a significant decrease in $Prop_{bar}$ across all three rivers in dry season but for the Bislak River only in the wet season. This may be due to the lower proportion of vegetation growing in the wet season in the Bislak River. Besides, late January to mid-March contributed the strongest correlation between $Prop_{water}$ and $Prop_{bar}$. This period could also be regarded as the time period in which vegetation has the least impact on the channel. Additionally, the correlations between $Prop_{veg}$ and $Prop_{bar}$ in the Laoag River are moderate to high from April to June, whilst these correlations for the Bislak River

varied across the five years. The reason of this difference between these two rivers could not be determined.

5.4.4 Temporal changes in sub-reach landforms

Temporal patterns in landform areas across the sub-reaches of each river were assessed using the EEMD to decompose time series of classified water, unvegetated bar and vegetated bar areas. Data for at least 32 dates covering >5.5 years were used. As noted in section 5.3.4, the IMF4 component of precipitation represents annual periodicity (c.12-13 months). For landform areas, the IMF2 components from the three rivers and three landform types typically had one main frequency, also with a period of around 12-months (Figure 5-10). Where the period of the IMF2 component is not 12 months, this reflects weak or absent seasonality in some years.

The decomposition shows that water and vegetated bar areas are close to being in phase with precipitation, with a lag of between 1 and 3 months. Unvegetated bar areas are close to anti-phase with precipitation, with peak areas always between March and May. Most sub-reaches of the three rivers show vegetation area expansion during September to December, with water surface area being maximum in August to November. Comparing the EEMD results with valley-scale geomorphology (Figure 5-6), there is no clear evidence that channel confinement controls annual changes in landform areas.

There are some periods of several months when the landform areas did not change significantly, even though precipitation followed the normal seasonal trend (Figure 5-10). In some cases, this reflects data gaps due to clouds obscuring the river in some images. For example, the Bislak River, reaches 2 and 3 (Figure 5-10, light grey shading) remained constant during 2017 due to data gaps, which also affected the Bislak River reach 5 in 2016.

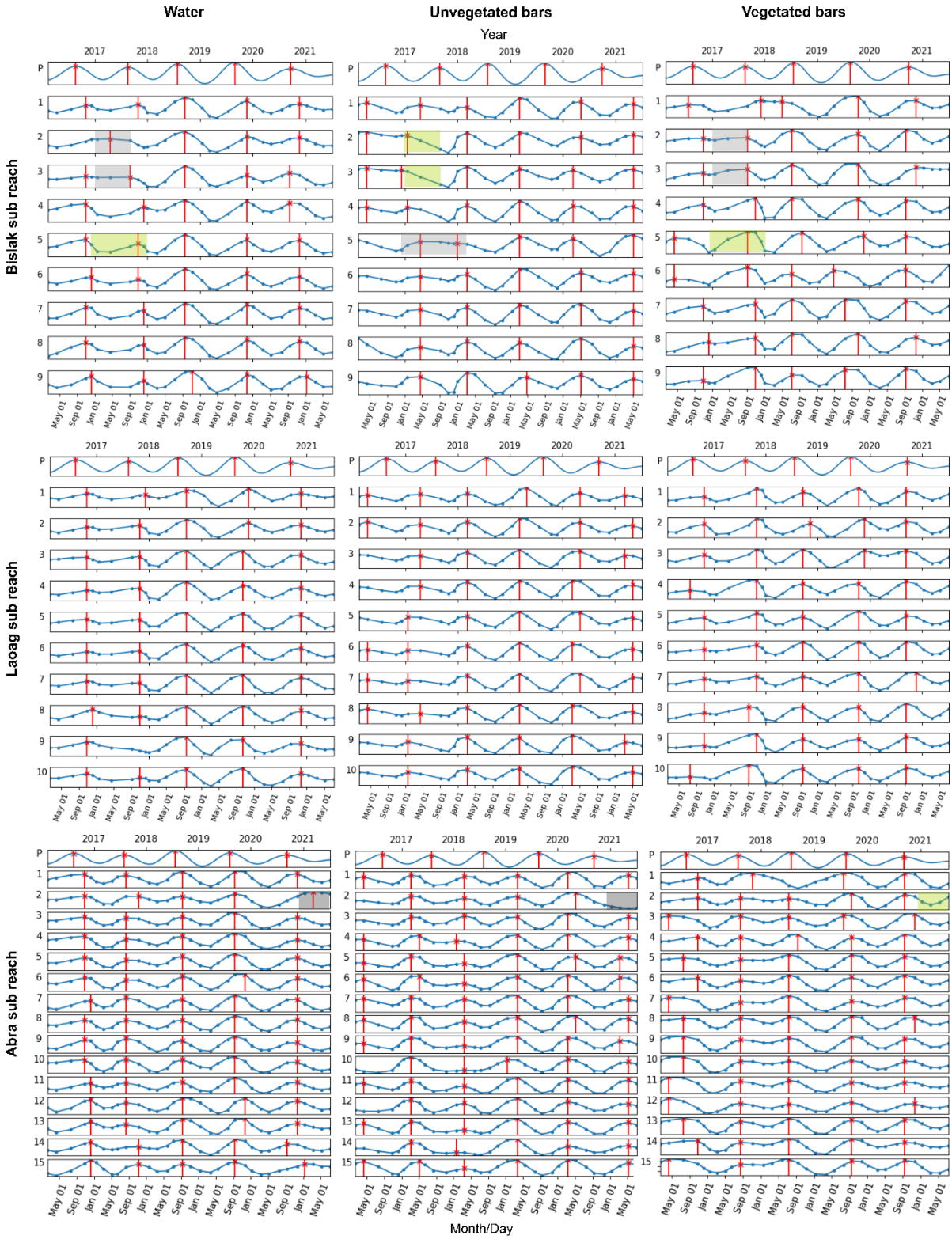

Figure 5-10. Ensemble Empirical Mode Decomposition (EEMD) IMF for precipitation (P; IMF 4) and landform (water, unvegetated bars, vegetated bars; IMF 2) areas. IMF 2 data (blue lines) are presented for sub-reaches (numbers as in Figure 5-6) for the Bislak, Laoag and Abra Rivers. In all cases, the periodicity is c.12-13 months. Red vertical lines are at each annual peak. Periods with light grey shading are not consistent with neighbouring reaches, whereas the light green shading shows periods that are consistent. See the text for explanations.

Where data are available continuously, the EEMD analysis could potentially provide an approach to detect anthropogenic disturbance such as gravel mining. For example, in Abra River reach 2 in 2021, the water area maintained close to its peak value and the unvegetated bar area remained low (Figure 5-10, light grey shading), although the area of vegetated bars followed a typical seasonal pattern (light green shading). When we refer to the spectral imagery in Figure 5-11, the unvegetated bars area was occupied, an obvious artificial bank was changed (in red circle) and water area was extended (in blue circle) between 11 March 2020 and 11 March 2021. As well as bank construction, these changes may also be affected by gravel mining activities. If mining is important, changes may be expected in active width (AW) over succeeding years (Bertrand and Liebault, 2019).

Figure 5-11. Detection of morphology change (in red and blue circle) between 2020 and 2021 in sub reach 2 of Abra River.

5.5. Discussions

5.5.1 River pattern classification

A hierarchical workflow (Li et al. 2022) has been applied to three rivers intra-annually, using free-to-access remote sensing data. The workflow adopted object-based analysis, as recommended by previous land surface classification investigations (Demarchi et al. 2016; Ma et al. 2017; Phiri, Simwanda, and Nyirenda 2021; Phiri et al. 2020). We applied the ATPRK algorithm to enhance the 20 m resolution Sentinel-2 imagery to 10 m resolution images. ATPRK was shown to be effective on Sentinel-2 imagery fusion by Wang et al. (2016) and has been confirmed by Li et al. (2022) and our implementation here. However, we suggest it is

essential to carefully choose and test downscaling approaches before applying object-based image classification. In addition to image downscaling, we also employed the LSMS algorithm, in open-source Orfeo-Toolbox, to perform an object-based segmentation. Ma et al. (2017) found that 80.9% of previous investigations have used commercial e-cognition software in their review of different software that has been applied to segment remote sensing imagery. Here, we obtained good classification results (overall above 0.86 in yearly overall accuracies for the three rivers) by using open-source software. Since Sentinel-2 is one of the most suitable satellite missions for monitoring vegetation with a medium to high spatial and temporal resolution, our investigation demonstrates the potential use of an open-source software workflow in fluvial settings.

Our classification results demonstrate that generating an active channel extent from multi-temporal data is useful for bounding the segmented geographical objects. This approach is especially important for the characterisation of tropical river dynamics as landforms within the active channel change more frequently than those in temperate settings due to the relatively high frequency of high flow events and strong seasonal effects. The latter have been described as the dominant feature of most tropical rivers (Syvitski et al. 2014). Due to the strong seasonality that is characteristic of the climate in north-west Luzon, we found that the single date-based machine learning model poorly fitted to imagery from a different season, whilst a multi-date based model was able to achieve higher accuracy across different dates of the year. From field observations, vegetation composition and condition vary seasonally, especially at the edges of the active channel due to agriculture development practices. For example, for a sub-reach of the Abra River (Figure 5-12) we identified that patches of water disconnected from the main channel on 11 January 2019. Looking at the same location over 5 years, we found the similar scattered water patterns between January and February in every year. Seasonal vegetation and soil moisture could be the reason that impacted the water retention (Milly 1994; Werner, Sanderman, and Melillo 2020). However, as for agricultural practices observed on the vegetated islands (Figure 5-12) of the sub-reach of the Abra River, the scattered water patches during January and February probably be related to irrigation practices, resulting in soil nitrate solubilization, transport and in upward migration of the groundwater piezometric head (Pinardi et al. 2022). Therefore, from the seasonal water patches (Figure 5-12), there is a potential to recognise the hotpot of soil nitrogen budget dynamics. Overall, the seasonal variations in the active channel led us to consider a multi-season classification model for change detection in the studied rivers.

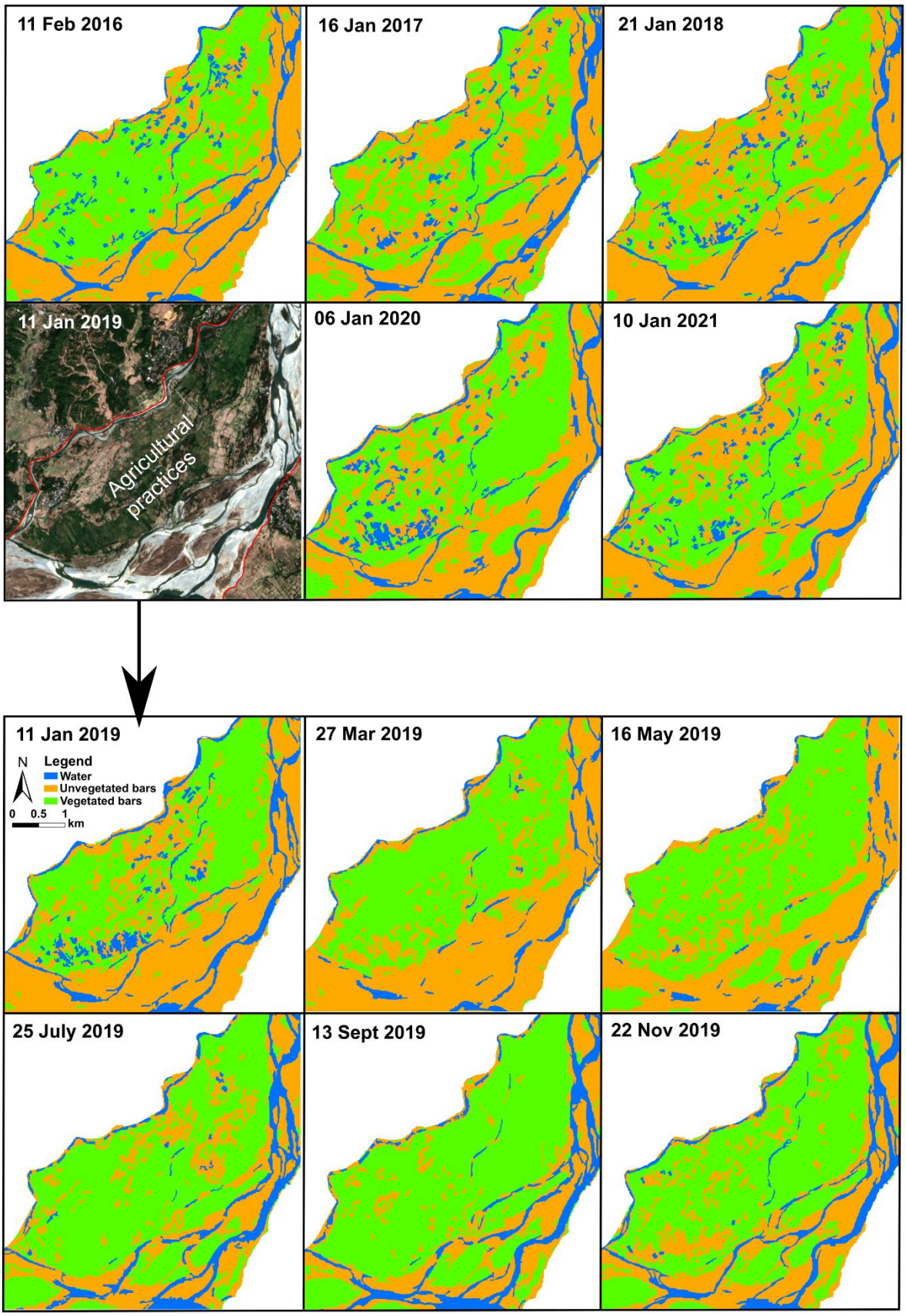

Figure 5-12. Mapped morphologic seasonal change and yearly change in a sub-reach of Abra River.

5.5.2. Spatial river landform sensitivity to channel settings

Whilst longer-term (>50 year) geomorphological processes, linked to tectonics, regional catchment settings and sediment supply, can cause changes in channel pattern (Baena-Escudero et al. 2019; Corenblit et al. 2020; Gilvear 1999), we constrained our study to a relatively short-term scale. In this section, we investigate landform stability, by establishing a covariance series of each landform area along each river, from downstream to upstream, for the 5.5-year time period. The coefficient of variation (COV) of a distribution is measured by the ratio of its standard deviation to its mean. This is designed to enable the comparison of series with different mean values. Large values of COV are associated with more dispersed distributions (Yang and Lo 2000). In this study, large values of COV represent high instability of the temporal landform data. We used a moving average window (9 data points) to smooth the COV series.

Figure 5-13 shows the longitudinal distribution of COV results, with confinement, faults and tributary locations indicated. Interpreted together with Figure 5-6, in general where faults are perpendicular to the channel centreline, vegetated bar stability increases. Conversely, where faults are at oblique angles to the channel centreline, vegetated bar stability decreases. Additionally, greater variability in the location of wetted areas is observed downstream of faults (for example, downstream of 11 km in the Abra River), which may reflect decreased gradient downstream of these faults. Where faults influence valley slope channel pattern adjusts, potentially leading to changes in sinuosity (Zámolyi et al. 2010), incision or the onset of wandering or braided behaviour. A sinuous reach downstream of the fault on the Bislak River at 27 km (Figure 5-6) indicates that the fault affects valley gradient and so causes increased meandering (Zámolyi et al. 2010).

Tributaries provide inputs of water and sediment that may impact mainstem morphology depending on the scale of these inputs and the calibre of introduced sediment (Ferguson & Hoey, 2008). In the Laoag River (Figure 5-13), the area occupied by water is highly unstable upstream of the confluences where three significant tributaries joining in (ca. 33-40 km downstream; Figure 5-6, reach 7 and 8), whilst unvegetated bars remain stable and vegetated bar proportions are relatively low but showing seasonality (Figure 5-5) in this reach. In the meantime, Figure 6 shows that the water frequency is extremely low in this reach. In this case, downstream of tributaries the wetted channel becomes more stable. A similar result is observed

for some tributaries in the Laoag and Abra Rivers where the wetter area becomes somewhat more stable downstream of tributary inputs. The impacts of tributaries depend on their sediment loads which we have not been able to quantify, and tributary locations are likely to be determined by fault locations and lithological changes. Hence, further investigation is required to understand the impacts of tributaries on channel form.

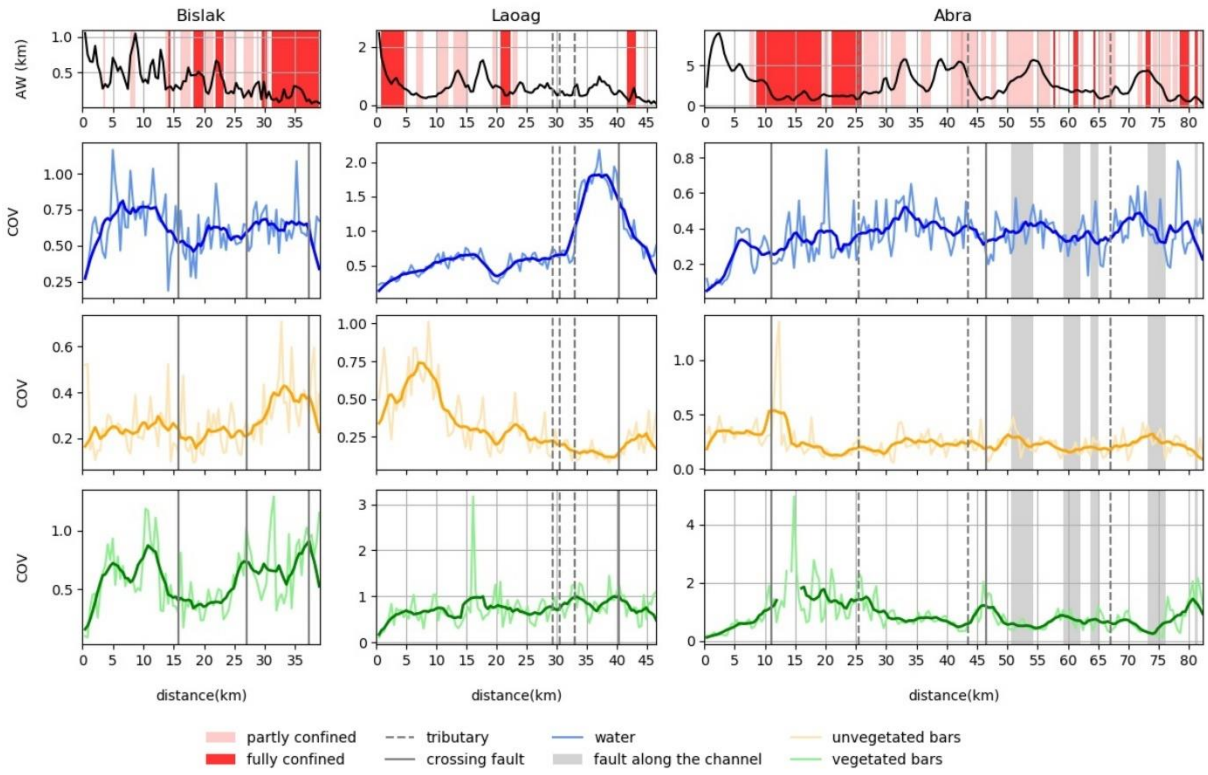

Figure 5-13. Channel settings, including active width, degree of confinement (confined / partly confined / unconfined), compared to the covariance (COV) spatial landform series for the Bislak, Laoag and Abra Rivers (water, unvegetated bars and vegetated bars shaded in thick lines are represented by smoothed values). Distance starts from the estuary to the upstream.

Fryirs (2017) reviewed challenges in analysing river sensitivity in geomorphology and argued that each river has its own history and ability to response to a given disturbance; this is also demonstrated in our investigation. Even though the three studied rivers are located near to each other and in the similar hydrological/climate system, the abilities they have to response to channel setting change are different. For example, in the Bislak River, unvegetated bars are extremely sensitive to continuous confined reach, whilst the unvegetated bars are also sensitive to partly confined reaches in the Laoag River. However, the unvegetated bars shows less sensitivity to the confinement in the Abra River. The Bislak River (0.0049 m/m) is significantly steeper than the Laoag (0.0029 m/m) and Abra (0.0015m/m) Rivers, which may lead to higher

sediment transport capacity in the Bislak. Moreover, averaged active width of the Abra River (2.626 km) is much wider than that of the Laoag (0.581 km) and Bislak (0.375 km) Rivers. In this study, steeper (i.e., those with higher sediment transport capacity) and narrower rivers tend to be more sensitive to lateral confinement. Transport capacity, sediment availability and lateral confinement interact to determine the locations of transport reaches and sedimentation zones (Church and Jones, 1983), and hence bar stability.

5.6. Conclusions

This investigation used a SVM machine learning method to classify tropical river landforms from multispectral, multi-temporal satellite imagery. Applied to three gravel-bed rivers in the Philippines, the machine learning method enabled rapid and objective classification of water, unvegetated bars and vegetated bars from Sentinel-2 imagery between 2016 and 2021. The overall accuracy (OA) exceeded 0.86 for all rivers, indicating that the model had an acceptable classification performance to analyse and interpret seasonal and annual changes in tropical river pattern.

Our results show longitudinal and temporal variation in landform areas and proportions (Figure 5-5). Longitudinal variation is strongly influenced by channel setting (e.g., active width, catchment size, confinement, tributaries and elevation). Landform areas are significantly correlated with active width (Figure 5-8 and 5-9), with the strongest correlation found between active width and vegetated bar area. Assessing longitudinal landform stability through the coefficient of variation (Figure 5-13), differences in gradient and the influence of faults demonstrated how rivers in similar hydrological/climate regimes can have different river sensitivities. Temporally, we show synchronous changes in the area/proportion of landform units between rivers. During the dry season, increases in the proportion of water corresponds to significant decreases in the proportion of unvegetated bars in the Bislak and Abra Rivers, whilst the relationship applies to both the wet and dry seasons of the Laoag River. The finding suggests the need to consider tropical river pattern as a dynamic entity; characterising river pattern from a single time period may not fully represent the considerable impact of seasonal change.

Temporal patterns in landform areas across sub-reaches of each river were assessed using Ensemble Empirical Mode Decomposition (EEMD) to decompose time series of classified water, unvegetated bar and vegetated bar areas (Figure 5-10). For landform areas, the IMF2 components from the three rivers and three landform types typically had one main frequency with a period of around 12-months. The data suggest water and vegetated bars commonly have a synchronised fluctuation with precipitation (close to in-phase), while unvegetated bars have an oscillation close to anti-phase with precipitation. The peak area of water and vegetated bars have a 1 to 3 months lag from the peak of precipitation in each year, while the peak for unvegetated bars occurred between March and May of every year. The time series decomposition method has capacity to detect local (sub-reach) abrupt change through consistency of the decomposed signal; deviations from periodic consistency in river pattern may reflect the influence of extreme events and/or human disturbance. We recommend EEMD as an appropriate statistical technique in geomorphology to decompose datasets that are generated from contemporary applications of machine learning to remotely sensed imagery.

Chapter 6 - Response of a lowland tropical river to tributary inputs, Cagayan River, the Philippines

The following chapter is a reformatted version of a manuscript submitted to the Geomorphology, by Qing Li, Trevor B. Hoey, Richard D. Williams, Brian Barrett, and preprint available at http://dx.doi.org/10.2139/ssrn.4392184.

Abstract

Tributaries add water, sediment, nutrients and organic materials to river mainstems. Increased discharge, and potentially total stream power, at confluences impacts river morphology at these junctions and downstream. We estimate stream power ratios of tributaries to the mainstem, based on catchment area, averaged accumulated precipitation, and slopes of the tributary river and the mainstem immediately upstream of the confluence. Using freely available Sentinel-2 imagery and Geographical Object-based Image Analysis (GEOBIA), we automatically classified river landforms from 2018 to 2021 in the tropical lowland Cagayan River, the Philippines, with eight significant tributaries. Multi-year classification enables assessment of annual dry-wet season and inter-annual variability. The machine learning model classified three landform types within the active channel: water, unvegetated bars, and vegetated bars. Accurate classification (overall accuracy of 0.939) was obtained from data spanning both wet and dry seasons. The Cagayan River is predominantly meandering with frequent stable reaches. Unstable reaches, many associated with tributary inputs, show seasonal dynamics in water and unvegetated bar areas in all years. Longitudinal variations in channel morphology and stability, and temporal changes in landform frequency (using Simpson's diversity index and coefficients of variation) show widening associated with tributaries that is controlled by water discharge, with a secondary sediment flux effect. Local widening and unstable bars are located around confluences, but most other reaches contain very little bar development, in part due to anthropogenic confinement. High landform diversity in confluence zones reflects local sediment deposition and provides riverine habitat diversity.

Highlights

- Tributary to mainstem stream power ratio explains channel adjustment at confluences in a large lowland tropical river
- Water and unvegetated bars respond to wet-dry season flow changes
- Bankfull width increases downstream of confluences which is explained by increased discharge
- Sediment loads exert a secondary control on channel morphological and habitat diversity, and width adjustment

- Tributary influence in this lowland river is consistent with previous studies from high gradient, coarse-bed catchments

6.1. Introduction

Tributaries add water, sediment, and organic materials to river mainstems (Benda et al. 2004; Ferguson and Hoey 2008). Confluences between tributaries and main channels are important geomorphological and ecological nodes, which control the downstream routing of water and sediment, and can generate preserved fluvial deposits (Simon et al. 2018) that may concentrate economic minerals (Rodríguez et al. 2018). As a consequence of the increased channel capacity necessary to transfer the additional water supplied by a tributary, channel widths increase downstream of confluences (Ferguson and Hoey, 2008). Channel morphology, in addition to width, changes both upstream and downstream of tributary inputs, particularly when coarse and/or high volumes of bedload are supplied (Rice and Church 1998). The morphological response to tributary inputs depends on the ratio between tributary discharge and that of the mainstem, and also on the capacity of the mainstem to transport the additional sediment supplied by the tributary (Ashworth and Lewin 2012; Ferguson and Hoey 2008; Rice and Church 1998; Singer 2008). However, in many cases tributaries produce no significant morphological response in the mainstems. In some circumstances, the additional discharge and sediment load provided by a tributary are accommodated by equilibrium responses in the main river (Candel et al. 2021), but there are many geomorphological conditions that may preclude such equilibrium response as may anthropogenic impacts (e.g. impoundments) (Zhao et al. 2017). Studies from high gradient rivers with abundant coarse sediment supplies (Kaushal et al. 2020; White et al. 2018; Swanson and Meyer 2014; Rice and Church 1998) show that excess coarse sediment is frequently delivered by tributaries, generating an upstream backwater and steepening of riverbed slope downstream of the junction in order to maintain sediment dispersal downstream (Rice 2017). Tributaries' impacts on mainstem sediment storage may be also controlled by valley confinement, lithological variations, past depositional history, and upstream sediment connectivity (Rice and Church 1998; Swanson and Meyer 2014).

Lowland rivers, which have predominantly sand or finer beds, are theoretically estimated to reduce their gradient by c.14% as their wider and deeper channels transport sediment more efficiently than the mainstream upstream of the confluence (Ferguson and Hoey 2008). The width adjustment in such rivers will also depend on the relative strength of the riverbank

materials (Kleinhans 2010; Nanson and Croke 1992; Schumm 1960). The dominant morphology in lowland rivers is meandering, although rates of lateral migration vary considerably (Horton and DeCelles 2001; Nanson and Knighton 1996). As such, away from confluence zones these rivers exhibit forced bars that remain stable, either absolutely or relatively to the channel thalweg, over multi-decadal timescales (Crosato and Mosselman 2020). Confluences may also contain bars that are forced by local geometry, including the confluence angle (Ashmore et al. 1992; Crosato and Mosselman 2020). However, inputs of large sediment volumes from tributaries may also produce free bars around and downstream of the confluence that evolve and migrate in response to variations in flow and sediment load (Cordier et al. 2020; Crosato and Mosselman 2020). Hence, multi-annual variability in bars close to tributary junctions provides a means for inferring the nature of the tributary inputs in terms of discharge, sediment flux and grain size.

Large river basins with low stream gradients are abundant throughout the tropics and represent analogues for many ancient fluvial deposits (Fielding et al. 2018; Gibling 2006; Latrubesse et al. 2005). In the wet tropics, frequent high magnitude events transport high suspended and bed sediment loads from rapidly eroding catchments (Saleem et al. 2020; Syvitski et al. 2014). Rapid seasonal vegetation development and erosion on bars cause local bank erosion and channel incision that generates multi-decadal channel change (Boothroyd et al. 2021; Dingle et al. 2020; Saleem et al. 2020). The grain-size and organic materials in tropical rivers also vary from temperate regions (Liu et al. 2009). Together, these factors suggest that tropical rivers may be more dynamic than rivers of the same size in temperate regions. For example, Dingle et al. (2019) reported higher lateral migration rates in the Cagayan River, the Philippines, than from temperate rivers and present an example of a highly dynamic complex confluence zone. However, Simon et al. (2018) found that confluence mobility over 40 years in the Amazon basin was less than in the Ganges-Brahmaputra-Meghna (GBM, temperate) basin.

The impact of a particular tributary on the mainstem river can be expressed as a function of ratios between tributary and mainstream discharge (Q_R), bed load flux (F_R) and bed load grain size (D_R) (Rice 2017). The capacity of both channels to transport sediment is also a function of the tributary to mainstem stream power ratio (SP_R), where stream power $SP = \rho QS$ in which S is river slope immediately upstream of the confluence and ρ is water density (Kaushal et al. 2020; Yang and Stall 1974). Where discharge data are scarce, for convenience catchment

discharge is replaced by catchment area (A) or area × precipitation ($A \times P$), and the impact of tributaries has been correlated with A_R (Rice and Church 1998; Benda et al. 2004). These scale ratios are highly autocorrelated, although numerical modelling suggests that F_R and D_R exert greater controls over tributary impact than does Q_R, at least in the case of coarse bed material.

Assessment of multi-year and seasonal patterns of river morphological change, including tributary impacts, can use both long sequences of Earth Observation data and intra-year data (Dingle et al. 2019; Jézéquel et al. 2022; Kaushal et al. 2020; Simon et al. 2018). Acquisition of images across wet and dry seasons allows seasonality and longer-term trends to be differentiated (Li et al. 2023). Here, we use a river landform classification workflow (Li et al. 2022) and freely available Sentinel-2 imagery to generate maps of water, unvegetated bars and vegetated bars during wet and dry seasons over five years for the lowland Cagayan River, the Philippines. Using these data and catchment information, we address the following questions: (1) Do fluvial landforms in the lowland Cagayan River show seasonality? (2) How does river morphology respond to tributary inflows? and (3) How does river planform morphology (e.g., active channel width, bar size and vegetation cover) and temporal diversity relate to Q_R, F_R and SP_R for tributaries entering the Cagayan River?

6.2. Study Area

The 27,684 km^2 Cagayan catchment (Figure 6-1) experiences heavy precipitation, frequent tropical storms and cyclones, flooding, landslides and earthquakes (Faustino-Eslava et al. 2013; Bautista and Oike 2000). Deforestation across Luzon Island (Forest Management Bureau 2013; Dingle et al. 2019) may impact sediment dynamics in parts of the catchment. Previous investigations have shown that the Cagayan River meander migration rates are higher than equivalent rivers in temperate regions (Dingle et al. 2019). Of the three climate types in Luzon Island, the Cagayan River is in Climate Zone III (Basconcillo et al. 2016; Tolentino et al. 2016), characterised by strong seasonality. Monthly rainfall statistics (1977-2009) show that annual rainfall in the Cagayan increases to a peak in October, associated with the winter monsoon (Kubota et al. 2017).

Forced bars (e.g. the mid-channel bar marked on Figure 6-1d) are common in the Cagayan River, with vegetation density on these surfaces changing through the year (Figure 6-1d and 1e). Over 95% of the mainstem segment (Figure 6-1c) investigated here is incised into Plio-

Pleistocene sediments (Liu et al. 2009). No faults cut through the mainstem of the river (Liu et al. 2009). The studied segment of the Cagayan River is predominantly meandering; the remaining 9.7% is braided. Mapping shows that 22.6% of the channel in the study area is confined by either valley margins or artificial banks. The mean active width of the mainstem reach is 604 m, ranging from 220 m to 2009 m. Eight significant tributaries enter the Cagayan's mainstem along the reach (Figure 6-1c), introducing additional water discharge and sediment. Anthropogenic structures, including bridges (Figure 6-1d and 1e; Boothroyd et al. 2021), and flood and erosion protection structures are observed along the Cagayan River. Dingle et al. (2019) quantified rates of confluence and lateral channel migration in the Pinacanauan de Ilagan River, a tributary of the Cagayan River, and its tributaries (Bintacan and Abuan Rivers). They found that aggradation and channel width increased on the lower gradient alluvial plain due to high sediment supply from the catchment headwaters.

The Cagayan bed is predominantly sand and silt (JICA-DPWH 2002), and riverbanks are predominantly silty. Tributaries in the upper catchment deliver significant quantities of gravel (Dingle et al. 2019; JICA-DPWH 2002) that lead to local aggradation and infilling of the Magat Dam. Bank erosion is locally significant, with both mass failure and granular erosion observed throughout the lowland catchment. Liu et al. (2009) report moderate chemical weathering in clay (<2μm) fractions, but low weathering rates in coarser (<63μm) sizes in the Cagayan River. High flow events are associated with highly turbid water (Figure 6-1d,e), and although high transport rates and sediment yields are estimated in the upper catchment (2600 $m^3.km^2.yr^{-1}$ in the Magat Dam; JICA-DPWH 2002), the lower reaches are considered to be in equilibrium with only 25% of material in the distal reach moving as bedload and suspended and wash loads being exported to the ocean (JICA-DPWH 2002).

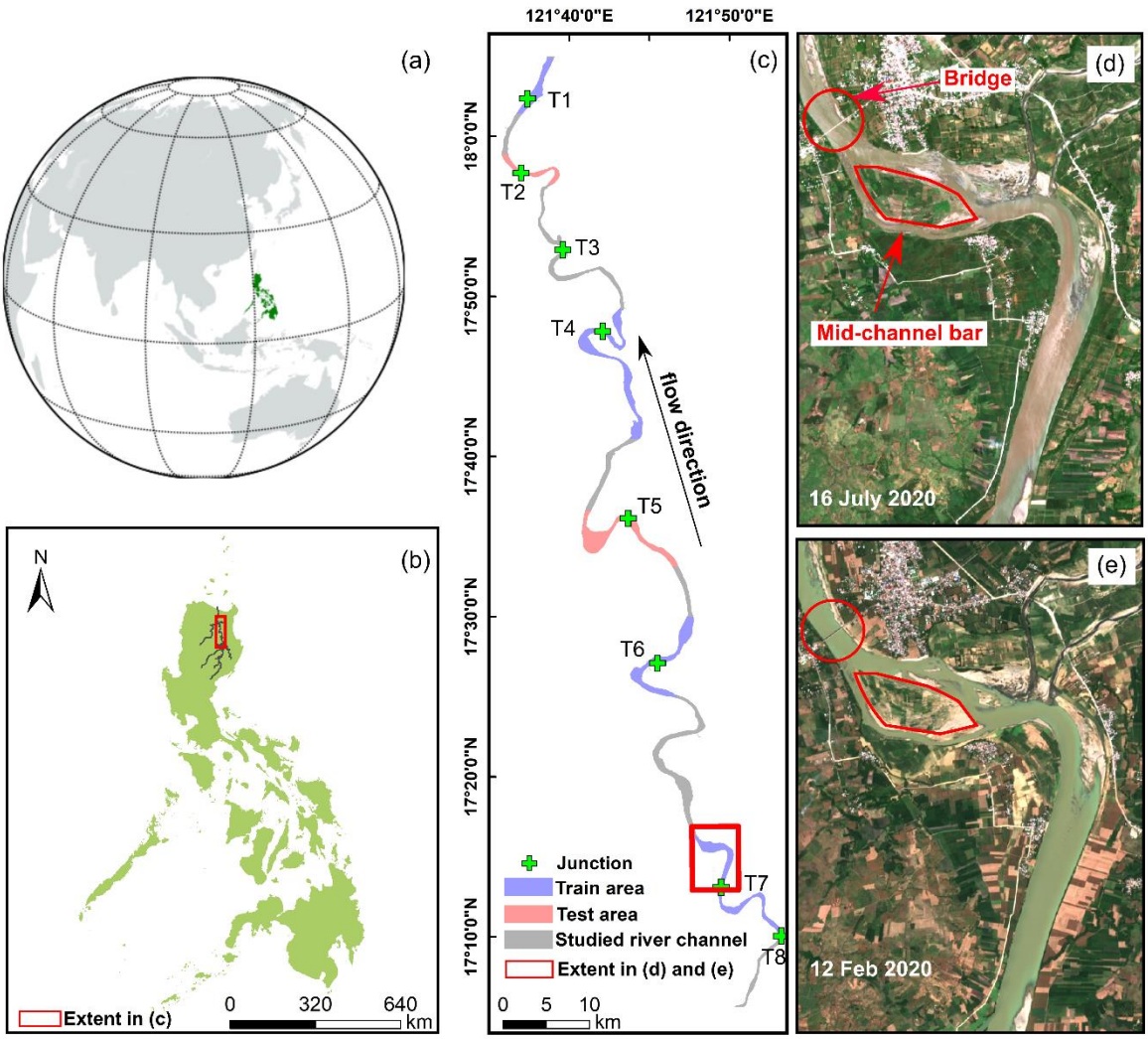

Figure 6-1. Cagayan River study area: (a) Global location of the Philippines. (b) The Cagayan River network on Luzon Island, the Philippines. (c) Study segment of the Cagayan River showing the location of remote sensing landform classification training and test areas, where T1-T8 are major tributaries. Reaches in the wet (d) and dry (e) seasons; (d) and (e) are true colour images from Sentinel-2 acquisitions.

6.3. Data and Methods

6.3.1. Tributary rivers and sub-catchments

The river network of the Cagayan catchment (Figure 6-1b) was extracted using the Hydrology Toolbox in ArcMap 10.8, using IfSAR DEM (5 km) data (Grafil and Castro 2014). This dataset was then used to define junction points along the lowland Cagayan River (Figure 6-1c). The Hydrology Toolbox required the positioning of pour points; user-supplied points to mark the cells of highest flow accumulation (Magesh et al. 2013). We firstly chose a place very slightly upstream to the junction point which is between mainstem water channel and tributary water

channel, and then set the pour point. When manually setting the pour point at a distal tributary river, the area that drains to the distal tributary river can be derived (A_T). Similarly, setting the pour point at the mainstem, immediately upstream of the junction between the mainstem and the tributary river, provides the mainstem sub-catchment area accumulating to the pour point (A_M). At each junction, we marked pour points respectively for the distal tributary river and the mainstem. The ratio between these areas, A_R, is used to calculate the relative size of the tributary catchment where it joins the mainstem. Benda et al. (2004) found that the ratio of tributary basin area to mainstem basin area was a good predictor of tributary impacts for both humid and semi-humid regions. The area ratio A_R is calculated as:

$$A_R = \frac{A_T}{A_M} \qquad (6-1)$$

6.3.2. Precipitation

Although a gauging station network in the Philippines is being established (Lagmay et al. 2017), discharge records are typically short in temporal duration, characterised by data gaps and there is considerable rating curve uncertainty. To overcome this data challenge, we used peak precipitation data to compensate for a lack of bankfull water discharge data, since precipitation typically has a very close relationship to water discharge (Friedman et al. 2021; Setti et al. 2020; Zhao et al. 2017). Due to the dearth of high temporal and spatial ground-based precipitation measurements (Veloria et al. 2021), we used satellite-derived precipitation data from the Integrated Multi-satellite Retrievals for Global Precipitation Measurement (GPM IMERG) mission (Huffman et al. 2019). These data are at a spatial resolution of 0.1° and a temporal resolution of 30 minutes. Veloria et al. (2021) reported that precipitation data measured by GPM IMERG have a good correlation with ground rainfall measurements in the Philippines. Therefore, in this study, we calculated catchment-averaged accumulated precipitation totals (mm) every 10 days for the duration of the landform classification time period: 20 January 2018 to 10 January 2022. We computed peak accumulated precipitation (per 10 days) for years 2018, 2019, 2020 and 2021 and then averaged them to obtain a four-year peak accumulated precipitation map (Figure 6-2a). The precipitation ratio P_R between tributaries and the mainstem was calculated as:

$$P_R = \frac{P_T}{P_M} \qquad (6-2)$$

where P_T is the average of the annual maximum accumulated 10-day precipitation in the tributary catchment, and P_M is for the main catchment upstream of the confluence.

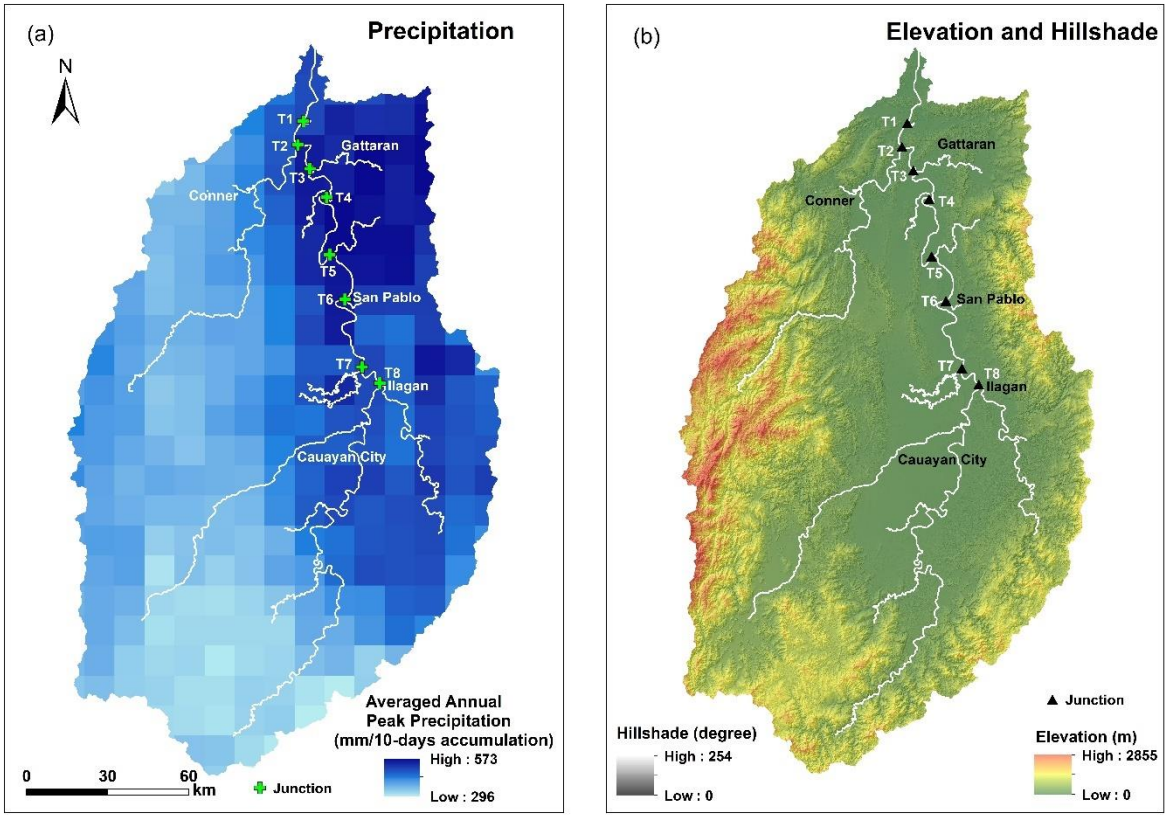

Figure 6-2. (a) Averaged annual peak accumulated precipitation (10 days) for 2018-2021 in the Cagayan catchment, based on analysis of Integrated Multi-satellite Retrievals for Global Precipitation Measurement (GPM IMERG) data. (b) Digital Elevation Model of the Cagayan catchment, from 5 m resolution IfSAR data (Grafil and Castro 2014). White lines show the mainstem and tributary network. T refers to tributary.

6.3.3. Elevation and Slope

Longitudinal gradient can be used along with a discharge estimate as a proxy for sediment transport capacity (Ferguson and Hoey 2008). Mean average slope was calculated from the total elevation change over a distance *x* upstream of the confluence along both the tributary and main channels as in Eq. (6-3):

$$S = \frac{E_D - E_o}{x} \quad (6-3)$$

Where E_D means the elevation at x distance while E_o means the elevation at the confluence. As above, the slope ratios S_R are defined by tributary slope (S_T) and mainstem slope (S_M):

$$S_R = \frac{S_T}{S_M} \quad (6-4)$$

where the distance *x* was taken as 5 km for both mainstem and tributary channels to avoid further confluences along the tributary channels. No abrupt gradient changes were observed on the tributaries or mainstems within 5 km of any of the confluences.

6.3.4. Stream Power ratio

Ratios of tributary to mainstem discharge (Q_R), bed load flux (F_R) and bed load grain size (D_R) control the mainstem responses to tributaries (Ferguson and Hoey 2008). Total precipitation (P) indicates water supply estimated at the pour point of the catchment (Pinardi et al. 2022). In some cases, drainage area is used as a surrogate for sediment and water discharge (Benda et al. 2004). As there is a paucity of measured discharge, sediment bedload flux and bedload grainsize from field observations, we used $P_R \times A_R$ as a proxy for Q_R. The flux ratio F_R depends on stream power and sediment size. In the absence of grainsize data for each site, we propose a stream power ratio (SP_R) to indicate the relative sediment transporting capacity of the tributary and the mainstem:

$$SP_R \propto (A_R \times P_R \times S_R) \quad (6-5)$$

We hypothesize that a high SP_R tends to deliver a greater amount of typically coarser sediment to the mainstem than a low SP_R which deliver less and typically finer sediment. Thus, the SP_R calculation provides a metric to infer bedload grainsize around the confluence and patterns of downstream aggradation.

6.3.5. Support Vector Machine (SVM) landform classification

An automated multi-temporal river landform classification workflow, previously applied to the Bislak, Abra and Laoag Rivers in North-West Luzon (Li et al. 2022) was adopted here to classify the active channel into water, unvegetated bars and vegetated bars. The Bislak, Abra and Laoag Rivers share similar hydro-geomorphological characteristics to the Cagayan River and its tributaries. In summary, the workflow first involved processing Sentinel-2 Level 1C imagery to Level 2A imagery. Subsequently, six 20 m Sentinel-2 bands were downscaled to 10 m resolution using area-to-point regression kriging (Wang et al. 2016). Five environmental indices were then calculated using ten bands (six downscaled 10 m bands; four original 10 m bands). These indices were: normalised difference vegetation index (NDVI; Carlson and Ripley 1997); normalised difference moisture index (NDMI; Wilson and Sader 2022); normalised difference water index (NDWI; Gao 1996); modified enhanced vegetation index 1 (MEVI1; Huete et al. 2002); and modified enhanced vegetation index 2 (MEVI2; Jiang et al. 2008). The ten 10 m bands and five environmental indices were then prepared as machine learning features for the landform classification. The active channel extent was generated using the method of Boothroyd et al. (2021), using Google Earth Engine. We automatically closed gaps in the annual active channel area caused by vegetated islands using standard image processing techniques. For vegetated bars connected to the active channel, we manually edited the active channel area to include the vegetated bars. Within the active channel, we defined training and testing areas for building the SVM machine learning model (Figure 6-1c). Large Scale Mean Shift segmentation (Orfeo Toolbox version 6.6.1) and Support Vector Machine (SVM) classification were combined to achieve Geographic Object Based Image Analysis (GEOBIA). The SVM classification was run with a regularisation parameter of 1.0 and a scale radial basis function kernel, completed using scikit-learn in Python 3.7.

In the study area, we analysed Sentinel-2 acquisitions for twenty dates from 2018 to 2021 (Table 6-1). The acquisition dates of each year covered different seasons and were evenly spaced, with the exception of the December to February period when clouds obscure the study area. Imagery with cloud coverage or shadowing over fluvial areas of interest were rejected due to their detrimental effect on landform classification accuracy when applying GEOBIA (Li et al., 2022). Data from five dates in 2019 were chosen to build the machine learning model to classify three landforms: water; unvegetated bars; and vegetated bars. The training dataset had 31,446 objects. The test dataset had 14,417 objects. The ratio of training to test data was 2:1.

The training and testing data were manually digitised through supervised remote sensing imagery interpretation. The classification performance was assessed by overall cross validation, overall accuracy, precision, recall and F1 Score. In addition to the overall classification assessment, we also analysed the water accuracy, unvegetated bar accuracy and vegetated bar accuracy. When an accurate machine learning model was developed, the landform classifications were applied to the years 2018, 2020 and 2021.

Table 6-1. Sentinel-2 acquisition dates for the Cagayan River from 2018 to 2021. Dates are in the format of DD/MM.

Year	2018	2019	2020	2021
Dates	19/03	19/03	12/02	28/03
	18/05	03/05	13/03	17/05
	02/07	07/07	12/05	01/07
	05/09	20/09	16/07	14/09
	09/11	04/11	09/09	
			23/11	

From the classified images, some areas such as main channels or stable islands with mature vegetation are within the same landform type at all dates, whereas other parts of the river show frequent changes. These differences in landform consistency were described using Simpson's diversity index (*SDI*; Simpson 1949), defined as:

$$SDI = 1 - \frac{\sum n(n-1)}{N(N-1)} \qquad (6-6)$$

where n is the number of a specific type of landform over the record period and N is the total number of all landforms. SDI lies between 0-1, with larger values denoting more diverse (unstable) record and lower values indicating relatively more consistent (stable) records.

Bankfull widths were measured using the water frequency maps from 2018 to 2021. Measured widths include all areas of the channel that are occupied by water on at least 10% of the images. This threshold excludes two dates when imagery shows overbank flood events. Following Dingle et al. (2019), bankfull width was measured 100 m upstream and downstream of the confluence.

6.4. Results

6.4.1. Tributary stream power

The lowland segment of the Cagayan River mainstem that is investigated here flows in an approximately northerly direction, ends at 28 km away from the sea mouth. Eight tributary rivers (numbered in Figure 6-1) and basins (Figure 6-3) were identified using the ArcGIS 10.8 Hydrology Tool and the 5 m spatial resolution IfSAR DEM. Table 6-2 shows the values of A_R, P_R, S_R and SP_R that were computed for each tributary junction.

Table 6-2. Ratios of tributary to mainstem area (A_R), precipitation (P_R), slope (S_R) and stream power (SP_R) for each tributary in the segment of the Cagayan River.

Tributary	A_R	P_R	S_R	SP_R
1	0.017	0.021	0.000	0.000
2	0.215	0.198	5.679	0.241
3	0.050	0.065	1.626	0.005
4	0.021	0.026	4.556	0.002
5	0.034	0.045	1.784	0.003
6	0.019	0.024	19.444	0.009
7	0.128	0.135	360.360	6.238
8	0.257	0.324	1.626	0.135

Figure 6-3 also shows the tributary impact indicators. The figures show the values relative to the largest value of each ratio for the eight tributaries; data are visualised in this way to assist comparison of the relative magnitude of each ratio. A_R and P_R have very similar spatial patterns, whereas S_R and SP_R exhibit greater variability. For all the ratios, T1 has the least impact of the eight tributaries. Some tributaries that have high values of A_R and P_R have lower values of S_R and SP_R. For example, T8 was recognised as the most important tributary based on the value of A_R and P_R but was the second least important tributary based on the value of S_R. T6 was the second least important tributary based on the A_R and P_R values but was recognised as the second most important tributary from its S_R value. T2 shows relatively high importance from values of A_R, P_R, S_R and SP_R. T7 was shown to be a tributary of moderate to high importance based on A_R and P_R but S_R increased its relative importance yielding a very high SP_R compared to the other seven tributaries. All indicators show T3, T4 and T5 have low to moderate impact on the mainstem. The results show that, even though A_R, P_R and S_R were all recommended as the indictors for analysing tributary impacts in previous studies, their individual application causes differences in the relative importance of each tributary. Thus, applying a synthesised indicator (SP_R) is a more integrative approach to understanding tributary impacts.

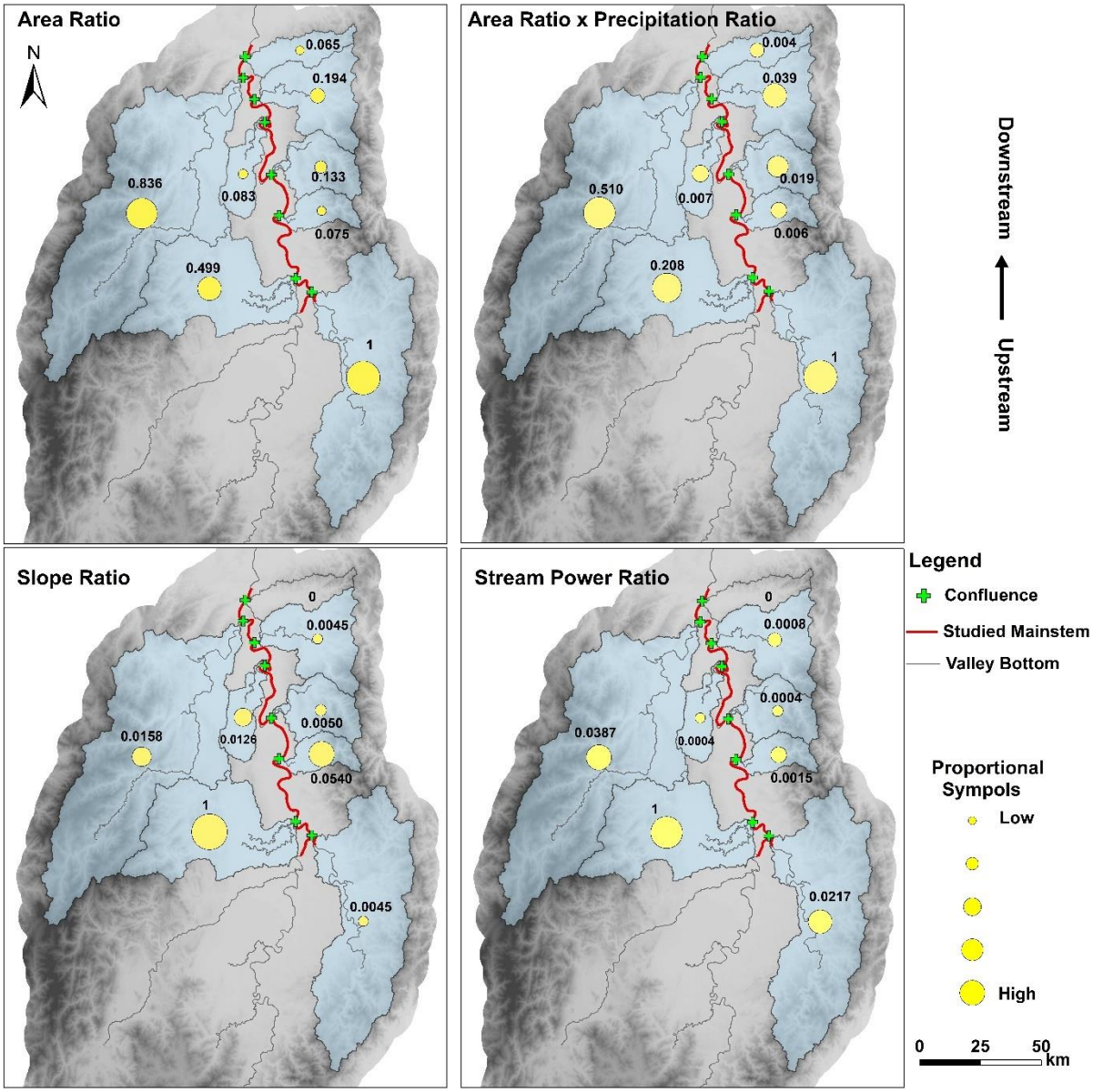

Figure 6-3. Ratios of tributary to mainstem area (A_R), area times precipitation ($A_R \times P_R$), slope (S_R) and stream power (SP_R) for each tributary in a segment of the Cagayan River. Ratios are shown as proportional symbols, normalised by the largest value among the eight ratios. T1 to T8 are in the direction from north to south.

6.4.2. River landform classification

For the 2019 test dataset, the overall cross validation accuracy for the identification of water, unvegetated bars and vegetated bars was 0.938 and the overall testing accuracy (OA) was 0.939. Precision, recall and F1 Score were 0.939, 0.939 and 0.938 respectively. Additionally, the water accuracy (WA) was 0.971, unvegetated bar accuracy (BA) was 0.915 and vegetated bar accuracy was 0.896. These assessments with high performance showed that the river

landform classification was reliable and suitable for application to data for the neighbouring years. To compare the landforms at different active channel width, we calculated the proportion of each landform along the studied river from 19 March 2018 to 14 September 2021 (Figure 6-4). We used the valley bottom line, obtained using the ArcGIS Hydrology Toolbox, to extract elevation from and plot variation in longitudinal gradient. To provide a longitudinal reference system to plot spatial changes in landforms, we used the centreline of the active channel.

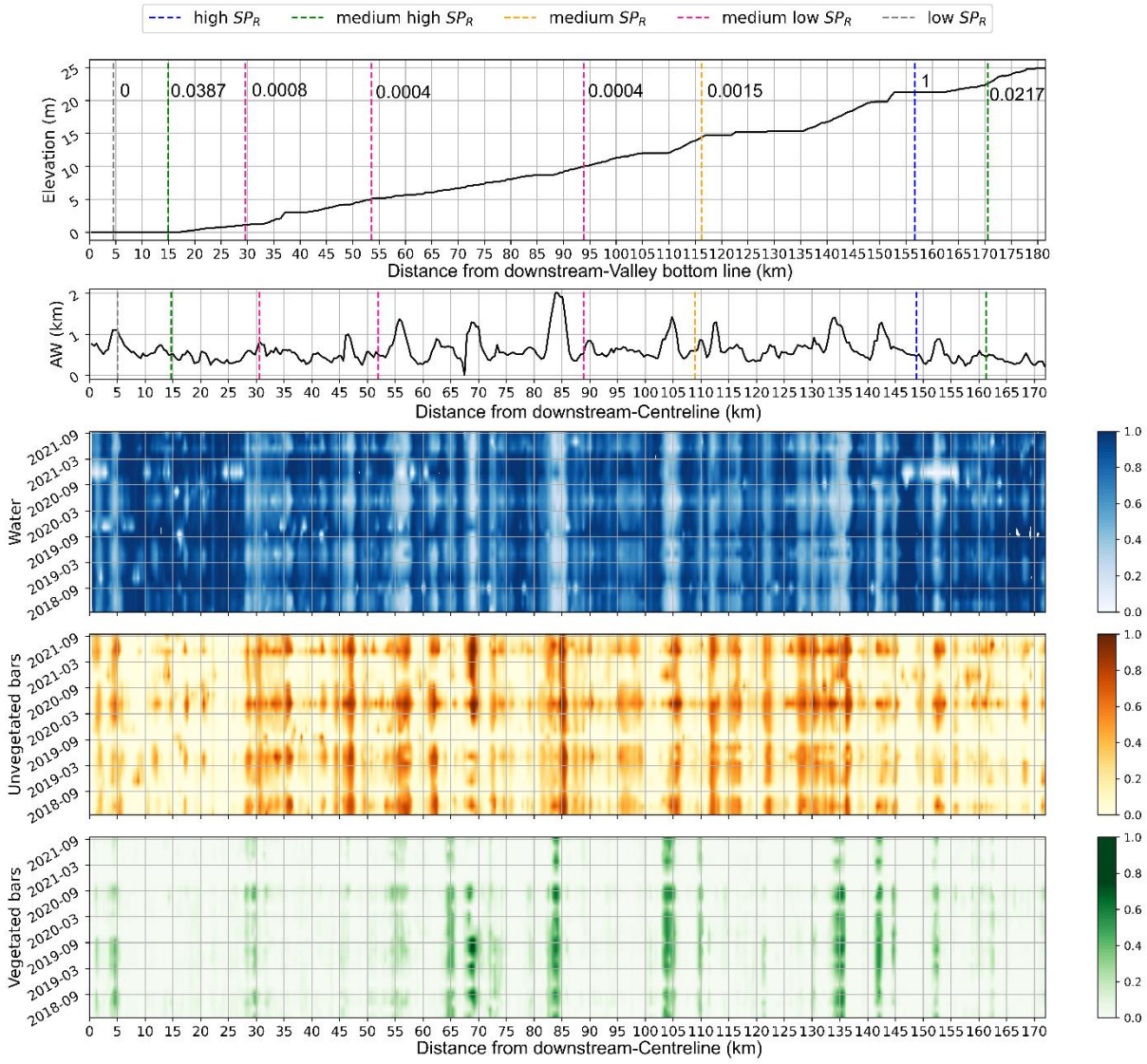

Figure 6-4. Longitudinal variation in elevation, active width and river landform proportion (water, unvegetated and vegetated bars) for a segment of the Cagayan River, the Philippines. Distance to downstream is measured from a point 28 km upstream of the sea. Landform proportions are shown from 19 March 2018 to 14 September 2021. Elevation is shown along a transect that corresponds to the longitudinal valley bottom. Active width and landform proportions are shown along a transect that corresponds to the centreline of the active channel. The valley bottom line is c.10 km longer than the channel centreline. Vertical dashed lines on

the figure indicate tributary locations. Relative SP_R values (0 to 1 scale, where 1 is the largest measured SP_R ratio) are noted on the elevation plot.

We observed that unvegetated bars showed strong seasonality along the whole segment of the Cagayan River. Water seasonality was found in reaches where the active channel width dynamically changed, corresponding to seasonal flow variation. Vegetation was not found to be as seasonally dynamic as unvegetated bars and water. However, in some reaches, vegetation proportion increased and then decreased for a short period of time during the years 2018 and 2021 (e.g., c. 30 km and 135 km). This may indicate a longer periodicity of vegetation change compared to the yearly seasonal changes shown for water and unnegated bars. However, higher temporal resolution data were not available and thus the periodicity of vegetation dynamics couldn't be further investigated. In addition to seasonality, a longitudinal spatial trend was also found. A lower water proportion and higher unvegetated bar proportions were characteristic of reaches from 30 to 152 km downstream (using the valley bottom line reference). Conversely, reaches with gentle gradients (0 to 30 km downstream; 152 to 181 km downstream) were characterised by a higher proportion of water and a lower proportion of unvegetated bars. The highest proportions of vegetated bars were mostly characteristic of wide, active channel reaches.

6.4.3. Landform Frequency

Figures 6-5a to 6-5c show frequency maps of water, unvegetated bars and vegetated bars in a reach of the Cagayan River, generated from twenty dates from 2018 to 2021. An example of a classification from a single date, 12 February 2020, is shown in Figure 6-5d. This classification shows areas of both unvegetated and vegetated bars were not as large in extent as shown by the historical analysis (Figures 6-5b and 6-5c), which show high frequencies of these landforms. However, water on 12 February 2020 covered most areas that are associated with high frequency water extent (Figure 6-5a). Figure 6-5b and 6-5c also presents four typical vegetated bars. Bar 1 was an in-channel migrating bar with vegetation growing at the front head of the bar. Bars 2, 3, 4 were point bars aligned with the edge of the active channel. Bars 1 and 2 both captured stable (high probability) vegetated area in the middle of the bar and unstable (less probability) vegetated area outwards. Bar 3 was regarded as a stable point vegetated bar with vegetation growing evenly across the bar. Bar 4 was a very young, vegetated bar with well-proportioned vegetation growing on it. The frequency maps of three landforms illustrated a temporal river history from remote sensing images, compensating the field work

in the remote regions and extending the study extent for a more comprehensive understanding of the river change.

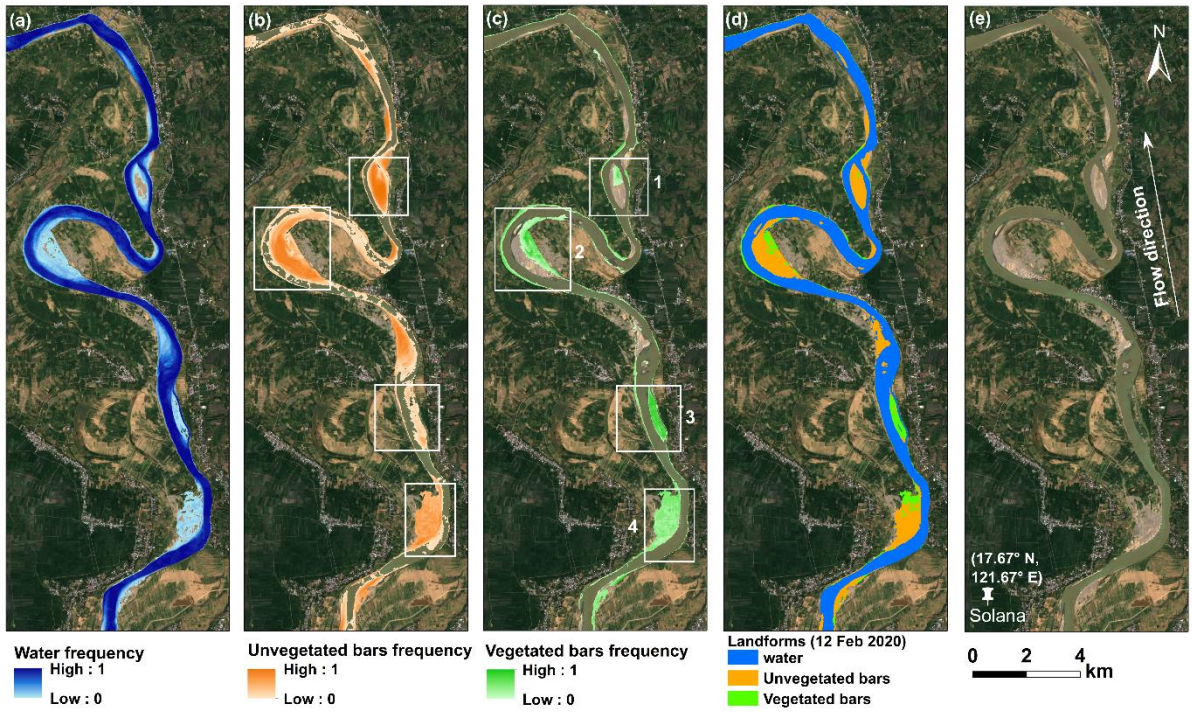

Figure 6-5. (a)-(c) Landform frequency of studied period; (d) landform classification on 12 February 2020; (e) True colour Sentinel-2 image on 12 February 2020. White rectangles represent typical vegetated bars.

In previous studies, the NDWI derived from near infrared and visible (green) reflectance band was used to classify the water extent and calculate river width (Andreadis et al. 2013). We considered here more features captured from satellite images to generate the water extent and therefore river width. Since the span of Sentinel-2 data is very short (less than ten years), permanent vegetation or bank cannot be defined and recognised. Alternatively, in this study, the water frequency extent is considered as a reference to measure the bankfull water width.

6.5. Analysis and discussion

6.5.1 Slope increase and bankfull width expansion

The impacts of water and sediment inputs from tributaries on mainstem geomorphology depends on the capacity of the combined flow to transport the total sediment delivered by the mainstream and the tributary. Hence, the relative water discharge, sediment flux and sediment

grainsize have been shown empirically (e.g., Rice and Church 1998; Rice 2017) and from modelling (Ferguson et al. 2006; Ferguson and Hoey 2008) to control riverbed slope, grainsize and, by implication, planform morphology in confluence regions. Where tributaries supply large volumes of relatively coarse material induce mainstem sediment storage, aggradation, upstream slope reduction and downstream slope increases (Rice and Church 1998; Rice 2017; Swanson and Meyer 2014). The downstream reach length over which the tributary influence remains significant depends on valley-scale geomorphology which may be autogenic in alluvial rivers or controlled by variations in lithology, tectonics and/or catchment geometry (Hassan et al. 2005; Menting et al. 2015; Rice and Church 1998). In lowland reaches with sand or finer sediment, material input from tributaries can be dispersed over long reaches (Hungr et al. 1984). Less frequently studied are cases where the sediment transport capacity downstream of the tributary input exceeds the sediment supply hence causing channel incision, lateral instability and/or channel widening (Soar et al. 2017).

Table 6-3. Slope and bankfull width changes after tributary inputs to the main Cagayan River (S_d: 5 km downstream averaged slope; S_u: 5 km upstream averaged slope; W_d: 100 m downstream width; W_u: 100 m upstream width; $Q_R = A_R \times P_R$).

Confluence	A_R	Q_R	S_R	SP_R	Width adjustment $(W_d\text{-}W_u)/W_u$	Slope adjustment $(S_d\text{-}S_u)$
C1	0.017	0.000343	0.00	0.000	-0.26	0.000
C2	0.215	0.0425	5.68	0.241	0.19	-0.060
C3	0.050	0.00324	1.63	0.005	-0.11	-0.043
C4	0.021	0.000548	4.56	0.002	0.14	0.091
C5	0.034	0.00153	1.78	0.003	0.09	0.013
C6	0.019	0.000466	19.4	0.009	0.01	0.312
C7	0.128	0.0173	360	6.240	0.07	0.197
C8	0.257	0.0832	1.63	0.135	0.48	-0.123

Tributaries entering at C4, C5, C6 and C7 produce steeper downstream mainstem slopes, whereas C1 has a very low gradient downstream reach (Figure 6-4) with very low mainstem power. In most cases, increases in relative bankfull width coincide with downstream steepening (C4, C5, C6, C7). Bankfull width decreases at C3, where slope also decreases downstream of the confluence, and C1 where there is no measurable difference in channel slope. In the remaining cases (C2, C8), slope decreases, and width increases are observed. T4, T5, T6 are all measured as low stream power supplying to the mainstem. In this case, slopes after C4, C5, C6 increased significantly. These may indicate T4, T5, T6 taking coarser sediments which deposited immediately, inducing channel aggradation near the confluence. Additionally, slope

increased dramatically right after C6 and C7, where T7 measured as high stream power ratio to mainstem. This can be explained either by relative high ability of sediment transport causing by high stream power ratio or high volume of coarse sediment supplies from the tributary river.

To understand how the tributary impacts mainstem bankfull width, we calculated predicted downstream width (Dingle et al. 2019) by Eq. (6-7):

$$W_u{}^2 + W_t{}^2 = W_d{}^2 \qquad (6-7)$$

Where W_u is upstream width, W_t is tributary width and W_d is downstream width. The predicted downstream width and observed downstream width were plotted in Figure 6-6a. Only tributary T1 has a predicted: observed width ratio less than 0.5 (or greater than 2.0), with the observed downstream width being much lower than that predicted. T1 joins at the anabranch on the right edge of an in-channel bar (Figure 6-8) with a very low stream power contribution. Therefore, downstream width was not impacted by T1 joining the mainstem. T3, T4 and T5 all have a relatively low stream power ratio, but downstream widening was still close to the predicted width. The widths of T2 to T7 were not observed to deviate a lot from predicted downstream width, even if T7 captured a very high stream power ratio.

Logarithmic values of the stream power ratio were also plotted against ratios of downstream width to upstream width (Figure 6-6b). The stream power calculation in this study was unable to account for sediment grainsize, therefore an explanation for the points that deviate from the line of agreement in Figure 6-6a may have been caused by variations in sediment transport capacity due, in part, to sediment grainsize. In Figure 6a, T4, T5 and T8 are located below the 1:1 line (red line), indicating that sediment grainsizes from tributaries were coarser than that from the mainstem at confluences. Similarly, T1, T2 and T3, which are located above the 1:1 line, may indicate finer sediment input to the mainstem. From field observations (JICA-DPWH 2002) supplemented by Google Earth Street View pictures taken from bridges across the Cagayan River (Table 6-4), bank sediments upstream of C8 tend to be a mixture of clay and silt, which were widely vegetated, whilst sediments exposed on the T8 riverbed were sandy and less vegetated. Street View pictures also suggest sediments from T7 were siltier than the mainstem upstream of C7, with dense vegetation. Street View for T6 was captured too far from the confluence to offer useful imagery. Table 6-3 indicated that SP_R at C6 was relatively low, around which T6 may not have the enough energy to transport the coarse sediments observed

in Table 6-4 to the mainstem. Fine sediments from T7 and coarse sediments from T8 can also be implied in Figure 6b, where bankfull width expansion (increasing value of downstream width/upstream width) was expected to be impacted by stream power. However, this relationship can be controlled by sediment size between tributaries and mainstem as well. Coarser sediments from tributaries with high SP_R may lead to deposition and increased bankfull width, whilst finer sediments from tributaries with very high SP_R may reduce the bankfull width. However, from the studied tributaries, we still suggest that SP_R has a positive linear relationship with downstream bankfull width expansion, especially when the sediment size difference between the tributary and mainstem is not obvious whilst SP_R is high.

Table 6-4. Sediment evaluations from Google Street View pictures on the nearby bridges.

Confluence	Upstream	Tributary	Downstream	Tributary to Upstream
C1	-	-	-	-
C2	-	-	-	-
C3	-	Silt-clay		-
C4	-	-	-	-
C5	-	Sand	Sand	-
C6	Clay	Sandy gravel	Sand	Coarser
C7	Sandy clay	Silt	-	Finer
C8	Clay-Silt	Sand	-	Coarser

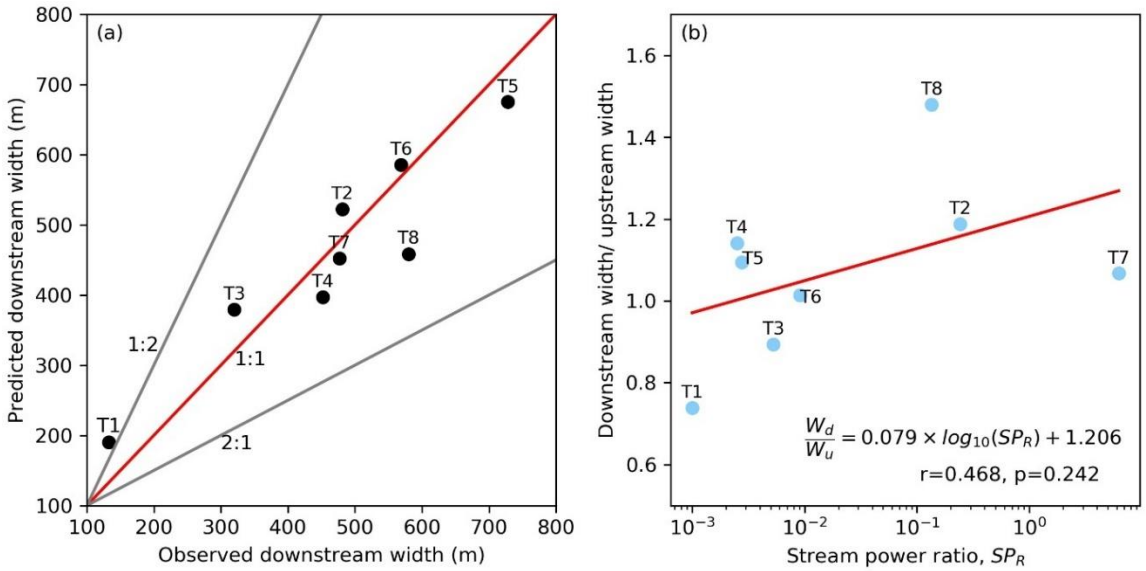

Figure 6-6. (a) Relationship between predicted (from Eq. 6-7) and observed bankfull river width. (b) Width changes downstream of tributaries as a function of stream power ratio (SPR).

6.5.2. Landform diversity at confluences

Tributaries abruptly introduce sediment and organic material in the vicinity of confluences and trigger a variety of morphological responses, including increases in channel width, pool depth and occurrence of bars (Benda et al. 2004). We calculated the coefficient of variations (COVs) of the three classified river landforms, using temporal landform area to trace landform diversity from 2018 to 2021 (Figure 6-7). COVs of water and unvegetated bars have an anti-phase fluctuation in most reaches of the river (Figure 6-7), whilst vegetated bars were not observed to have a consistent in-phase or anti-phase fluctuation. This suggests water and unvegetated bars are the dominant landforms in the active channel and their dynamism is not affected by tributary inputs. However, vegetated bars are more sensitive to these abrupt changes. We observed that T2, T6 and T7, surrounding the 1:1 line (Figure 6-6a), showed temporal instability (vegetation growth and decay) in the vicinity of confluences, while vegetated bars were relatively stable below C1, C3, C4, C5 and C8 (Figure 6-7).

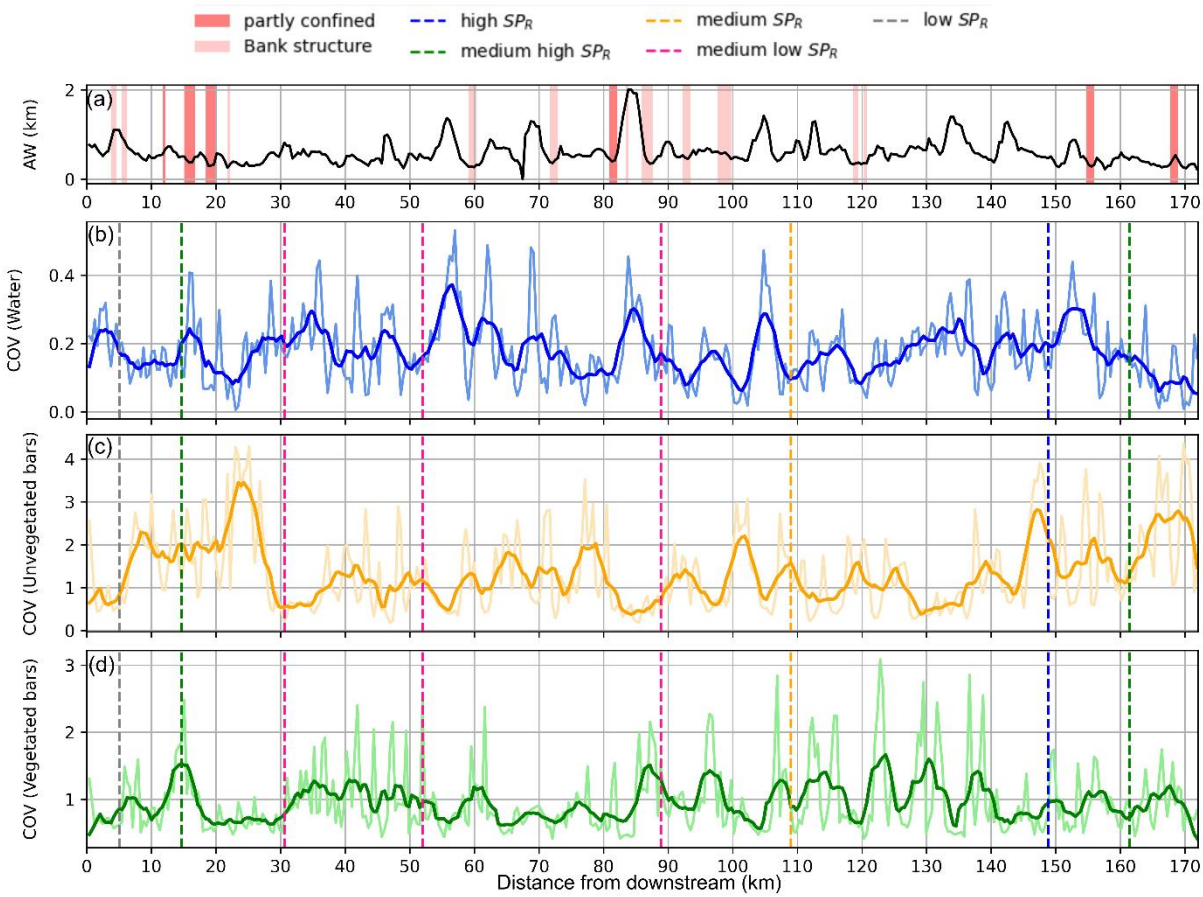

Figure 6-7. Longitudinal trends in active width and confinement, with positions of anthropogenic bank structures. (b-d) Longitudinal trends in coefficient of variation (COV) for water area, unvegetated bar area and vegetated bar area.

Confluences have been identified as hotspots for ecological and topographic diversity (Benda et al. 2004; Rice 2017). We employed Simpson's diversity index (*SDI*) (Simpson 1949) to represent landform diversity at 10 m pixel resolution (Figure 6-8). Migrating bars (Crosato and Mosselman 2020) are observed downstream of confluences C3, C4 and C5. In these locations, the outer edges of the bars were characterised by high diversity (Figure 8, in red circle). T3, T4 and T5 have the lowest SP_R values, except for T1 ($SP_R = 0$). We suggest that low SP_R leads to only limited activation of downstream bars, concentrated around bar margins. A parallel example is the migrating bar downstream from confluence C6. With medium SP_R, the three landform types changed very frequently at this downstream migrating bar (red circle, Figure 6-8). Tributaries that were characterised by high SP_R (T2, T7 and T8) corresponded with stable landforms downstream of their confluences with the mainstem. Figure 8 also shows that bridges are associated with high landform diversity in the vicinity of the structures, corroborating a finding by Boothroyd et al. (2021) from analysis of bridge structures in the Philippines over a longer temporal duration. As the studied segment of the Cagayan contains extensive stable reaches, the roles of locally unstable reaches, those disturbed by bridges, and others adjacent to confluences are important sources of habitat and geomorphic diversity.

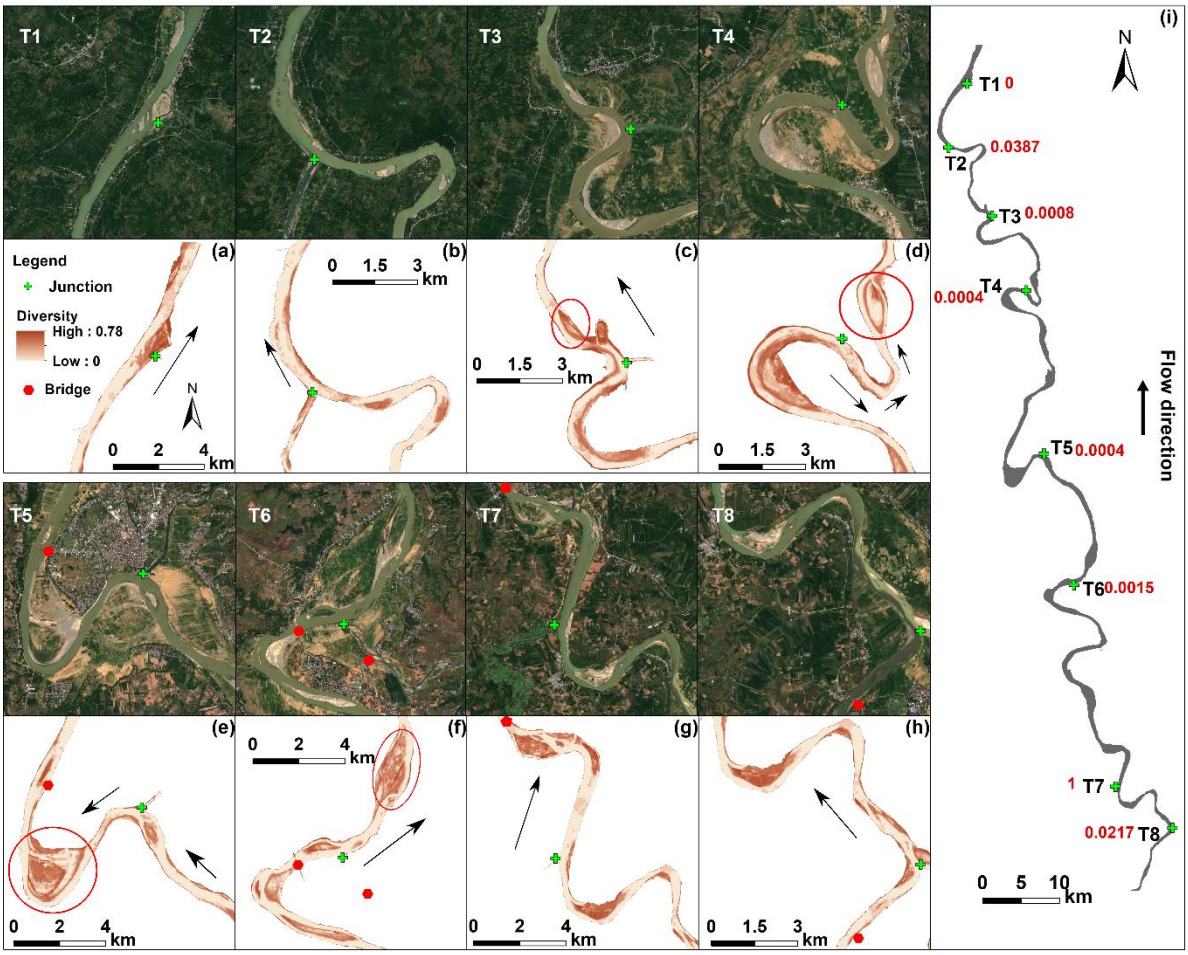

Figure 6-8. River landform diversity measured using Simpson's Diversity Index (*SDI*) at river confluences along a segment of the Cagayan River. *SDI* is in the range 0 (the same landform type present on all images) to 1 (each landform type is present in 33.3% of the available images). Darker shading shows where landform types vary most between images during the four-year study period. Both forced bars (e.g., point bars on (d), (e), (g) and (h)) and free bars (bar complexes on (a), (d), (f) and (g)) show high diversity due to unvegetated sediment deposits being colonized by vegetation during dry seasons.

6.6. Conclusions

Fluvial landforms in the active channel of the lowland Cagayan River were classified for a four-year period, 2018 to 2021. Throughout the study area, strong seasonality was found in the extent of water and unvegetated bars, whilst some sub-reaches showed seasonality in vegetated bar extent. We established a parameter SP_R to represent the stream power ratio of tributaries to the mainstem, from the product of ratios of catchment area, basin averaged accumulated precipitation and slope immediately upstream the confluence. Results showed that tributary inflows with a high SP_R cause an increase to the longitudinal slope downstream. Downstream bankfull width changes were less clearly associated with stream power and may be related to

sediment size which affects sediment transport rates. Tributary inflows can trigger downstream morphological change. In addition to river morphological responses to tributary inflows, we found SP_R can also be related to landform diversity downstream from confluences. Moderate to low SP_R was associated with the development of migrating bars downstream, whilst high SP_R was associated with constant channel diversity downstream. Thus, SP_R may be an important indicator for analysing and predicting tributary river impacts in the regions without sufficient water discharge and sediment data to use these variables for analyse the response of mainstems to tributary inputs. Since most previous investigations on mainstem response to tributary inputs have been conducted in upland temperate regions, this investigation diversifies the global database in considering a lowland, tropical river where rates of seasonal vegetation growth are very high. Further investigations of tributaries in tropical settings are encouraged.

Chapter 7 - Discussion

The overall aim of the thesis is to develop an efficient workflow to classify the inter- and intra-annual river landforms in the river active channel. With river landform datasets classified accurately from remote sensing imagery, the seasonality and landform diversity can be analysed quantitatively together with channel settings. In this thesis, I studied four rivers located in north Luzon, the Philippines. They are the Bislak, Laoag, Abra Rivers in Northwest Luzon and the Cagayan River in Northeast Luzon. The Bislak, Laoag and Abra Rivers lie in the same climate zone, but the Cagayan is in a different climate zone (Figure 7-1) (Wichmann 1904), which leads to variations in precipitation, vegetation species, and hydrology between the four rivers. The rivers also lie in different geological and tectonic regimes, with the Northwest catchments being relatively small (586-4,893 km^2) and showing strong tectonic control, whereas the Cagayan is a large (27,684 km^2) inter-montane catchment. Dynamic fluvial processes controlled by hydraulics, vegetation and sediments increase control of the river landforms and their patterns of change. The accuracy and ease of recognising these landforms from Earth observation data is also dependent on these processes and rates of landform change. The variations (i.e., in climate, precipitation, sediment, channel settings) in the Bislak, Laoag, Abra and Cagayan Rivers provide good cases for analysing and comparing factors impacting river landform dynamics.

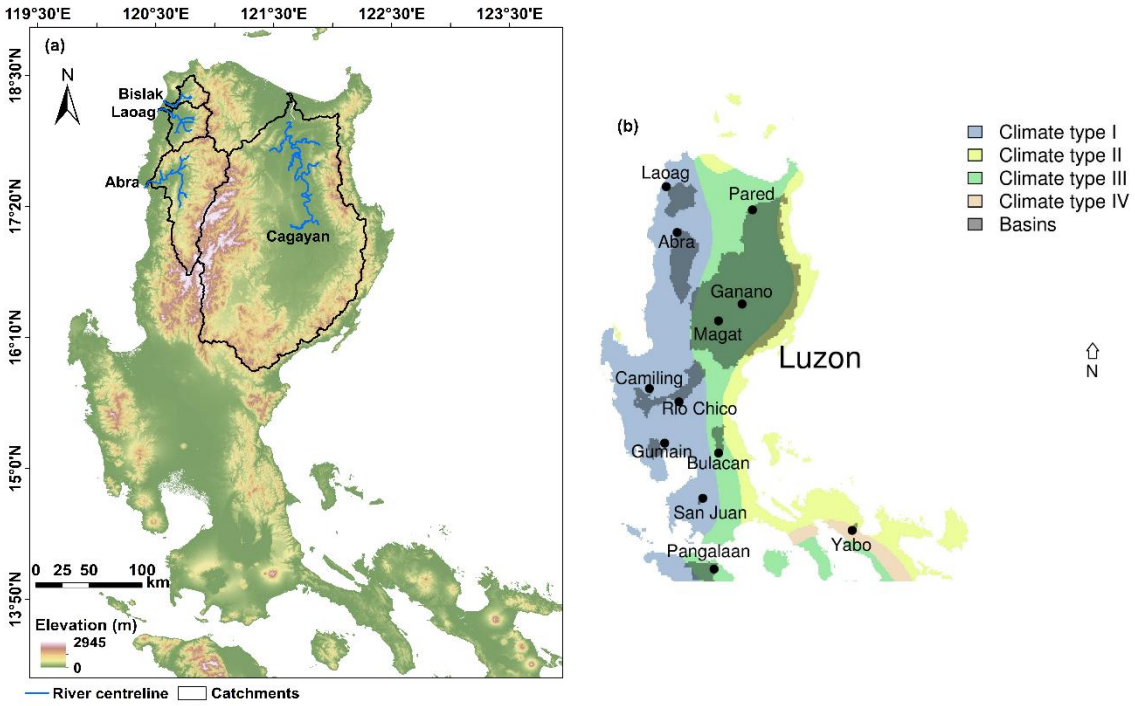

Figure 7-1. (a) Locations of Bislak, Laoag, Abra and Cagayan River catchments in north Luzon. (b) Climate types in North Luzon (source: Tolentino et al. 2016).

Both climate zones in which these rivers lie show strong seasonality in precipitation. In previous chapters, seasonality of river landforms (vegetated and unvegetated bars) was found in all four rivers. However, relationships between the landform extent and active channel width show differences between the dry and wet seasons. In addition to seasonality, spatial-temporal analysis of the river landforms was used to examine landform dynamics over four (for the Cagayan River) or five (for the Bislak, Laoag and Abra Rivers) years. Chapters 5 and 6 presented a variety of spatial-temporal analysis methods. In this chapter, these methods are discussed and compared, and their implications for river dynamics are considered.

There are four sections in this chapter: river landform classification strategy, seasonality of river landforms in North Luzon, spatial-temporal analysis application and perspectives for future work.

7.1. River landform classification strategy

In Chapter 4, the machine learning model established on data from the Bislak River was shown to apply to three rivers (Bislak, Laoag and Abra Rivers) in Northwest Luzon (characterised as

$Model_{NW}$). However, when $Model_{NW}$ was applied to the Cagayan River in Northeast Luzon, the classification performed poorly (Figure 7-2), so a new machine learning model $Model_{NE}$ was designed for classifying river landforms in the Cagayan River (Figure 6-1, Chapter 6). However, the classification using $Model_{NW}$ did perform relatively well for the Cagayan (Figure 7-2a and 7-2c) during the dry season. In this case, model performance differences might be caused by either the model itself or training data used for building models. Table 7-1 lists several key aspects for building both $Model_{NW}$ and $Model_{NE}$. All the models used in this project selected 15 features (four bands at 10 m resolution from Sentinel-2 acquisitions, six bands at 10 m resolution from downscaled Sentinel-2 acquisitions and five environmental indices as presented in Table 4-2) and the feature types of all models were kept the same. Similarly, the parameters used for segmenting the image objects were not changed when building different models. Consequently, in this case, feature selection and object segmentation procedures cannot answer the reason of difference between two classification performances. In Chapter 4, it was found that, data from multiple dates can help improve model classification performance, and it is unlikely to cause classification accuracies under 0.5. Meanwhile, data from neighbouring years were believed to be transferable when undertaking machine learning classification (Chapter 4). Therefore, factors (Year and Month) in Table 7-1 were not considered as dominant reasons for poor classification. To investigate whether more training samples would contribute to high classification performance, $Model_{NW}$ was firstly applied to an upland segment of the Bislak River (Figure 4-6, white extent) on 1 January 2018. For this area, the overall accuracy was 0.842, water was 0.769, unvegetated bar was 0.899 and vegetated bar was 0.810. Subsequently, $Model_{NE}$ was applied to this segment, and the classification remained very poor. The overall accuracy was 0.247, water was 0.228, unvegetated bar was 0.074, and vegetated bar was 0.59. These results imply that training data size cannot explain the difference between the two models. Additionally, these two models both used a support vector machine (SVM) classifier to classify the river landforms. It has been shown that SVM was a reliable classifier in all four studied rivers (Chapter 4, Chapter 5 and Chapter 6).

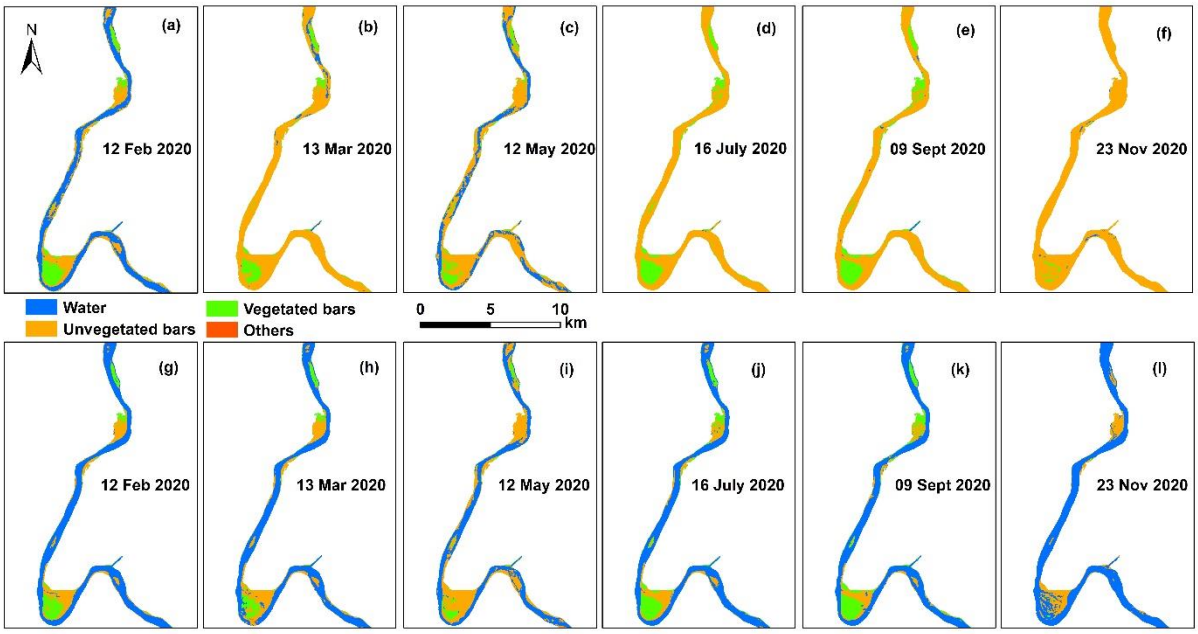

Figure 7-2. Landform classification maps in the Cagayan River using $Model_{NW}$ and $Model_{NE}$. (a)-(f) were derived from $Model_{NW}$ and (g)-(l) were derived from $Model_{NE}$.

Table 7-1. Comparisons between machine learning models used in three rivers of Northwest Luzon and the Cagayan River.

Factors	**$Model_{NW}$**	**$Model_{NE}$**	**Note**
Feature selection	15 features	15 features	same
Object segmentation	3 parameters	3 parameters	same
Year	2018	2019	-
Month	Jan, Mar, May, July, Sept, Nov	Mar, May, July, Sept, Nov	-
Acquisition date	6 dates	5 dates	Not same
Training samples	7,458 objects	31,446 objects	Not same
Machine learning	SVM	SVM	same

There may be several reasons causing land reflectance differences in spectral bands within the rivers: water discharge; sediment transport; vegetation density/species, etc. Whilst these factors can be controlled by climate, ENSO activities, drainage networks (e.g., tributary inputs) and the scale of the river (Bijeesh and Narasimhamurthy 2020; Li, Dang, et al. 2022; Nelson, Cheruvelil, and Soranno 2006; Yu et al. 2013). Table 7-2 illustrates nine types of Earth surface observations and measurements in the Bislak, Laoag, Abra and Cagayan Rivers. In Table 7-2, landform proportions along each river were averaged (spatial data series at distance) and calculated mean value of dates over year 2018-2020 (temporal data series at date). Therefore,

the averaged mean landform proportion over the three years is a spatial-temporal index. In Figure 7-1, note that the Bislak, Laoag and Abra Rivers are in the same climate zone (type I), while the Cagayan River is in climate type III. Although the Cagayan River catchment is much larger than the Bislak, Laoag and Abra River catchments, the mean accumulated precipitation over three years in the four river catchments (Table 7-2) were similar (7242-8405 mm). As catchment area is greater for the Cagayan, the total precipitation in the Cagayan catchment is much higher than that in the three rivers of the Northwest Luzon. Therefore, the Cagayan mainstem would have higher water supply, which leads to the highest averaged proportion of water being found in the Cagayan River (Table 7-2). Meanwhile, the active channel width in the Cagayan is only 0.604 km on average, which is merely slightly wider than the Laoag River (average width 0.581 km) and much lower than the Abra River (2.626 km). Figure 7-2 shows that $Model_{NW}$ only performed well on 12 February, and in most cases poorly identified water extent but produced relatively good classification for unvegetated bars and vegetated bars.

The above results may indicate that water reflectance in the Cagayan River is different from the Bislak, Laoag and Abra Rivers. From the water frequency maps of the four rivers, braided channel reaches were identified and the percentages of the whole rivers that are braided were calculated relative to the river centrelines (Table 7-2). Braided rivers, characterised by multiple, unstable channel and ephemeral bars formed by intense bed-load transport, usually occur in environments associated with high flow energy, coarse sediment and limited development of riparian vegetation (Ashmore 2013). 54.8% of the studied length of the Abra River was characterised as braided, whilst braided reaches occupied 20.5% and 28.5% for the Bislak River and Laoag River, respectively. However, only 9.7% of the length of the Cagayan River was detected as braided. These findings suggest that, compared to the Bislak, Laoag and Abra Rivers, the Cagayan River is predominantly single thread and due to its lower gradient has lower flow energy and bed-load transport capacity. These factors lead to a stable planform morphology, which is also evident from the lower Simpson's diversity index (Table 7-2) in most reaches of the Cagayan. Reflectance of the water surface can also be influenced by water energy dissipation and sediment transport that can induce surface water waves at different scales (Zeng, Richardson, and King 2017). Additionally, regional climate variability may affect reflectance through impacting water chemistry, for example through Chlorophyll-a (Chl-a) concentration (Park, Park, and Kang 2022). Water reflectance could be impacted by these factors and also water depth, turbidity, coloured dissolved organic matter (CDOM) and others (Odermatt et al. 2012; Chen et al. 2014; Matsushita et al. 2015; Knudby, Ahmad, and Ilori

2016; Watanabe et al. 2016; Song et al. 2017; Zeng, Richardson, and King 2017). In the case of shallow waters in the more braided Northwest Luzon rivers, sediment particles or vegetation in the water or growing on the bottom substrate can also impact water reflectance (Mobley and Mobley 1994; Zeng, Richardson, and King 2017). Therefore, considering variabilities of climate and river morphology is essential when applying machine learning models to river landform classifications in different rivers.

Table 7-2. Earth surface observations and measurements in the Bislak, Laoag, Abra and Cagayan Rivers.

Earth surface observation	**Bislak**	**Laoag**	**Abra**	**Cagayan**
Climate type (Figure 7-1)	I	I	I	III
Mean accumulated precipitation (mm) of three years (2018-2020)	7795	8190	8405	7242
Catchment area (km^2)	586	1261	4893	27684
Averaged active channel width (km)	0.375	0.581	2.626	0.604
Averaged mean water proportion (0-1) over three years (2018-2020)	0.202	0.240	0.258	0.752
Averaged mean unvegetated bar proportion (0-1) over three years (2018-2020)	0.626	0.615	0.561	0.165
Averaged mean vegetated bar proportion (0-1) over three years (2018-2020)	0.162	0.140	0.153	0.065
Braided reach length percentage of the whole studied river segment	20.5%	28.5%	54.8%	9.7%
Averaged Simpson's diversity index (0-1) of studied periods (5 years for the Bislak, Laoag and Abra Rivers, and 4 years for the Cagayan River)	0.310	0.297	0.267	0.232

7.2. Seasonality in tropical river patterns of north Luzon

Chapter 5 illustrated correlations between active channel width (AW) and the three landforms' areas and proportions in the dry and wet seasons. Chapter 6 did not focus on the seasonality of relationships for the Cagayan River. This section presents the seasonality of results from the Cagayan River, and then compares this with results from the Bislak, Laoag and Abra Rivers. Considering the interplay of AW with landforms' areas, correlation coefficients were calculated between AW and the three landforms' areas (Figure 7-3b). In the Cagayan River, a strong correlation was found between AW and unvegetated bar area (0.84 in the dry season, 0.83 in the wet season). AW and vegetated bar area have a moderate to high correlation (0.69

in the dry season, 0.73 in the wet season), whilst AW and water area give a moderate to high correlation (0.74) in the wet season but a moderate correlation (0.51) in the dry season. In the Cagayan River, the areas of unvegetated and vegetated bars gave a higher correlation (0.61) in the wet season than the dry season (0.51). However, in the Bislak, Laoag and Abra Rivers, vegetated bar and unvegetated bar areas produce very low correlations in both seasons. In the Cagayan River, water area was always the dominant landform in the wet season, but was surpassed by vegetated bars, or unvegetated bars in some wider reaches, in the dry season (Figure 7-3a). The correlations between AW and landform proportions (Figure 7-4) show very significant negative correlation coefficients between water and unvegetated bar proportions in both dry and wet seasons. Moreover, this relationship is higher in the dry season than in the wet season, and it is coherent between all four rivers in this study. In Figure 7-3b, the AW of the Cagayan River remained substantially below 1 km, locally being between 1- 2 km. Where AW is under 1 km, water area and unvegetated bar area both show positive correlation to AW during either dry or wet season. Vegetated bar areas were extremely low compared to water and unvegetated areas (dot and histogram graph), and vegetated bar area increased mildly with AW getting wider when AW below 1 km. However, when the AW is above 1 km, the vegetated area increased dramatically. In previous studies, 'thresholds', above which certain patterns emerge, were identified as a function of bed sediment size, which can discriminate and predict bar patterns (or parallel channels) well (Henshaw et al. 2019; Kleinhans and van den Berg 2011). For instance, when the river is too narrow and deep with high stream power, the excess energy would be spent on channel enlargement (Kleinhans and van den Berg 2011). Channel widening can help bars development, for establishing a less uniform bed topography that enhances habitat heterogeneity (Crosato and Mosselman 2020). Bar formation is key to discriminate rivers from braiding to meandering. Using the case of the Cagayan River, the empirically derived threshold of AW-vegetation could probably reflect sediment motion, and then potentially indicate the onset of meandering with chute and scroll bars, and moderate braiding (Henshaw et al. 2019; Kleinhans and van den Berg 2011). In this case, where AW is above 1 km, the river pattern would be predicted to getting more stable with an onset of meandering. Additionally, in the Cagayan River, AW had a highly significant negative correlation with water proportion, while AW and water area show a moderate significant positive correlation. These results indicate that, although water area increases as AW increases, the rate of water area enlargement was much lower than the AW widening rate. The same phenomenon is also seen to some extent in the Bislak River but was not observed in the Laoag

or Abra Rivers (Table 7-3). These differences might also be related to the braiding and wandering channel patterns in the Laoag and Abra Rivers.

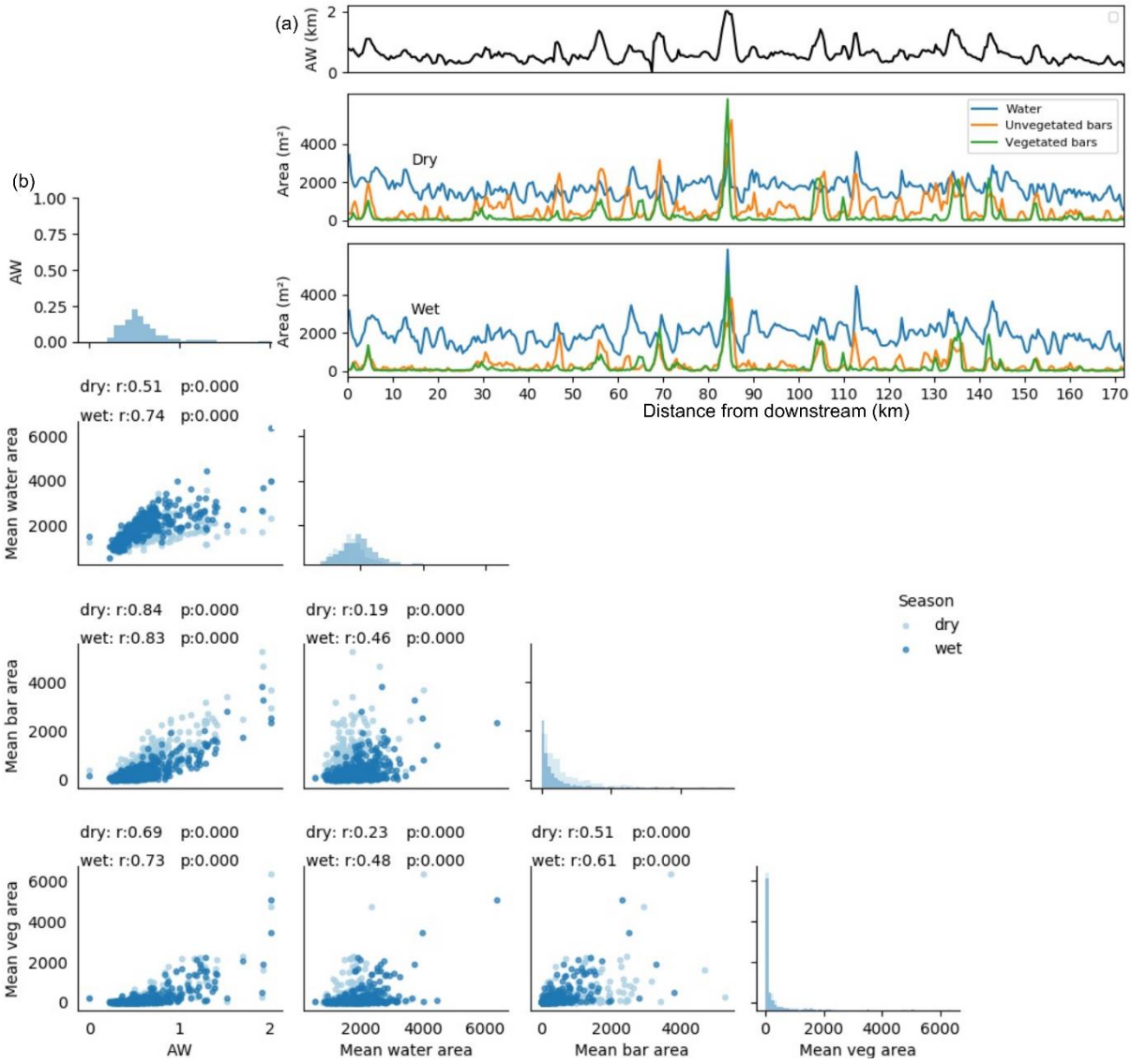

Figure 7-3. (a) Longitudinal trends in active width (AW) and mean area of three landforms (water, unvegetated bars, vegetated bars) for the Cagayan River, for wet and dry seasons. (b) Matrix plots representing correlations between mean values of landform areas and AW. Histograms illustrate mean value distributions at ~440 m intervals along the river. Labels summarise correlation coefficients (r) and associated statistical significance (p) between landforms' areas and AW in wet and dry seasons.

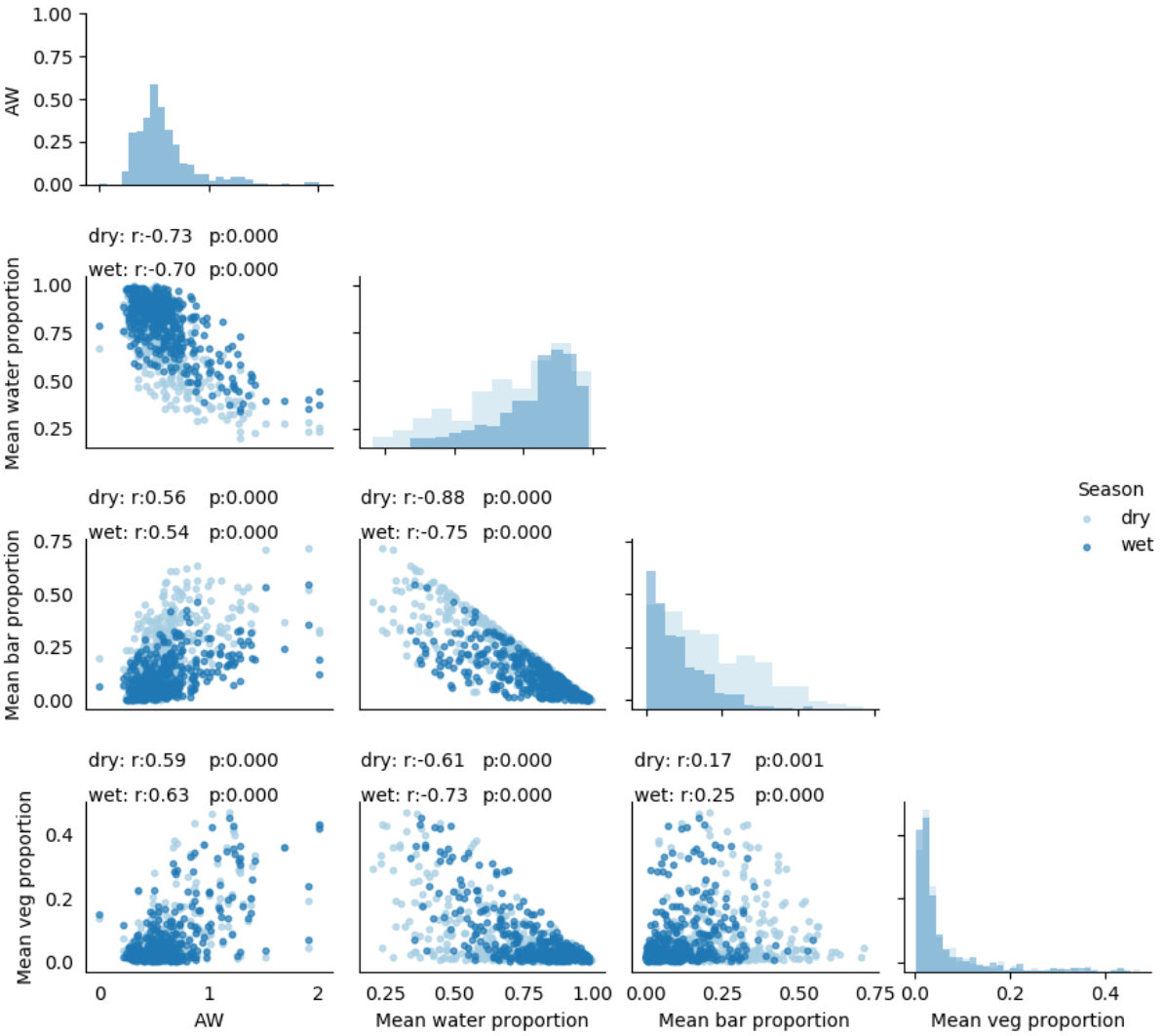

Figure 7-4. Matrix plots to represent correlations between mean values of landform proportions and AW. Histograms illustrate mean value distributions at ~440 m intervals along the river. Labels summarise correlation coefficients (r) and associated statistical significance (p) between landforms proportion and AW in wet and dry seasons.

In Chapters 5 and 6, seasonality in river landforms was reported and discussed for the Bislak, Laoag, Abra Rivers and the Cagayan River, respectively. In Section 7.1 it was noted that climate should be one factor impacting the variability in river landform classifications. Therefore, this section aims to compare the seasonality differences between rivers in two climate regions. In Chapter 5, periods with 10-day mean accumulated precipitation consistently below 100 mm were defined as dry seasons, whilst periods starting from the first time when 10-day mean accumulated precipitation above 100 mm to the start of next dry season were defined as wet seasons. Using this definition, dry seasons and the time of peak precipitation in all the studied rivers were sorted and are listed in Table 7-3. In most cases, the dry seasons

were synchronous in the Bislak, Laoag and Abra Rivers, while in the Cagayan River, dry seasons were shorter and commenced later than the other three rivers before 2020. In 2020, the dry season in the Abra and Cagayan Rivers was slightly later than that in the Bislak and Laoag Rivers, whilst peak precipitation in all four rivers was observed in October 2020. These results indicate that seasonality in precipitation in the two climate zones was not significantly different in the study years. Precipitation is strongly affected by circulation change on local scales (Naik, Seager, and Vecchi 2010; Bony et al. 2013; Chadwick, Boutle, and Martin 2013; Forster et al. 2016). Moreover, rapid circulation changes are not only being associated with changes in atmosphere absorption but are also being linked to rapid land surface response (Bony et al. 2013; Forster et al. 2016; Richardson et al. 2018). This suggests that it may be valuable to analyse river landform area changes between and during wet and dry seasons to assess potential different landform responses between the four rivers. Table 7-3 shows that in all four rivers, the AW and three landform areas all show positive relationships. However, correlation coefficients of AW with water area and AW with vegetated bar area in the wet season were both higher than that in the dry season, whilst correlation coefficients of AW with unvegetated bar area were lower in the wet season than in the dry season. The statistical relationships imply that water area and vegetated bar area responded to the active channel width more strongly during the wet season, indicating that seasonality should be considered while assessing the channel settings impact on river landform changes.

In the dry season, the correlations between AW and landform areas in the Bislak and Cagayan Rivers were showing similar coefficients, whilst AW- landform areas were showing similar coefficients between the Laoag and Abra Rivers. Table 7-2 indicates that mean accumulated precipitation over three years (2018-2020) in the Bislak and Cagayan Rivers were lower than those in the Laoag and Abra Rivers. Also, as noted previously, braided reach percentages in the Bislak and Cagayan Rivers were lower than those in the Laoag and Abra Rivers. These findings indicate that, except for AW and water area correlation during the wet season, precipitation strength and channel stability can impact the strength of river landform correlations with the active channel width. In the wet seasons, the water area may reach the bankfull width. However, when the river channel is confined, either naturally or anthropogenically, the channel may reach close bankfull width at a moderate discharge and not get any wider as flow rises further. Contrasting with over 41.1% of the study segment being confined in the Bislak, Laoag and Abra Rivers, the Cagayan River only has 22.6% of confinements (Table 7-4). Further, there are no reaches with two-side confinement observed in

the Cagayan River. This provides an explanation why the wet season correlation coefficient of AW with water area in the Cagayan River was higher than that in the other three rivers. Therefore, these results suggest that river confinement needs to be assessed when analysing relationships between AW and water area in wet seasons.

Table 7-3. Seasonality in the Bislak, Laoag, Abra and Cagayan Rivers.

Seasonality	**Bislak**	**Laoag**	**Abra**	**Cagayan**
Range of mean accumulated precipitation below 100 mm (dry)	Dec 2016- May 2017; Nov 2017- June 2018 Sept 2018- Apr 2019; Nov 2019- May 2020	Dec 2016- May 2017; Nov 2017- May 2018; Sept 2018- Apr 2019; Nov 2019- May 2020	Nov 2016- May 2017; Nov 2017- May 2018; Sept 2018 – May 2019; Dec 2019 – May 2020	Jan 2018- June 2018; Jan 2019- May 2019; Dec 2019- May 2020; Oct 2020- July 2021
Range of peak precipitation	July 2016; Aug 2017; Aug 2018; Aug 2019; Oct 2020	July 2016; May, Sept 2017; Aug 2018; Aug 2019; Oct 2020	Aug 2016; July 2017; Aug 2018; Aug 2019; Oct 2020	Sept 2018; Nov 2019; Oct 2020; Oct 2021
Correlation coefficient between **AW** and **water area** (dry)	0.46 (p=0.000)	0.64 (p=0.000)	0.63 (p=0.000)	0.51(p=0.000)
Correlation coefficient between **AW** and **water area** (wet)	0.60 (p=0.000)	0.69 (p=0.000)	0.67 (p=0.000)	0.74 (p=0.000)
Correlation coefficient between **AW** and **unvegetated bar area (**dry)	0.86 (p=0.000)	0.73 (p=0.000)	0.78 (p=0.000)	0.84 (p=0.000)
Correlation coefficient between **AW** and **unvegetated bar area** (wet)	0.78 (p=0.000)	0.50 (p=0.000)	0.74 (p=0.000)	0.83 (p=0.000)
Correlation coefficient between **AW** and **vegetated bar area** (dry)	0.67 (p=0.000)	0.81 (p=0.000)	0.82 (p=0.000)	0.69 (p=0.000)
Correlation coefficient between **AW** and **vegetated bar area** (wet)	0.76 (p=0.000)	0.86 (p=0.000)	0.88 (p=0.000)	0.73 (p=0.000)
Correlation coefficient between AW and **water proportion** (dry)	-0.45 (p=0.000)	0.10 (p=0.292)	-0.24 (p=0.001)	-0.73 (p=0.000)
Correlation coefficient between **AW** and **water proportion** (wet)	-0.41 (p=0.000)	-0.07 (p=0.467)	-0.35 (p=0.000)	-0.70 (p=0.000)
Correlation coefficient between **water** and	-0.71 (p=0.000)	-0.86 (p=0.000)	-0.70 (p=0.000)	-0.88 (p=0.000)

unvegetated bar proportion (dry)				
Correlation coefficient between **water** and **unvegetated bar proportion** (wet)	-0.44 (p=0.000)	-0.79 (p=0.000)	-0.41 (p=0.000)	-0.75 (p=0.000)
Correlation coefficient between **vegetated bar** and **unvegetated bar proportion** (dry)	-0.68 (p=0.000)	-0.64 (p=0.000)	-0.47 (p=0.000)	0.17 (p=0.001)
Correlation coefficient between **vegetated bar** and **unvegetated bar proportion** (wet)	-0.63 (p=0.000)	-0.47 (p=0.000)	-0.47 (p=0.000)	0.25 (p=0.000)

In Chapter 5, it was proposed that the correlation between AW and vegetated bar area increases with the catchment area. However, in this chapter, as the larger Cagayan catchment was introduced to the dataset, this correlation was not found to continue. As the available information on riparian vegetation (e.g., vegetation and soil types between two climatic regions) was limited, this evidence does not overturn the conclusions in Chapter 5. However, in this Chapter, it was suggested that the correlation between AW and vegetated bar area should be considered to apply to a common climatic environment. Additionally, Table 7-3 shows that there were significant negative correlations between vegetated bar and unvegetated bar proportions in the Bislak, Laoag and Abra Rivers, but that vegetated bar and unvegetated bar proportions in the Cagayan River were significantly positively correlated in both seasons. Table 7-2 indicates that unvegetated and vegetated bar proportions in the three rivers of Northwest Luzon were much higher than in the Cagayan River. For example, in the Bislak River, water played a less important role in determining the proportions of bar landforms (including vegetated and unvegetated bars) in both seasons. However, compared to the dry season in the Laoag River, increased precipitation in the wet season induced greater water impact on the bars. The negative correlation between unvegetated bar and vegetated bar was not observed in the Cagayan River, which indicates that bar dynamics interplay with water more in the Cagayan River as there were only three landforms classified in the river. The high proportion of water within the Cagayan River (Table 7-2, averaged mean water proportion over three years is 0.752) may explain this phenomenon, whilst high water proportion in the Cagayan River could be impacted by a variety of factors such as lower longitudinal gradient, finer sediment size and total catchment precipitation, etc. Therefore, this Chapter suggests that absolute high/low areas of individual landforms may be key to infer correlations between landform proportions. Therefore, it is important to evaluate the space available for landforms

within river channels, before undertaking statistical analysis. The active width provides a good indication of this available space, supplemented by information on confinement. Additionally, separating the dataset into dry and wet seasons dramatically helps in extracting informative statistical information.

7.3. River landform dynamic change analysis

River morphology is impacted by a variety of factors. Recently, valley confinement has been identified as a primary control on river morphology in some settings (Fryirs, Wheaton, and Brierley 2016). In addition, faults (Li, Dong, et al. 2022) and tributary rivers (Benda et al. 2004) are also important controls over river morphology. Table 7-4 summarises confinement, faults, and tributaries in the four rivers of this study.

Table 7-4. Channel settings of the Bislak, Laoag, Abra and Cagayan Rivers.

Disturbance	Bislak	Laoag	Abra	Cagayan
Total confinement percentage	54.8%	41.1%	63.8%	22.6% (contain artificial banks)
Partly confinement percentage	18.3%	21.4%	43.2%	22.6% (contain artificial banks)
Two-side confinement percentage	36.5%	19.7%	20.6%	0
Faults cutting through the river/ river length	2 faults/ 46.6 km	2 faults/ 38.9 km	6 faults/ 82.2 km	0 faults/ 171.9 km
Tributaries/ river length	1 tributary/ 46.6 km	4 tributaries/ 38.9 km	5 tributaries/ 82.2 km	8 tributaries/ 171.9 km

The extent to which various confinement factors occur determines the capacity that the river has to adjust (Phillips 2010). For example, full or partial confinement limits the capacity of the river planform to adjust and can often cause the assemblage of geomorphic units to be forced so producing forced landforms which are controlled by forcing effects such as confinement (Fryirs, Wheaton, and Brierley 2016). Table 7-4 indicates that the Cagayan River is the least confined of the four studied rivers, which may be interpreted as meaning that the Cagayan River has the highest capacity to adjust. However, through analysing landform diversity maps (Figure 7-5), the landforms within the Cagayan channel were found to be the most stable, which

was statistically confirmed in Table 7-2. Combining the confinement data and the landform diversity index, although the Bislak River was not obtaining the highest percentage of total confinement among the four rivers, the Bislak River had the highest percentage of two-side confinements along with the highest averaged landform diversity (Table 7-2), which is consistent with the theory of Phillips (2010) that the degree of the confinement determines the capacity of rivers to adjust. Table 7-4 also indicates that the Laoag River had lower percentage of confinement than the Abra River, however, its averaged landform diversity is slightly higher than the Abra River. This can be explained by Figure 7-5, which shows that the upland Laoag River is mostly unconfined with lower diversity and the lowland reaches of the Laoag River are mostly confined and highly diversified. Figure 7-5 indicates that the confinement may induce high diversity in river landforms in the Bislak, Laoag River and Cagayan Rivers. However, in the Abra River, the confinement does not appear to have caused significantly increased landform diversity. This may be due to the active channel width of the Abra River being much higher than the other three rivers (see Table 7-2) and therefore, forcing effects from confinement on the in-channel landforms were reduced. Less forcing effects from the confinement provide more free space for river landforms to develop stably and thereby, reduce the landform diversity. Aside from confinement, faults and tributaries were also considered as factors increasing the river landform diversity. This is because abrupt stream power changes caused by faults and tributaries tends to change local sediment transport patterns which may induce aggradation that then leads to the frequent landform change (see Chapter 5 and Chapter 6). Additionally, the relatively high stability of the lowland Cagayan River may be also explained by the low longitudinal gradient (Table 3-1), which leads to lower stream power than the Bislak, Laoag and Abra Rivers.

The preceding discussion implies that river landform diversity is impacted by multiple factors. River setting factors, such as active channel width, river longitudinal gradients, and the location and abundance of faults, tributaries and confinements, together provide a synthesised constraint on river landform change within the channel. The relative abundance of free and forced bars, and associated changes in landform diversity, reflect these combined constraints. Locally abrupt disturbances from the geological setting (e.g., faults, lithological boundaries) and the catchment network (e.g., tributary rivers) also play important roles in river landform diversity and stability.

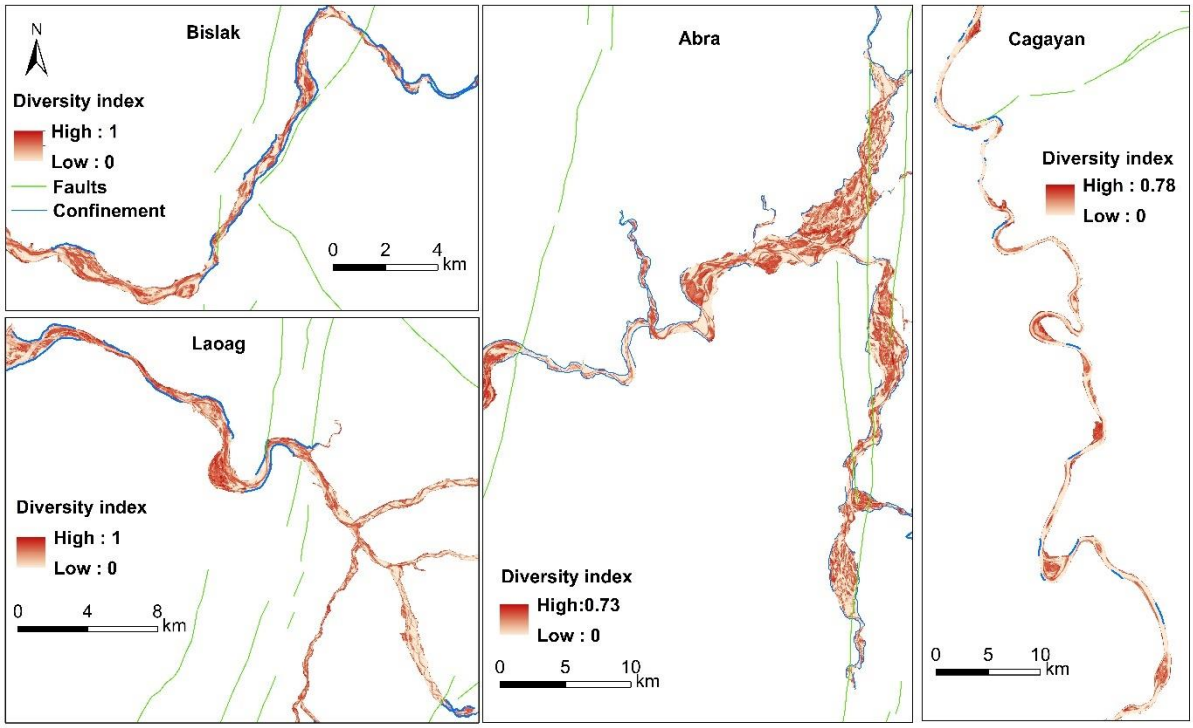

Figure 7-5. Simpson's diversity indices of the Bislak, Laoag, Abra and Cagayan Rivers.

7.4. Perspectives of research

This project has used remote sensing data to derive a variety of indices and information for analysing river morphological change (response) in North Luzon, the Philippines which has distinct wet and dry seasons. The new technology (e.g., image downscaling, segmentation, machine learning classification) and workflow (e.g., Geographic Object-Based Image Analysis) extends the boundaries of river morphology research and is particularly relevant to situations where sufficient field data are sparse (e.g., sediment size, water discharge, vegetation species). Using remotely sensed data, a set of parameters were considered to describe the river dynamics within the river channel over a multi-year period. For example, in Chapter 6 a stream power ratio parameter was introduced without quantitative consideration of sediment size. Although there is a possibility to infer the sediment size through empirical models from previous studies in other rivers, the quality of the research can be improved by obtaining real sediment size information from the studied rivers. Improving the database in this way may lead to more accurate results that could enable more specific comparison with previous studies. Table 7-5 illustrates some examples using indices beyond this project that have been considered in previous river morphology studies. There are many factors impacting river morphology, however, it remains difficult to consider all these factors in any one study.

In many cases, access to all of the data that could be useful represents the biggest challenge for a comprehensive synthesised study. River morphological change is a vast topic, which has seen complicated research over many decades. A combination of high spatial-temporal resolution Earth observation data with targeted field data collection has the potential to significantly improve our understanding of system dynamics at multiple temporal and spatial scales. The high accuracy of river morphology detection also benefits from high resolution or very high-resolution remote sensing imagery. However, using high-resolution imagery to analyse catchment-scale river dynamics demands for very high capability of computing power of computer devices, which could be too expensive to be widely used among researchers. The potential solution is to combine the medium-resolution imagery and high-resolution imagery together to do analysis. For instance, the faster and low-cost method (e.g. workflow in this study) can be used to generate river patterns at catchment scale. Through initial investigation using medium-resolution imagery, the sub-reaches with special characteristics and interests could be further explored using high-resolution imagery. This kind of hierarchical river pattern recognition is also expected to be applied to global/regional-scale rivers by using adaptable image classification methods and appropriate remote sensing imagery. On the other hand, cloud-computing using the Internet ('the cloud') to offer faster innovation and flexible resources without requesting very high computing capability of user's device, arises and becomes popular in recent years. For example, Google Earth Engine (GEE), which is integrated with Google Cloud Platform, enables spatial-temporal analysis using accessible free remote sensing data at a bigger scale. However, when establishing a workflow with algorithms coming from different sources, especially for those complicated but welcomed algorithms achieved by existing easy-operating software or coding packages, ensemble algorithms in GEE would be a technique challenge for researchers of river science. However, the technique challenge can be overcome by interdisciplinary studies between river science, computing science and mathematics. Hence, as Earth observation data become more readily accessible and processing tools continue to be developed and made readily available, a further revolution in river morphology studies may be seen in the near future.

Table 7-5. Examples using indices in river morphology studies which are excluded from this project.

Literature	Sediment transport/ size	Water discharge	Flow velocity	Vegetation types	Organisms in water	Water temperature	Bedrock types	Bed level	Bathymetric survey
(Johnson, Snyder, and Hitt 2017)						√	√		
(Raven et al. 2009)	√							√	
(Rice et al. 2009)	√								√
(Dingle et al. 2019)	√	√							
(van Oorschot et al. 2016)		√	√	√				√	√
(Im et al. 2011)		√	√		√		√		√

Chapter 8 - Synthesis and Conclusions

8.1. Assessment of Research Objectives

This Chapter provides a synthesis to answer the research objectives listed in Chapter 1, and then provides a summary conclusion of the work in this thesis. The objectives from Chapter 1 (in italics below) are as follows:

(1) to design and apply an automated river landform classification workflow using free Sentinel-2 multi-spectral data and validate with manually digitised ground truth data:

A hierarchical workflow was designed (illustrated in Chapter 4) that considers (spatial and temporal data resolution, data quality (obscured or not), data downscaling performance, training dataset selection, testing dataset selection, and model transferability to neighbouring years and rivers (Chapter 4). The classification model performed very well for the rivers in northwest Luzon but did not perform well at classifying the landforms in the Cagayan River in northeast Luzon (Chapter 7). By using new training data derived from ground truth in the Cagayan River, the classification was significantly improved, which is due to the Cagayan having different physical characteristics to the other rivers. Chapters 4 and 7 results indicate that the designed hierarchical workflow can be efficient and robust for river landform classification. However, development of the training model (one step of the hierarchical workflow) needs to be fully assessed for the particular sites under investigation before the full workflow is applied.

(2) to further develop and evaluate the classification workflow in (1) by applying it to four rivers in North Luzon inter- and intra-annually, producing data for spatial-temporal analysis:

There were 32 dates (Feb 2016- July 2021) when river landforms (water, unvegetated bars and vegetated bars) were classified in the Bislak and Laoag Rivers, 34 dates (Jan 2016- July 2021) for the Abra River, and 20 dates (Mar 2018- Sept 2021) in the Cagayan River. Prior to 2018, many images were partly or fully obscured by heavy clouds along the Cagayan River channels. The availability of data at two-monthly intervals provides time series of sufficient temporal resolution to allow identification of seasonal patterns, and multi-year data availability extended

this time series sufficiently for statistical analysis to be used to interpret the results across several years.

(3) to generate river landform (water, unvegetated bars and vegetated bars) spatial-temporal classification maps for the Bislak, Laoag, Abra and Cagayan Rivers:

The automated river landform classification workflow in (1) was successfully developed and evaluated in Chapter 4 and was applied to the Bislak, Laoag, Abra and Cagayan Rivers in Chapters 5 and 6. The spatial-temporal patterns in the classified river landforms were investigated inter- and intra-annually (Figure 5-5 and Figure 6-4). These plots visualise the impacts of regional geomorphology (valley slope, confinement, drainage network structure), seasonal and inter-annual climatic variations, and anthropogenic disturbance (confinement, aggregate mining) on river landform patterns and dynamics.

(4) to evaluate whether there is strong seasonality in the morphological dynamics of the North Luzon rivers and, if so, explore how the river landforms interplay with each other and with the active channel width:

Figures 5-5 and 6-4 show that the proportion of water in the active channels of the four rivers, except for some very low gradient reaches, all show strong seasonality induced by seasonal precipitation fluctuations in tropical North Luzon. Unvegetated bar proportions also show seasonality in every river, however, seasonality of this landform type in the Bislak River (Figure 5-5) was weaker than in the Laoag, Abra and Cagayan Rivers (Figure 5-5 and Figure 6-4). Seasonality for vegetated bars is extensively observed in many reaches of the wandering/braided gravel-bed Bislak, Laoag, Abra Rivers, but is less common in most reaches of the meandering, sand-bed Cagayan River.

(5) to assess how the river landforms respond to external river channel settings (valley confinement, faults, tributaries, etc.); and how does river morphology respond to tributary inflows:

From quantitative analyses of the active channel width, landform area and landform proportion in the four rivers, it is suggested that active channel widths tend to have significant correlations with the areas of all three landforms (Table 7-3). Notably, there are significant negative

correlations between vegetated bar and unvegetated bar proportions in the Bislak, Laoag and Abra Rivers. However, in the Cagayan River vegetated and unvegetated bar proportions were significantly positively correlated in both wet and dry seasons (Table 7-3). The details in the results suggest that the ways in which river landforms respond to the different river channel settings are related to multiple factors, including active channel widths, river longitudinal gradients, and the locations of faults, lithological boundaries, tributaries and confinement. Chapter 7 also discussed how landform diversity is impacted by confinement. In Chapter 6, it was shown that unstable reaches, many associated with tributary inputs, show seasonal dynamics in water and unvegetated bar areas in all years, whilst the stream power ratios of tributaries to the mainstream upstream of confluences could impact the landform diversity and stability downstream of the confluence differently according to the relative magnitude of the tributary input. Aside from river landform response to tributary inflows, tributary inputs can also contribute to the widening of bankfull river width downstream of the confluences.

(6) to discuss how the generated data can be used to identify the impact of disturbance analysis on landforms change:

Spatial-temporal heatmaps were used to visualise the generated landform data so revealing spatial-temporal data distributions (Figure 5-5 and Figure 6-4). Mapping frequency (Figure 5-7 and Figure 6-5) and diversity (Figure 6-8 and Figure 7-5) helped to estimate the probability of landform change. Locations with abrupt changes on these plots and maps can be examined to identify local controls over the landform processes. Using the coefficient of variation to calculate landform stability (Figure 5-11 and Figure 6-7) reveals hotspots of dynamism and also reaches that show consistency between seasons and years. Representing the dynamism in 2-Dimensions with Simpson's Diversity Index (Chapter 6 and 7) reveals reach-scale processes that can be related to geomorphic and/or anthropogenic causes. Moreover, the EEMD signal decomposition method, was introduced to differentiate local abrupt changes from periodic consistency (see 6.4.4).

8.2 Conclusions

This thesis firstly developed a workflow to automatically classify river landforms in the Bislak, Laoag, Abra and Cagayan Rivers, North Luzon, the Philippines. Image processing technology, including image downscaling and object-based segmentation, was explored for enhancing

classification performance. Subsequently, the support vector machine classifier was employed to classify the river landforms into water, unvegetated bars and vegetated bars within the river active channel. The results not only suggest that the image quality (e.g., obscured extent, image resolution) and image processing approaches are important, but also that the selection of training data and testing data should be carefully considered before finalising the machine learning classification model. The generated river landform datasets for the four rivers in north Luzon provided the quantitative data base for analysis of river morphological change and morphological responses to channel settings.

In this thesis, seasonal and annual landform changes were detected in the four rivers. The data show longitudinal and temporal variation in landform areas and proportions. Meanwhile, longitudinal variation is strongly influenced by channel setting (e.g., active width, catchment size, confinement, tributaries, slope and elevation). There are distinct dry and wet seasons in the studied catchments, although their timing and duration vary between years. Separating the river morphology dataset into dry and wet seasons significantly improves the statistical information that can be used to understand river processes. For example, landform areas are significantly correlated with active width, with very strong correlation found between active width and vegetated bar area in both wet and dry seasons in all four rivers. Landform data processed by EEMD indicated that water and vegetated bars are commonly synchronised with precipitation (close to in-phase, with a 1 to 3 months lag from the peak of precipitation in each year,), while unvegetated bars have an oscillation close to anti-phase with precipitation.

Several approaches were applied to statistically analyse landform temporal change. Assessing longitudinal landform stability through the coefficient of variation, differences in river gradient and the influence of faults demonstrated how rivers in similar hydrological/climate regimes can have different sensitivities. Mappings of landform frequency and diversity show local patterns of stability and instability within the active channel. Using this variety of visualizations of landform changes, channel setting impacts on river morphological dynamics were addressed. For example, tributary inflows lead to widening of bankfull width downstream, whilst stream power ratios of tributaries to mainstem upstream confluences result in various impacts on downstream morphology and landform diversity, and consequently will affect instream habitats and ecology. This thesis shows how advanced technology (i.e., image processing, machine learning) and interdisciplinary statistical tools (i.e., EEMD, COV and Simpson’s diversity index) can be employed to enhance river landform classification and

visualization. Nevertheless, external controls (e.g., seasonal precipitation, geological setting, sediment transport and anthropogenic factors) can induce changes in river morphology and landform change at different magnitudes. Spatial-temporal analysis of river landforms not only trace the river patterns change, but also contribute to dig into hotspot event location of the river. For example, identifying the high frequency water trajectory and seasonal water patterns can help detect potential hotspot of floods. Whilst combining river morphology with bar development and vegetation growth, river process and high risk of floods could be predicted. The synthetic analysis applied to the studied tropical rivers in this thesis has the potential to benefit future flood risk assessment, river management and river channel restoration. The methods used throughout the thesis can be applied to rivers worldwide, although training data will need to be selected as appropriate for different local conditions. The results from north Luzon have relevance across the tropics, and in other regions where seasonal variation in river flows is accompanied by significant in-channel vegetation growths.

References

Abanco, C., G. L. Bennett, A. J. Matthews, M. A. M. Matera, and F. J. Tan. 2021. "The role of geomorphology, rainfall and soil moisture in the occurrence of landslides triggered by 2018 Typhoon Mangkhut in the Philippines." Natural Hazards and Earth System Sciences 21 (5):1531-50. doi: 10.5194/nhess-21-1531-2021.

Abd El-Kawy, O. R., J. K. Rød, H. A. Ismail, and A. S. Suliman. 2011. "Land use and land cover change detection in the western Nile delta of Egypt using remote sensing data." Applied Geography 31 (2):483-94. doi: 10.1016/j.apgeog.2010.10.012.

Abon, C. C., C. P. C. David, and N. E. B. Pellejera. 2011. "Reconstructing the Tropical Storm Ketsana flood event in Marikina River, Philippines." Hydrology and Earth System Sciences 15 (4):1283-9. doi: 10.5194/hess-15-1283-2011.

Abukawa, K., M. Yamamuro, Z. Kikvidze, A. Asada, C. H. Xu, and K. Sugimoto. 2013. "Assessing the biomass and distribution of submerged aquatic vegetation using multibeam echo sounding in Lake Towada, Japan." Limnology 14 (1):39-42. doi: 10.1007/s10201-012-0383-7.

Achanta, R., A. Shaji, K. Smith, A. Lucchi, P. Fua, and S. Susstrunk. 2012. "SLIC Superpixels Compared to State-of-the-Art Superpixel Methods." Ieee Transactions on Pattern Analysis and Machine Intelligence 34 (11):2274-81. doi: 10.1109/Tpami.2012.120.

Adagbasa, Efosa G., Samuel A. Adelabu, and Tom W. Okello. 2019. "Application of deep learning with stratified K-fold for vegetation species discrimation in a protected mountainous region using Sentinel-2 image." Geocarto International 37 (1):142-62. doi: 10.1080/10106049.2019.1704070.

Agnihotri, A. K., A. Ohri, and S. Mishra. 2019. "Channel planform dynamics of lower Ramganga River, Ganga basin, GIS and remote sensing analyses." Geocarto International 35 (9):934-53. doi: 10.1080/10106049.2018.1552323.

Altenau, E. H., T. M. Pavelsky, D. Moller, C. Lion, L. H. Pitcher, G. H. Allen, P. D. Bates, S. Calmant, M. Durand, and L. C. Smith. 2017. "AirSWOT measurements of river water surface elevation and slope: Tanana River, AK." Geophysical Research Letters 44 (1):181-9. doi: 10.1002/2016gl071577.

Anderson, K., and H. Croft. 2009. "Remote sensing of soil surface properties." Progress in Physical Geography-Earth and Environment 33 (4):457-73. doi: 10.1177/0309133309346644.

Andreadis, K. M., G. J. P. Schumann, and T. Pavelsky. 2013. "A simple global river bankfull width and depth database." Water Resources Research 49 (10):7164-8. doi: 10.1002/wrcr.20440.

Ashmore, P. 2013. "9.17 Morphology and Dynamics of Braided Rivers." In Treatise on Geomorphology, 289-312. doi: 10.1016/B978-0-12-374739-6.00242-6

Ashmore, P. E., R. I. Ferguson, K. L. Prestegaard, P. J. Ashworth, and C. Paola. 1992. "Secondary flow in anabranch confluences of a braided, gravel-bed stream." Earth Surface Processes and Landforms 17 (3):299-311. doi: 10.1002/esp.3290170308.

Ashworth, P. J., and J. Lewin. 2012. "How do big rivers come to be different?" Earth-Science Reviews 114 (1-2):84-107. doi: 10.1016/j.earscirev.2012.05.003.

Baena-Escudero, R., M. Rinaldi, B. Garcia-Martinez, I. C. Guerrero-Amador, and L. Nardi. 2019. "Channel adjustments in the lower Guadalquivir River (southern Spain) over the last 250 years." Geomorphology 337:15-30. doi: 10.1016/j.geomorph.2019.03.027.

Bagtasa, G. 2017. "Contribution of Tropical Cyclones to Rainfall in the Philippines." Journal of Climate 30 (10):3621-33. doi: 10.1175/Jcli-D-16-0150.1.

Bangira, T., S. M. Alfieri, M. Menenti, and A. van Niekerk. 2019. "Comparing Thresholding with Machine Learning Classifiers for Mapping Complex Water." Remote Sensing 11 (11). doi: 10.3390/rs11111351.

Bartley, R., R. J. Keen, A. A. Hawdon, P. B. Hairsine, M. G. Disher, and A. E. Kinsey-Henderson. 2008. "Bank erosion and channel width change in a tropical catchment." Earth Surface Processes and Landforms 33 (14):2174-200. doi: 10.1002/esp.1678.

Basconcillo, J., A. Lucero, A. Solis, Jr R. Sandoval, E. Bautista, T. Koizumi, and H. Kanamaru. 2016. "Statistically Downscaled Projected Changes in Seasonal Mean Temperature and Rainfall in Cagayan Valley, Philippines." Journal of the Meteorological Society of Japan. Ser. II 94A (0):151-64. doi: 10.2151/jmsj.2015-058.

Bautista, M. L. P., and K. Oike. 2000. "Estimation of the magnitudes and epicenters of Philippine historical earthquakes." Tectonophysics 317 (1-2):137-69. doi: 10.1016/S0040-1951(99)00272-3.

Bedeian, A. G, and K. W. Mossholder. 2000. "On the use of the coefficient of variation as a measure of diversity." Organizational Research Methods 3 (3):285-97. doi: 10.1029/2010wr010319

Belgiu, M., and L. Dragut. 2016. "Random forest in remote sensing: A review of applications and future directions." Isprs Journal of Photogrammetry and Remote Sensing 114:24-31. doi: 10.1016/j.isprsjprs.2016.01.011.

Belletti, B., S. Dufour, and H. Piegay. 2015. "What Is the Relative Effect of Space and Time to Explain the Braided River Width and Island Patterns at a Regional Scale?" River Research and Applications 31 (1):1-15. doi: 10.1002/rra.2714.

Benda, L., K. Andras, D. Miller, and P. Bigelow. 2004. "Confluence effects in rivers: Interactions of basin scale, network geometry, and disturbance regimes." Water Resources Research 40 (5). doi: 10.1029/2003wr002583.

Benda, L., N. L. Poff, D. Miller, T. Dunne, G. Reeves, G. Pess, and M. Pollock. 2004. "The network dynamics hypothesis: How channel networks structure riverine habitats." Bioscience 54 (5):413-27. doi: 10.1641/0006-3568(2004)054[0413:Tndhhc]2.0.Co;2.

Benz, U. C., P. Hofmann, G. Willhauck, I. Lingenfelder, and M. Heynen. 2004. "Multi-resolution, object-oriented fuzzy analysis of remote sensing data for GIS-ready information."

Isprs Journal of Photogrammetry and Remote Sensing 58 (3-4):239-58. doi: 10.1016/j.isprsjprs.2003.10.002.

Bertrand, M., and F. Liebault. 2019. "Active channel width as a proxy of sediment supply from mining sites in New Caledonia." Earth Surface Processes and Landforms 44 (1):67-76. doi: 10.1002/esp.4478.

Bertrand, M., H. Piegay, D. Pont, F. Liebault, and E. Sauquet. 2013. "Sensitivity analysis of environmental changes associated with riverscape evolutions following sediment reintroduction: geomatic approach on the Drome River network, France." International Journal of River Basin Management 11 (1):19-32. doi: 10.1080/15715124.2012.754444.

Bijeesh, T. V., and K. N. Narasimhamurthy. 2020. "Surface water detection and delineation using remote sensing images: a review of methods and algorithms." Sustainable Water Resources Management 6 (4). doi: 10.1007/s40899-020-00425-4.

Bony, S., G. B., D. Klocke, S. Sherwood, S. Fermepin, and S. Denvil. 2013. "Robust direct effect of carbon dioxide on tropical circulation and regional precipitation." Nature Geoscience 6 (6):447-51. doi: 10.1038/ngeo1799.

Boota, M. W., C. Yan, M. B. Idrees, Z. Li, S. Soomro, M. Dou, M. Zohaib, and A. Yousaf. 2021. "Assessment of the morphological trends and sediment dynamics in the Indus River, Pakistan." Journal of Water and Climate Change 12 (7):3082-98. doi: 10.2166/wcc.2021.125.

Boothroyd, R. J., R. D. Williams, T. B. Hoey, B. Barrett, and O. A. Prasojo. 2021. "Applications of Google Earth Engine in fluvial geomorphology for detecting river channel change." Wiley Interdisciplinary Reviews-Water 8 (1). doi: 10.1002/wat2.1496.

Boothroyd, R. J., R. D. Williams, T. B. Hoey, P. L. M. Tolentino, and X. Yang. 2021. "National-scale assessment of decadal river migration at critical bridge infrastructure in the Philippines." Science of the Total Environment 768. doi: 10.1016/j.scitotenv.2020.144460.

Boulton, A. J., L. Boyero, A. P. Covich, M. Dobson, S. Lake, and R. Pearson. 2008. "Are Tropical Streams Ecologically Different from Temperate Streams?" In Tropical Stream Ecology, 257-84. doi: 10.1016/B978-012088449-0.50011-X.

Brice, J. C. 1978. "Countermeasures for hydraulic problems at bridges, volume I: analysis and assessment." https://rosap.ntl.bts.gov/view/dot/25311.

Bridge, J., and R. Demicco. 2008. "Earth surface processes, landforms and sediment deposits." Earth Surface Processes. doi: 10.1017/CBO9780511805516.

Bridge, J. S., and I. A. Lunt. 2006. "Depositional Models of Braided Rivers." In Braided Rivers, 11-50. doi: 10.1002/9781444304374.ch2.

Brodu, N. 2017. "Super-Resolving Multiresolution Images With Band-Independent Geometry of Multispectral Pixels." Ieee Transactions on Geoscience and Remote Sensing 55 (8):4610-7. doi: 10.1109/TGRS.2017.2694881.

Buffington, J. M., and D. R. Montgomery. 2022. "Geomorphic Classification of Rivers: An Updated Review." In Treatise on Geomorphology, 1143-90. doi: 10.1016/b978-0-12-818234-5.00077-8.

Candel, J., M. Kleinhans, B. Makaske, and J. Wallinga. 2021. "Predicting river channel pattern based on stream power, bed material and bank strength." Progress in Physical Geography-Earth and Environment 45 (2):253-78. doi: 10.1177/0309133320948831.

Carbonari, C., A. Recking, and L. Solari. 2020. "Morphology, Bedload, and Sorting Process Variability in Response to Lateral Confinement: Results From Physical Models of Gravel - bed Rivers." Journal of Geophysical Research: Earth Surface 125 (12). doi: 10.1029/2020jf005773.

Carbonneau, P. E., B. Belletti, M. Micotti, B. Lastoria, M. Casaioli, S. Mariani, G. Marchetti, and S. Bizzi. 2020. "UAV-based training for fully fuzzy classification of Sentinel-2 fluvial scenes." Earth Surface Processes and Landforms 45 (13):3120-40. doi: 10.1002/esp.4955.

Carling, P., J. Jansen, and L. Meshkova. 2014. "Multichannel rivers: their definition and classification." Earth Surface Processes and Landforms 39 (1):26-37. doi: 10.1002/esp.3419.

Carlson, T. N., and D. A. Ripley. 1997. "On the relation between NDVI, fractional vegetation cover, and leaf area index." Remote Sensing of Environment 62 (3):241-52. doi: 10.1016/S0034-4257(97)00104-1.

Carson, M. A. 1984. "Observations on the Meandering-Braided River Transition, The Canterbury Plains, New Zealand: Part Two." New Zealand Geographer 40 (2):89-99. doi: 10.1111/j.1745-7939.1984.tb01044.x.

Cerna, M., and A. F Harvey. 2000. "The fundamentals of FFT-based signal analysis and measurement." In.: Application Note 041, National Instruments.

Chadwick, R., I. Boutle, and G. Martin. 2013. "Spatial Patterns of Precipitation Change in CMIP5: Why the Rich Do Not Get Richer in the Tropics." Journal of Climate 26 (11):3803-22. doi: 10.1175/jcli-d-12-00543.1.

Chen, J., T. W. Cui, Z. F. Qiu, and C. S. Lin. 2014. "A simple two-band semi-analytical model for retrieval of specific absorption coefficients in coastal waters." Isprs Journal of Photogrammetry and Remote Sensing 91:85-97. doi: 10.1016/j.isprsjprs.2014.01.002.

Chen, Y. H., W. Su, J. Li, and Z. P. Sun. 2009. "Hierarchical object oriented classification using very high resolution imagery and LIDAR data over urban areas." Advances in Space Research 43 (7):1101-10. doi: 10.1016/j.asr.2008.11.008.

Church, M. 2006. "Bed Material Transport and the Morphology of Alluvial River Channels." Annual Review of Earth and Planetary Sciences 34 (1):325-54. doi: 10.1146/annurev.earth.33.092203.122721.

Ciecholewski, M. 2017. "River channel segmentation in polarimetric SAR images: Watershed transform combined with average contrast maximisation." Expert Systems with Applications 82:196-215. doi: 10.1016/j.eswa.2017.04.018.

Cinco, T. A., R. G. de Guzman, A. M. D. Ortiz, R. J. P. Delfino, R. D. Lasco, F. D. Hilario, E. L. Juanillo, R. Barba, and E. D. Ares. 2016. "Observed trends and impacts of tropical cyclones in the Philippines." International Journal of Climatology 36 (14):4638-50. doi: 10.1002/joc.4659.

Comaniciu, D., and P. Meer. 2002. "Mean shift: A robust approach toward feature space analysis." Ieee Transactions on Pattern Analysis and Machine Intelligence 24 (5):603-19. doi: 10.1109/34.1000236.

Condat, L. 2013. "A Direct Algorithm for 1-D Total Variation Denoising." Ieee Signal Processing Letters 20 (11):1054-7. doi: 10.1109/Lsp.2013.2278339.

Cordier, F., P. Tassi, N. Claude, A. Crosato, S.Rodrigues, and D. P. V. Bang. 2020. "Bar pattern and sediment sorting in a channel contraction/expansion area: Application to the Loire River at Bréhémont (France)." Advances in Water Resources 140. doi: 10.1016/j.advwatres.2020.103580.

Corenblit, D., F. Vautier, E. Gonzalez, and J. Steiger. 2020. "Formation and dynamics of vegetated fluvial landforms follow the biogeomorphological succession model in a channelized river." Earth Surface Processes and Landforms 45 (9):2020-35. doi: 10.1002/esp.4863.

Costa, H., G. M. Foody, and D. S. Boyd. 2018. "Supervised methods of image segmentation accuracy assessment in land cover mapping." Remote Sensing of Environment 205:338-51. doi: 10.1016/j.rse.2017.11.024.

Cristiano, E., M. C. ten Veldhuis, and N. van De Giesen. 2017. "Spatial and temporal variability of rainfall and their effects on hydrological response in urban areas - a review." Hydrology and Earth System Sciences 21 (7):3859-78. doi: 10.5194/hess-21-3859-2017.

Crosato, A., and E. Mosselman. 2020. "An Integrated Review of River Bars for Engineering, Management and Transdisciplinary Research." Water 12 (2). doi: 10.3390/w12020596.

Crosato, A., and E. Mosselman. 2009. "Simple physics-based predictor for the number of river bars and the transition between meandering and braiding." Water Resources Research 45 (3). doi: 10.1029/2008wr007242.

Daryaei, A., H. Sohrabi, C. Atzberger, and M. Immitzer. 2020. "Fine-scale detection of vegetation in semi-arid mountainous areas with focus on riparian landscapes using Sentinel-2 and UAV data." Computers and Electronics in Agriculture 177. doi: 10.1016/j.compag.2020.105686.

Davidson, E. A., and I. A. Janssens. 2006. "Temperature sensitivity of soil carbon decomposition and feedbacks to climate change." Nature 440 (7081):165-73. doi: 10.1038/nature04514.

Davies, P. M., S. E. Bunn, and S. K. Hamilton. 2008. "Primary Production in Tropical Streams and Rivers." In Tropical Stream Ecology, 23-42. doi: 10.1016/B978-012088449-0.50004-2.

De Luca, G., J. M. N. Silva, S. Cerasoli, J. Araujo, J. Campos, S. Di Fazio, and G. Modica. 2019. "Object-Based Land Cover Classification of Cork Oak Woodlands using UAV Imagery and Orfeo ToolBox." Remote Sensing 11 (10). doi: 10.3390/rs11101238.

De Ridder, S., X. Neyt, N. Pattyn, and P. F. Migeotte. 2011. "Comparison between EEMD, wavelet and FIR denoising: influence on event detection in impedance cardiography." Annu Int Conf IEEE Eng Med Biol Soc 2011:806-9. doi: 10.1109/iembs.2011.6090184.

De Fries, R., M. Hansen, and J. Townshend. 1995. "Global discrimination of land cover types from metrics derived from AVHRR pathfinder data." Remote Sensing of Environment 54 (3):209-22. doi: 10.1016/0034-4257(95)00142-5.

del Rio-Mena, T., L. Willemen, G. T. Tesfamariam, O. Beukes, and A. Nelson. 2020. "Remote sensing for mapping ecosystem services to support evaluation of ecological restoration interventions in an arid landscape." Ecological Indicators 113. doi: 10.1016/j.ecolind.2020.106182.

Demarchi, L., S. Bizzi, and H. Piegay. 2016. "Hierarchical Object-Based Mapping of Riverscape Units and in-Stream Mesohabitats Using LiDAR and VHR Imagery." Remote Sensing 8 (2). doi: 10.3390/rs8020097.

Demarchi, L., Bizzi, S.,Piegay, H.. 2017. "Regional hydromorphological characterization with continuous and automated remote sensing analysis based on VHR imagery and low-resolution LiDAR data." Earth Surface Processes and Landforms 42 (3):531-51. doi: 10.1002/esp.4092.

Demarchi, L., W. van de Bund, and A. Pistocchi. 2020. "Object-Based Ensemble Learning for Pan-European Riverscape Units Mapping Based on Copernicus VHR and EU-DEM Data Fusion." Remote Sensing 12 (7). doi: 10.3390/rs12071222.

Desnos, Y., M. Borgeaud, M. Doherty, M. Rast, and V. Liebig. 2014. "The European Space Agency's Earth Observation Program." IEEE Geoscience and Remote Sensing Magazine 2 (2):37-46. doi: 10.1109/MGRS.2014.2319270.

Dingle, E. H., M. J. Creed, H. D. Sinclair, D. Gautam, N. Gourmelen, A. G. L. Borthwick, and M. Attal. 2020. "Dynamic flood topographies in the Terai region of Nepal." Earth Surface Processes and Landforms. doi: 10.1002/esp.4953.

Dingle, E. H., E. C. Paringit, P. L. M. Tolentino, R. D. Williams, T. B. Hoey, B. Barrett, H. Long, C. Smiley, and E. Stott. 2019. "Decadal-scale morphological adjustment of a lowland tropical river." Geomorphology 333:30-42. doi: 10.1016/j.geomorph.2019.01.022.

Dragut, L., and C. Eisank. 2012. "Automated object-based classification of topography from SRTM data." Geomorphology 141:21-33. doi: 10.1016/j.geomorph.2011.12.001.

Drusch, M., U. Del Bello, S. Carlier, O. Colin, V. Fernandez, F. Gascon, B. Hoersch, et al. 2012. "Sentinel-2: ESA's Optical High-Resolution Mission for GMES Operational Services." Remote Sensing of Environment 120:25-36. doi: 10.1016/j.rse.2011.11.026.

Du, Z., B. Linghu, F. Ling, W. Li, W. Tian, H. Wang, Y. Gui, B. Sun, and X. Zhang. 2012. "Estimating surface water area changes using time-series Landsat data in the Qingjiang River Basin, China." Journal of Applied Remote Sensing 6 (1). doi: 10.1117/1.Jrs.6.063609.

Duan, Y. P., F. Liu, L. C. Jiao, P. Zhao, and L. Zhang. 2017. "SAR Image segmentation based on convolutional-wavelet neural network and markov random field." Pattern Recognition 64:255-67. doi: 10.1016/j.patcog.2016.11.015.

Fausch, K. D., C. E. Torgersen, C. V. Baxter, and H. W. Li. 2002. "Landscapes to riverscapes: Bridging the gap between research and conservation of stream fishes." Bioscience 52 (6):483-98. doi: 10.1641/0006-3568(2002)052[0483:Ltrbtg]2.0.Co;2.

Faustino-Eslava, D. V., C. B. Dimalanta, G. P. Yumul, N. T. Servando, and N. A. Cruz. 2013. "Geohazards, Tropical Cyclones and Disaster Risk Management in the Philippines: Adaptation in a Changing Climate Regime." Journal of Environmental Science and Management 16 (1):84-97. doi: 10.47125/jesam/2013_1/10.

Fazelpoor, K., V. Martínez-Fernández, S. Yousefi, and D. García de Jalón. 2022. "Remote sensing and machine learning techniques to monitor fluvial corridor evolution: The Aras River between Iran and Azerbaijan." In Computers in Earth and Environmental Sciences, 289-97. doi: 10.1016/B978-0-323-89861-4.00021-X.

Ferguson, R. I. 1987a. "Hydraulic and sedimentary controls of channel pattern." River channels: Environments and processes, Institute of British Geographers Special Publication 18, Oxford: Blackwell:129-58.

Ferguson, R. I., J. R. Cudden, T. B. Hoey, and S. P. Rice. 2006. "River system discontinuities due to lateral inputs: generic styles and controls." Earth Surface Processes and Landforms 31 (9):1149-66. doi: 10.1002/esp.1309.

Ferguson, R. I. 1987b. "Hydraulic and sedimentary controls of channel pattern." River channels: Environments and processes, Institute of British Geographers Special Publication 18, Oxford: Blackwell:129-58.

Ferguson, R., and T. Hoey. 2008. "Effects of Tributaries on Main-Channel Geomorphology." In River Confluences, Tributaries and the Fluvial Network, 183-208. doi: 10.1002/9780470760383.ch10.

Fielding, C. R., J. Alexander, and J. P. Allen. 2018. "The role of discharge variability in the formation and preservation of alluvial sediment bodies." Sedimentary Geology 365:1-20. doi: 10.1016/j.sedgeo.2017.12.022.

Forest Management Bureau, 2013. Philippine Forest Facts and Figures. Department of Environment and Natural Resources, Philippines. Second Edition. http://forestry.denr.gov.ph/pdf/ref/PF3_2013.pdf; accessed: 04/09/2018.

Forster, P. M., T. B. Richardson, T. Andrews, and D. J. Parker. 2016. "Understanding the Rapid Precipitation Response to CO2 and Aerosol Forcing on a Regional Scale*." Journal of Climate 29 (2):583-94. doi: 10.1175/jcli-d-15-0174.1.

Fotherby, L. M. 2009. "Valley confinement as a factor of braided river pattern for the Platte River." Geomorphology 103 (4):562-76. doi: 10.1016/j.geomorph.2008.08.001.

Frasson, R. P. D., R. Wei, M. Durand, J. T. Minear, A. Domeneghetti, G. Schumann, B. A. Williams, et al. 2017. "Automated River Reach Definition Strategies: Applications for the Surface Water and Ocean Topography Mission." Water Resources Research 53 (10):8164-86. doi: 10.1002/2017wr020887.

Freitas, P., G. Vieira, J. Canario, D. Folhas, and W. F. Vincent. 2019. "Identification of a Threshold Minimum Area for Reflectance Retrieval from Thermokarst Lakes and Ponds Using Full-Pixel Data from Sentinel-2." Remote Sensing 11 (6). doi: 10.3390/rs11060657.

Friedman, A. R., M. A. Bollasina, G. Gastineau, and M. Khodri. 2021. "Increased Amazon Basin wet-season precipitation and river discharge since the early 1990s driven by tropical Pacific variability." Environmental Research Letters 16 (3). doi: 10.1088/1748-9326/abd587.

Frissell, C. A., W. J. Liss, C. E. Warren, and M. D. Hurley. 1986. "A Hierarchical Framework for Stream Habitat Classification - Viewing Streams in a Watershed Context." Environmental Management 10 (2):199-214. doi: 10.1007/Bf01867358.

Fryirs, K. A. 2017. "River sensitivity: a lost foundation concept in fluvial geomorphology." Earth Surface Processes and Landforms 42 (1):55-70. doi: 10.1002/esp.3940.

Fryirs, K. A., J. M. Wheaton, and G. J. Brierley. 2016. "An approach for measuring confinement and assessing the influence of valley setting on river forms and processes." Earth Surface Processes and Landforms 41 (5):701-10. doi: 10.1002/esp.3893.

Fu, Z., L. Hu, Z. Chen, F. Zhang, Z. Shi, B. Hu, Z. Du, and R. Liu. 2020. "Estimating spatial and temporal variation in ocean surface pCO2 in the Gulf of Mexico using remote sensing and machine learning techniques." Science of the Total Environment 745. doi: 10.1016/j.scitotenv.2020.140965.

Gaci, S. 2016. "A new ensemble empirical mode decomposition (EEMD) denoising method for seismic signals." European Geosciences Union General Assembly 2016 97:84-91. doi: 10.1016/j.egypro.2016.10.026.

Gago, J., C. Douthe, R. E. Coopman, P. P. Gallego, M. Ribas-Carbo, J. Flexas, J. Escalona, and H. Medrano. 2015. "UAVs challenge to assess water stress for sustainable agriculture." Agricultural Water Management 153:9-19. doi: 10.1016/j.agwat.2015.01.020.

Gailleton, B., S. M. Mudd, F. J. Clubb, D. Peifer, and M. D. Hurst. 2019. "A segmentation approach for the reproducible extraction and quantification of knickpoints from river long profiles." Earth Surface Dynamics 7 (1):211-30. doi: 10.5194/esurf-7-211-2019.

Gao, B. C. 1996. "NDWI - A normalized difference water index for remote sensing of vegetation liquid water from space." Remote Sensing of Environment 58 (3):257-66. doi: 10.1016/S0034-4257(96)00067-3.

Garcia-Pedrero, A., C. Gonzalo-Martin, and M. Lillo-Saavedra. 2017. "A machine learning approach for agricultural parcel delineation through agglomerative segmentation." International Journal of Remote Sensing 38 (7):1809-19. doi: 10.1080/01431161.2016.1278312.

Garcia Lugo, G. A., W. Bertoldi, A. J. Henshaw, and A. M. Gurnell. 2015. "The effect of lateral confinement on gravel bed river morphology." Water Resources Research 51 (9):7145-58. doi: 10.1002/2015wr017081.

Gerhards, M., M. Schlerf, K. Mallick, and T. Udelhoven. 2019. "Challenges and Future Perspectives of Multi-/Hyperspectral Thermal Infrared Remote Sensing for Crop Water-Stress Detection: A Review." Remote Sensing 11 (10). doi: 10.3390/rs11101240.

Gibling, M. R. 2006. "Width and Thickness of Fluvial Channel Bodies and Valley Fills in the Geological Record: A Literature Compilation and Classification." Journal of Sedimentary Research 76 (5):731-70. doi: 10.2110/jsr.2006.060.

Gilvear, D. J. 1999. "Fluvial geomorphology and river engineering: future roles utilizing a fluvial hydrosystems framework." Geomorphology 31 (1-4):229-45. doi: 10.1016/S0169-555x(99)00086-0.

Gilvear, D., and R. Bryant. 2016. "Analysis of remotely sensed data for fluvial geomorphology and river science." In Tools in Fluvial Geomorphology, 103-32. doi: 10.1002/9781118648551.ch6.

Gonzalo-Martin, C., M. Lillo-Saavedra, E. Menasalvas, D. Fonseca-Luengo, A. Garcia-Pedrero, and R. Costumero. 2016. "Local optimal scale in a hierarchical segmentation method for satellite images An OBIA approach for the agricultural landscape." Journal of Intelligent Information Systems 46 (3):517-29. doi: 10.1007/s10844-015-0365-4.

Goutte, C., Gaussier, E. (2005). A Probabilistic Interpretation of Precision, Recall and F-Score, with Implication for Evaluation. In: Losada, D.E., Fernández-Luna, J.M. (eds) Advances in Information Retrieval. ECIR 2005. Lecture Notes in Computer Science, vol 3408. Springer, Berlin, Heidelberg. doi: 10.1007/978-3-540-31865-1_25.

Govender, M., K. Chetty, and H. Bulcock. 2007. "A review of hyperspectral remote sensing and its application in vegetation and water resource studies." Water SA 33 (2):145-51. doi: 10.4314/wsa.v33i2.49049.

Grafil, L, and O Castro. 2014. "Acquisition of IfSAR for the production of nationwide DEM and ORI for the Philippines under the unified mapping project." Infomapper 21 (12-13):40-3. http://www.namria.gov.ph/jdownloads/Info_Mapper/21_im_2014.pdf.

Gran, K. B., and D. R. Montgomery. 2005. "Spatial and temporal patterns in fluvial recovery following volcanic eruptions: Channel response to basin-wide sediment loading at Mount Pinatubo, Philippines." Geological Society of America Bulletin 117 (1-2):195-211. doi: 10.1130/B25528.1.

Grill, G., B. Lehner, M. Thieme, B. Geenen, D. Tickner, F. Antonelli, S. Babu, et al. 2019. "Mapping the world's free-flowing rivers." Nature 569 (7755):215-21. doi: 10.1038/s41586-019-1111-9.

Gurnell, A. 2014. "Plants as river system engineers." Earth Surface Processes and Landforms 39 (1):4-25. doi: 10.1002/esp.3397.

Gurnell, A. M., M. Rinaldi, B. Belletti, S. Bizzi, B. Blamauer, G. Braca, A. D. Buijse, et al. 2016. "A multi-scale hierarchical framework for developing understanding of river behaviour to support river management." Aquatic Sciences 78 (1):1-16. doi: 10.1007/s00027-015-0424-5.

Hajdukiewicz, H., and B. Wyzga. 2019. "Aerial photo-based analysis of the hydromorphological changes of a mountain river over the last six decades: The Czarny Dunajec, Polish Carpathians." Science of the Total Environment 648:1598-613. doi: 10.1016/j.scitotenv.2018.08.234.

Ham, D., and M. Church. 2012. "Morphodynamics of an extended bar complex, Fraser River, British Columbia." Earth Surface Processes and Landforms 37 (10):1074-89. doi: 10.1002/esp.3231.

Han, B., and Y. Q. Wu. 2017. "A novel active contour model based on modified symmetric cross entropy for remote sensing river image segmentation." Pattern Recognition 67:396-409. doi: 10.1016/j.patcog.2017.02.022.

Hassan, M. A., M. Church, T. E. Lisle, F. Brardinoni, L. Benda, and G. E. Grant. 2005. "Sediment transport and channel morphology of small, forested streams." Journal of the American Water Resources Association 41 (4):853-76. doi: 10.1111/j.1752-1688.2005.tb03774.x.

Helm, J. M., A. M. Swiergosz, H. S. Haeberle, J. M. Karnuta, J. L. Schaffer, V. E. Krebs, A. I. Spitzer, and P. N. Ramkumar. 2020. "Machine Learning and Artificial Intelligence: Definitions, Applications, and Future Directions." Current Reviews in Musculoskeletal Medicine 13 (1):69-76. doi: 10.1007/s12178-020-09600-8.

Henshaw, A. J., P. W. Sekarsari, G. Zolezzi, and A. M. Gurnell. 2019. "Google Earth as a data source for investigating river forms and processes: Discriminating river types using form-based process indicators." Earth Surface Processes and Landforms. doi: 10.1002/esp.4732.

Hicks, D. M., E. R. C. Baynes, R. Measures, G. Stecca, J. Tunnicliffe, and H. Friedrich. 2020. "Morphodynamic research challenges for braided river environments: Lessons from the iconic

case of New Zealand." Earth Surface Processes and Landforms 46 (1):188-204. doi: 10.1002/esp.5014.

Hohensinner, S., G. Egger, S. Muhar, L. Vaudor, and H. Piegay. 2021. "What remains today of pre-industrial Alpine rivers? Census of historical and current channel patterns in the Alps." River Research and Applications 37 (2):128-49. doi: 10.1002/rra.3751.

Holden, D., J. Saito, and T. Komura. 2016. "A Deep Learning Framework for Character Motion Synthesis and Editing." Acm Transactions on Graphics 35 (4). doi: 10.1145/2897824.2925975.

Hook, S. J., A. R. Gabell, A. A. Green, and P. S. Kealy. 1992. "A Comparison of Techniques for Extracting Emissivity Information from Thermal Infrared Data for Geologic Studies." Remote Sensing of Environment 42 (2):123-35. doi: 10.1016/0034-4257(92)90096-3.

Hooke, J. M. 2022. "Morphodynamics of a meandering channel over decadal timescales in response to hydrological variations." Earth Surface Processes and Landforms 47 (8):1902-20. doi: 10.1002/esp.5354.

Horacio, J., A. Ollero, and A. Perez-Alberti. 2017. "Geomorphic classification of rivers: a new methodology applied in an Atlantic Region (Galicia, NW Iberian Peninsula)." Environmental Earth Sciences 76 (21). doi: 10.1007/s12665-017-7072-0.

Horton, B. K., and P. G. DeCelles. 2001. "Modern and ancient fluvial megafans in the foreland basin system of the central Andes, southern Bolivia: implications for drainage network evolution in fold-thrust belts." Basin Research 13 (1):43-63. doi: 10.1046/j.1365-2117.2001.00137.x.

Hua, A. K. 2017. "Land Use Land Cover Changes in Detection of Water Quality: A Study Based on Remote Sensing and Multivariate Statistics." Journal of Environmental and Public Health 2017. doi: 10.1155/2017/7515130.

Huang, N. E., Z. Shen, S. R. Long, M. L. C. Wu, H. H. Shih, Q. N. Zheng, N. C. Yen, C. C. Tung, and H. H. Liu. 1998. "The empirical mode decomposition and the Hilbert spectrum for nonlinear and non-stationary time series analysis." Proceedings of the Royal Society a-

Mathematical Physical and Engineering Sciences 454 (1971):903-95. doi: 10.1098/rspa.1998.0193.

Huang, N. E., Z. Wu. 2004. "A study of the characteristics of white noise using the empirical mode decomposition method." The Royal Society:1597-611. doi: 10.1098/rspa.2003.1221.

Huete, A., K. Didan, T. Miura, E. P. Rodriguez, X. Gao, and L. G. Ferreira. 2002. "Overview of the radiometric and biophysical performance of the MODIS vegetation indices." Remote Sensing of Environment 83 (1-2):195-213. doi: 10.1016/S0034-4257(02)00096-2.

Huete, A. R. 1988. "A Soil-Adjusted Vegetation Index (Savi)." Remote Sensing of Environment 25 (3):295-309. doi: 10.1016/0034-4257(88)90106-X.

Huffman, GJ., Stocker, EF., Bolvin, DT., Nelkin, EJ., and Tan, J. 2019. GPM IMERG Final Precipitation L3 1 day 0.1 degree x 0.1 degree V06, Edited by Andrey Savtchenko, Greenbelt, MD, Goddard Earth Sciences Data and Information Services Center (GES DISC), Accessed:1 June 2023. doi: 10.5067/GPM/IMERGDF/DAY/06.

Hungr, O., G. C. Morgan, and R. Kellerhals. 1984. "Quantitative-Analysis of Debris Torrent Hazards for Design of Remedial Measures." Canadian Geotechnical Journal 21 (4):663-77. doi: 10.1139/t84-073.

Hupp, C. R., and M. Rinaldi. 2007. "Riparian Vegetation Patterns in Relation to Fluvial Landforms and Channel Evolution Along Selected Rivers of Tuscany (Central Italy)." Annals of the Association of American Geographers 97 (1):12-30. doi: 10.1111/j.1467-8306.2007.00521.x.

Huylenbroeck, L., M. Laslier, S. Dufour, B. Georges, P. Lejeune, and A. Michez. 2020. "Using remote sensing to characterize riparian vegetation: A review of available tools and perspectives for managers." Journal of Environmental Management 267. doi: 10.1016/j.jenvman.2020.110652.

Im, D., H. Kang, K. H. Kim, and S. U. Choi. 2011. "Changes of river morphology and physical fish habitat following weir removal." Ecological Engineering 37 (6):883-92. doi: 10.1016/j.ecoleng.2011.01.005.

Jaballah, M., B. Camenen, L. Penard, and A. Paquier. 2015. "Alternate bar development in an alpine river following engineering works." Advances in Water Resources 81:103-13. doi: 10.1016/j.advwatres.2015.03.003.

Jézéquel, C., T. Oberdorff, P. A. Tedesco, and L. Schmitt. 2022. "Geomorphological diversity of rivers in the Amazon Basin." Geomorphology 400. doi: 10.1016/j.geomorph.2021.108078.

Ji, L., L. Zhang, B. K. Wylie, and J. Rover. 2011. "On the terminology of the spectral vegetation index (NIR - SWIR)/(NIR + SWIR)." International Journal of Remote Sensing 32 (21):6901-9. doi: 10.1080/01431161.2010.510811.

Jiang, Z. Y., A. R. Huete, K. Didan, and T. Miura. 2008. "Development of a two-band enhanced vegetation index without a blue band." Remote Sensing of Environment 112 (10):3833-45. doi: 10.1016/j.rse.2008.06.006.

JICA-DPWH, 2002. The Feasibility study of the flood control project for the lower Cagayan River in the Republic of the Philippines. Japan International Cooperation Agency-Department of Public Works and Highways, Philippines. https://openjicareport.jica.go.jp/pdf/11871175.pdf; accessed: 28/02/2023.

Johnson, B., and Z. X. Xie. 2013. "Classifying a high resolution image of an urban area using super-object information." Isprs Journal of Photogrammetry and Remote Sensing 83:40-9. doi: 10.1016/j.isprsjprs.2013.05.008.

Johnson, Z. C., C. D. Snyder, and N. P. Hitt. 2017. "Landform features and seasonal precipitation predict shallow groundwater influence on temperature in headwater streams." Water Resources Research 53 (7):5788-812. doi: 10.1002/2017wr020455.

Jordan, M. I., and T. M. Mitchell. 2015. "Machine learning: Trends, perspectives, and prospects." Science 349 (6245):255-60. doi: 10.1126/science.aaa8415.

Kaushal, R. K., A. Sarkar, K. Mishra, R. Sinha, S. Nepal, and V. Jain. 2020. "Spatio-temporal variability in stream power distribution in the Upper Kosi River basin, Central Himalaya: Controls and geomorphic implications." Geomorphology 350. doi: 10.1016/j.geomorph.2019.106888.

Keylock, C. J. 2005. "Simpson diversity and the Shannon-Wiener index as special cases of a generalized entropy." Oikos 109 (1):203-7. doi: 10.1111/j.0030-1299.2005.13735.x.

Khatami, R., G. Mountrakis, and S. V. Stehman. 2016. "A meta-analysis of remote sensing research on supervised pixel-based land-cover image classification processes: General guidelines for practitioners and future research." Remote Sensing of Environment 177:89-100. doi: 10.1016/j.rse.2016.02.028.

Kim, C. R. 2019. "Framework of Extreme Flood Risk Management in the Typhoon Country Region." Tropical Cyclone Research and Review 8 (1):35-45. doi: 10.6057/2019tcrr01.01.

Kleinhans, M. G. 2010. "Sorting out river channel patterns." Progress in Physical Geography: Earth and Environment 34 (3):287-326. doi: 10.1177/0309133310365300.

Kleinhans, M. G., and J. H. van den Berg. 2011. "River channel and bar patterns explained and predicted by an empirical and a physics-based method." Earth Surface Processes and Landforms 36 (6):721-38. doi: 10.1002/esp.2090.

Knudby, A., S. K. Ahmad, and C. Ilori. 2016. "The Potential for Landsat-Based Bathymetry in Canada." Canadian Journal of Remote Sensing 42 (4):367-78. doi: 10.1080/07038992.2016.1177452.

Kondolf, G. Mathias, Hervé Piégay, Laurent Schmitt, and David R. Montgomery. 2016. "Geomorphic classification of rivers and streams." In Tools in Fluvial Geomorphology, 133-58.

Kong, Y. L., Y. Meng, W. Li, A. Z. Yue, and Y. Yuan. 2015. "Satellite Image Time Series Decomposition Based on EEMD." Remote Sensing 7 (11):15583-604. doi: 10.3390/rs71115583.

Korhonen, L., Hadi, P. Packalen, and M. Rautiainen. 2017. "Comparison of Sentinel-2 and Landsat 8 in the estimation of boreal forest canopy cover and leaf area index." Remote Sensing of Environment 195:259-74. doi: 10.1016/j.rse.2017.03.021.

Kuan, H. F., J. Li, X. J. Zhang, J. P. Zhang, H. Cui, and Q. Sun. 2020. "Remote Estimation of Water Quality Parameters of Medium- and Small-Sized Inland Rivers Using Sentinel-2 Imagery." Water 12 (11). doi: 10.3390/w12113124.

Kubota, H., R. Shirooka, J. Matsumoto, E. O. Cayanan, and F. D. Hilario. 2017. "Tropical cyclone influence on the long-term variability of Philippine summer monsoon onset." Progress in Earth and Planetary Science 4. doi: 10.1186/s40645-017-0138-5.

Lagmay, A. M. F. A., B. A. Racoma, K. A. Aracan, J. Alconis-Ayco, and I. L. Saddi. 2017. "Disseminating near-real-time hazards information and flood maps in the Philippines through Web-GIS." Journal of Environmental Sciences 59:13-23. doi: 10.1016/j.jes.2017.03.014.

Lanaras, C., J. Bioucas-Dias, S. Galliani, E. Baltsavias, and K. Schindler. 2018. "Super-resolution of Sentinel-2 images: Learning a globally applicable deep neural network." Isprs Journal of Photogrammetry and Remote Sensing 146:305-19. doi: 10.1016/j.isprsjprs.2018.09.018.

Laso, F. J., F. L. Benitez, G. Rivas-Torres, C. Sampedro, and J. Arce-Nazario. 2020. "Land Cover Classification of Complex Agroecosystems in the Non-Protected Highlands of the Galapagos Islands." Remote Sensing 12 (1). doi: 10.3390/rs12010065.

Laszuk D. 2017. PyEMD: Python implementation of Empirical Mode Decompoisition (EMD) method. Available: https://github.com/laszukdawid/PyEMD. Accessed: 10/02/2023.

Latrubesse, E. M., J. C. Stevaux, and R. Sinha. 2005. "Tropical rivers." Geomorphology 70 (3-4):187-206. doi: 10.1016/j.geomorph.2005.02.005.

Lei, Y. G., Z. J. He, and Y. Y. Zi. 2009. "Application of the EEMD method to rotor fault diagnosis of rotating machinery." Mechanical Systems and Signal Processing 23 (4):1327-38. doi: 10.1016/j.ymssp.2008.11.005.

Leopold, L. B., and M. G. Wolman. 1957. "River channel patterns: Braided, meandering, and straight." doi: 10.3133/pp282B.

Li, A. B., T. T. Dong, S. Y. Xu, X. L. Xie, and H. Chen. 2022. "Automatic detection of fault-controlled rivers using spatial pattern matching." Computers & Geosciences 169. doi: 10.1016/j.cageo.2022.105246.

Li, J. L., and Y. W. Sheng. 2012. "An automated scheme for glacial lake dynamics mapping using Landsat imagery and digital elevation models: a case study in the Himalayas." International Journal of Remote Sensing 33 (16):5194-213. doi: 10.1080/01431161.2012.657370.

Li, Q., B. Barrett, R. Williams, T. Hoey, and R. Boothroyd. 2022. "Enhancing performance of multi-temporal tropical river landform classification through downscaling approaches." International Journal of Remote Sensing 43 (17):6445-62. doi: 10.1080/01431161.2022.2139164.

Li, Q., R. Williams, T. Hoey, B. Barrett, and R. Boothroyd. 2023. "Seasonal and annual tropical river pattern change detection using machine learning." Preprint, doi: 10.31223/x5d66g.

Li, Y., B. Dang, Y. Zhang, and Z. Du. 2022. "Water body classification from high-resolution optical remote sensing imagery: Achievements and perspectives." Isprs Journal of Photogrammetry and Remote Sensing 187:306-27. doi: 10.1016/j.isprsjprs.2022.03.013.

Li, Z., C. Yan, and M. W. Boota. 2022. "Review and outlook of river morphology expression." Journal of Water and Climate Change 13 (4):1725-47. doi: 10.2166/wcc.2022.449.

Liu, H. Y., S. M. Chen, W. B. Li, R. Fang, Z. Li, and Y. S. Wu. 2019. "Atmospheric Response to Oceanic Cold Eddies West of Luzon in the Northern South China Sea." Atmosphere 10 (5). doi: 10.3390/atmos10050255.

Liu, J. G., E. Pattey, M. C. Nolin, J. R. Miller, and O. Ka. 2008. "Mapping within-field soil drainage using remote sensing, DEM and apparent soil electrical conductivity." Geoderma 143 (3-4):261-72. doi: 10.1016/j.geoderma.2007.11.011.

Liu, T., L. X. Yang, and D. Lunga. 2021. "Change detection using deep learning approach with object-based image analysis." Remote Sensing of Environment 256. doi: 10.1016/j.rse.2021.112308.

Liu, Z. F., Y. L. Zhao, C. Colin, F. P. Siringan, and Q. Wu. 2009. "Chemical weathering in Luzon, Philippines from clay mineralogy and major-element geochemistry of river sediments." Applied Geochemistry 24 (11):2195-205. doi: 10.1016/j.apgeochem.2009.09.025.

Lopez-Fuentes, L., C. Rossi, and H. Skinnemoen. 2017. "River segmentation for flood monitoring." 2017 IEEE International Conference on Big Data (Big Data):3746-9. doi: 10.1109/BigData.2017.8258373.

Lu, D., P. Mausel, E. Brondízio, and E. Moran. 2010. "Change detection techniques." International Journal of Remote Sensing 25 (12):2365-401. doi: 10.1080/0143116031000139863.

Luo, X., H. Xie, X. Xu, H. Y. Pan, and X. H. Tong. 2016. "A hierarchical processing method for subpixel surface water mapping from highly heterogeneous urban environments using Landsat OLI data." 2016 Ieee International Geoscience and Remote Sensing Symposium (Igarss):6221-4. doi: 10.1109/Igarss.2016.7730625.

Ma, L., M. C. Li, X. X. Ma, L. Cheng, P. J. Du, and Y. X. Liu. 2017. "A review of supervised object-based land-cover image classification." Isprs Journal of Photogrammetry and Remote Sensing 130:277-93. doi: 10.1016/j.isprsjprs.2017.06.001.

Magesh, N. S., K. V. Jitheshlal, N. Chandrasekar, and K. V. Jini. 2013. "Geographical information system-based morphometric analysis of Bharathapuzha river basin, Kerala, India." Applied Water Science 3 (2):467-77. doi: 10.1007/s13201-013-0095-0.

Main-Knorn, M., B. Pflug, J. Louis, V. Debaecker, U. Muller-Wilm, and F. Gascon. 2017. "Sen2Cor for Sentinel-2." Image and Signal Processing for Remote Sensing Xxiii 10427. doi: 10.1117/12.2278218.

Mainali, J., and H. Chang. 2018. "Landscape and anthropogenic factors affecting spatial patterns of water quality trends in a large river basin, South Korea." Journal of Hydrology 564:26-40. doi: 10.1016/j.jhydrol.2018.06.074.

Mandarino, A., M. Maerker, and M. Firpo. 2019. "Channel planform changes along the Scrivia River floodplain reach in northwest Italy from 1878 to 2016." Quaternary Research 91 (2):620-37. doi: 10.1017/qua.2018.67.

Matsushita, B., W. Yang, G. L. Yu, Y. Oyama, K. Yoshimura, and T. Fukushima. 2015. "A hybrid algorithm for estimating the chlorophyll-a concentration across different trophic states in Asian inland waters." Isprs Journal of Photogrammetry and Remote Sensing 102:28-37. doi: 10.1016/j.isprsjprs.2014.12.022.

Maxwell, A. E., T. A. Warner, and F. Fang. 2018. "Implementation of machine-learning classification in remote sensing: an applied review." International Journal of Remote Sensing 39 (9):2784-817. doi: 10.1080/01431161.2018.1433343.

Melis, M. T., S. Da Pelo, I. Erbi, M. Loche, G. Deiana, V. Demurtas, M. A. Meloni, et al. 2020. "Thermal Remote Sensing from UAVs: A Review on Methods in Coastal Cliffs Prone to Landslides." Remote Sensing 12 (12). doi: 10.3390/rs12121971.

Menting, F., A. L. Langston, and A. J. A. M. Temme. 2015. "Downstream fining, selective transport, and hillslope influence on channel bed sediment in mountain streams, Colorado Front Range, USA." Geomorphology 239:91-105. doi: 10.1016/j.geomorph.2015.03.018.

Milliman, J. D., and R. H. Meade. 1983. "World-Wide Delivery of River Sediment to the Oceans." The Journal of Geology 91 (1):1-21. doi: 10.1086/628741.

Milly, P. C. D. 1994. "Climate, Soil-Water Storage, and the Average Annual Water-Balance." Water Resources Research 30 (7):2143-56. doi: 10.1029/94wr00586.

Ming, D. P., J. Y. Yang, L. X. Li, and Z. Q. Song. 2011. "Modified ALV for selecting the optimal spatial resolution and its scale effect on image classification accuracy." Mathematical and Computer Modelling 54 (3-4):1061-8. doi: 10.1016/j.mcm.2010.11.036.

Mobley, C. D, and C. D. Mobley. 1994. Light and water: radiative transfer in natural waters. Academic, San Diego.

Mohguen, W., and R. E. Bekka. 2015. "Improvement of Ensemble Empirical Mode Decomposition by a Band-Limited White Noise." 2015 4th International Conference on Electrical Engineering (ICEE), Boumerdes, Algeria, 2015, pp. 1-4, doi: 10.1109/INTEE.2015.7416816.

Nagendra, H. 2002. "Opposite trends in response for the Shannon and Simpson indices of landscape diversity." Applied Geography 22 (2):175-86. doi: 10.1016/s0143-6228(02)00002-4.

Naik, N., R. Seager, and G. A. Vecchi. 2010. "Thermodynamic and Dynamic Mechanisms for Large-Scale Changes in the Hydrological Cycle in Response to Global Warming*." Journal of Climate 23 (17):4651-68. doi: 10.1175/2010jcli3655.1.

Nalepa, J. 2021. "Recent Advances in Multi- and Hyperspectral Image Analysis." Sensors 21 (18). doi: 10.3390/s21186002.

Nanson, G. C., and J. C. Croke. 1992. "A genetic classification of floodplains." Geomorphology 4 (6):459-86. doi: 10.1016/0169-555x(92)90039-q.

Nanson, G. C., and A. D. Knighton. 1996. "Anabranching rivers: Their cause, character and classification." Earth Surface Processes and Landforms 21 (3):217-39. doi: 10.1002/(SICI)1096-9837(199603)21:3<217::AID-ESP611>3.0.CO;2-U

Nass, A., S. van Gasselt, R. Jaumann, and H. Asche. 2011. "Implementation of cartographic symbols for planetary mapping in geographic information systems." Planetary and Space Science 59 (11-12):1255-64. doi: 10.1016/j.pss.2010.08.022.

Nelson, S. A. C., K. S. Cheruvelil, and P. A. Soranno. 2006. "Satellite remote sensing of freshwater macrophytes and the influence of water clarity." Aquatic Botany 85 (4):289-98. doi: 10.1016/j.aquabot.2006.06.003.

Newson, M. D., M. J. Clark, D. A. Sear, and A. Brookes. 1998. "The geomorphological basis for classifying rivers." Aquatic Conservation: Marine and Freshwater Ecosystems 8 (4):415-30. doi: 10.1002/(sici)1099-0755(199807/08)8:4<415::Aid-aqc276>3.0.Co;2-6.

Nikora, V. I. 1991. "Fractal Structures of River Plan Forms." Water Resources Research 27 (6):1327-33. doi: 10.1029/91wr00095.

Nur, A. A., I. Syafri, D. Muslims, F. Hirnawan, P. P. Raditya, M. Sulastri, and F. Abdulah. 2016. "Fractal Characteristics of Geomorphology Units as Bouguer Anomaly Manifestations in Bumiayu, Central Java, Indonesia." Padjadjaran Earth Dialogues: International Symposium on Geophysical Issues, Pedisgi 29. doi: 10.1088/1755-1315/29/1/012019.

Odermatt, D., A. Gitelson, V. E. Brando, and M. Schaepman. 2012. "Review of constituent retrieval in optically deep and complex waters from satellite imagery." Remote Sensing of Environment 118:116-26. doi: 10.1016/j.rse.2011.11.013.

Ohsaki, M., P. Wang, K. Matsuda, S. Katagiri, H. Watanabe, and A. Ralescu. 2017. "Confusion-Matrix-Based Kernel Logistic Regression for Imbalanced Data Classification." Ieee Transactions on Knowledge and Data Engineering 29 (9):1806-19. doi: 10.1109/Tkde.2017.2682249.

Omer, A., N. A. Elagib, Z. G. Ma, F. Saleem, and A. Mohammed. 2020. "Water scarcity in the Yellow River Basin under future climate change and human activities." Science of the Total Environment 749. doi: 10.1016/j.scitotenv.2020.141446.

Paola, C. 2017. "A Mind of Their Own: Recent Advances in Autogenic Dynamics in Rivers and Deltas." In Autogenic Dynamics and Self-Organization in Sedimentary Systems, 5-17. doi: 10.2110/sepmsp.106.04.

Park, K. A., J. E. Park, and C. K. Kang. 2022. "Satellite-Observed Chlorophyll-a Concentration Variability in the East Sea (Japan Sea): Seasonal Cycle, Long-Term Trend, and Response to Climate Index." Frontiers in Marine Science 9. doi: 10.3389/fmars.2022.807570.

Pentland, A. P. 1984. "Fractal-Based Description of Natural Scenes." Ieee Transactions on Pattern Analysis and Machine Intelligence 6 (6):661-74. doi: 10.1109/Tpami.1984.4767591.

Phillips, J. D. 2010. "The job of the river." Earth Surface Processes and Landforms 35 (3):305-13. doi: 10.1002/esp.1915.

Phiri, D., M. Simwanda, and V. Nyirenda. 2021. "Mapping the impacts of cyclone Idai in Mozambique using Sentinel-2 and OBIA approach." South African Geographical Journal 103 (2):237-58. doi: 10.1080/03736245.2020.1740104.

Phiri, D., M. Simwanda, S. Salekin, V. R. Nyirenda, Y. Murayama, and M. Ranagalage. 2020. "Sentinel-2 Data for Land Cover/Use Mapping: A Review." Remote Sensing 12 (14). doi: 10.3390/rs12142291.

PHIVOLCS, Philippine Institute of Volcanology and Seismology. 2015. "Distribution of active faults and trenches in the Philippines map." https://www.phivolcs.dost.gov.ph/index.php/earthquake/earthquake-1110generators-of-the-philippines. Accessed: 20 July 2021.

Pinardi, M., E. Soana, E. Severini, E. Racchetti, F. Celico, and M. Bartoli. 2022. "Agricultural practices regulate the seasonality of groundwater-river nitrogen exchanges." Agricultural Water Management 273. doi: 10.1016/j.agwat.2022.107904.

Prakash, N., A. Manconi, and S. Loew. 2020. "Mapping Landslides on EO Data: Performance of Deep Learning Models vs. Traditional Machine Learning Models." Remote Sensing 12 (3). doi: 10.3390/rs12030346.

Rabanaque, M. P., V. Martinez-Fernandez, M. Calle, and G. Benito. 2022. "Basin-wide hydromorphological analysis of ephemeral streams using machine learning algorithms." Earth Surface Processes and Landforms 47 (1):328-44. doi: 10.1002/esp.5250.

Rapinel, S., C. Mony, L. Lecoq, B. Clément, A. Thomas, and L. Hubert-Moy. 2019. "Evaluation of Sentinel-2 time-series for mapping floodplain grassland plant communities." Remote Sensing of Environment 223:115-29. doi: 10.1016/j.rse.2019.01.018.

Raven, E. K., S. N. Lane, R. I. Ferguson, and L. J. Bracken. 2009. "The spatial and temporal patterns of aggradation in a temperate, upland, gravel-bed river." Earth Surface Processes and Landforms 34 (9):1181-97. doi: 10.1002/esp.1783.

Reid, H. E., and G. J. Brierley. 2015. "Assessing geomorphic sensitivity in relation to river capacity for adjustment." Geomorphology 251:108-21. doi: 10.1016/j.geomorph.2015.09.009.

Ren, X. F., and J. Malik. 2003. "Learning a classification model for segmentation." Ninth IEEE International Conference on Computer Vision, Vols I and Ii, Proceedings:10-7. doi: 10.1109/ICCV.2003.1238308

Rice, S. P. 2017. "Tributary connectivity, confluence aggradation and network biodiversity." Geomorphology 277:6-16. doi: 10.1016/j.geomorph.2016.03.027.

Rice, S. P., M. Church, C. L. Wooldridge, and E. J. Hickin. 2009. "Morphology and evolution of bars in a wandering gravel-bed river; lower Fraser river, British Columbia, Canada." Sedimentology 56 (3):709-36. doi: 10.1111/j.1365-3091.2008.00994.x.

Rice, S., and M. Church. 1998. "Grain size along two gravel-bed rivers: statistical variation, spatial pattern and sedimentary links." Earth Surface Processes and Landforms 23 (4):345-63. doi: 10.1002/(SICI)1096-9837(199804)23:4<345::AID-ESP850>3.0.CO;2-B.

Richardson, T. B., P. M. Forster, T. Andrews, O. Boucher, G. Faluvegi, D. Fläschner, Ø Hodnebrog, et al. 2018. "Drivers of Precipitation Change: An Energetic Understanding." Journal of Climate 31 (23):9641-57. doi: 10.1175/jcli-d-17-0240.1.

Rodrigues, M. O., N. Abrantes, F. J. M. Goncalves, H. Nogueira, J. C. Marques, and A. M. M. Goncalves. 2018. "Spatial and temporal distribution of microplastics in water and sediments of a freshwater system (Antua River, Portugal)." Science of the Total Environment 633:1549-59. doi: 10.1016/j.scitotenv.2018.03.233.

Rokni, K., A. Ahmad, A. Selamat, and S. Hazini. 2014. "Water Feature Extraction and Change Detection Using Multitemporal Landsat Imagery." Remote Sensing 6 (5):4173-89. doi: 10.3390/rs6054173.

Rowan, G. S. L., and M. Kalacska. 2021. "A Review of Remote Sensing of Submerged Aquatic Vegetation for Non-Specialists." Remote Sensing 13 (4). doi: 10.3390/rs13040623.

Roy, D. P., and O. Dikshit. 1994. "Investigation of Image Resampling Effects Upon the Textural Information-Content of a High-Spatial-Resolution Remotely-Sensed Image." International Journal of Remote Sensing 15 (5):1123-30. doi: 10.1080/01431169408954146.

Rusnak, M., J. Sladek, A. Kidova, and M. Lehotsky. 2018. "Template for high-resolution river landscape mapping using UAV technology." Measurement 115:139-51. doi: 10.1016/j.measurement.2017.10.023.

Salama, M. S., L. Spaias, K. Poser, S. Peters, and M. Laanen. 2022. "Validation of Sentinel-2 (MSI) and Sentinel-3 (OLCI) Water Quality Products in Turbid Estuaries Using Fixed Monitoring Stations." Frontiers in Remote Sensing 2. doi: 10.3389/frsen.2021.808287.

Saleem, A., A. Dewan, M. M. Rahman, S. M. Nawfee, R. Karim, and X. X. Lu. 2020. "Spatial and Temporal Variations of Erosion and Accretion: A Case of a Large Tropical River." Earth Systems and Environment 4 (1):167-81. doi: 10.1007/s41748-019-00143-8.

Schick, A., and R. Stiefelhagen. 2011. "Evaluating Image Segments by Applying the Description Length to Sets of Superpixels." 2011 IEEE International Conference on Computer Vision Workshops (Iccv Workshops). doi: 10.1109/ICCVW.2011.6130414.

Schmitt, M. 2020. "Potential of Large-Scale Inland Water Body Mapping from Sentinel-1/2 Data on the Example of Bavaria's Lakes and Rivers." Pfg-Journal of Photogrammetry Remote Sensing and Geoinformation Science 88 (3-4):271-89. doi: 10.1007/s41064-020-00111-2.

Schneider, W. F., and H. Guo. 2018. "Machine Learning." Journal of Physical Chemistry C 122 (4):1889-. doi: 10.1021/acs.jpcc.8b00036.

Schumm, S. A. 1960. "The effect of sediment type on the shape and stratification of some modern fluvial deposits." American Journal of Science 258 (3):177-84. doi: 10.2475/ajs.258.3.177.

Schumm, S. A. 1985. "PATTERNS OF ALLUVIAL RIVERS." Annual Review of Earth and Planetary Sciences 13 (1):5-27. doi: 10.1146/annurev.ea.13.050185.000253.

Schumm, S. A. 1963. "A tentative classification of alluvial river channels an examination of similarities and differences among some Great Plains rivers." In Circular. doi: 10.3133/cir477

Selva, M., B. Aiazzi, F. Butera, L. Chiarantini, and S. Baronti. 2015. "Hyper-Sharpening: A First Approach on SIM-GA Data." Ieee Journal of Selected Topics in Applied Earth Observations and Remote Sensing 8 (6):3008-24. doi: 10.1109/Jstars.2015.2440092.

Serlet, A. J., A. M. Gurnell, G. Zolezzi, G. Wharton, P. Belleudy, and C. Jourdain. 2018. "Biomorphodynamics of alternate bars in a channelized, regulated river: An integrated historical and modelling analysis." Earth Surface Processes and Landforms 43 (9):1739-56. doi: 10.1002/esp.4349.

Setti, S., R. Maheswaran, D. Radha, V. Sridhar, K. K. Barik, and M. L. Narasimham. 2020. "Attribution of Hydrologic Changes in a Tropical River Basin to Rainfall Variability and Land-Use Change: Case Study from India." Journal of Hydrologic Engineering 25 (8). doi: 10.1061/(Asce)He.1943-5584.0001937.

Shen, X. H., L. J. Zou, G. F. Zhang, N. Su, W. Y. Wu, and S. F. Yang. 2011. "Fractal characteristics of the main channel of Yellow River and its relation to regional tectonic evolution." Geomorphology 127 (1-2):64-70. doi: 10.1016/j.geomorph.2010.12.007.

Simon, J. D., H. S. S. Gregory, L. B. James, P. N. Andrew, M. B. Jon, E. V. Mark, H. S. Maminul, and G. Steven. 2018. "The planform mobility of river channel confluences: Insights from analysis of remotely sensed imagery." Earth-Science Reviews 176:1-18. doi: 10.1016/j.earscirev.2017.09.009.

Simpson, E. H. 1949. "Measurement of Diversity." Nature 163 (4148):688-. doi: 10.1038/163688a0.

Singer, M. B. 2008. "Downstream patterns of bed material grain size in a large, lowland alluvial river subject to low sediment supply." Water Resources Research 44 (12). doi: 10.1029/2008wr007183.

Singh, A. 1989. "Digital Change Detection Techniques Using Remotely-Sensed Data." International Journal of Remote Sensing 10 (6):989-1003. doi: Doi 10.1080/01431168908903939.

Singh, A. 2010. "Review Article Digital change detection techniques using remotely-sensed data." International Journal of Remote Sensing 10 (6):989-1003. doi: 10.1080/01431168908903939.

Singh, U., A. Crosato, S. Giri, and M. Hicks. 2017. "Sediment heterogeneity and mobility in the morphodynamic modelling of gravel-bed braided rivers." Advances in Water Resources 104:127-44. doi: 10.1016/j.advwatres.2017.02.005.

Slater, J. A., G. Garvey, C. Johnston, J. Haase, B. Heady, G. Kroenung, and J. Little. 2006. "The SRTM data "finishing" process and products." Photogrammetric Engineering and Remote Sensing 72 (3):237-47. doi: 10.14358/Pers.72.3.237.

Smith, D. G., and N. D. Smith. 1980. "Sedimentation in Anastomosed River Systems - Examples from Alluvial Valleys near Banff, Alberta." Journal of Sedimentary Petrology 50 (1):157-64. doi: 10.1306/212f7991-2b24-11d7-8648000102c1865d.

Smith, N. D., G. S. Morozova, M. Perez-Arlucea, and M. R. Gibling. 2016. "Dam-induced and natural channel changes in the below the EB Campbell Dam, Canada." Geomorphology 269:186-202. doi: 10.1016/j.geomorph.2016.06.041.

Soar, P. J., N. P. Wallerstein, and C. R. Thorne. 2017. "Quantifying River Channel Stability at the Basin Scale." Water 9 (2). doi: 10.3390/w9020133.

Song, K., J. Ma, Z. Wen, C. Fang, Y. Shang, Y. Zhao, M.Wang, and J. Du. 2017. "Remote estimation of Kd (PAR) using MODIS and Landsat imagery for turbid inland waters in Northeast China." Isprs Journal of Photogrammetry and Remote Sensing 123:159-72. doi: 10.1016/j.isprsjprs.2016.11.010.

Song, Y., Y. Q. Wu, and Y. M. A. Dai. 2016. "A new active contour remote sensing river image segmentation algorithm inspired from the cross entropy." Digital Signal Processing 48:322-32. doi: 10.1016/j.dsp.2015.10.005.

Sonobe, R., Y. Yamaya, H. Tani, X. F. Wang, N. Kobayashi, and K. Mochizuki. 2018. "Crop classification from Sentinel-2-derived vegetation indices using ensemble learning." Journal of Applied Remote Sensing 12 (2). doi: 10.1117/1.Jrs.12.026019.

Sokolova, M., N. Japkowicz, and S. Szpakowicz. 2006. "Beyond accuracy, F-Score and ROC: A family of discriminant measures for performance evaluation." In: Sattar, A., Kang, Bh. (eds) AI 2006: Advances in Artificial Intelligence. AI 2006. Lecture Notes in Computer Science, vol 4304. Springer, Berlin, Heidelberg. doi: 10.1007/11941439_114.

Spada, D., P. Molinari, W. Bertoldi, A. Vitti, and G. Zolezzi. 2018. "Multi-Temporal Image Analysis for Fluvial Morphological Characterization with Application to Albanian Rivers." Isprs International Journal of Geo-Information 7 (8). doi: 10.3390/ijgi7080314.

Swanson, B. J., and G. Meyer. 2014. "Tributary confluences and discontinuities in channel form and sediment texture: Rio Chama, NM." Earth Surface Processes and Landforms 39 (14):1927-43. doi: 10.1002/esp.3586.

Syvitski, J. P. M., S. Cohen, A. J. Kettner, and G. R. Brakenridge. 2014. "How important and different are tropical rivers? - An overview." Geomorphology 227:5-17. doi: 10.1016/j.geomorph.2014.02.029.

Talukdar, S., P. Singha, S. Mahato, Shahfahad, S. Pal, Y. A. Liou, and A. Rahman. 2020. "Land-Use Land-Cover Classification by Machine Learning Classifiers for Satellite Observations-A Review." Remote Sensing 12 (7). doi: 10.3390/rs12071135.

Tarpanelli, A., S. Camici, K. Nielsen, L. Brocca, T. Moramarco, and J. Benveniste. 2021. "Potentials and limitations of Sentinel-3 for river discharge assessment." Advances in Space Research 68 (2):593-606. doi: 10.1016/j.asr.2019.08.005.

Théau, J. 2022. "Change Detection." (eds) Springer Handbook of Geographic Information. Springer Handbooks. Springer, Cham. doi: 10.1007/978-3-030-53125-6_7

Tolentino, P. L. M., J. E. G. Perez, E. L. Guardian, R. J. Boothroyd, T. B. Hoey, R. D. Williams, K. A. Fryirs, G. J. Brierley, and C. P. C. David. 2022. "River Styles and stream power analysis reveal the diversity of fluvial morphology in a Philippine tropical catchment." Geoscience Letters 9 (1). doi: 10.1186/s40562-022-00211-4.

Tolentino, P. L. M., A. Poortinga, H. Kanamaru, S. Keesstra, J. Maroulis, C. P. C. David, and C. J. Ritsema. 2016. "Projected Impact of Climate Change on Hydrological Regimes in the Philippines." Plos One 11 (10). doi: 10.1371/journal.pone.0163941.

Torres, M. E., M. A. Colominas, G. Schlotthauer, and P. Flandrin. 2011. "A Complete Ensemble Empirical Mode Decomposition with Adaptive Noise." 2011 IEEE International Conference on Acoustics, Speech, and Signal Processing:4144-7. doi: 10.1109/ICASSP.2011.5947265.

Townshend, J. R. G., and C. O. Justice. 1986. "Analysis of the Dynamics of African Vegetation Using the Normalized Difference Vegetation Index." International Journal of Remote Sensing 7 (11):1435-45. doi: 10.1080/01431168608948946.

van Oorschot, M., M. Kleinhans, G. Geerling, and H. Middelkoop. 2016. "Distinct patterns of interaction between vegetation and morphodynamics." Earth Surface Processes and Landforms 41 (6):791-808. doi: 10.1002/esp.3864.

van Vliet, Michelle T. H., Wietse H. P. Franssen, John R. Yearsley, Fulco Ludwig, Ingjerd Haddeland, Dennis P. Lettenmaier, and Pavel Kabat. 2013. "Global river discharge and water temperature under climate change." Global Environmental Change 23 (2):450-64. doi: 10.1016/j.gloenvcha.2012.11.002.

Vargas-Luna, A., G. Duro, A. Crosato, and W. Uijttewaal. 2019. "Morphological Adaptation of River Channels to Vegetation Establishment: A Laboratory Study." Journal of Geophysical Research-Earth Surface 124 (7):1981-95. doi: 10.1029/2018jf004878.

Veettil, B. K., J. Li, B. Peng, Y. Wei, and H. Ye. 2021. "Accurate extraction of surface water in complex environment based on Google Earth Engine and Sentinel-2." Plos One 16 (6). doi: 10.1371/journal.pone.0253209.

Veloria, A., G. J. Perez, G. Tapang, and J. Comiso. 2021. "Improved Rainfall Data in the Philippines through Concurrent Use of GPM IMERG and Ground-Based Measurements." Remote Sensing 13 (15). doi: 10.3390/rs13152859.

Vercruysse, K., and R. C. Grabowski. 2021. "Human impact on river planform within the context of multi-timescale river channel dynamics in a Himalayan river system." Geomorphology 381. doi: 10.1016/j.geomorph.2021.107659.

Vijith, H., and D. Dodge-Wan. 2018. "Morphology and channel characteristics of an equatorial tropical river in Malaysian Borneo: a detailed evaluation through spatially explicit geomorphometric modelling." Modeling Earth Systems and Environment 4 (1):325-37. doi: 10.1007/s40808-017-0407-8.

Wang, C., and H. Zhang. 2020. "Trend and Variance of Continental Fresh Water Discharge over the Last Six Decades." Water 12 (12). doi: 10.3390/w12123556.

Wang, Q. M., W. Z. Shi, P. M. Atkinson, and Y. L. Zhao. 2015. "Downscaling MODIS images with area-to-point regression kriging." Remote Sensing of Environment 166:191-204. doi: 10.1016/j.rse.2015.06.003.

Wang, Q. M., W. Z. Shi, Z. B. Li, and P. M. Atkinson. 2016. "Fusion of Sentinel-2 images." Remote Sensing of Environment 187:241-52. doi: 10.1016/j.rse.2016.10.030.

Wang, X., and H. Xie. 2018. "A Review on Applications of Remote Sensing and Geographic Information Systems (GIS) in Water Resources and Flood Risk Management." Water 10 (5). doi: 10.3390/w10050608.

Ward, J. V., F. Malard, and K. Tockner. 2002. "Landscape ecology: a framework for integrating pattern and process in river corridors." Landscape Ecology 17:35-45. doi: 10.1023/A:1015277626224.

Watanabe, F., D. R. Mishra, I. Astuti, T. Rodrigues, E. Alcantara, N. N. Imai, and C. Barbosa. 2016. "Parametrization and calibration of a quasi-analytical algorithm for tropical eutrophic waters." Isprs Journal of Photogrammetry and Remote Sensing 121:28-47. doi: 10.1016/j.isprsjprs.2016.08.009.

Welber, M., W. Bertoldi, and M. Tubino. 2012. "The response of braided planform configuration to flow variations, bed reworking and vegetation: the case of the Tagliamento River, Italy." Earth Surface Processes and Landforms 37 (5):572-82. doi: 10.1002/esp.3196.

Werner, W. J., J. Sanderman, and J. M. Melillo. 2020. "Decreased Soil Organic Matter in a Long-Term Soil Warming Experiment Lowers Soil Water Holding Capacity and Affects Soil Thermal and Hydrological Buffering." Journal of Geophysical Research-Biogeosciences 125 (4). doi: 10.1029/2019JG005158.

White, M. S., B. G. Tavernia, P. B. Shafroth, T. B. Chapman, and J. S. Sanderson. 2018. "Vegetative and geomorphic complexity at tributary junctions on the Colorado and Dolores Rivers: a blueprint for riparian restoration." Landscape Ecology 33 (12):2205-20. doi: 10.1007/s10980-018-0734-9.

Wichmann, A. 1904. "Volcanoes and seismic centers of the Philippine Archipelago. Census of the Philippine Islands." Petermanns Mitteilungen 50 (12): A204-A5.

Wilson, E. H., and S. A. Sader. 2002. "Detection of forest harvest type using multiple dates of Landsat TM imagery." Remote Sensing of Environment 80 (3):385-96. doi: 10.1016/S0034-4257(01)00318-2.

Xie, Y., Z. Sha, and M. Yu. 2008. "Remote sensing imagery in vegetation mapping: a review." Journal of Plant Ecology 1 (1):9-23. doi: 10.1093/jpe/rtm005.

Xu, X. B., G. S. Yang, Y. Tan, J. P. Liu, and H. Z. Hu. 2018. "Ecosystem services trade-offs and determinants in China's Yangtze River Economic Belt from 2000 to 2015." Science of the Total Environment 634:1601-14. doi: 10.1016/j.scitotenv.2018.04.046.

Xu, X. J., H. Y. Liu, Z. S. Lin, F. S. Jiao, and H. B. Gong. 2019. "Relationship of Abrupt Vegetation Change to Climate Change and Ecological Engineering with Multi-Timescale Analysis in the Karst Region, Southwest China." Remote Sensing 11 (13). doi: 10.3390/rs11131564.

Yang, C. T., and J. B. Stall. 1974. Unit Stream Power for Sediment Transport in Natural Rivers. http://hdl.handle.net/2142/90150.

Yang, X. C., S. S. Zhao, X. B. Qin, N. Zhao, and L. G. Liang. 2017. "Mapping of Urban Surface Water Bodies from Sentinel-2 MSI Imagery at 10 m Resolution via NDWI-Based Image Sharpening." Remote Sensing 9 (6). doi: 10.3390/rs9060596.

Yang, X. J., and C. P. Lo. 2000. "Relative radiometric normalization performance for change detection from multi-date satellite images." Photogrammetric Engineering and Remote Sensing 66 (8):967-80.

Ye, S., R. G. Pontius, and R. Rakshit. 2018. "A review of accuracy assessment for object-based image analysis: From per-pixel to per-polygon approaches." Isprs Journal of Photogrammetry and Remote Sensing 141:137-47. doi: 10.1016/j.isprsjprs.2018.04.002.

Yu, D., P. Shi, Y. Liu, and B. Xun. 2013. "Detecting land use-water quality relationships from the viewpoint of ecological restoration in an urban area." Ecological Engineering 53:205-16. doi: 10.1016/j.ecoleng.2012.12.045.

Zámolyi, A., B. Székely, E. Draganits, and G. Timár. 2010. "Neotectonic control on river sinuosity at the western margin of the Little Hungarian Plain." Geomorphology 122 (3-4):231-43. doi: 10.1016/j.geomorph.2009.06.028.

Zeng, C. Q., M. Richardson, and D. J. King. 2017. "The impacts of environmental variables on water reflectance measured using a lightweight unmanned aerial vehicle (UAV)-based spectrometer system." Isprs Journal of Photogrammetry and Remote Sensing 130:217-30. doi: 10.1016/j.isprsjprs.2017.06.004.

Zhang, C. Y., and Z. X. Xie. 2013. "Object-based Vegetation Mapping in the Kissimmee River Watershed Using HyMap Data and Machine Learning Techniques." Wetlands 33 (2):233-44. doi: 10.1007/s13157-012-0373-x.

Zhao, Y. F., X. Q. Zou, Q. Liu, Y. L. Yao, Y. L. Li, X. W. Wu, C. L. Wang, W. W. Yu, and T. Wang. 2017. "Assessing natural and anthropogenic influences on water discharge and sediment load in the Yangtze River, China." Science of the Total Environment 607:920-32. doi: 10.1016/j.scitotenv.2017.07.002.

Zheng, H. R., P. J. Du, J. K. Chen, J. S. Xia, E. Z. Li, Z. G. Xu, X. J. Li, and N. Yokoya. 2017. "Performance Evaluation of Downscaling Sentinel-2 Imagery for Land Use and Land Cover Classification by Spectral-Spatial Features." Remote Sensing 9 (12). doi: 10.3390/rs9121274.

Zhu, L. C., and A. Malekjafarian. 2019. "On the Use of Ensemble Empirical Mode Decomposition for the Identification of Bridge Frequency from the Responses Measured in a Passing Vehicle." Infrastructures 4 (2). doi: 10.3390/infrastructures4020032.

Appendix

A.1.

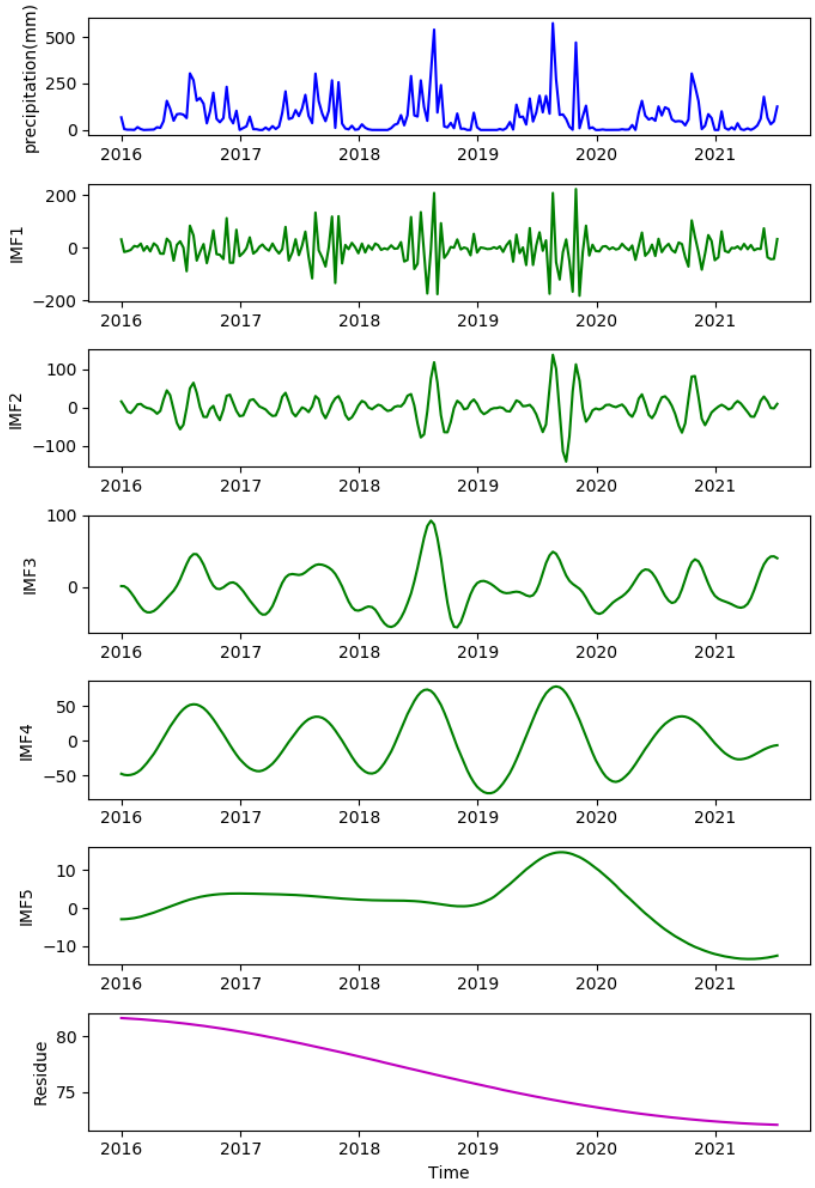

Figure A1. Ensemble Empirical Mode Decomposition (EEMD) on GPM IMERG catchment-averaged (every 10 days) precipitation data from the Bislak catchment. Upper plot (blue) is the precipitation data for the Bislak River catchment. The subsequent five plots (green) are decomposed Instinct Mode Functions (IMFs), and the lowest plot (purple) is the residual of the decomposition.

A.2.

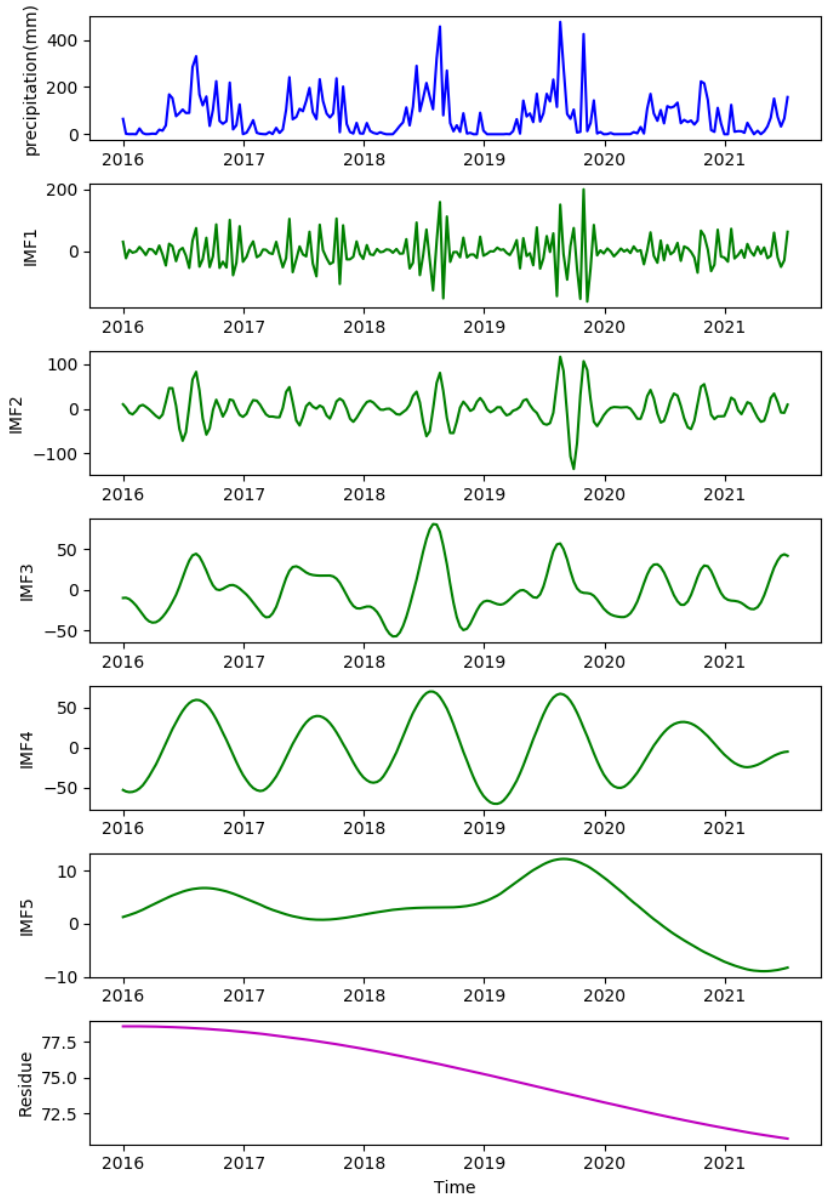

Figure A2. Ensemble Empirical Mode Decomposition (EEMD) on GPM IMERG catchment-averaged (every 10 days) precipitation data from the Laoag catchment. Upper plot (blue) is the precipitation data for the Laoag River catchment. The subsequent five plots (green) are decomposed Instinct Mode Functions (IMFs), and the lowest plot (purple) is the residual of the decomposition.

A.3.

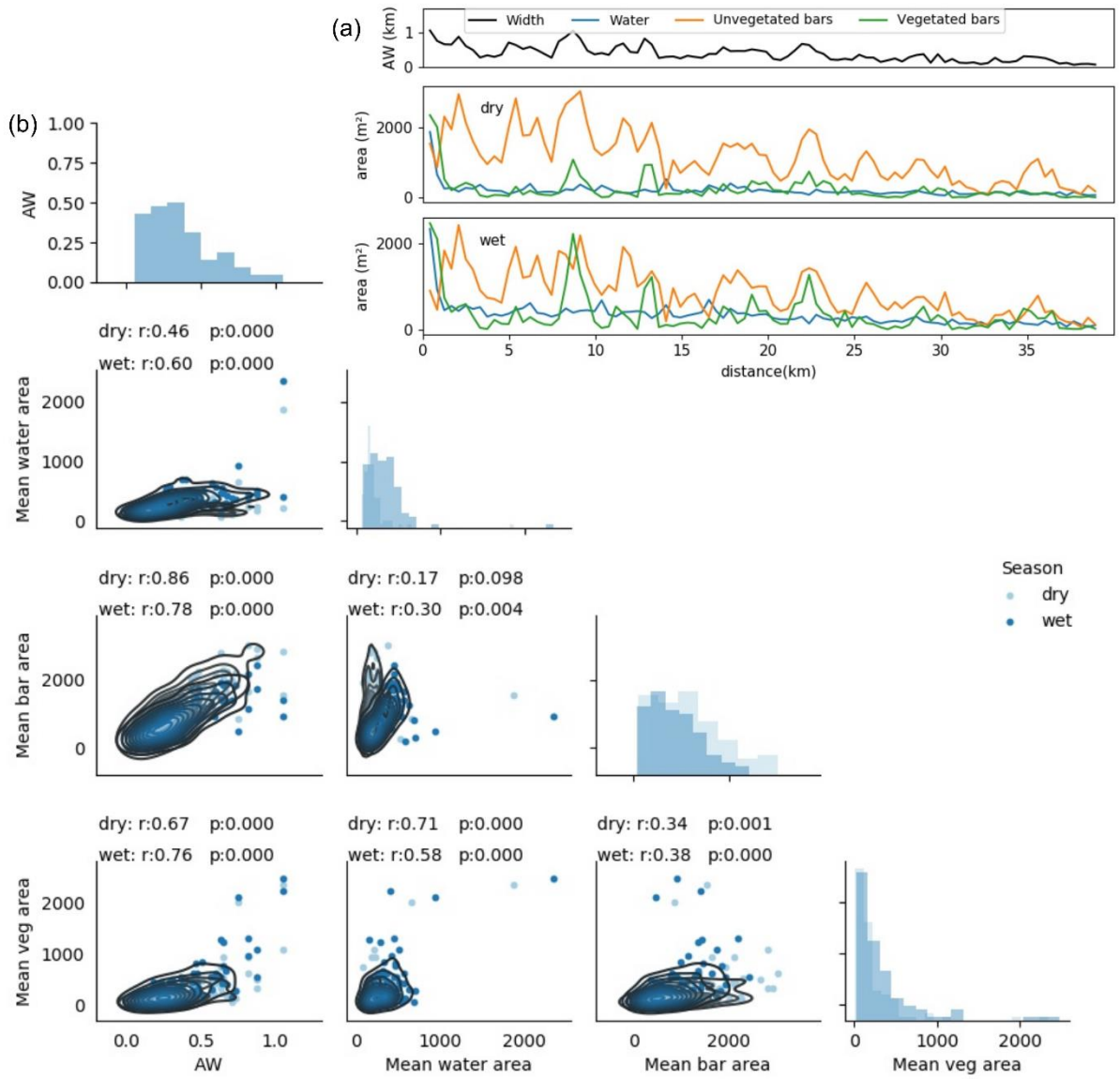

Figure A3. (a) Longitudinal trend in active width (AW) and mean area of three landforms (water, unvegetated bars, vegetated bars) for the Laoag River, for wet and dry seasons. (b) Matrix plots to represent correlations between mean values of landform areas and AW. Histograms illustrate mean value distributions at equal spaced spatial distance along the river. Kernel distribution estimation is shown using contour plots. Tables above each matrix plot summarise correlation coefficients (r) and associated statistical significance (p) between landforms area and AW in wet season and dry season.

A.4.

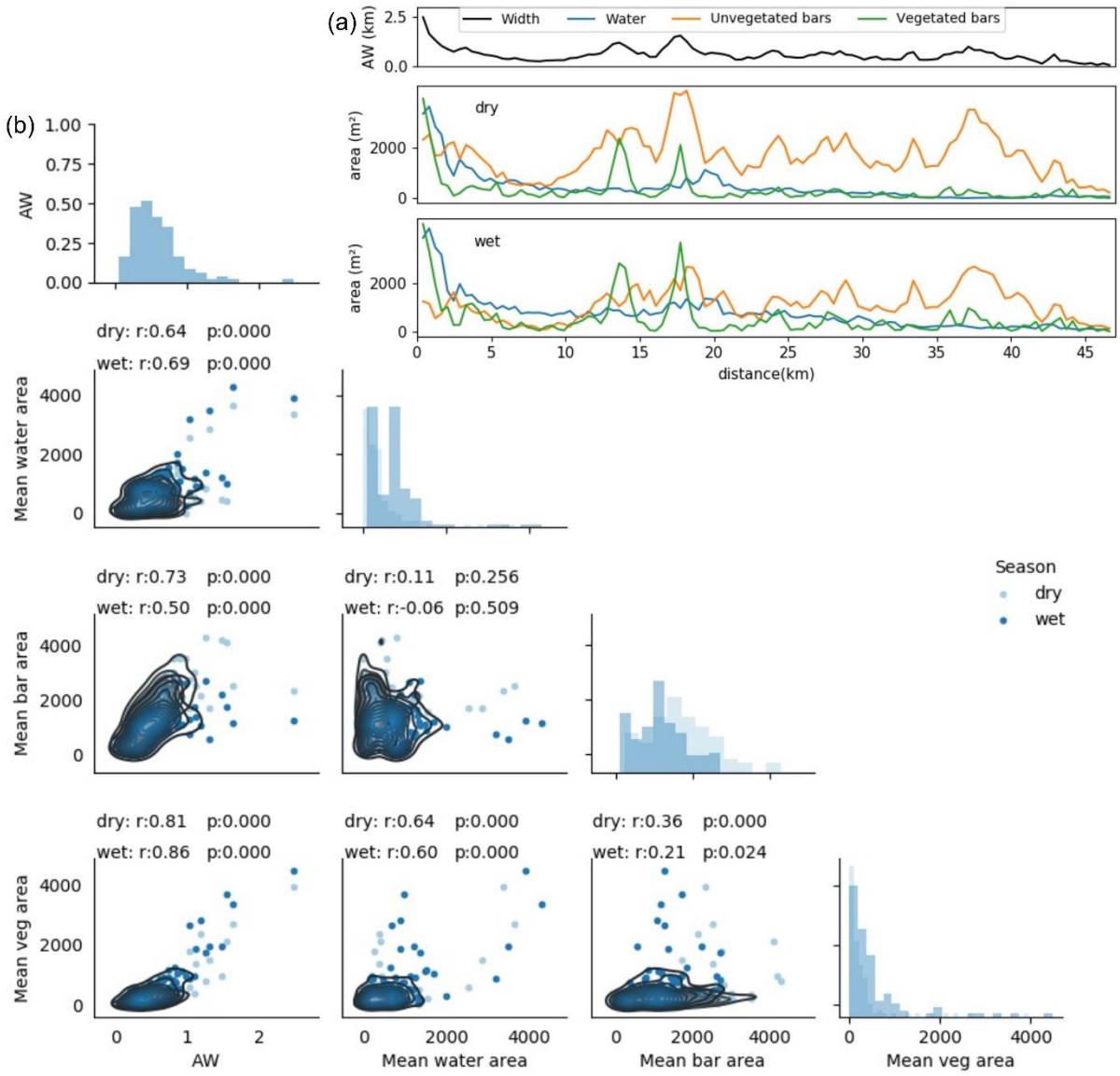

Figure A4. (a) Longitudinal trend in active width (AW) and mean area of three landforms (water, unvegetated bars, vegetated bars) for the Laoag River, for wet and dry seasons. (b) Matrix plots to represent correlations between mean values of landform areas and AW. Histograms illustrate mean value distributions at equal spaced spatial distance along the river. Kernel distribution estimation is shown using contour plots. Tables above each matrix plot summarise correlation coefficients (r) and associated statistical significance (p) between landforms area and AW in wet season and dry season.

A.5.

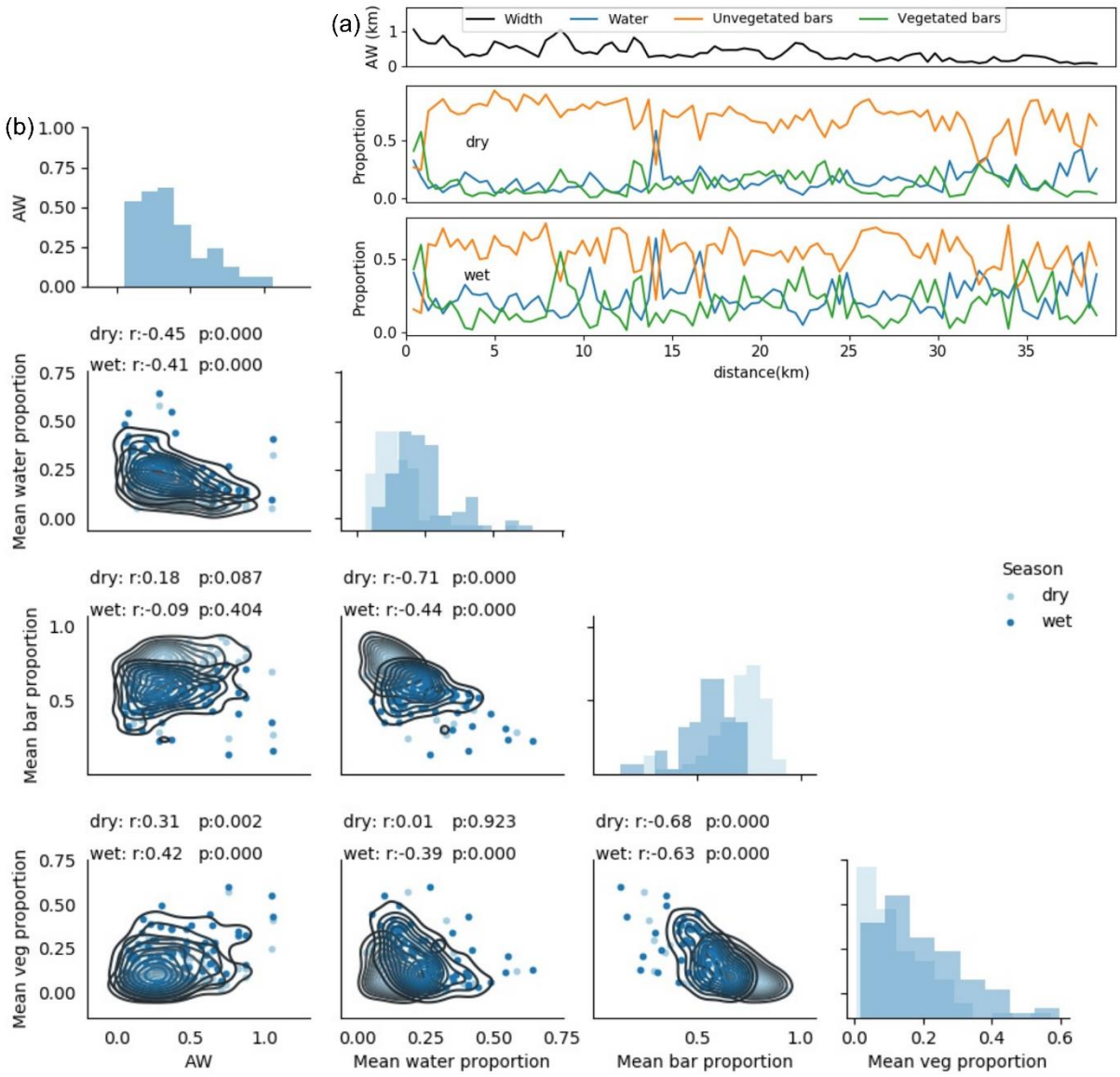

Figure A5. (a) Longitudinal trend in active width (AW) and mean proportion of three landforms (water, unvegetated bars, vegetated bars) for the Bislak River, for wet and dry seasons. (b) Matrix plots to represent correlations between mean values of landform proportions and AW. Histograms illustrate mean value distributions at ~410 m spatial distance along the river. Kernel distribution estimation is shown using contour plots. Tables above each matrix plot summarise correlation coefficients (r) and associated statistical significance (p) between landforms proportion and AW in wet season and dry season.

A.6.

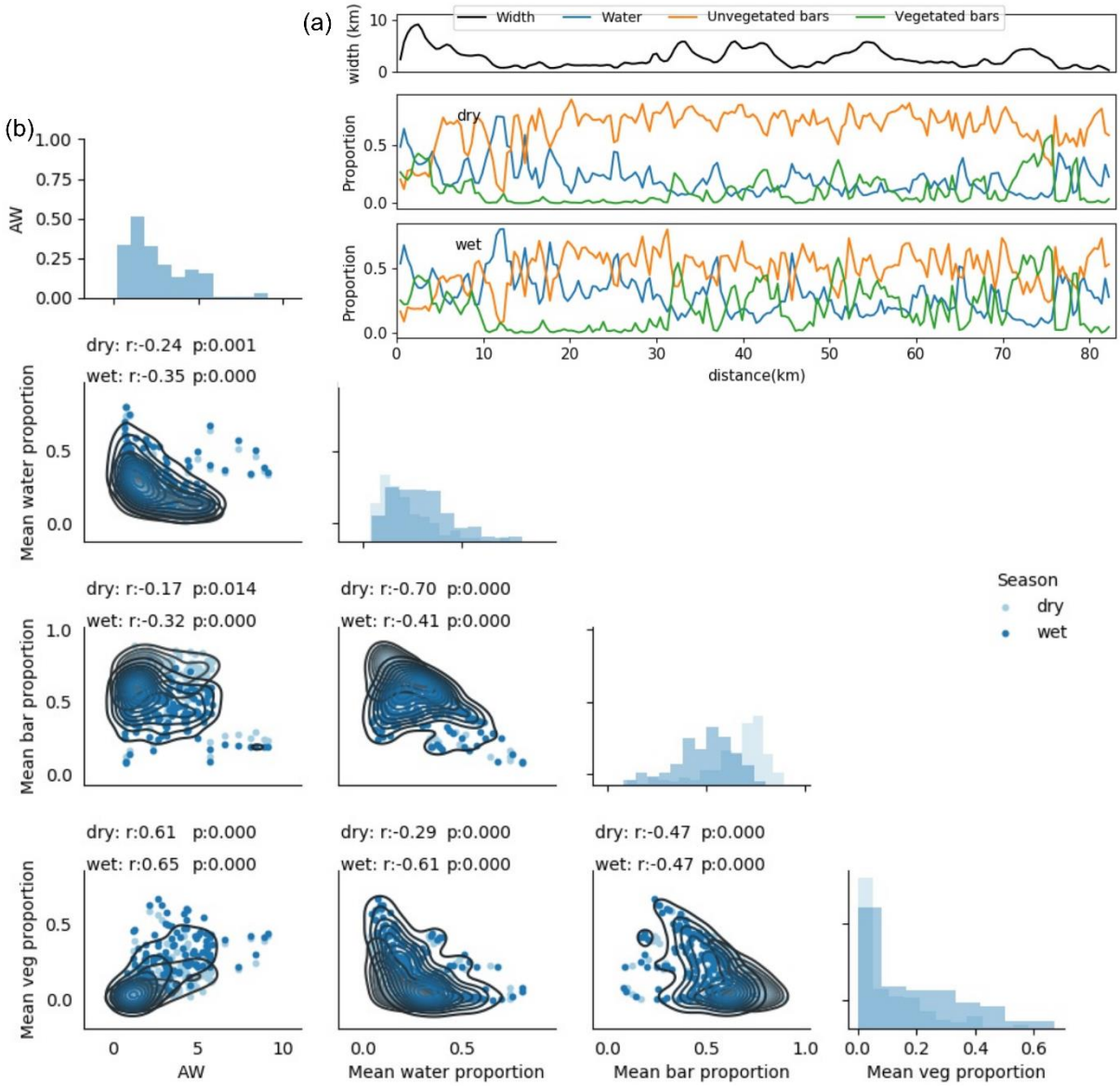

Figure A6. (a) Longitudinal trend in active width (AW) and mean proportion of three landforms (water, unvegetated bars, vegetated bars) for the Abra River, for wet and dry seasons. (b) Matrix plots to represent correlations between mean values of landform proportions and AW. Histograms illustrate mean value distributions at ~410 m spatial distance along the river. Kernel distribution estimation is shown using contour plots. Tables above each matrix plot summarise correlation coefficients (r) and associated statistical significance (p) between landforms proportion and AW in wet season and dry season.

A.7.

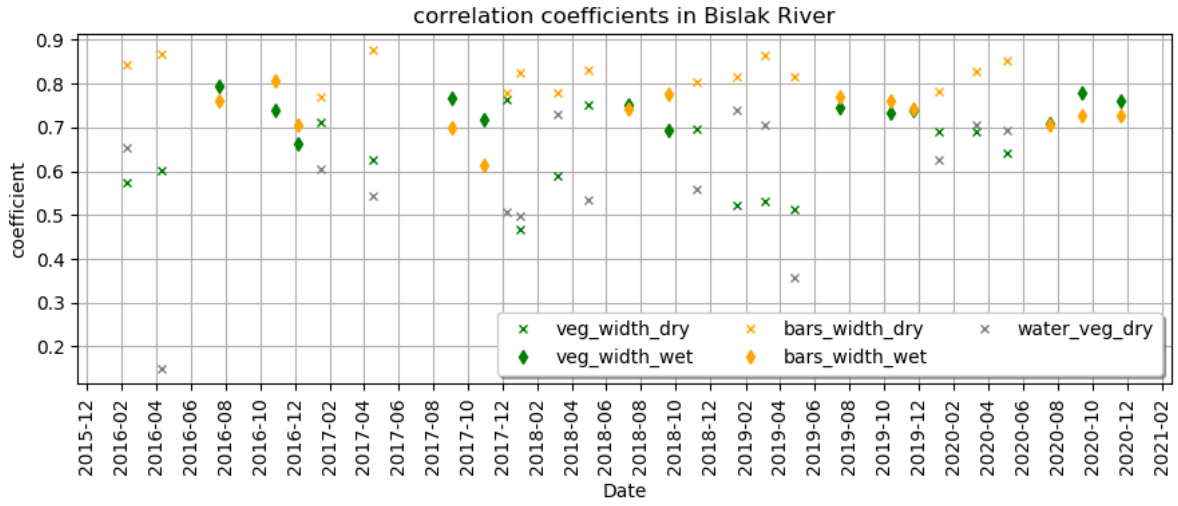

Figure A7. Bislak landforms Area- AW correlation coefficients time series.

A.8.

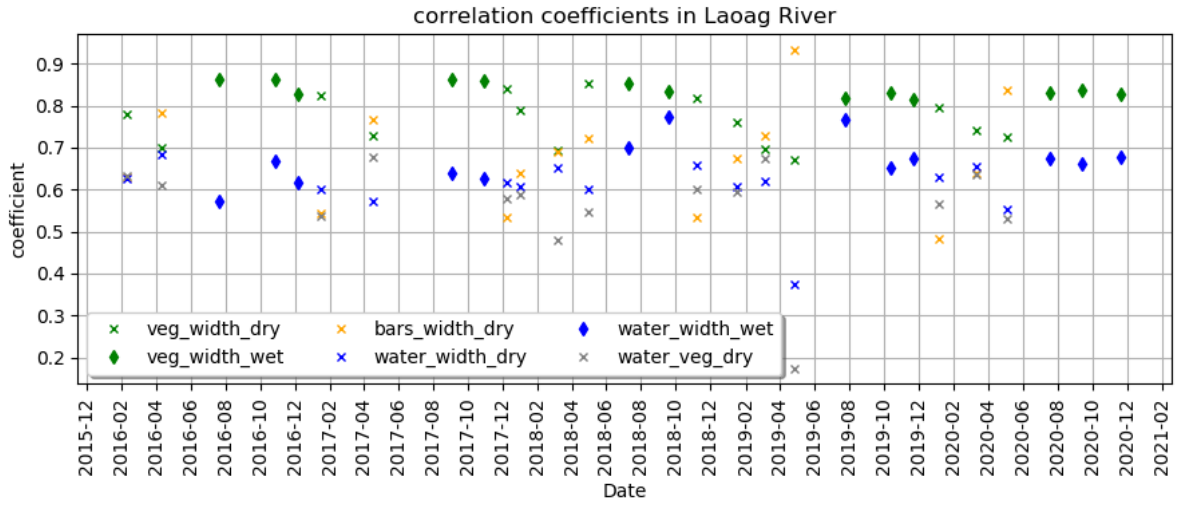

Figure A8. Laoag landforms Area- AW correlation coefficients time series.

A.9.

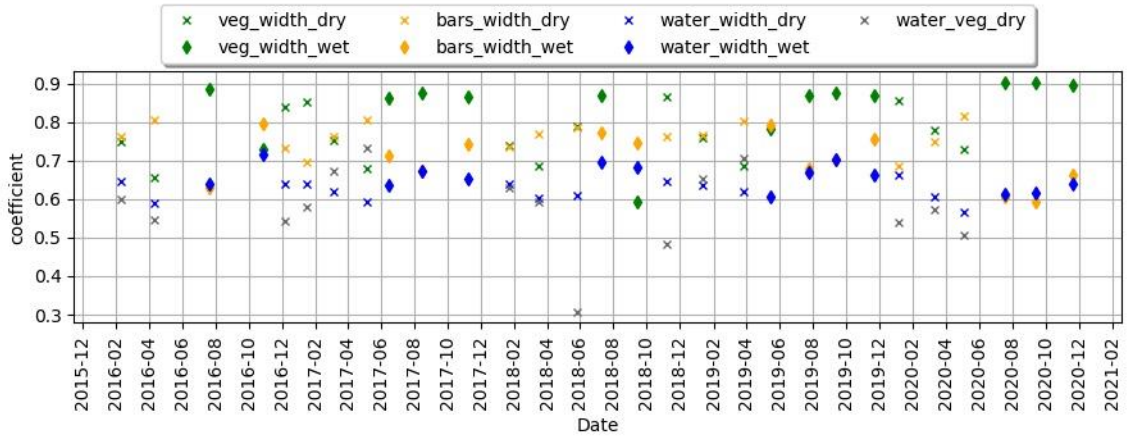

Figure A9. Abra landforms Area- AW correlation coefficients time series.

A.10.

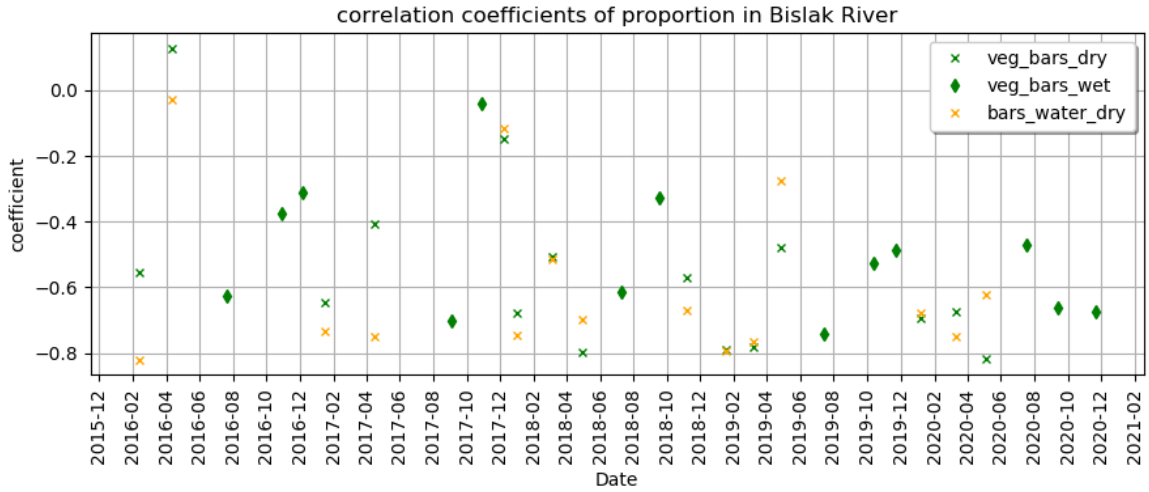

Figure A10. Bislak landforms Proportion- AW correlation coefficients time series.

A.11.

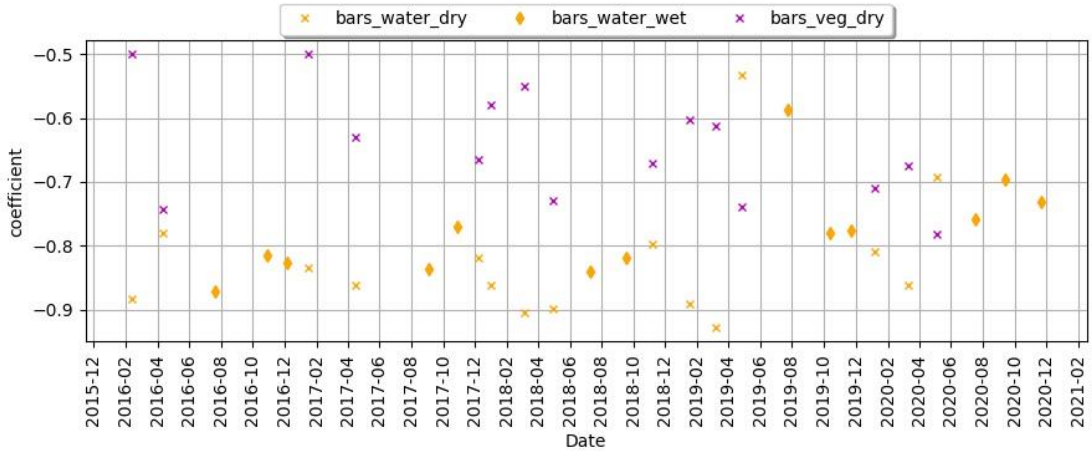

Figure A11. Laoag landforms Proportion- AW correlation coefficients time series.

A.12.

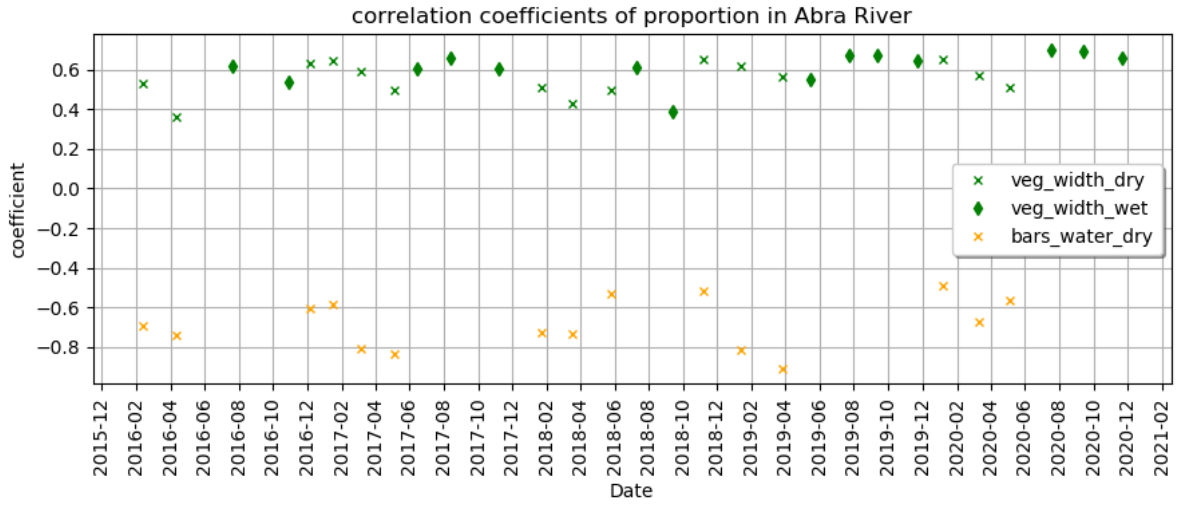

Figure A12. Abra landforms Proportion- AW correlation coefficients time series.